

Nonclassical Light  
for  
Atomic Physics  
and  
Quantum Teleportation

Jens Lykke Sørensen  
*Institute of Physics and Astronomy*  
*University of Aarhus*  
*DK-8000 Aarhus C, Denmark*

September 1998  
Ph. D. thesis  
Institute of Physics and Astronomy  
University of Aarhus  
Thesis advisor: E. S. Polzik

# Contents

<b>1</b>	<b>Prologue</b>	<b>5</b>
1.1	The Quantum Optics Lab . . . . .	5
1.2	Publications and presentations . . . . .	6
1.3	This Thesis . . . . .	7
<b>2</b>	<b>Squeezing in the Optical Parametric Oscillator</b>	<b>10</b>
2.1	Introduction . . . . .	10
2.2	Quantum theory of the OPO . . . . .	12
<b>3</b>	<b>Blue Light Induced Infrared Absorption</b>	<b>16</b>
3.1	The influence of BLIIRA on the OPO squeezing . . . . .	16
3.2	Experimental setup . . . . .	17
3.3	Results . . . . .	21
3.4	A qualitative explanation of BLIIRA . . . . .	24
3.5	Conclusions . . . . .	26
<b>4</b>	<b>Production of Squeezed Light</b>	<b>28</b>
4.1	Second harmonic generation . . . . .	28
4.1.1	Theoretical considerations . . . . .	29
4.1.2	Experimental results . . . . .	30
4.2	Parametric amplification . . . . .	32
4.3	Squeezed light generation and detection . . . . .	34
4.3.1	Homodyne detection of Squeezing . . . . .	34
4.3.2	Experiment . . . . .	35
4.4	Summary . . . . .	38
<b>5</b>	<b>Nonclassical Polarization Spectroscopy</b>	<b>40</b>
5.1	The Polarization Interferometer . . . . .	40
5.1.1	The setup . . . . .	40
5.1.2	The lineshape . . . . .	42
5.2	The Magneto Optical Trap . . . . .	44
5.2.1	Theory . . . . .	45
5.2.2	Characterization . . . . .	45
5.3	Polarization Squeezing . . . . .	47
5.4	Sub- Shot noise polarization spectroscopy . . . . .	49
5.5	Conclusions . . . . .	51

<b>6</b>	<b>Modulation spectroscopy on a MOT</b>	<b>53</b>
6.1	Motivation . . . . .	53
6.2	The setup . . . . .	55
6.3	Modulated absorption . . . . .	55
6.3.1	Experiment . . . . .	55
6.3.2	Modelling . . . . .	57
6.4	Modulated polarization rotation . . . . .	60
6.5	Diode laser phase noise spectroscopy . . . . .	61
6.6	Summary . . . . .	63
<b>7</b>	<b>Quantum noise of the Atomic Spin</b>	<b>64</b>
7.1	The physics of the Spin Noise . . . . .	65
7.1.1	Modelling spin noise in a V system . . . . .	66
7.1.2	Dependencies . . . . .	68
7.2	Experimental setup . . . . .	69
7.3	Measurements and results . . . . .	72
7.4	Being limited by the quantum spin noise . . . . .	77
7.5	Summary . . . . .	78
<b>8</b>	<b>Quantum Teleportation of Continuous Quantum Variables</b>	<b>80</b>
8.1	Basic principles in quantum teleportation . . . . .	80
8.1.1	Creating EPR correlated fields . . . . .	81
8.1.2	Teleportation of continuous variables . . . . .	86
8.2	Experimental setup . . . . .	89
8.3	Teleportation results . . . . .	90
8.4	Conclusions . . . . .	93
<b>9</b>	<b>The Internally Pumped Optical Parametric Oscillator</b>	<b>95</b>
9.1	Introduction . . . . .	95
9.2	Equations of motion . . . . .	97
9.3	Steady state solutions . . . . .	99
9.4	Quantum noise . . . . .	102
9.4.1	Fundamental field . . . . .	103
9.4.2	Subharmonics . . . . .	105
9.4.3	IOPO reflection . . . . .	106
9.5	Summary . . . . .	108
<b>10</b>	<b>Epilogue</b>	<b>109</b>
10.1	Conclusions . . . . .	109
10.1.1	Frequency tunable squeezed light generation . . . . .	109
10.1.2	MOT spectroscopy and spin noise . . . . .	110
10.1.3	Quantum teleportation . . . . .	112
10.1.4	Internally pumped OPO . . . . .	113
10.2	Outlook . . . . .	114
10.2.1	Spin squeezing and entangled atomic ensembles . . . . .	114
10.2.2	Quantum communication for teleportation and cryptography . . . . .	114
10.2.3	The IOPO as a compact squeezer . . . . .	115
<b>A</b>	<b>Classical OPO theory</b>	<b>116</b>
<b>B</b>	<b>Teleportation of discrete Quantum Variables</b>	<b>122</b>



# Chapter 1

## Prologue

### 1.1 The Quantum Optics Lab

The Quantum Optics Group in Aarhus started in 1993 with nothing but an empty room and a handful of money at its disposal. When I joined the group in 1994 this room was furnished and an optics table together with an Argon ion laser pumped Ti:Sapphire was about the only scientific equipment present in the lab. Since then the development of the lab has been almost explosive and the Quantum Optics Group has flourished. This should be accredited to the group leader Eugene Polzik, whose ideas, sometimes crazy, sometimes not, really has challenged me and my fellow students in the lab and inspired us to use abilities we did not know we had.

Having been with the group almost from its beginning, I have had the privilege of working with a multitude of very skilled people. The first of these is Lior Shiv with whom I worked on the BLIIRA measurements. The MOT work was done together with Jan Hald. He and I have shared many frustrations in the last couple of years with mode jumping lasers, burned ion pumps and one extremely playful Argon ion laser. We have however also shared many successes, and I am sure that without Jan the MOT work would not have turned out to be so fruitful as it is the case. Also involved in the MOT work have been Lasse Leick together with Nicolaj Jørgensen and John Erland. In fact the last two have been responsible for the construction of the MOT. During my visit at California Institute of Technology in the Quantum Optics Group of professor H. J. Kimble I have enjoyed to work together with Akira Furusawa, Nikos Georgiades and David Vernooy. I am specially grateful to Jeff Kimble for his hospitality and for giving me the possibility of participating in an exciting new project. Working in the stimulating environment at Caltech has taught me that a lot about the spirit needed to perform the complicated experiments often encountered in quantum optics. Furthermore I have assisted Peter Lodahl with his work on frequency doubling of diode lasers and the investigation of the phase noise in these. This work will not be presented in this thesis because my involvement here only was minor. Apart from the above mentioned people I have enjoyed the company of Christian Schori, Jens Peter Christensen, Jacob Skovborg and Mikkel Andersen. These guys have made the life in a dark basement a bit more interesting and they have contributed generously to the beerlist with a series of burned fuses, holes burnt in the wall by high power laser beams and interesting discussions for instance about the hole size in swiss cheese. Finally my warmest gratitude goes to my thesis advisor Eugene Polzik. With his eternal optimism and great patience he has been truly a great inspiration and a pleasure to work with.

I cannot thank my wife Line enough for her great patience and for supporting me on days when the lab work has left me with more questions than answers.

## 1.2 Publications and presentations

The work presented in this thesis has been the basis of the following publications

1. L. Shiv, J. L. Sørensen E. S. Polzik and G. Mizell, *Inhibited light-induces absorption in KNbO<sub>3</sub>*, Opt. Lett. **20**, 2270 (1995).
2. J. L. Sørensen, J. Hald, N. Jørgensen, J. Erland and E. S. Polzik, *Squeezing with  $\chi^{(2)}$  for atomic physics and spectroscopy*, Quantum Semiclass. Opt. **9**, 239 (1997).
3. P. Lodahl, J. L. Sørensen and E. S. Polzik, *High efficiency second harmonic generation with a low power diode laser*, Appl. Phys. B **64**, 383 (1997).
4. J. L. Sørensen, J. Hald and E. S. Polzik, *Fundamental noise of an atomic spin measurement*, Journ. Mod. Opt. **44**, 1917 (1997).
5. J. L. Sørensen, J. Hald and E. S. Polzik, *Spectroscopy on a modulated magneto-optical trap*, Opt. Lett. **23**, 25 (1998).
6. J. Hald, J. L. Sørensen, L. Leich and E. S. Polzik, *Quantum noise of cold atomic spins illuminated with non-classical light*, Optics Express **2**, 93 (1998). Found on WWW at <http://epubs.osa.org/oearchive/source/3024.htm>.
7. J. L. Sørensen, J. Hald and E. S. Polzik, *Quantum noise of an atomic spin polarization measurement*, Phys. Rev. Lett. **80**, 3487 (1998).
8. J. L. Sørensen and E. S. Polzik, *Internally pumped subthreshold OPO*, Appl. Phys. B **66**, 711 (1998).
9. E. S. Polzik, J. L. Sørensen and J. Hald, *Subthreshold tunable OPO: a source of nonclassical light for atomic physics experiments*, Appl. Phys. B **66**, 759 (1998).
10. A. Furasawa, J. L. Sørensen, S. L. Braunstein, C. A. Fuchs, H. J. Kimble and E. S. Polzik, *Unconditional quantum teleportation*, Submitted to *Science*, July 1998.

In addition to these publications the work has been presented at the following conferences and summer schools

- Enrico Fermi School of Physics CXXXI *Coherent and Collective Interactions of Particles and Radiation Beams*. July 1995, Varenna, Italy. Organizers: A. Aspect, W. Barletta and R. Bonifacio.
- L'Ecole de Physique des Houches  $\chi^{(2)}$  *Second Order Nonlinear Optics: From Fundamentals to Applications*. April 1996, Les Houches, France. Organizers: C. Fabre and J. P. Pocholle.
- Annual Meeting of the Danish Physical Society. May 1996, Nyborg, Denmark.
- European Science Foundation annual conference on Quantum Optics. September 1996, Castelvecchio Pascoli, Italy. Organizers: K. Burnett and L. Lugiato.
- *Fundamentals of Quantum Optics IV*. February 1997, Kuhtai, Austria. Organizer: F. Ehlotzky.
- Annual Meeting of the Danish Physical Society. May 1997, Nyborg, Denmark.
- *New Frontiers in Laser-Atom Interactions* June 1997, Sandbjerg Manor, Denmark. Organizer: N. O. Andersen.
- Annual Meeting of the Optical Society of America. October 1997, Long Beach, USA.

### 1.3 This Thesis

The work presented in this thesis has been devoted to the production and use of nonclassical states of light for improving the performance of normally classical behaving optical systems. Here we have chosen to focus on improved sensitivity in spectroscopy and the teleportation with high efficiency of states of the radiation field. However nonclassical light may prove useful in many other aspects of physics such as optical communication, cryptography and the altering of fundamental atomic radiation processes, which together with quantum non-demolition measurements probably are of more academic interest. For a general introduction to the field of Quantum Optics and the role of nonclassical states of light in this field, the reader is referred to ref. [1].

The thesis has been divided into four major topics: The generation of frequency tunable squeezed light covering chapters 2-4, spectroscopy and spin noise in a magneto optical trap in chapters 5-7, quantum teleportation in chapter 8 and the theory of the Internally Pumped OPO in chapter 9. The thesis is intended to be written so that each chapter to a great extent can be read independent of the others, however to obtain a coherent picture it is recommended to read the chapters in a consecutive way.

Chapter 2 is intended to give a general introduction to the OPO with emphasis on the generation of squeezed vacuum in this device. In addition to this the squeezing work presented in the following chapters will be fit into a greater picture, where experiments involving the use of nonclassical light are reviewed.

It turned out that a limitation on the quantum noise reduction achieved in the subthreshold OPO, used in this work, was the nonlinear loss associated with Blue Light Induced InfraRed Absorption (BLIIRA) in the OPO  $\text{KNbO}_3$  crystal. Chapter 3 is devoted to an investigation of the BLIIRA and the most important result in this chapter is that the BLIIRA is reduced as the crystal temperature is increased. As a result the OPO escape efficiency, being the governing factor of the degree of squeezing in this work, is increased. From the theoretical side a qualitative model accounting for the behavior of BLIIRA is put forward. The work from chapter 3 has been published in (1.).

Based on the BLIIRA results chapter 4 describes our frequency tunable squeezed light source. This is centered around a subthreshold OPO pumped with the second harmonic of a Ti:Sapphire laser operating at 917 nm. The performance of our external cavity frequency doubler is described and the OPO is characterized. Quantum noise reduction in the OPO output of as much as -5 dB is demonstrated. This considerable amount of squeezing was within reach because our nonclassical light source was operating around 917 nm, where the phasematching temperature in  $\text{KNbO}_3$  is around 130°C and consequently BLIIRA was reduced by a factor of 2-3. The publication (2.) is based upon the work in chapter 4.

In chapter 5 it is demonstrated how the squeezed vacuum output of the OPO can be used to produce a polarization squeezed beam. This beam is used to probe a polarization interferometer providing sub-shot noise sensitivity. In this experiment a quantum noise reduction of -3 dB is achieved. The polarization interferometer is used to probe the anisotropy of an ensemble of cold, trapped Cs atoms. With a probe in a coherent state, shot noise limited sensitivity is demonstrated, and with a nonclassical probe the limiting noise is reduced by -2.3 dB. The target of the polarization interferometer is a Caesium Magneto Optical Trap (MOT), which is characterized in chapter 5 as well. Parts of the results from this chapter can be found in the publications (2.), (4.), (6.), (7.) and (9.).

The atomic signal obtained in the polarization interferometer turned out to be rather complicated and a more thorough investigation of this signal together with the modulated absorption signal is the basis of chapter 6. The spectroscopic signals in the MOT were generated by modulating the trapping laser frequency and transferring this modulation to the probe via the atoms. The trapping laser was a semiconductor laser and consequently full of phase noise. In chapter 6 we also demonstrate MOT spectroscopy using this phase noise to generate the atomic signal. The lineshapes are modelled by a simple three level theory serving to provide a qualitatively understanding of the atomic signals. These results are published in (5.).

When the atoms were trapped with an almost ideal laser and the optical depth in the MOT was appreciable, the intrinsic atomic spin noise was seen to contribute significantly to the polarization in-

terferometer signal. In chapter 7 the results of our spin noise measurements in a MOT are presented. Although the experiments described in chapters 6 and 7 are not directly involving nonclassical light, they can be considered to be the initial stage of our attempts of mapping the nonclassical correlation of the OPO output onto the ensemble of trapped atoms. The result of this mapping would be a squeezed spin state in which the fluctuations are reduced in one component of the collective atomic angular momentum. The results of chapter 7 reveal the atomic quantum noise and show the distinction between this and technical atomic noise. A simplified model, accounting for the atomic noise, is put forward and the relevant atomic and optical parameters are pointed out. The publications (4.), (6.) and (7.) cover the work presented in chapter 7. This chapter concludes the line of work done by the author with the goal of studying the interaction between nonclassical light and atoms.

The outcome of a joint project between the Quantum Optics Group at California Institute of Technology and the Quantum Optics Group in Aarhus is presented in chapter 8. This project was devoted to demonstrate quantum teleportation of continuous variables. Using two subthreshold OPO's and mixing the squeezed vacuum outputs with an appropriate phase, two entangled fields were created in an EPR like state. This nonlocal state was used to teleport the continuous quadrature phases of an optical field over roughly  $\frac{1}{2}$  meter. A measure of the quality of the teleportation protocol, called the fidelity, is defined. It is shown that the use of only classical states of light will limit the fidelity to be smaller 0.50. The teleportation experiment yielded a fidelity of 0.58, proving that the input quantum state was teleported more efficient than it is possible with classical means. The results of chapter 8 will hopefully soon be published in (10.).

As a theoretical project the author has analyzed the system of a doubling cavity in which the second harmonic is nondegenerately downconverted into subharmonics in the adjacent longitudinal cavity modes. This system is denoted The Internally Pumped OPO (IOPO) since the OPO pump is generated inside the OPO nonlinear medium. The results of this analysis can be found in chapter 9. The general approach allows the second harmonic to be resonated in the cavity with an arbitrary detuning and with (almost) arbitrary losses. Due to the analytic procedure used, the second harmonic losses must always be somewhat larger than the fundamental losses. The threshold for parametric oscillations is derived and the squeezing spectra for the fundamental and the subharmonics are derived below the threshold. Arbitrary strong squeezing is predicted in the subharmonics and an experiment, in which the fundamental field reflected off the IOPO cavity acts as a local oscillator for the subharmonics, is simulated. This shows that perfect squeezing can be found in the cavity reflection at frequencies being an integer times the free spectrum range of the IOPO cavity. This work has been published in (8.).

Finally the thesis is concluded in chapter 10 with a resumé containing the most important results. This is followed by an outlook on the future prospects of the various projects in which the author has been involved.



Figure 1.1: The Experimental Quantum Optics Group in Aarhus in the spring of 1998. From the left: Jens Peter Christensen, Lasse Leick, Christian Schori, Mikkel Andersen, Jens Lykke Sørensen, Jacob Andersen, Jan Hald and Eugene Polzik.

## Chapter 2

# Squeezing in the Optical Parametric Oscillator

Since a lot of the work and many of the results presented in this thesis utilize the theory of the Optical Parametric Oscillator (OPO), we will start by considering this device in some detail and derive some useful formulas in this context. This will also serve to establish a notation, which will be used throughout the thesis. The chapter starts with some general remarks about the OPO followed by a review of experiments performed so far, in which nonclassical light from OPO's has been used for atomic physics and spectroscopy. After this introduction we will go into more detail with the quantum theory of the OPO and derive the spectrum of quantum fluctuations of the OPO output. This will enable us to identify the conditions under which the quantum noise reduction in the OPO output is optimized.

### 2.1 Introduction

By an Optical Parametric Oscillator is understood an optical resonator made up of spherical reflectors with a nonlinear  $\chi^{(2)}$  medium placed between them. The nonlinear medium can be pumped by a resonant or nonresonant field with a frequency  $2\omega$ , and by means of the nonlinear interaction any signal field injected into the resonator at a frequency  $\omega_-$  will together with the pump generate an idler field at the frequency  $\omega_+$ . In the rest of this chapter the pump is assumed not to be resonant in the OPO cavity. In order to preserve energy the frequencies must fulfill the relation  $\omega_+ + \omega_- = 2\omega$ . This process is known as Difference Frequency Generation. If however the frequency of the external input is exactly half the pump frequency, meaning that the signal and idler fields are indistinguishable, the OPO will act as a phase sensitive amplifier. This should be understood in the sense that if the pump has the time dependence  $\cos 2\omega t$ , the component of the injected fields with the dependence  $\cos \omega t$  will be amplified whereas the component with the dependence  $\sin \omega t$  will be deamplified in the OPO. Since it is not possible to compare phases between fields oscillating at different frequencies, the above arguments are only true within a common phaseshift. When the signal and idler frequencies are different or the fields have different polarizations, the OPO is said to be operated nondegenerate as opposed to the degenerate OPO in which the signal and idler fields are indistinguishable. The mode of operation of the OPO is determined by the phasematching conditions in the nonlinear medium. In the OPO's described in this thesis only noncritical phasematching is used, and in this case switching between degenerate and nondegenerate operation can be done by changing the temperature of the nonlinear medium. For a more elaborate treatment of the classical properties of the OPO, the reader is referred to Appendix A.

If the pump field reaches a certain critical value, a phase transition occurs, and the OPO will acquire a coherent output even without any input. This operating point is known as the threshold of the OPO. Above threshold operation results in two coherent output fields at frequencies  $\omega_+$  and  $\omega_-$ . The

frequency splitting between these fields can become very large depending on the phasematching conditions and the resonance properties of the OPO[2]. This makes the OPO above threshold very attractive for atomic and molecular spectroscopy since signal and idler can cover a wavelength range of several hundreds of nanometers stretching into regions otherwise inaccessible to more conventional laser sources. Unfortunately the OPO is very unstable above threshold, and single frequency operation of such a device is a nontrivial task. In the rest of this thesis only the subthreshold OPO will be considered.

From a quantum mechanical point of view the OPO is interesting as well. Just as the OPO below threshold acts as a phase sensitive amplifier for a coherent input, it is also amplifying or deamplifying the input vacuum fluctuations always being present. Quantum Electrodynamics tells us that the ground state of the electromagnetic field possess a certain amount of energy stored in the vacuum fluctuations[3]. These field fluctuations do not have a well defined phase, but it is always possible to divide them into two independent components oscillating like  $\cos \omega t$  and  $\sin \omega t$ . In Quantum Optics these components are called the *Quadrature Phases*[4]. When the vacuum fluctuations enter the subthreshold OPO, the  $\cos \omega t$  component will be amplified and the  $\sin \omega t$  component deamplified. As a result the OPO can create a so called *Squeezed Vacuum* state[5] in which quantum fluctuations in one quadrature can be reduced at the expense of increased fluctuations in the complementary quadrature.

In many optical experiments only one of the quadrature phases are detected and in these experiments appropriately phased squeezed states can be utilized to achieve sensitivity beyond the standard quantum limit. In atomic physics experiments squeezed light was first employed in 1992, where a squeezed probe generated by a subthreshold OPO state was used in FM saturation spectroscopy to improve the probe shot noise limited signal to noise ratio with 3 dB[6][7]. This experiment was followed up by a demonstration of nonclassical two photon excitation, where the quantum correlated photon pairs in the OPO output excited a double optical resonance[8]. Here a deviation from the usual  $I^2$  dependence of the two photon excitation rate was observed.  $I$  is the intensity of the field driving the two photon transition. This deviation was attributed to the quantum correlated nature of the OPO output, which ideally should cause a linear dependence on  $I$  in the weak intensity limit. This series of experiments was concluded by a demonstration of the applicability of atoms as nonlinear frequency mixers for ultrahigh frequencies. By driving an atomic three level ladder transition with the subthreshold OPO output as well as a coherent field, quantum correlations present at 25 THz were demodulated to yield the DC interference signal[9].

The work presented in this thesis on sub-shot noise spectroscopy utilize the subthreshold OPO as well. However we employed the squeezed vacuum output to generate polarization squeezed light, which, used in our polarization interferometer, reduced the noise floor with 3 dB[10]. When probing the spin state of atoms with the polarization interferometer, we demonstrated a quantum noise reduction of 2.5 dB[11]. The details of this experiment can be found in chapter 5.

The orthogonally polarized twin beams coming from the type II phasematched OPO has also proven useful for sub-shot noise spectroscopy as demonstrated in ref. [12]. A triply resonant semi monolithic OPO, pumped with the second harmonic of a Nd:YAG laser, generated two correlated beams of which one was driving the  $4S_{1/2} \rightarrow 5S_{1/2}$  two photon transition in potassium together with a diode laser. The second beam was detected independently and the photocurrents were subtracted to yield a sub-shot noise signal in the absence of atomic absorption. This procedure resulted in a reduction of the noise floor of the measurement of 1.9 dB relative to the coherent state level and a sensitivity to absorption at the level of  $10^{-7}$ .

A worthy competitor to the OPO in terms of producing sub-shot noise signals is the amplitude squeezed diode laser. By injection locking these lasers and/or filtering the drive current, the longitudinal sidemodes can be suppressed dramatically, resulting in an amplitude squeezed central mode well suited for spectroscopy purposes[13]. Using this approach 1.9 dB of amplitude noise reduction below the shot noise level has been demonstrated and the light source was used for exciton spectroscopy with a reduction of the noise floor of 1 dB relative to the coherent state limit[14]. The same technique has been used for highly sensitive atomic spectroscopy with a lowering of the noise floor close to 1 dB[15] and a sensitivity around a few parts in  $10^8$ [16]. A more practical application of amplitude squeezed diode lasers is the gas flow velocimetry demonstrated in ref. [17]. Here a 2 dB noise reduction in the probe was observed,

yielding an increase in signal to noise of 1 dB in the Doppler Anemometry.

In order to familiarize ourselves with the quantum features of the subthreshold OPO, we will now derive the squeezing spectrum of the output of this device.

## 2.2 Quantum theory of the OPO

From a quantum mechanically point of view, the degenerate OPO is described by the Hamiltonian

$$\mathcal{H} = \hbar\omega a^\dagger a + \hbar\zeta (a^2 \alpha_2^* + \alpha_2 a^{\dagger 2}) + \mathcal{H}_{Decay} \quad (2.1)$$

Here  $\alpha_2$  is the pump field, which is assumed to be strong, and can therefore be described by the  $c$  number expectation value of its field operator.  $\zeta$  is the nonlinear coupling constant closely related to the  $\xi$  defined Appendix A and finally the coupling of the downconverted quantum field  $a$  to the reservoir of electromagnetic field modes outside the OPO cavity is described through the Hamiltonian  $\mathcal{H}_{Decay}$ .

The approach that will be used here is what is usually called the Semiclassical Method[18]. Here we derive the Heisenberg equations of motion and solve these for the expectation values of the field operators. This gives us the steady state operating point for the OPO around which we can linearize the fluctuations of the quantum fields. Due to the linearization procedure we do not expect our treatment to be valid in the regions of the parameter space where the quantum fluctuations become very large. Here higher order corrections come into play and more rigorous treatments are needed[19][20][21].

From (2.1) we derive the equation of motion for the field  $a$

$$\frac{da}{dt} = -i\omega a - 2i\zeta\alpha_2 a^\dagger - \gamma a + \sqrt{2\kappa}a^{in} + \sqrt{2(\gamma - \kappa)}b^{in} \quad (2.2)$$

where the 'in' fields are assumed to be in the vacuum state.

We now define the quadrature phase operator for the slowly varying envelope of  $a$  to be

$$X(\theta) = ae^{-i(\omega t + \theta)} + a^\dagger e^{i(\omega t + \theta)} \quad (2.3)$$

and note that the commutator between two quadrature operators is

$$[X(\theta), X(\theta')] = 2i \sin(\theta' - \theta) \quad (2.4)$$

since the downconverted field  $a$  must obey standard Boson commutation relations  $[a, a^\dagger] = 1$ . In contrast to the annihilation operator  $a$  the quadrature operators are Hermitian and consequently observables. In fact it turns out that the quadrature  $X(\theta)$  is what a homodyne detector with local oscillator phase  $\theta$  relative to  $a$  detects[22]. Having the commutator at hand we can write up a Heisenberg uncertainty relation for the quadratures

$$\langle \delta X(\theta)^2 \rangle \langle \delta X(\theta')^2 \rangle \geq \sin^2(\theta' - \theta) \quad (2.5)$$

From this it is now clear that the quadratures  $X(\theta)$  and  $X(\theta + \pi/2)$  are complementary, meaning that we can never know the exact expectation value of both simultaneously. As a result of (2.5), a measurement of both  $X(\theta)$  and  $X(\theta + \pi/2)$  has to be accompanied by a certain amount of noise, which is what we mean by the quantum noise of light. The vacuum state and the coherent state are minimum uncertainty states, meaning that the equality sign in (2.5) applies for these states, and moreover the quantum noise is distributed equally between the two complementary quadratures. Furthermore we see that the quadratures  $X(\theta)$  and  $X(\theta \pm \pi)$  are equivalent in terms of the quantum noise. This is because the fluctuations associated with the quantum noise are defined with respect to an axis in phase space along which the variance of these fluctuations has a certain value.

Inserting (2.3) in (2.2) we find the equation of motion for the quadrature phases.

$$\frac{dX(\theta)}{dt} = 2\zeta\alpha_2 X(-\theta - \pi/2) - \gamma X(\theta) + \sqrt{2\kappa}X^{in}(\theta) + \sqrt{2(\gamma - \kappa)}Y^{in}(\theta) \quad (2.6)$$

where  $X^{in}(\theta)$  is the quadrature of the incoming field  $a^{in}$  and  $Y^{in}(\theta)$  is the same for the  $b^{in}$  field. These are still assumed to be vacuum fields. We have chosen the pump field  $\alpha_2$  to be real, so that its phase will set the overall phase of this problem. If we now take the expectation value of (2.6) and look for nontrivial steady state solutions, we obtain the threshold condition

$$(\alpha_2^{th})^2 = \left(\frac{\gamma}{2\zeta}\right)^2 \quad (2.7)$$

where we have used that the expectation value of the 'in' fields is zero.

Restricting ourselves to analyze the fluctuations of the OPO below threshold, we define the fluctuating part of the field operator as

$$q(\theta) = X(\theta) - \langle X(\theta) \rangle \quad (2.8)$$

Furthermore we define the OPO pump parameter  $\sigma$  as  $\sigma = \alpha_2/\alpha_2^{th}$ . Using (2.7) and (2.8) in (2.6) we find the equations of motion for the fluctuations of the quadrature phases

$$\frac{dq(\theta)}{dt} = -\gamma [q(\theta) - \sigma q(-\theta - \pi/2)] + \sqrt{2\kappa}q^{in}(\theta) + \sqrt{2(\gamma - \kappa)}p^{in}(\theta) \quad (2.9)$$

The vacuum fluctuation quadratures  $q^{in}$  and  $p^{in}$  have been defined analogous to  $q$  by substituting  $X$  with  $X^{in}$  and  $Y^{in}$  respectively. From (2.9) it is seen that the eigenvectors of our linear system of equations are directed along  $\theta = \pm\pi/4$ , and by using that  $q(\theta \pm \pi) = -q(\theta)$ , we can readily write up the noise equations in this basis

$$\begin{aligned} \frac{dq(-\pi/4)}{dt} &= -\gamma(1 - \sigma)q(-\pi/4) + \sqrt{2\kappa}q^{in}(-\pi/4) + \sqrt{2(\gamma - \kappa)}p^{in}(-\pi/4) \\ \frac{dq(\pi/4)}{dt} &= -\gamma(1 + \sigma)q(\pi/4) + \sqrt{2\kappa}q^{in}(\pi/4) + \sqrt{2(\gamma - \kappa)}p^{in}(\pi/4) \end{aligned} \quad (2.10)$$

With the goal of finding the spectrum of fluctuations, (2.10) is now Fourier transformed, and the fields going out from the OPO are found by using the beamsplitter relation on the output coupler

$$q^{out}(\theta) = \sqrt{2\kappa}q(\theta) - q^{in}(\theta) \quad (2.11)$$

where high reflectivity of the output coupler has been assumed. As a result we find

$$\begin{aligned} q^{out}(-\pi/4, \Omega) &= \left(\frac{2\eta}{i\Omega + 1 - \sigma} - 1\right)q^{in}(-\pi/4) + 2\sqrt{\eta(1 - \eta)}p^{in}(-\pi/4) \\ q^{out}(\pi/4, \Omega) &= \left(\frac{2\eta}{i\Omega + 1 + \sigma} - 1\right)q^{in}(\pi/4) + 2\sqrt{\eta(1 - \eta)}p^{in}(\pi/4) \end{aligned} \quad (2.12)$$

Here  $\eta$  is the OPO escape efficiency defined as  $\eta = \kappa/\gamma \simeq \mathcal{T}/(\mathcal{T} + \mathcal{L})$ , where  $\mathcal{T}$  is the output coupler transmission and  $\mathcal{L}$  are the remaining intracavity losses. The last equality applies for  $\mathcal{T} + \mathcal{L} \ll 1$ . The frequency  $\Omega$  has been normalized to the OPO cavity bandwidth  $\gamma$ . It should be noted here that the field operators after the Fourier transformation are defined in the frequency space  $q = q(\Omega)$  in contrast to before the transformation, where the fields were time dependent  $q = q(t)$ . To keep the notation simple, we use the same symbols for the field operators before and after the Fourier transformation, and just keep in mind the space in which they are defined.

In order to obtain the spectra of fluctuations we now utilize that orthogonal 'in' fields are uncorrelated and that the fields  $q^{in}$  and  $p^{in}$  are uncorrelated since they are different modes of the vacuum field.

$$\langle q^{in}(\pm\pi/4, -\Omega)p^{in}(\pm\pi/4, \Omega) \rangle = \langle p^{in}(\pm\pi/4, -\Omega)q^{in}(\pm\pi/4, \Omega) \rangle = 0 \quad (2.13)$$

Furthermore we utilize that the spectrum of vacuum fluctuations is white, meaning that we can normalize these in the bandwidth of interest,  $B$ , to yield a vacuum noise level of 1

$$B \langle q^{in}(\pm\pi/4, -\Omega)q^{in}(\pm\pi/4, \Omega) \rangle = B \langle p^{in}(\pm\pi/4, -\Omega)p^{in}(\pm\pi/4, \Omega) \rangle = 1 \quad (2.14)$$

This leads us to the spectra of fluctuations for the outgoing field quadratures of the OPO

$$\langle q^{out}(-\pi/4)^2 \rangle = 1 + \eta \frac{4\sigma}{\Omega^2 + (1 - \sigma)^2} \quad (2.15)$$

$$\langle q^{out}(\pi/4)^2 \rangle = 1 - \eta \frac{4\sigma}{\Omega^2 + (1 + \sigma)^2} \quad (2.16)$$

The '1' in front of each of the variances above corresponds to the vacuum noise level. It is now clear that the quantum fluctuations in the output of the OPO can be reduced below the vacuum noise level in the  $\theta = \pi/4$  quadrature if  $\eta$  and  $\sigma$  both are nonzero. In fact the fluctuations go to zero corresponding to perfect squeezing when  $\eta = \sigma = 1$ , these parameters are relevant for an OPO with no internal losses being exactly on threshold. Of course our linearized theory is not valid too close to threshold since the fluctuations in the  $\theta = -\pi/4$  quadrature become very large close to threshold, which is leaving us no justification of the linearization procedure. In figure 2.1(A) the spectrum of squeezing for  $\eta = \sigma = 1$  is shown. From (2.16) it is seen that this is an inverted Lorentzian with a HWHM of  $(1 + \sigma)$ , meaning that the bandwidth of squeezing close to threshold is about twice the empty cavity linewidth. The best squeezing is found around  $\Omega = 0$ , and in figure 2.1(B), we find the zero frequency squeezing versus the OPO pump parameter  $\sigma$  for  $\eta = 1$ . Here we see that even for  $\sigma = 0.5$  the quantum noise reduction is close to 90%. This illustrates that it is by no means necessary to bring the OPO very close to threshold in order to observe appreciable quantum noise reduction.

It should be noted here that the phase of the quadrature in which the squeezing is obtained depends on the choice of phase of the coupling constant in the Hamiltonian. If we instead had started out with an interaction Hamiltonian of the form  $i\hbar\zeta (a^2 a_2^* - a_2 a^{\dagger 2})$ , corresponding to a purely imaginary coupling constant, we would have found squeezing in the quadrature  $X(\pi/2)$  and antisqueezing in  $X(0)$ . All choices of the coupling constant phase are equally valid since the overall phase of the system, defined by the pump phase, can be chosen arbitrarily. The particular choice we made in (2.1) was used because this yields the same equation of motion as the one we derived for the field amplitudes in the classical treatment (A.21).

The physics behind the quantum noise reduction is that the pump photons are downconverted into pairs of low frequency photons. The fields made up by these pairs are always created in such a way that the sum of their phases adds up to a constant depending on the phase of the pump field. Let the phase of this constant, given by  $\theta = (\theta_2 + \phi - \pi/2)/2$ , define the real axis in a phasor diagram. Here  $\theta_2$  is the phase of the pump and  $\phi$  is the phase of the coupling constant. In this frame the sum of the imaginary parts of the two downconverted fields (if they are distinguishable) and the difference between the real parts both will fluctuate very little since the spontaneously emitted photon pairs below threshold always are created with their relative phase locked to the pump phase. Conversely the difference between the imaginary parts and the sum of the real parts will fluctuate a lot. When the two downconverted fields are indistinguishable the difference between the real parts and the imaginary parts is identical to zero and hence we find the imaginary part ( $\theta = -\pi/4 + \pi/2 = \pi/4$  when  $\theta_2 = \phi = 0$ ) of the downconverted field to be squeezed and the real part ( $\theta = -\pi/4$ ) to be antisqueezed. The distribution of vacuum fluctuations in the squeezed OPO output is indicated as the shaded ellipse in the insert of fig. 2.1. If the photons in the pairs were created in an uncorrelated fashion, the resulting vacuum fluctuations would lie mainly inside the circle shown in the insert. Alternatively we can consider the degenerate OPO to be a phase sensitive amplifier for the vacuum input. The OPO amplifies the fluctuations in  $\theta = (\theta_2 + \phi - \pi/2)/2$  component of the vacuum and deamplifies the  $\theta = (\theta_2 + \phi + \pi/2)/2$  component.

The role of the escape efficiency  $\eta \simeq \mathcal{T}/(\mathcal{T} + \mathcal{L})$  in (2.16) is obviously to reduce the degree of squeezing in the OPO output. Intuitively this can be understood from the following argument. The quantum noise reduction in the OPO output arises from the fact that the high frequency pump photons are downconverted into photon pairs at the lower frequency. As we have seen, the fields made up of the downconverted photons (which are in the same mode for the degenerate OPO) must obey a certain phase relation. If however both photons do not exit through the same output port of the OPO, the

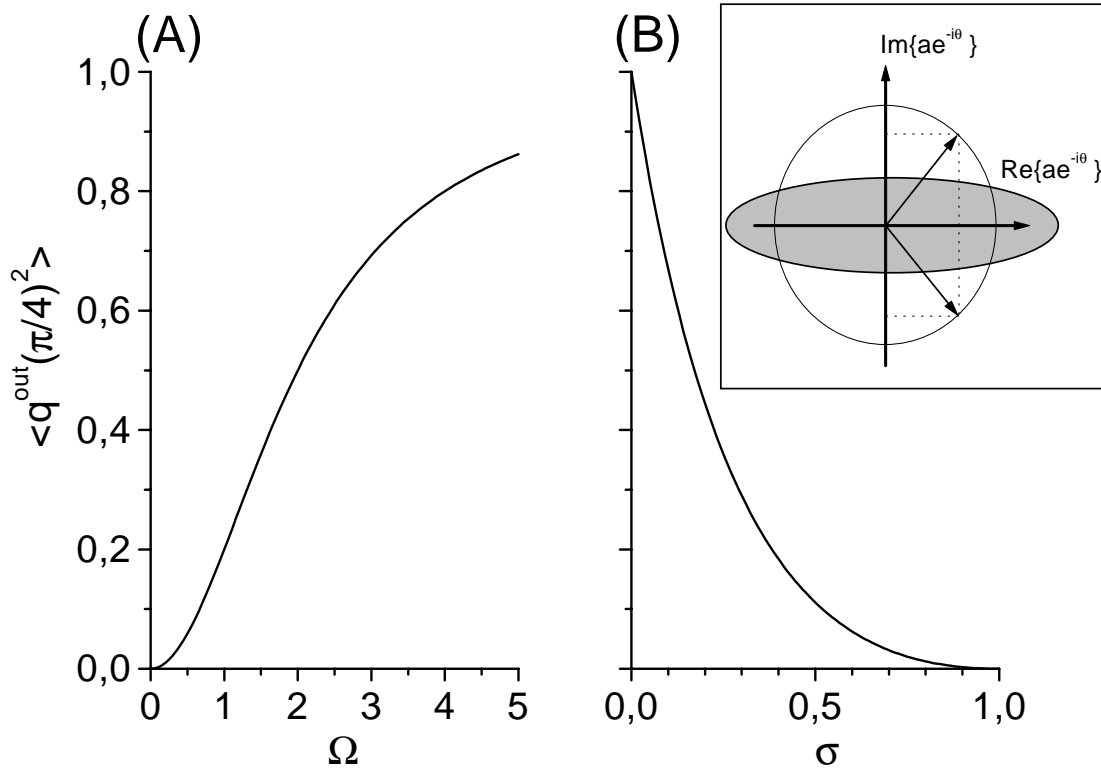


Figure 2.1: (A) The power spectrum of fluctuations in the squeezed quadrature of the OPO output for  $\eta = \sigma = 1$ . Best noise reduction is found at zero frequency. (B) The zero frequency fluctuations versus the OPO pump parameter  $\sigma = \sqrt{P/P_{th}}$ . The insert shows the phasor diagram of the downconverted photons always created with a total phase adding up to a constant. As a result the fluctuations of the emitted squeezed vacuum can be considered to be mainly inside the shaded ellipse.

correlations hidden in our phase relation are lost, and the squeezing will reduce. The probability that a photon escapes the OPO through the output coupler is  $\mathcal{T}/(\mathcal{T} + \mathcal{L})$ , which is just our escape efficiency  $\eta$ .

What we have learned from this treatment is that in order to achieve good squeezing from the OPO it is required that the intracavity losses,  $\mathcal{L}$ , are minimized in order to maximize the escape efficiency. The nonlinear  $\chi^{(2)}$  material used throughout this Ph. D. work is Potassium Niobate. This medium has the unattractive feature that it displays nonlinear absorption, which naturally can be fatal to the OPO correlations. For this reason my Ph. D. project started with an investigation of this effect, and the next chapter is devoted to a description of this work.

## Chapter 3

# Blue Light Induced Infrared Absorption

It was shown in the previous chapter, that significant intracavity losses except for the transmission through the output coupler of the OPO cavity are fatal if good squeezing is to be achieved. The nonlinear medium preferred in the work presented throughout this thesis is Potassium Niobate,  $\text{KNbO}_3$ . This is an attractive material for nonlinear conversion in the near infrared region due to its small passive losses and high second order nonlinearity[23]. However, the applicability of this material for squeezing purposes is seriously limited by the effect called Blue Light Induced InfraRed Absorption, or BLIIRA in short[24].

This chapter is started with some general considerations of the impact of BLIIRA on the OPO squeezing. This is followed by a description of the setup used to measure BLIIRA and a discussion of means to measure intracavity losses. Then the results of our measurements will be presented and interpreted and a qualitative explanation of the mechanisms responsible for BLIIRA is given. The chapter is ended with the conclusions on the BLIIRA experiment.

### 3.1 The influence of BLIIRA on the OPO squeezing

The BLIIRA manifests itself by increasing the absorption of the  $\text{KNbO}_3$  crystal in the near infrared region when visible or ultraviolet light is present in the same volume of the crystal as the infrared light occupies. This effect was first observed in  $\text{KNbO}_3$  in 1992 by Polzik *et. al.* [7], where the second harmonic pump was found to induce additional losses in an OPO, and thereby limiting the degree of quantum noise reduction obtained. However, this effect was not unknown at the time, in fact a similar type of behavior has been observed in  $\text{BaTiO}_3$  as early as 1987[25].

To illustrate that BLIIRA can become a serious obstacle on the avenue towards good squeezing, let us consider an OPO with an output coupler transmission of 10% and residual passive losses of the cavity of 0.3%. Without any BLIIRA these values will give us an escape efficiency of  $\eta = 97\%$ , corresponding to a degree of squeezing (in the absence of other loss sources) of -15 dB. If we now consider a realistic value of the BLIIRA of 2%[26], we find that the escape efficiency drops to 81%, corresponding to -7.3 dB of noise reduction at best.

It is now natural to ask the question: Why don't we just increase the output coupler transmission of the OPO in order to reduce the significance of the residual losses? To answer this, let us consider the escape efficiency from the previous chapter. Keeping in mind that the losses now depend on the pump power of the OPO, we find  $\eta = \mathcal{T}/(\mathcal{T} + \mathcal{L}_0 + \mathcal{L}(P)) = 1 - (\mathcal{L}_0 + \mathcal{L}(P))/(\mathcal{T} + \mathcal{L}_0 + \mathcal{L}(P))$ . Here  $\mathcal{T}$  is the output coupler transmission,  $\mathcal{L}_0$  are the passive losses of the OPO cavity and  $\mathcal{L}(P)$  is the BLIIRA. The pump power of the OPO is given by  $P = \sigma^2 P_{th}$ , where  $\sigma$  is the pump parameter appearing

in the spectrum of squeezing (2.16), and  $P_{th}$  is the power required to drive the OPO in threshold. In Appendix A this is found to be  $P_{th} = (\mathcal{T} + \mathcal{L}_0 + \mathcal{L}(P))^2 / 4E_{NL}$ , where  $E_{NL}$  is the single pass nonlinearity. Combining our definitions we now find the escape efficiency to be given by

$$\eta = 1 - \frac{\sigma [\mathcal{L}_0 + \mathcal{L}(P)]}{2\sqrt{P}E_{NL}} \quad (3.1)$$

From (3.1) it is clear that, provided we have unlimited pump power available, we only gain in squeezing by increasing the output coupler transmission as long as the BLIIRA,  $\mathcal{L}(P)$ , does not grow faster than  $\sqrt{P}$ . As it will be shown later in this chapter, the BLIIRA can under certain conditions grow at rates comparable to  $\sqrt{P}$ . This necessitates the investigation of other means to circumvent this problem, by for instance doping the  $\text{KNbO}_3$  with certain elements or changing the operational parameters of the crystal such as the temperature, angle etc.

### 3.2 Experimental setup

In order to make the measurements of BLIIRA mimic any experimental situation of second harmonic generation or parametric downconversion as close as possible, we wanted to measure this effect for a broad spectrum of input powers as well as for a broad spectrum of wavelengths. As a result we had to be able to observe changes in absorption of a  $\text{KNbO}_3$  crystal spanning from 0.1% to several percent. Towards this end a high finesse nonlinear resonator with a  $\text{KNbO}_3$  crystal inside was constructed. This

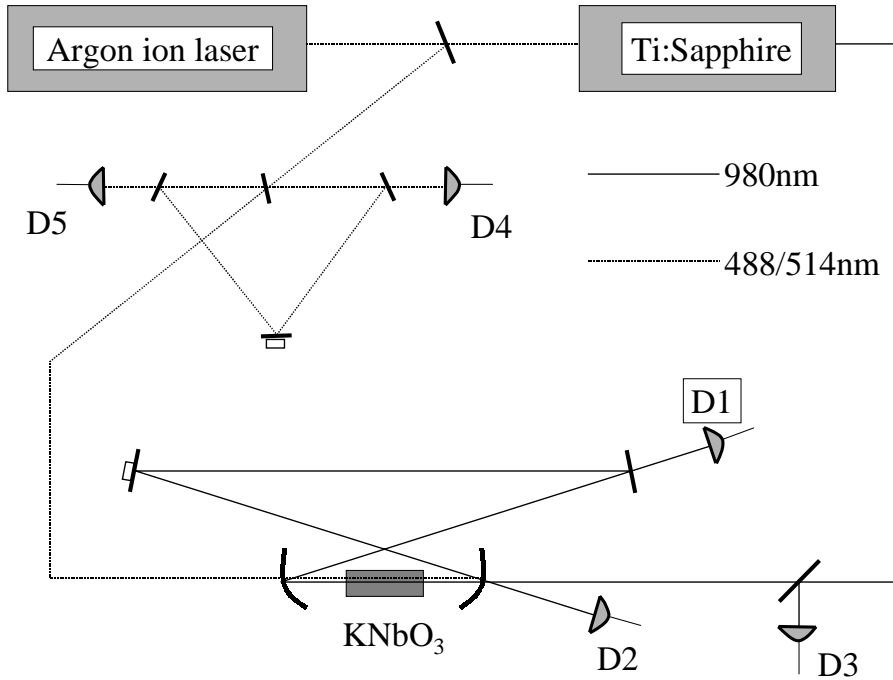


Figure 3.1: The experimental configuration used to measure BLIIRA. Full lines illustrate infrared beams, and dotted lines are second harmonic beams.

cavity was resonant to the fundamental light in the near infrared region at wavelengths around 980nm. We chose to examine BLIIRA at wavelengths longer than in ref. [24] in the hope of finding a reduction of the effect here for reasons which will be explained later in this chapter. Having typically a transmission of the input coupler of 0.1% (depending on the exact wavelength) and a finesse around 400 in the absence of BLIIRA, this cavity was by no means optimized for good nonlinear conversion. However the small intracavity losses were required in order to be sensitive to the small contribution from BLIIRA in the low pump power region.

The infrared light was provided by a single frequency Titanium:Sapphire laser, which gave about 100-200 mW for pumping the cavity. Since we wanted good control on the amount of second harmonic light present in the crystal, this light was generated externally by a single frequency Argon ion laser. This laser had two lines powerful enough to pump the Ti:Sapphire laser as well as the nonlinear resonator. These lines are located at 488 nm and 514 nm, which both are close to the second harmonic wavelength around 490nm. Both lines were used in this experiment and henceforth they will simply be denoted the 'second harmonic field'. It should be noted here, that this way of providing the (almost) second harmonic precluded measurements of any coherent contributions to the BLIIRA. However most theories on BLIIRA make use of a charge transport model[24][27][28], meaning that the process is likely to be mainly of incoherent nature. Some coherent contribution to the BLIIRA cannot be ruled out, but due to our experimental procedure, where we operated far from phasematching, such contributions were not likely to be recorded.

The cavity was designed to have a waist of 18  $\mu\text{m}$ , which is close to the optimum focusing for nonlinear conversion, according to the calculations in Appendix A. Here we find the optimum focussing to give  $\Lambda_{cr} = \ell_{cr}/z_0 = \ell_{cr}\lambda/\pi n w_0^2 = 5.675$ . For an index of refraction of  $n = 2.3$ , a wavelength of  $\lambda = 980$  nm and a crystal length of  $\ell_{cr} = 10$  mm, this corresponds to a cavity waist of  $w_0 = 15.5$   $\mu\text{m}$ . In order to provide an almost perfect modematching of the second harmonic to the infrared cavity mode, the second harmonic was produced inside the cavity, and, as illustrated in figure 3.1, this spatial mode was modematched into a designated reference cavity. Injecting the Argon laser output into this cavity in the counterpropagating direction, and optimizing the modematching, ensured good spatial modematching with the cavity mode.

There are several techniques to use when the losses of a resonator are to be inferred and knowing the mirror transmissions is important for most of these. Scanning the cavity across several free spectrum ranges, one can measure the finesse of the resonator, which in turn can provide information about the intracavity losses. Another method is measuring the power transmitted through a mirror different from the input coupler as the cavity is scanned across resonance. Due to energy conservation a dip must appear in the power reflected off the cavity as it is swept through resonance, since the transmission is increased around this point. To infer the losses from these three features, let us consider a cavity with the input coupler reflectivity  $r_1$ , crystal transmission  $k$  and reflectivity of another mirror of  $r_2$ . All other cavity components are assumed to be lossless. This is shown in figure 3.2. We now calculate the intracavity field in two places inside the cavity:  $E_{c1}$  is the field just before the input coupler and  $E_{c2}$  is just before the second transmitting cavity mirror. Assuming a good cavity, we can consider the field to have the same phase,  $\delta$ , at any point inside the resonator. Normalizing to the input field  $E_i$  we can now easily find the intracavity fields to be  $E_{c1}/E_i = \sqrt{1 - r_2^2} r_2 k e^{i\delta} / (1 - r_1 r_2 k e^{i\delta})$  and  $E_{c2}/E_i = \sqrt{1 - r_1^2} k e^{i\delta} / (1 - r_1 r_2 k e^{i\delta})$ . The field reflected off the cavity at the input coupler,  $E_r$ , will now be given by  $E_r/E_i = -r_1 + \sqrt{1 - r_1^2} E_{c1}/E_i$ , and the field transmitted through the cavity,  $E_t$ , will be given by  $E_t/E_i = \sqrt{1 - r_2^2} E_{c2}/E_i$ . By taking the square modulus of these two expressions, we find the normalized reflected and transmitted powers respectively. These are given by

$$\begin{aligned} \frac{P_r}{P_i} &= \frac{r_1^2 + (r_2 k)^2 - 2r_1 r_2 k \cos \delta}{1 + (r_1 r_2 k)^2 - 2r_1 r_2 k \cos \delta} \\ \frac{P_t}{P_i} &= \frac{(1 - r_1^2)(1 - r_2^2) k^2}{1 + (r_1 r_2 k)^2 - 2r_1 r_2 k \cos \delta} \end{aligned} \quad (3.2)$$

Focusing first on the reflected power, we define  $\rho$  as the ratio of the power reflected off the cavity on

resonance ( $\delta = 0$ ) to the reflected power off resonance ( $\delta = \pi$ ). This is given by

$$\rho = \left( \frac{(r_1 - r_2k)(1 + r_1r_2k)}{(r_1 + r_2k)(1 - r_1r_2k)} \right)^2 \simeq \left( \frac{1 - \frac{\mathcal{T}_2 + \mathcal{L}}{\mathcal{T}_1}}{1 + \frac{\mathcal{T}_2 + \mathcal{L}}{\mathcal{T}_1}} \right)^2 \quad (3.3)$$

where the last equality was obtained by defining  $r_1 = \sqrt{1 - \mathcal{T}_1}$ ,  $r_2 = \sqrt{1 - \mathcal{T}_2}$  and  $k = \sqrt{1 - \mathcal{L}}$ , and expanding these quantities to first order in the transmissions and losses. Now it is clear that provided we know the input coupler transmission  $\mathcal{T}_1$ , we can find the remaining losses of the cavity by observing the reflection dip. If the input coupler transmission is the dominating loss, these will be given by

$$\mathcal{T}_2 + \mathcal{L} = \mathcal{T}_1 \frac{1 - \sqrt{\rho}}{1 + \sqrt{\rho}} \quad (3.4)$$

otherwise the fraction has to be inverted. On resonance ( $\delta = 0$ ) the cavity transmission is found to be

$$\frac{P_t}{P_i} = \frac{4\mathcal{T}_1\mathcal{T}_2}{(\mathcal{T}_1 + \mathcal{T}_2 + \mathcal{L})^2} \quad (3.5)$$

where the same expansion of  $r_1$ ,  $r_2$  and  $k$  as above has been performed. To visualize the last method

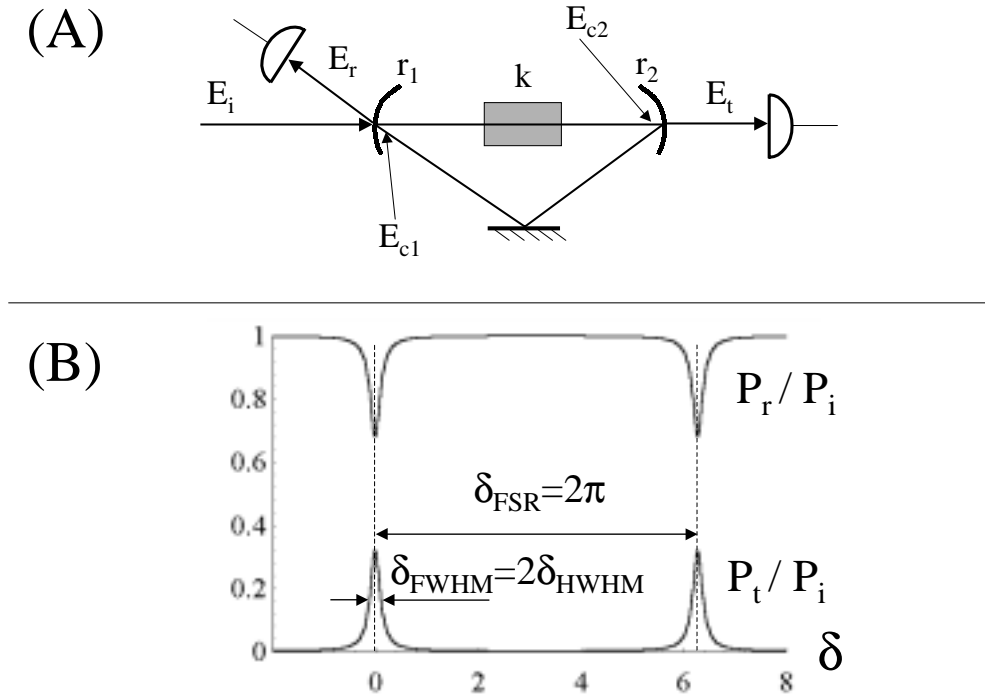


Figure 3.2: (A) The cavity under consideration. The passive losses can be inferred from the reflected or the transmitted power. (B) The reflected power (upper trace) and the transmitted power (lower trace), in units of the input power, vs. the roundtrip phase shift,  $\delta$ . The phase shift of  $2\pi$  corresponds to one Free Spectrum Range (FSR) of the cavity. The traces correspond to  $r_1 = 0.9$ ,  $r_2 = 0.99$  and  $k = 1$ .

of measuring the finesse,  $\mathcal{F}$ , of the resonator, we consider small phaseshifts,  $\delta$ , and expand the cosine in the denominator of the cavity transmission. This results in the Lorentzian

$$\frac{P_t}{P_i} = \frac{(1 - r_1^2)(1 - r_2^2)k^2}{(1 - r_1 r_2 k)^2 + r_1 r_2 k \delta^2} \quad (3.6)$$

which has the half width at half maximum

$$\delta_{HWHM} = \frac{1 - r_1 r_2 k}{\sqrt{r_1 r_2 k}} \quad (3.7)$$

If we now remember that the finesse,  $\mathcal{F}$ , is defined as the free spectrum range ( $\delta_{FSR} = 2\pi$ ) divided by the full width at half maximum[29], and we perform our expansion of  $r_1$ ,  $r_2$  and  $k$  as above, we obtain to first order in the losses

$$\mathcal{F} = \frac{\delta_{FSR}}{2\delta_{HWHM}} \simeq \frac{2\pi}{\mathcal{T}_1 + \mathcal{T}_2 + \mathcal{L}} \quad (3.8)$$

The finesse measurement has the advantage that it is independent of any additional measurements. It is therefore always a good idea to compare the losses obtained from one of the first two methods with a finesse measurement.

From a practical viewpoint these methods all have their drawbacks. It is usually not easy to measure the finesse with a precision better than 10% due to acoustic vibrations in the setup. The reflection dip method relies on a good determination of the power reflected off the cavity off resonance, however fluctuations in the input power complicates this measurement substantially. Finally the transmitted power will possess the same fluctuations as the input power to the cavity, and will therefore fluctuate correspondingly. This was the main source of uncertainty in this experiment, since the Ti:Sapphire power fluctuated about 10% at a timescale of about 100 ms.

For these reasons the following strategy was used in the experiment. The input coupler transmission was measured as accurately as possible. This was found to be 0.1-0.2% depending on the exact wavelength used. The uncertainty in this measurement was about 10% this was attributed mainly to the power fluctuations of the Ti:Sapphire output. Then the losses of the passive cavity were measured. These included the KNbO<sub>3</sub> crystal losses in the absence of any second harmonic in the cavity. The cavity passive losses were measured with D2 (fig. 3.1) using the reflection dip method and crosschecked using the less accurate finesse. Typically these losses were at the level of 0.9-1.5% depending on the crystal quality. The cavity transmission turned out to be the easiest and consequently fastest method of obtaining the losses. Hence this method was used for the final measurements of BLIIRA. Without any second harmonic light in the cavity, the transmission was measured about 5-10 times on D1, and for each measurement the result was normalized to the input power measured on D3. Now the second harmonic was unblocked, and due to BLIIRA the cavity transmission dropped. From (3.5) we found the amount of BLIIRA,  $\mathcal{L}(P_{SH})$ , to be

$$\mathcal{L}(P_{SH}) = (\mathcal{T}_1 + \mathcal{T}_2 + \mathcal{L}_0) \left( \sqrt{\frac{\frac{P_t(P_{SH}=0)}{P_i}}{\frac{P_t(P_{SH})}{P_i}}} - 1 \right) \quad (3.9)$$

where  $P_{SH}$  is the incoming second harmonic power,  $\mathcal{L}_0$  are the cavity passive losses and  $P_t$  is the power transmitted through the cavity. We also recorded the cavity transmission without the normalization from D3, and the result with the smallest statistical fluctuations was chosen. This result was not necessarily the normalized transmission. Because the power fluctuations of the Ti:Sapphire had frequency components around the inverse data acquisition time, the normalization procedure could in some cases increase the error of the measurement. Typically the statistical fluctuations of the measurements were on the order of 10%, even when BLIIRA was only about 0.2%.

This measurement procedure was repeated with second harmonic powers ranging from about 500 $\mu$ W up to 400mW for 7 different KNbO<sub>3</sub> crystals. These are listed in the table below.

Crystal number	Crystal length [mm]	Doping	Doping concentration
1	8,5	Undoped	-
2	8,5	Undoped	-
3	10,0	Tantalum	0,1 wt. %
4	10,0	Magnesium	0,1 wt. %
5	9,0	Vanadium	N/A
6	7,0	Rubidium	N/A
7	9,5	Magnesium	0.05 wt. %

### 3.3 Results

The measurements were taken as a function of two parameters: The second harmonic intensity in the cavity waist and the crystal temperature. The crystals 3, 5 and 6 turned out to be of poor optical quality. As a result the modematching of the Ti:Sapphire output into the cavity was rather bad and consequently the uncertainties of the BLIIRA measurements were high. However the behavior of the crystals were found to resemble the behavior of the undoped crystals 1 and 2 very much. In the rest of this chapter we will focus on the crystals 1, 4 and 7, since the comparison of these lent us the most insight to the BLIIRA problem. Both the 488 and the 514 nm lines of the Argon ion laser were used as the second

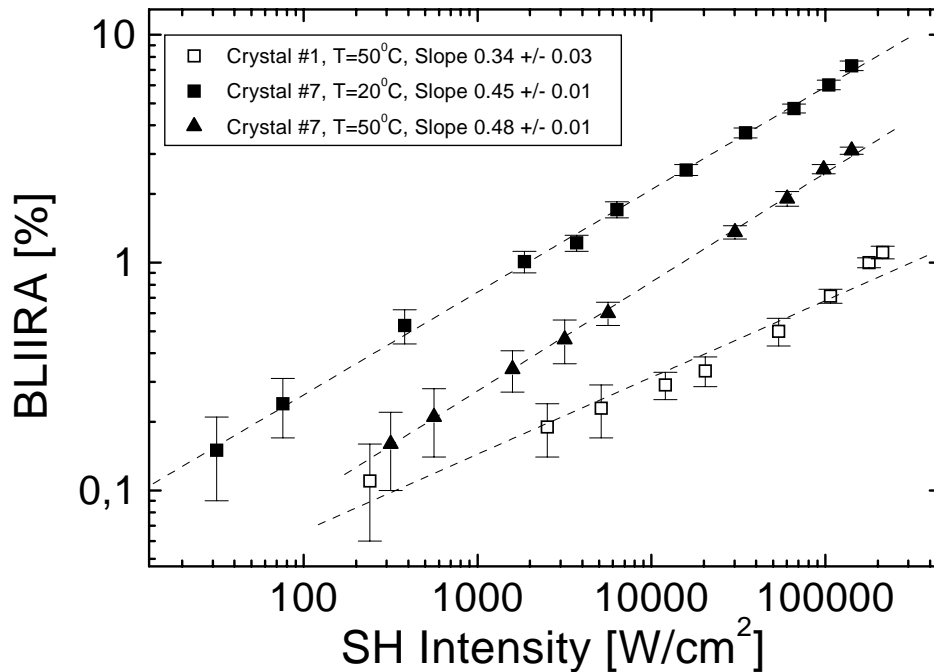


Figure 3.3: The BLIIRA dependence on the second harmonic (SH) intensity in the cavity waist. The BLIIRA in the Mg doped crystal 7 is seen to be more than a factor of 2 higher than in the undoped crystal 1. The growth of BLIIRA in crystal 7 with the SH power is seen to follow a power law to a good approximation whereas the agreement is worse for crystal 1.

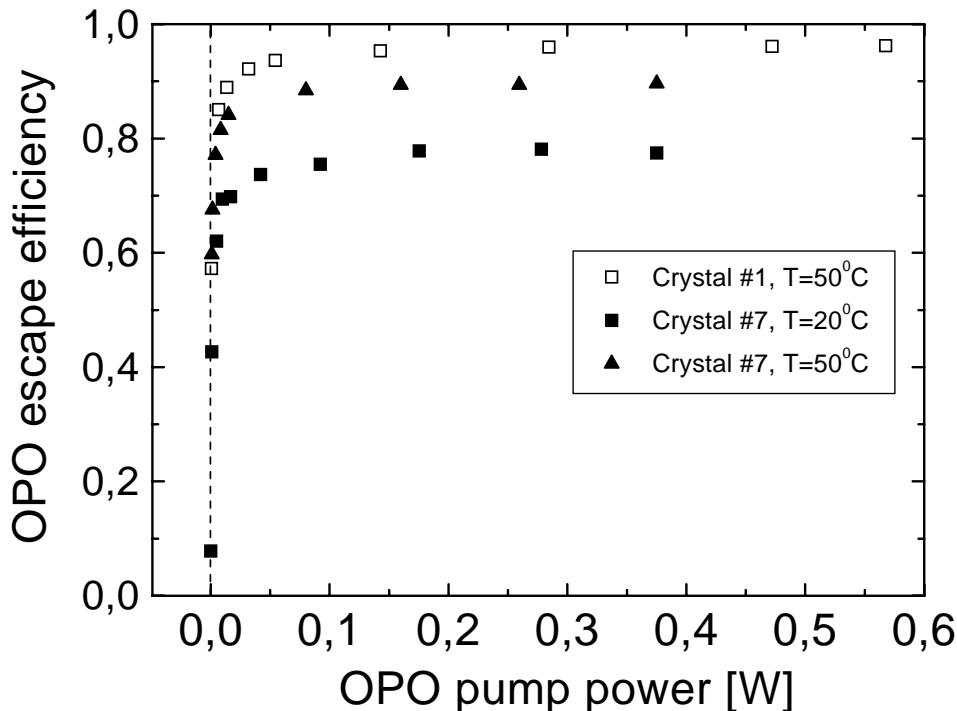


Figure 3.4: The OPO escape efficiency vs. the pump power. This has been derived from the BLIIRA data, by using the parameters  $\sigma = 0.5$ ,  $\mathcal{L}_0 = 0.005$ ,  $E_{NL} = 0.02 \text{ W}^{-1}$  and  $w_0 = 13 \text{ }\mu\text{m}$ .

harmonic pump, but since no difference was observed in the BLIIRA, we will omit the specification of which line we used in the following.

As is shown in figure 3.3, the BLIIRA grows rapidly with an increasing intensity of the second harmonic. This growth is found to almost follow a power law, where the power is about 0.45 for the Magnesium doped crystal 7 at 20°C, 0.48 at 50°C and 0.34 for the undoped crystal 1 at 50°C. However the latter does not follow the power law very well and hence the slope for high intensities is in fact close to 0.5. This indicates that different processes are responsible for the BLIIRA in the doped and undoped crystals. We will return to this observation in section 3.4. According to our simple theory leading to (3.1), this power dependence leaves us some hope that the OPO escape efficiency may grow as the pump power is increased and the output coupler transmission is optimized accordingly. In order to convert the measured BLIIRA to a realistic conversion efficiency for an OPO, we now use (3.1), remembering that the peak intensity of a Gaussian beam is given by  $I_0 = 2P/\pi w_0^2$ , where  $P$  is the total power in the beam, and  $w_0$  is the beam waist. If we furthermore use some realistic values of  $\sigma = 0.5$ ,  $\mathcal{L}_0 = 0.005$ ,  $E_{NL} = 0.02 \text{ W}^{-1}$  and  $w_0 = 13 \text{ }\mu\text{m}$ , we obtain the escape efficiency optimized with respect to  $\mathcal{T}$  as a function of the second harmonic pump power available. This is plotted in figure 3.4. From here it is clear that the gain in the escape efficiency with increasing pump power is very small above 100 mW. It should be kept in mind that the OPO pump typically is produced in second harmonic generation[6], and high pump powers therefore are nontrivial to produce. The maximum pump power appearing in fig 3.4 is about 600 mW, which is close to the highest second harmonic power achieved by frequency doubling in  $\text{KNbO}_3$ [30]. For this reason it may not turn out to be worth taking up the challenge to increase the OPO pump power in order to gain a few percent in the escape efficiency.

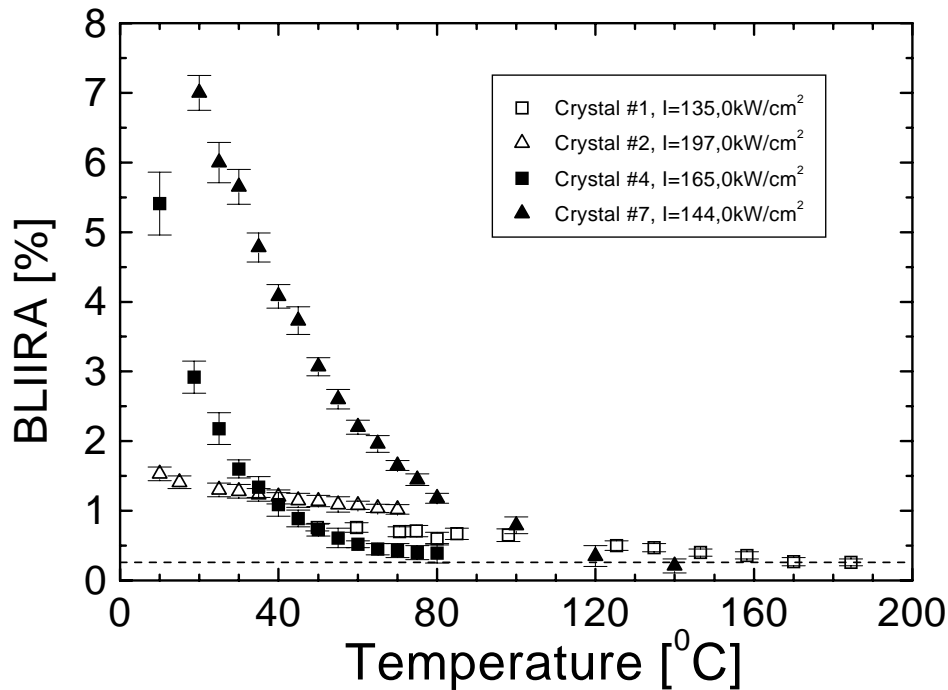


Figure 3.5: The temperature dependence of BLIIRA. The open symbols are the results from the undoped crystals and the filled symbols are data for the Mg doped crystals. The dotted line indicated the lowest level of BLIIRA for the undoped crystals. All data were taken with comparable second harmonic intensities.

Another interesting result that can be observed from the figures 3.3 and 3.4 is that the BLIIRA in the Magnesium doped crystal 7 is reduced with about a factor of 2 when the temperature is increased from 20 to 50°C. Consequently the predicted OPO escape efficiency is increasing from 79% to 90%. The high level of absorption as well as the temperature dependence of BLIIRA in the Mg doped crystals is also observed in ref. [24] for a single crystal out of a collection of 10 samples. However this subject is not pursued further in this paper, and consequently we chose to undertake a more thorough investigation of this feature.

In the measurements outlined above, the crystal was thermally stabilized by means of a thermoelectric element. We now put this element to the test by monitoring BLIIRA for our crystals in the temperature region from 10 to 180°C. The measurement procedure used in this series of experiments was the same described above, and the results are shown in figure 3.5.

From this figure it is found that the Mg doped crystals display a much stronger temperature dependence than the undoped crystals. For the former, the BLIIRA started from a level close to 7% absorption at room temperature, which would leave them useless for squeezing experiments. However as the temperature was increased, the absorption dropped relatively fast, and it went below 1% around 90°C for the medium doped crystal 7 and around 40°C for the heavier doped crystal 4. The undoped crystals 1 and 2 showed a much weaker temperature dependence, but as a general trend, the BLIIRA also decreased with temperature for these samples. In the next section we will present a simple model, which will cover these main features of the BLIIRA.

Looking at figure 3.5, the main question that arise is: Can we gain in the escape efficiency by using a Mg doped crystal and heat it up to more than  $100^{\circ}\text{C}$ ? At a first glance the answer is yes. In fact it was found that the strong temperature dependence of BLIIRA in the Mg doped crystals brought their absorption even lower than the smallest absorption in the undoped crystals. This level is indicated with the dashed line in figure 3.5. However we found that the behavior of BLIIRA in different crystal samples was so individual, that one should be careful concluding, that BLIIRA as a general rule is smaller at high temperatures in the Mg doped  $\text{KNbO}_3$ .

A final thing worth noting from figure 3.5 is, that the amount of BLIIRA seems to be a non monotonic function of the concentration of Mg in the crystal. If we draw a vertical line at, say,  $80^{\circ}\text{C}$ , we find the BLIIRA to be 0.7% for the undoped crystal 1, 1.2% for the 0.05% doped crystal 7 and 0.4% for the 0.1% doped crystal 4. This behavior can probably be attributed to an interaction between the Mg atoms in the crystal, which become important at higher concentrations. As a result the Mg atoms are likely to form pairs or even to cluster in larger groups in the crystal.

### 3.4 A qualitative explanation of BLIIRA

In the following a qualitative explanation of the BLIIRA dependence will be outlined. The full problem of the electronic structure of  $\text{KNbO}_3$  with its impurities and crystal defects is a formidable task to take on and it is beyond the scope of this Ph.D. work. We are however capable of understanding our results in a more general sense, especially the remarkable behavior of the Mg doped crystals deserves an explanation.

The behavior of BLIIRA is usually explained within a charge transport model[31][24]. Here impurity levels located in the bandgap of the crystal can interact with the light fields and thereby absorb a substantial fraction of this light. In the two center model two kinds of impurity levels are considered, some of which are positioned high in the bandgap  $|2\rangle$  and others lying close to the valence band  $|1\rangle$ . This is illustrated in figure 3.6(A). The bandgap of  $\text{KNbO}_3$  is between 3.1 and 3.2 eV, and consequently electrons cannot be excited from the valence band to the conduction band as long as the wavelength of the second harmonic is longer than about 400 nm. The low lying impurity levels  $|1\rangle$  can however be thermally excited from the valence band, and in thermodynamical equilibrium at room temperature, these levels are in fact all filled by electrons so that no infrared light can be absorbed between the valence band and these levels. The situation is different when the second harmonic is present. The high lying impurity levels, which are unpopulated in thermodynamical equilibrium, can now be excited by electrons from the valence band via the interaction with the second harmonic field. This leaves holes in the valence band, and consequently electrons from the low lying impurity levels can now recombine with the holes leaving their initial levels unpopulated. As a result the fundamental infrared light is now free to interact with the transition from the valence band to the low lying levels and thereby being absorbed. Furthermore we can account for the decreasing BLIIRA with increasing temperature in the following way. A higher temperature will move the chemical potential higher in the bandgap, and consequently the low lying impurity levels are less likely to become depopulated. This leaves less final states available to the transition driven by the infrared light, and consequently the BLIIRA is reduced as the temperature is increased. The above outlined mechanism and closely related variants is likely to form the basis of BLIIRA in undoped crystals. On a quantitative basis this model has successfully described a series of experiments on light induced absorption[31][27][28], it is however not sufficient, when the strong temperature dependence of the Mg doped crystals must be explained.

The failure of the two center model relies on two facts: (a) From theoretical work[32] it is known that Mg acts as a donor when embedded in  $\text{KNbO}_3$ . This means that the low lying impurity levels should be filled up when Mg is added to the crystal, and consequently the BLIIRA should reduce. This is not what we have observed. (b) If Mg should contribute to increase the BLIIRA in the two center model, it would have to participate in the absorption process of the second harmonic. As a result the absorption of the second harmonic field should be higher in Mg doped crystals, this is however in contradiction to the measurements of ref. [33]. Here the second harmonic absorption in Mg doped samples was found to

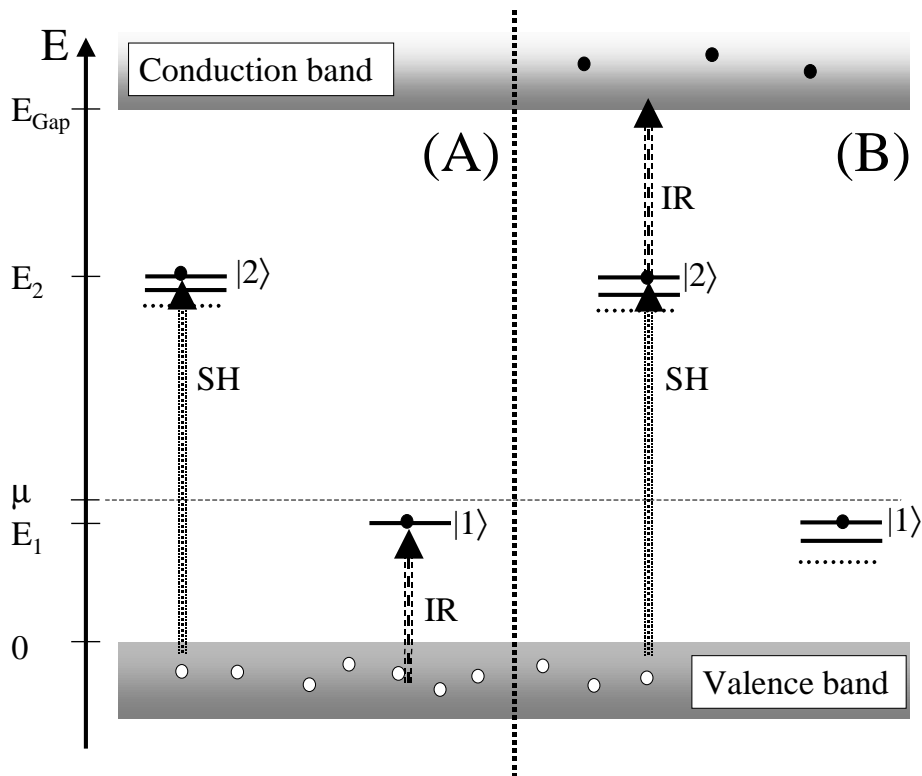


Figure 3.6: The impurity levels in the bandgap relevant for BLIIRA. (A) The two center model where the infrared (IR) is exciting the level  $|1\rangle$  and thereby being absorbed. (B) The cascade model where the second harmonic (SH) excites the level  $|2\rangle$ , from which the IR can populate the conduction band.

be *smaller* than in undoped samples. In fact the theoretical work of ref. [32] supports this result. Here the binding energy of an electron to a Magnesium defect in  $\text{KNbO}_3$  is calculated to be 0.27 eV, meaning that it is not possible for our 2.5 eV second harmonic photons to excite the 2.9 eV transition from the valence band to the Mg impurity level.

Instead of the two center model we propose a cascade model to account for the strong BLIIRA in the Mg doped crystals. Here an impurity level located in the bandgap far from the conduction and valence bands,  $|2\rangle$ , can be excited with the second harmonic light. By the interaction with the infrared light, electrons in this level can now be excited to the conduction band. The levels are shown in figure 3.6(B). Naturally the absorption of the infrared will depend on the population of this impurity level. If we write up simple rate equations for this population, we find it to depend critically on the number of holes in the valence band and lower lying levels. This will account for the strong BLIIRA in the Mg doped crystals, since the Mg donors will reduce the number of holes in the valence band and thereby increase the chemical potential,  $\mu$ , and the mean population of the impurity level and hence the BLIIRA. The strong temperature dependence is attributed to a low lying impurity level,  $|1\rangle$ , close to the chemical potential. The generation rate of holes in the valence band will now depend critically on the exact level of the chemical potential relative to this impurity level. As the temperature is increased, the chemical potential increases and consequently the concentration of holes in the valence band will increase. This will enhance the recombination rate of electrons in  $|2\rangle$  with holes in the valence band, and as a result the mean population in  $|2\rangle$  and the BLIIRA will go down. For a more quantitative analysis of the cascaded model the reader is referred to ref. [34], where good quantitative agreement between our experimental

results and the cascade model is found.

It should be stressed, that the models described above all depend on a great number of parameters, such as the exact energy of the impurity levels, the chemical potential etc. These quantities are not very well known experimentally, which leaves a lot of space for adjusting them within each model in such a way that the relevant experiment is accounted for as good as possible. This of course limits the credibility of the models on the quantitative level, however they are still valuable in the sense, that they provide us with an insight into the mechanisms responsible for BLIIRA.

### 3.5 Conclusions

In summary the BLIIRA experiment has taught us, that the light induced absorption grows so fast with the second harmonic pump power that the optimized OPO escape efficiency does not grow significantly when the pump power is higher than about 100 mW. This motivated the investigation of a way to circumvent BLIIRA in  $\text{KNbO}_3$ . Here the temperature dependence of BLIIRA seemed to provide us with a solution. In the undoped as well as the doped crystal, the BLIIRA was found to decrease with increasing temperature. In the Magnesium doped crystal this effect was seen to be particularly strong, and at temperatures above  $100^\circ\text{C}$  the BLIIRA seemed to drop below the level of the undoped crystals. As a result an improvement in the OPO escape efficiency from 80% to 90% was anticipated according to figure 3.4. In the next chapter we will show how this temperature dependence was used to our advantage in an experiment with the goal of producing strong squeezing.

Finally we put forward an alternative to the commonly used two center model. This was needed because the two center model failed to explain the high degree of BLIIRA in the Mg doped crystals as well as the strong temperature dependence of BLIIRA in these crystals.

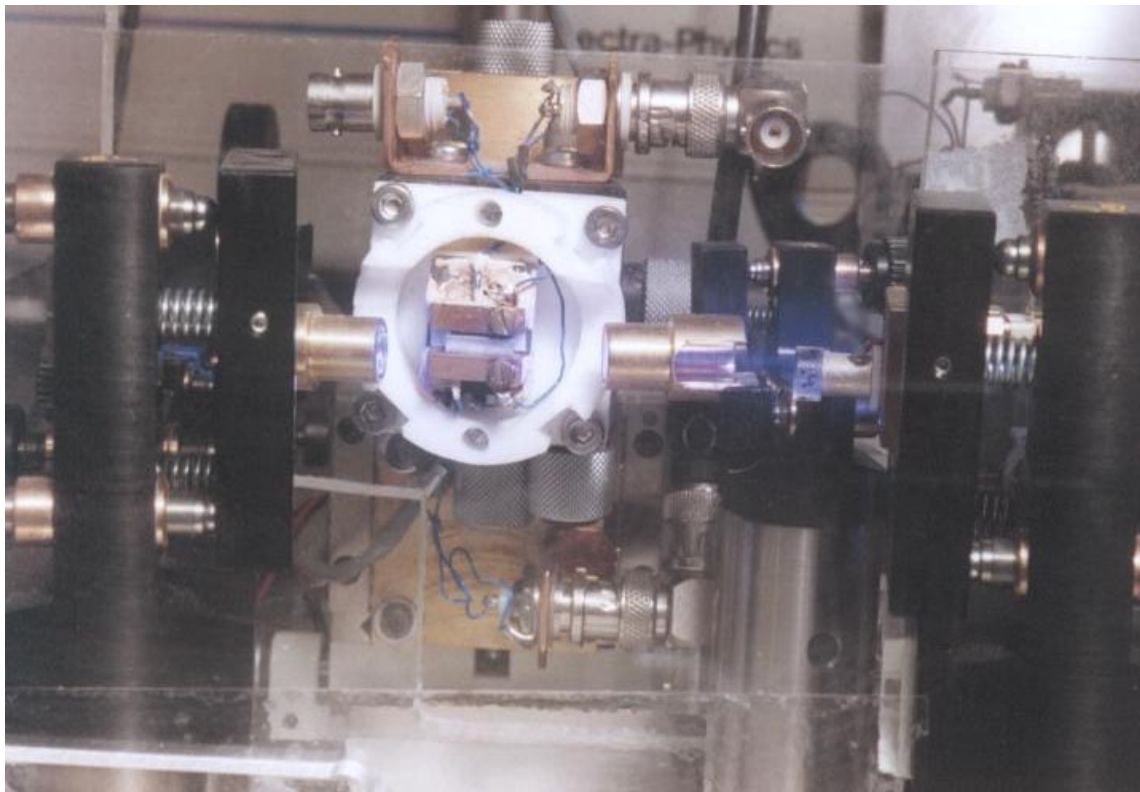


Figure 3.7: The  $\text{KNbO}_3$  crystal located inside the OPO resonator. A teflon housing isolates the crystal from the surroundings and an electrical heater is keeping the crystal at  $130^\circ\text{C}$ . In order to preserve the ferroelectricity of the crystal a bias of 30 Volts is applied along the  $c$ -axis.

## Chapter 4

# Production of Squeezed Light

Armed with the knowledge from our BLIIRA experiment as described in the previous chapter, we were now ready to take on the challenge associated with the production of nonclassical light. Keeping in mind future experiments involving nonclassical light and atomic physics, we chose the wavelength 917 nm as the carrier of our squeezing, since this corresponds to the  $6P_{3/2} \rightarrow 6D_{5/2}$  transition in atomic Caesium. Another motivation for using this wavelength is that the phasematching temperature for *a* cut KNbO<sub>3</sub> is around 130°C at 917 nm. According to the discussion in the previous chapter, the BLIIRA should be reduced with about a factor of two as compared to operation around room temperature. Because of the great individuality of the behavior of the crystals, we did not take the chance of using Magnesium doped KNbO<sub>3</sub>. If we had done this, we would have to trust that the BLIIRA of all Mg doped crystals will drop just as much with temperature as the two, we tested in the previous chapter. This was by no means certain, since the vendor did not have the required control on the growth process of these crystals to be able to guarantee this.

Several nonlinear processes have been proposed, in which squeezing can be produced. These include  $\chi^{(2)}$  as well as  $\chi^{(3)}$  nonlinearities such as Second Harmonic Generation (SHG)[35], Parametric Downconversion[36], Four Wave Mixing[37] etc. Historically the process of Parametric Downconversion has proven to be the most efficient method of generating good squeezing[6][7][38], and therefore we chose to generate squeezing utilizing this process taking place in an OPO. In chapter 9 we present a theoretical treatment of the Internally Pumped OPO which may prove to be a source of squeezed light just as efficient as the regular OPO but requiring a simpler setup.

In order to provide the pump for the OPO, the second harmonic had to be created first. An OPO optimized to produce good squeezing usually has a quite high threshold (several hundreds of milliwatts). For this reason most of our 917 nm light was used to produce this pump. However high power second harmonic generation is never a trivial task, and in the following section the achievements in this direction will be discussed. Then we will move on to consider the classical properties of our OPO, including the cavity design and threshold, and finally the squeezing experiment will be described together with a comparison to the theory derived in chapter 2.

### 4.1 Second harmonic generation

By using (A.19) with total losses in the vicinity of 10% and a nonlinearity of about 1%/W, we arrive at a threshold for the OPO around 250 mW. This is the power required inside the OPO crystal in the cavity mode to drive the OPO above threshold. However imperfect modematching and nonzero reflectivities of crystal surface and mirrors can easily increase this threshold to 400-500 mW outside the OPO. In chapter 2 we found that, in principle, about 50% of this power is sufficient to produce more than 95% of quantum noise reduction. As a result we were in need of more than 200 mW of second harmonic light to pump our OPO. Having a limited amount of fundamental (917 nm) light available, this required

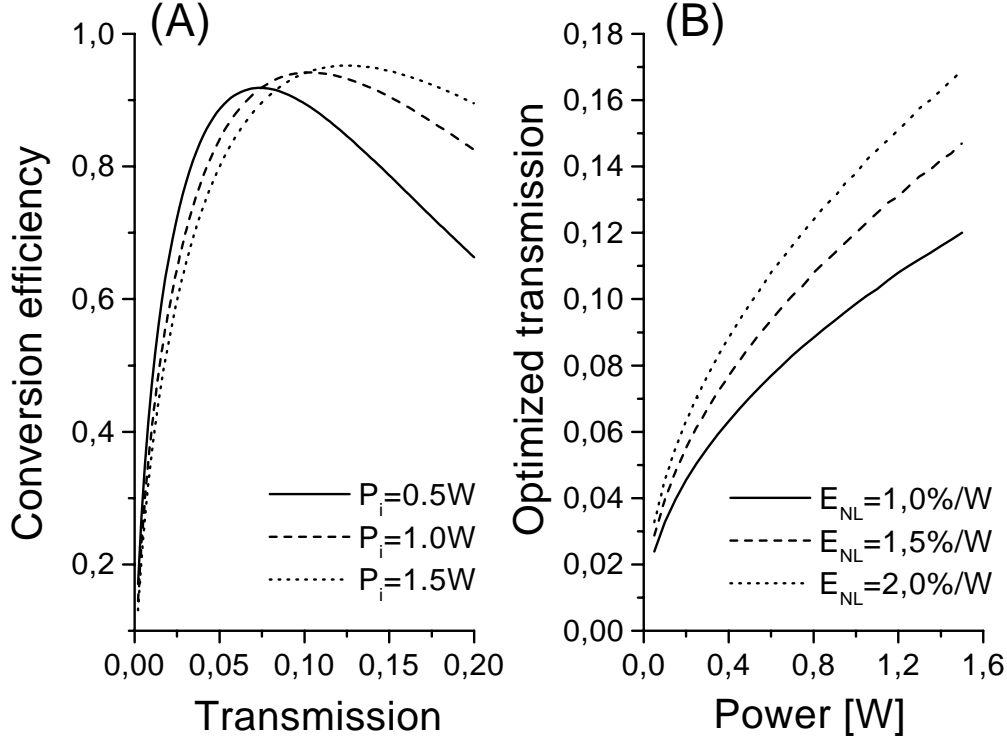


Figure 4.1: (A) The nonlinear conversion efficiency vs. the input coupler transmission. The plot corresponds to  $\mathcal{L} = 0.6\%$  and  $E_{NL} = 1 \%/W$ . (B) The input coupler transmission yielding the highest conversion efficiency in (A) vs. the available pump power. Again the losses were chosen to be  $\mathcal{L} = 0.6\%$ .

second harmonic generation with a high efficiency. Previous experiments have shown that  $\text{KNbO}_3$  offers the high nonlinearity, which is necessary in order to achieve the high conversion efficiency[23][30], and encouraged by our experience gained with BLIIRA, the choice of  $\text{KNbO}_3$  as the nonlinear material in our frequency doubler seemed obvious.

#### 4.1.1 Theoretical considerations

With the goal of finding the optimum parameters for nonlinear conversion in our second harmonic generator, let us now turn towards the theory for this device. In order to keep the experimental setup simple and reliable, we chose a singly resonant cavity, in which only the fundamental was built up. From (3.5) it is easy to see, that the cavity build up for this field is given by

$$\frac{P_c}{P_i} = \frac{4\mathcal{T}}{(\mathcal{T} + \mathcal{L} + P_c E_{NL})^2} \quad (4.1)$$

Here  $P_c$  is the intracavity fundamental power,  $P_i$  is the input fundamental power,  $\mathcal{T}$  is the input coupler transmission,  $\mathcal{L}$  are residual losses including BLIIRA and  $P_c E_{NL}$  is the nonlinear loss due to the conversion of the fundamental into the second harmonic. We are interested in solving (4.1) for  $P_c$ , in which

case we obtain a cubic equation with the solution

$$x = \frac{\lambda}{3} \left( \left[ 1 + \frac{27}{2} \frac{\rho}{\lambda^3} \left( 1 + \sqrt{1 + \frac{4}{27} \frac{\lambda^3}{\rho}} \right) \right]^{\frac{1}{6}} - \left[ 1 + \frac{27}{2} \frac{\rho}{\lambda^3} \left( 1 + \sqrt{1 + \frac{4}{27} \frac{\lambda^3}{\rho}} \right) \right]^{-\frac{1}{6}} \right)^2 \quad (4.2)$$

where we have defined  $x = P_c E_{NL}$ ,  $\lambda = \mathcal{T} + \mathcal{L}$  and  $\rho = 4\mathcal{T}P_i E_{NL}$ . The second harmonic power is now given by  $P_2 = E_{NL} P_c^2 = x^2 / E_{NL}$ , and using (4.2) this gives us

$$P_2 = \frac{\lambda^2}{9E_{NL}} \left( \left[ 1 + \frac{27}{2} \frac{\rho}{\lambda^3} \left( 1 + \sqrt{1 + \frac{4}{27} \frac{\lambda^3}{\rho}} \right) \right]^{\frac{1}{6}} - \left[ 1 + \frac{27}{2} \frac{\rho}{\lambda^3} \left( 1 + \sqrt{1 + \frac{4}{27} \frac{\lambda^3}{\rho}} \right) \right]^{-\frac{1}{6}} \right)^4 \quad (4.3)$$

Given the available pump power  $P_i$ , the internal losses  $\mathcal{L}$  and the nonlinearity of the doubling cavity,  $E_{NL}$ , we can optimize the input coupler transmission to obtain the highest nonlinear conversion efficiency,  $P_2/P_i$ . This is shown in figure 4.1(A), from which we find that the optimized value of the conversion efficiency depends on the available pump power, the nonlinearity and the cavity losses. The curves in figure 4.1(A) all correspond to a realistic value of  $\mathcal{L} = 0.6\%$ , and  $E_{NL} = 1 \text{ \%}/\text{W}$ . Having  $\mathcal{L}$  and  $E_{NL}$  fixed, we find the optimized conversion efficiency to be growing with increasing pump power. This is the reason why the highest achieved conversion efficiency known to the author of 89%[39], was obtained with a pump power as high as 1.25 W. In figure 4.1(B) the optimum input coupler transmission has been plotted versus the available pump power. This is shown for three different nonlinearities, and as a general trend, the best input coupler transmission is increasing with the available power. This is because the highest intracavity buildup of fundamental power occurs when the cavity is impedance matched[40], meaning that the input coupler transmission matches the total intracavity losses. The latter include the nonlinear losses due to the conversion, which grows significantly with increasing pump power.

In our treatment we have totally neglected BLIIRA and, as it will be shown in the next section, this nonlinear loss can seriously limit the conversion efficiency for higher pump powers. Another nonlinear effect arising in high power frequency doubling is thermal lensing, which tend to reduce the modematching and consequently the coupling efficiency of the pump into the doubling cavity. In some nonlinear materials, such as LiNbO<sub>3</sub>, the third order nonlinearity responsible for the photorefractive properties can come into play. As a result the second harmonic can change the index of refraction locally in the crystal, and self focusing effects arise. Here we have just mentioned just a few effects, which can limit the efficiency, with which we can produce the second harmonic. They should serve to remind us, that high power second harmonic generation is never a trivial task.

### 4.1.2 Experimental results

Guided by our theory from the previous section, we now turn to look at the actual experiment. The optimum focusing for nonlinear conversion we find from figure A.2 to be 15  $\mu\text{m}$  for a 10 mm crystal at 917 nm. By focusing our Ti:Sapphire output to this spotsize inside our KNbO<sub>3</sub> crystal, and measuring the generated second harmonic power, we were able to infer the single pass nonlinearity of 1.2  $\text{\%/W}$  for this particular crystal. The buildup cavity used to enhance the nonlinear interaction was chosen to be a folded ring design with an opening angle minimized to about 6<sup>0</sup> in order to avoid aberrations. The resonator contained two concave mirrors with a radius of curvature of 5 cm and two plane mirrors. The length of the cavity was chosen to yield a waist between the curved mirrors peaked at 17  $\mu\text{m}$  at the center of the stability curve. By inserting the crystal into the resonator the nonlinearity was found to be (1.0 $\pm$ 0.1)  $\text{\%/W}$ , and the intracavity losses in the absence of nonlinear interaction were measured to be (0.6 $\pm$ 0.1)  $\%$ . By estimating an amount of BLIIRA of 0.7  $\%$  in the presence of the second harmonic, and anticipating 500 mW of pump power at 917 nm, we obtain the optimum input coupler transmission of 7.9  $\%$ . For this experiment we chose an input coupler transmission of 7  $\%$ , since we were likely to use smaller pumping powers as well.

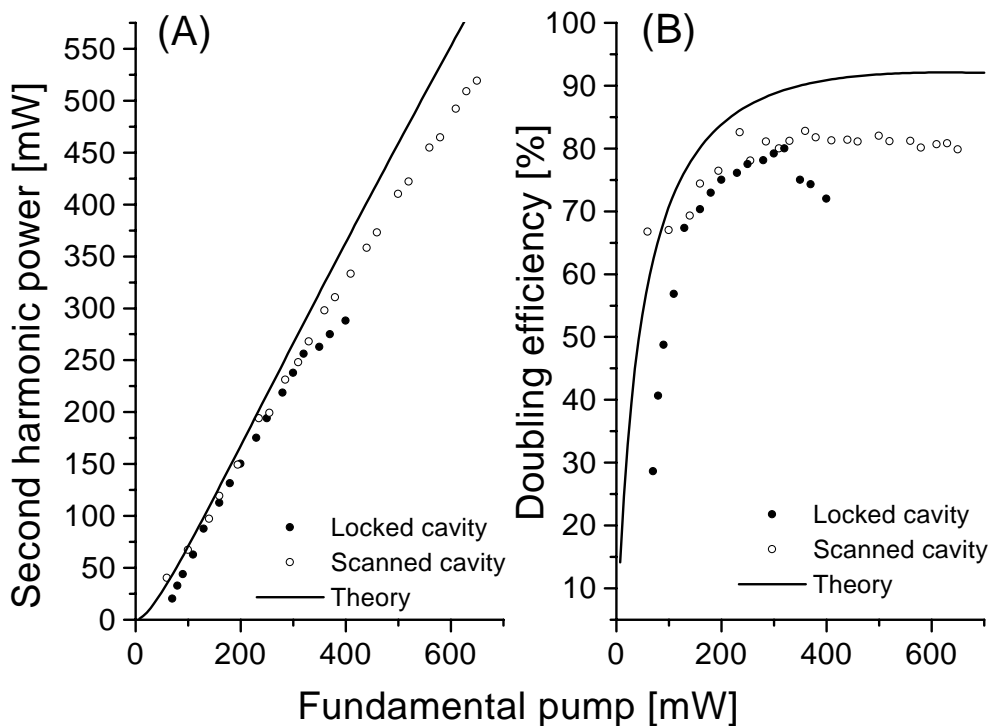


Figure 4.2: (A) The second harmonic power generated with a scanned and locked resonator. (B) The doubling efficiency with scanned and locked cavity. The full lines are derived from our theory with  $\mathcal{L} = 0.6\%$ ,  $T = 7\%$  and  $E_{NL} = 1\%/W$ .

The second harmonic efficiency was optimized first while scanning the doubling cavity sufficiently fast, so that thermal effects appeared on a longer timescale (typically hundreds of milliseconds) than the time it took to scan across resonance (a few milliseconds). The obtained doubling power on resonance was measured as a function of the pump power coupled into the nonlinear resonator.

After a crystal spot with high nonlinearity and low losses had been found in the scanning cavity, the crystal temperature was tuned away from phasematching and the cavity was locked to the laser line by means of a standard frequency modulation technique[41]. Then the crystal was slowly heated up to the phasematching temperature, and minor adjustments were applied to the cavity in order to optimize the second harmonic output. This procedure was necessary because the thermal effects made the resonator bistable. When the crystal temperature was increased above the phasematching temperature, the second harmonic output would drop drastically, and one would be unable to retain the maximum power by cooling down across the phasematching temperature. In order to reach the high second harmonic power, the cavity had to be unlocked and the procedure outlined above had to be repeated. It is needless to say, that this kind of operation required a servoloop performing very well in order to minimize fluctuations in the cavity detuning and consequently the intracavity fundamental power. The results from the scanned and locked frequency doubler are plotted in figure 4.2. The second harmonic power plotted in figure 4.2(A) is corrected for the finite reflection of the crystal surface and the output mirror resulting in an overall transmission of 83 %. Scanning the cavity we got as much as 520 mW peak power of second harmonic power, however when the cavity was locked, the thermal effects got so severe, that stable operation could only be obtained up to about 370 mW of pump power. Fortunately the conversion efficiency was high,

so that this pumping power actually was converted into 275 mW of the second harmonic. Correcting this number for the cavity escape efficiency, we ended up with about 225 mW for pumping the OPO. On a day to day basis we had more than 200 mW from the doubling cavity. The doubling efficiency is seen from figure 4.2(B) to peak at about 80% for a pump of 300 mW, at higher pump powers thermal effects became serious, and the efficiency dropped. Comparing to our theory with the measured parameters  $\mathcal{T} = 7\%$ ,  $\mathcal{L} = 0.6\%$  and  $E_{NL} = 1.0 \text{ \%}/\text{W}$ , we find good agreement for small second harmonic powers. As the pump power is increasing, the deviation from the theory becomes larger. This we attribute to BLIIRA, since this is not taken into account in our theory, and from the previous chapter we know, that BLIIRA grows strongly with increasing second harmonic power. Since the deviations from the theory are found in the scanning as well as the locked cavity, we can preclude the thermal effects as responsible for this feature.

If we attribute the discrepancy between the theory and the measured points to BLIIRA, we find the latter to be about 0.9% at 500 mW pumping power corresponding to 400 mW second harmonic power. Having a waist of the second harmonic of around  $10 \text{ }\mu\text{m}$  in the crystal, we find this power to yield an intensity of  $230 \text{ kW}/\text{cm}^2$  in the waist. The second harmonic in the doubling is created along the fundamental path in the crystal, whereas in the measurements devoted specifically to measure BLIIRA[34][24], the second harmonic was present throughout the crystal. If we correct for this in a crude way by dividing our intensity by a factor of two, we end up with the second harmonic intensity of about  $10^5 \text{ W}/\text{cm}^2$ . If we now compare our 0.9 % BLIIRA at  $100 \text{ kW}/\text{cm}^2$  with the results of ref. [24] taken at 860 nm, we again find that the BLIIRA has been reduced by more than a factor of two by going to the longer wavelength and consequently higher temperature.

## 4.2 Parametric amplification

With the good doubling results at hand we now moved on to the construction of the OPO. From (2.16) we see, that the observed squeezing decreases with increasing frequency of the observation. In (2.16) this frequency is measured in units of the OPO linewidth. This means that in order to minimize the loss of squeezing due to the finite bandwidth of the measurement, we should build an OPO resonator with as large linewidth as possible. Consequently the resonator should be short and have a large output coupler transmission. Keeping in mind that we later wanted to observe the interaction of our squeezed light with atoms, it was even more desirable that the bandwidth of the squeezing and consequently the linewidth of the OPO was as large as possible. The maximum output coupler transmission was limited by the available pump power and BLIIRA according to the discussion in the previous chapter, and the minimum length was set by the geometry of the resonator. Standard ABCD matrix calculations show that strong focusing mirrors are required in order to produce the optimum waist for nonlinear conversion for a short resonator. The total cavity length for our OPO was about 20 cm. In order to produce the waist in the vicinity of  $15 \mu\text{m}$ , we needed mirrors with a radius of curvature of 2.5 cm. The opening angle of our folded ring resonator was about 10 degrees, and with the strong focusing of our curved mirrors, this was on the edge of what could be tolerated in order to avoid significant aberrations in the cavity mode.

The OPO was not driven above threshold, and for this reason no coherent field was present inside the cavity. However it was still needed to keep the cavity in resonance with the fundamental wavelength of 917 nm in order to achieve an appreciable parametric gain. This was done by injecting a weak coherent field at the fundamental frequency into the OPO cavity through a high reflector in a direction counterpropagating to the second harmonic pump. Looking at the transmission of the field through the output coupler, an errorsignal could be generated by means of standard FM techniques[41]. The output coupler transmission of the cavity was measured to be  $\mathcal{T} = 7.3\%$  and the residual losses in the absence of BLIIRA were about  $\mathcal{L} = 0.3\%$ .

In order to observe the phase sensitive gain characteristic to the OPO below threshold, we injected another weak coherent field through a high reflector, this time in the direction copropagating to the

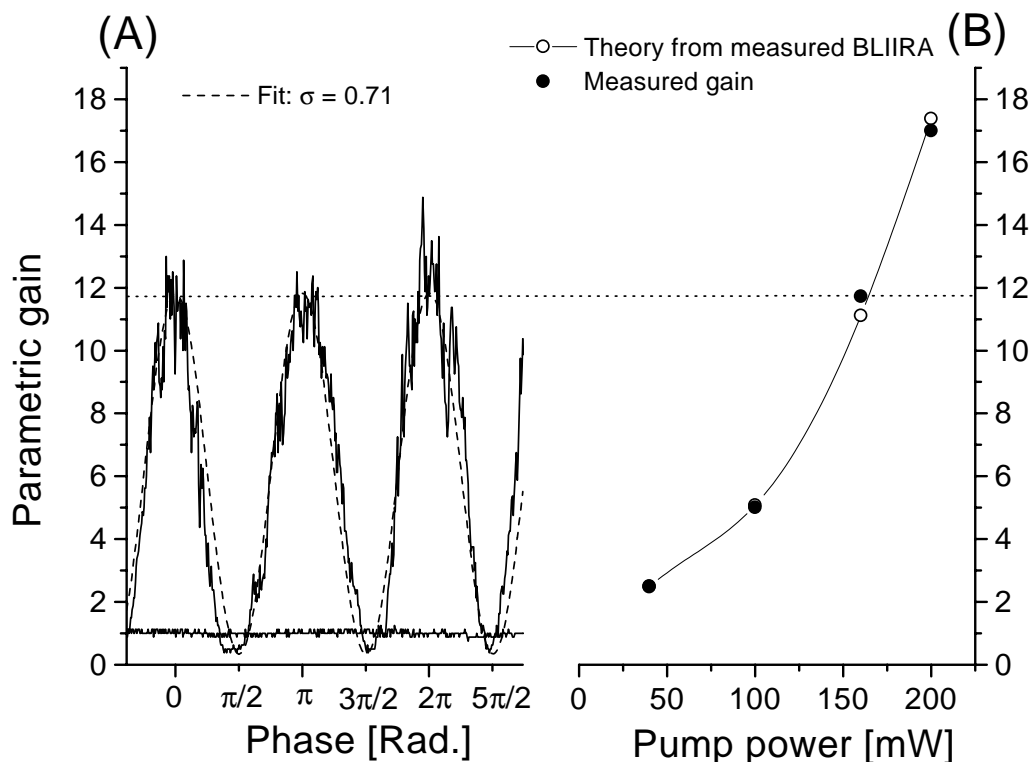


Figure 4.3: (A) The phase sensitive gain for a fixed pump power with the phase scanned. The dashed line corresponds to a theoretical fit yielding  $\sigma = 0.71$ . (B) The maximum gain as function of the pump power. The open points are obtained by using our theory with the measured values of BLIIRA. As a result we find the nonlinearity of about  $E_{NL} = 0.5 \text{ \%}/\text{W}$ .

pump. The amplification of this field was observed as its phase relative to the pump phase was being scanned. A typical trace is shown in figure 4.3(A) together with a fit (dashed line) relying on our theory for the gain (A.26). This fit gave us the value of the pump parameter  $\sigma = \sqrt{P/P_{th}}$  and consequently the OPO threshold. It should be noted here, that the obtained threshold depended on the BLIIRA, and consequently it was pump power dependent. Because of this, we measured BLIIRA for a series of pump powers together with the gain. This was done by lowering the temperature from phasematching and observing the variation of the transmission of the OPO with and without the pump present. By means of eqs. (A.19) and (A.26), we were now able to model the power dependence of the gain, and thereby obtain the crystal nonlinearity. These results are shown in fig. 4.3(B). The nonlinearity was found to be  $E_{NL} = (0.5 \pm 0.1) \text{ \%}/\text{W}$ , which is rather low. The reason for this loss of nonlinearity is still unclear, but it is likely to be caused by astigmatism in the OPO cavity. Astigmatism would reduce the overlap of the pump with the cavity mode and thereby reduce the nonlinear coupling. The pump powers on the horizontal axis of fig. 4.3(B) have been corrected for the coupling efficiency of 67% into the OPO. This was limited by the finite modematching and reflections from mirror and crystal surfaces of the pump.

The measured BLIIRA at 917 nm in the OPO ranged from 0.1 % at 40 mW pump power to 0.7 % at 200 mW pump, the latter corresponding to the intensity of  $10^5 \text{ W}/\text{cm}^2$ . Again comparing to ref. [24] we see, that the shift towards longer wavelengths and higher temperatures paid off in terms of reduced BLIIRA. The BLIIRA resulted in a threshold derived from the gain, which varied from 300 mW with 40 mW pump to 350 mW with 200 mW pump.

## 4.3 Squeezed light generation and detection

### 4.3.1 Homodyne detection of Squeezing

With the classical properties of the OPO under control, we now continued to examine the quantum features of the OPO output. According to the discussion in chapter 2, the output of a sub-threshold OPO does not possess a coherent amplitude, furthermore the photon number of this squeezed vacuum state is so small that the state is hard to observe using a conventional detector. In a sense our squeezing is just a weak optical signal, and from basic optics we know that such signals can be greatly enhanced by using a heterodyne detection scheme. Here a strong beam in a coherent state, called the Local Oscillator (LO), is mixed with our weak beam with an adjustable relative phase, and the resulting beam is sent onto a detector. The detector output will contain the beatnote between the signal and local oscillator. The strength of the beatnote is set by the product of the amplitude of the weak beam with the local oscillator amplitude, and consequently the signal strength has been increased by the ratio of the LO amplitude to the weak field amplitude. The heterodyne signal can be encoded at frequencies spanning from a few Hertz to several THz[9] depending on the frequency of the LO. The term 'homodyne detection' is usually used for the low frequency region. Since the squeezing of an OPO output basically is located within the OPO bandwidth, the LO frequency should match half the OPO pump frequency within this bandwidth. Obviously phase coherence between the squeezed vacuum and the LO is required in order to be able to separate the squeezed and antisqueezed quadratures, and as a result, the LO in our experiment was generated by splitting off a small portion of the pump for our frequency doubler. Hence the frequency of the LO was exactly the same as the frequency of the squeezed vacuum, and we ended up with a homodyne detector.

Our homodyne detector consisted of a 50% transmitting beamsplitter on which our LO containing about 1-5 mW of power was overlapped with the OPO mode. The two outputs of the beamsplitter were monitored on two high quantum efficiency photodiodes, and the two photocurrents were subtracted. It is easy to show that the differential photocurrent is given by[42]

$$i_- = 2\varepsilon\beta \left\langle X\left(\theta + \frac{\pi}{2}\right) \right\rangle \quad (4.4)$$

where we have used the detector quantum efficiency  $\varepsilon$  and that the LO has the real amplitude  $\beta$  and the phase  $\theta$ . The squeezed field quadrature  $X(\phi)$  is defined in (2.3). In order to arrive at (4.4), we have used that the LO is much stronger than the squeezed vacuum, such that the quantum nature of the former can be ignored, and the field operator replaced by a  $c$ -number. If almost every photon is detected,  $\varepsilon \lesssim 1$ , it is possible to define an operator for the photocurrents in such a way that the operator equality

$$\hat{i}_- = 2\varepsilon\beta X\left(\theta + \frac{\pi}{2}\right) \quad (4.5)$$

applies. And now it is straight forward to relate the noise of the photocurrent to the optical noise of the weak squeezed field

$$\delta i_-^2 = \langle \delta \hat{i}_-^2 \rangle = 4\varepsilon^2\beta^2 \left\langle q^2\left(\theta + \frac{\pi}{2}\right) \right\rangle \quad (4.6)$$

where the noise operator  $q$  has been defined in (2.8). It should be mentioned here that the photon flux  $\beta^2$  is given in units of the bandwidth of the measurement, and the photocurrent  $i_-$  is in units of the elementary charge.

The homodyne detection of  $i_-$  had the other advantage that the technical noise of our laser was cancelled out to a great extent, whereas the incoherent quantum noise could not be balanced out in this way. The balancing of technical noise in our detectors was typically more than 30 dB.

In order to observe the quantum noise reduction associated with squeezing, we were interested in eliminating all losses. In terms of the homodyne detector two sources of losses can occur. The first is imperfect modematching of the squeezed vacuum mode to the LO mode on the 50/50 beamsplitter. Only the component of the squeezed vacuum mode overlapping with the LO mode was observed in the

detection, and consequently a factor of  $\zeta^2$  of squeezing was lost on this account. Here  $\zeta$  is the fringe visibility of the interference fringe between the LO and the OPO output mode. In this experiment we found  $\zeta = 0.98 \pm 0.01$ . The second loss mechanism in the detection scheme was the imperfect quantum efficiency of the photodiodes. If this number was not 1, we could not detect all the field correlations, and as a result the squeezing was degraded with a factor of  $\varepsilon$ . In our experiment we used specially designed pin Silicon photodiodes from Hamamatsu Photonics with an  $\varepsilon$  of 0.995. A final important issue when detecting squeezing is that the electronic amplifiers in the detectors must have a good noise figure in order to have the optical noise dominating. To quantify this for our experiment, we observed that the quantum noise of light exceeded all other noise sources with 15 dB with a LO power of about 5 mW incident on the homodyne beamsplitter.

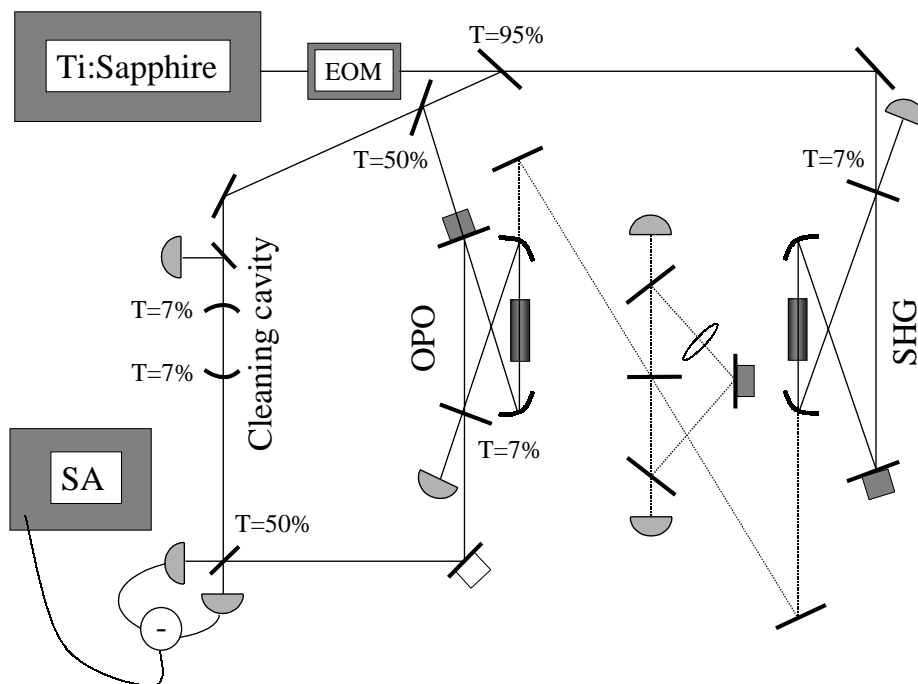


Figure 4.4: The setup used for squeezed light production. The second harmonic generator (SHG) was producing the pump for the OPO. The squeezed OPO output was sent onto the homodyne detector and the noise was analyzed in the spectrum analyzer (SA). All cavities except the triangular cavity were locked with an FM technique. For this purpose the electro optic modulator (EOM) was producing RF sidebands on the Ti:Sapphire output.

### 4.3.2 Experiment

As mentioned above we produced our local oscillator by splitting off a bit of the pump for our doubling cavity. However, the spatial mode of this light did not allow for more than 92 % fringe visibility on the homodyne beamsplitter. In order to clean this mode we designed a Fabry Perot resonator, which was locked to have its  $TEM_{00}$  mode resonant with the laser. Since a Fabry Perot resonator is virtually

aberration free, the transmission of this cavity was a clean  $TEM_{00}$  mode, which gave a fringe visibility of as much as 98 % on the 50/50 beamsplitter. The entire squeezing setup is illustrated in figure 4.4.

The OPO pump was modematched to the output of our frequency doubler by pumping the OPO through the output coupler with light at 917 nm. The nonlinear crystal was phasematched and the generated second harmonic was modematched to a designated reference cavity. This is illustrated by the triangular cavity in between the SHG and the OPO in figure 4.4. Then the doubling cavity output was modematched to the reference cavity in the counterpropagating direction and hence to the OPO. The quality of the modematching was typically about 95 % in each direction.

The differential photocurrent from the homodyne detector was monitored on a Radio Frequency (RF) Spectrum Analyzer (SA) at a frequency of 3 MHz with a bandwidth of 100 kHz. The 3 MHz frequency was chosen because above this frequency, a 2.5 mW beam from the Ti:Sapphire laser was displaying technical noise 8 dB above the shot noise corresponding to 6.3 times. This meant that after 30 dB of balancing only 0.5 % of technical noise relative to shot noise would be present in the differential photocurrent.

Now the OPO was pumped while the relative phase between the squeezed vacuum and the LO was scanned, and the SA signal is shown in figure 4.5. The flat trace around 0 dB was measured with the OPO pump blocked, this indicated our shot noise level. It was checked that the noise responsible for this level really was stochastic in nature, as is quantum noise, by attenuating the LO power in steps of 50%. For technical noise, which is coherent, this means that the noise power will go down with -6 dB corresponding to 75%. However for quantum noise, which has a stochastic phase, a reduction of 50% in the power will only result in a reduction of -3 dB in the noise power corresponding to 50%. In other words, quantum noise is growing linearly with the number of photons in the LO whereas technical noise grows quadratically. The quantum noise level in figure 4.5 was checked to grow linearly with the power to within 10%.

As the OPO pump was increased, the phase sensitive gain started to show. From the dashed line, which is a fit to the modulated curve, we find that the gain was about 11.5 dB corresponding to 14 times. More interesting are the dips in the curve. For a phase difference around  $\pi/2$ ,  $3\pi/2$  etc. we see that the noise level is reduced below the shot noise limit, meaning that we have reduced the quantum fluctuations of the OPO output below the standard quantum limit. In this series of measurements the quantum noise reduction was about -5 dB, which is equivalent to 32% remaining quantum fluctuations in the squeezed quadrature of the OPO mode.

Ideally the squeezing should go as low as the 11.5 dB gain, that we observed, however in practice a number of factors limited this number. 1) We did not look for squeezing a zero frequency, where we found in chapter 2 that the best squeezing is found. This reduced the squeezing with 6%. 2) Our detectors did not have 100% quantum efficiency, meaning that not all correlations were detected. 3) Even though good optics was used, the propagation of the squeezed vacuum was lossy. Our best estimate showed that about 1% of the squeezing was lost in propagation to the detector. 4) The fringe visibility on the homodyne detector was not 100%, and consequently not all of the squeezed mode was probed by the LO. This reduced the squeezing by 4%. 5) Finally not all the correlated photons circulating inside the OPO cavity escaped in the desired direction through the output coupler. The finite escape efficiency of the OPO reduced the squeezing with 12.2%. The final balance is shown in the table below.

1)	Finite frequency of the measurement	0.94
2)	Quantum efficiency of the photodiodes	0.995
3)	Propagation losses from OPO to detectors	0.99
4)	Homodyne efficiency on 50/50 beamsplitter	0.98 <sup>2</sup>
5)	OPO escape efficiency	0.878
6)	Finite OPO gain of 11.5dB	0.93
TOTAL		0.73

Adding up all the limiting factors, we end up with 73% quantum noise reduction to be observed. This is -5.6 dB of squeezing in reasonable agreement with the observed -5 dB of squeezing from figure

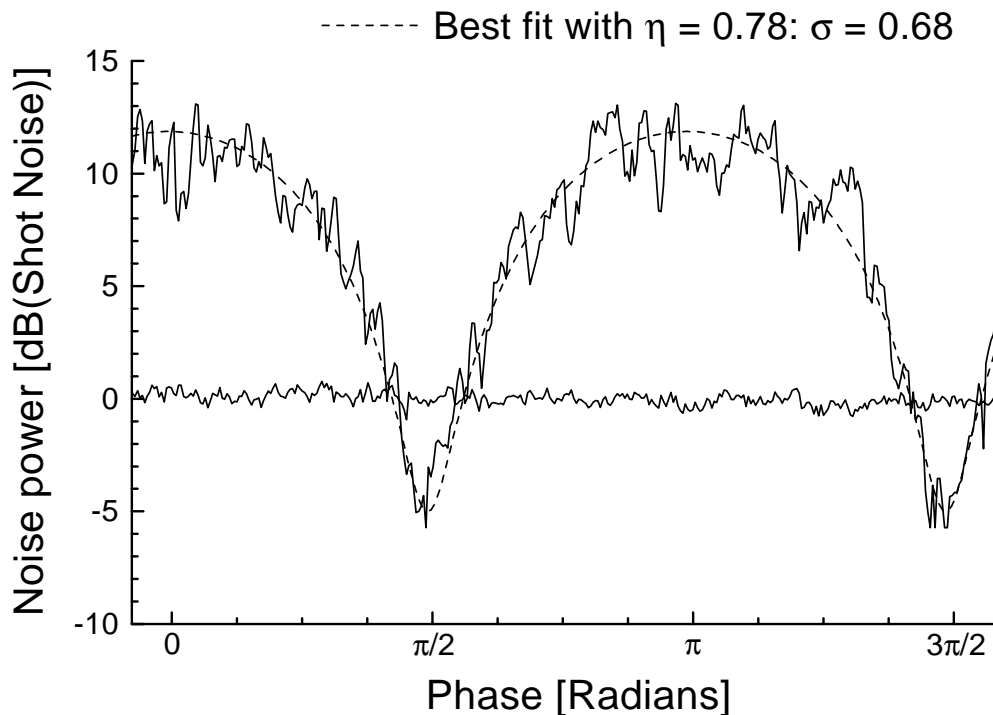


Figure 4.5: The phase sensitive noise of the OPO output recorded on the RF spectrum analyzer. The noise was measured in a 100 kHz frequency window around 3 MHz. The flat trace around 0 dB is the measured photocurrent with the OPO output blocked. This sets the shot noise level. When the squeezed vacuum enters on the beamsplitter, the noise levels oscillates depending on the relative phase between the LO and the squeezing. The trace shows a parametric gain of 11.5 dB and a quantum noise reduction of about 5 dB relative to the shot noise level. The dashed curve is the best fit with an overall efficiency of 78% yielding  $\sigma = 0.68$ .

4.5. The last number is obtained from a fit to our data using the 78% efficiency inferred from the points 1) to 5) above. This fit is shown as the dashed curve on fig. 4.5, from which we could derive the OPO pump parameter to be  $\sigma = 0.68 \pm 0.01$ .

Although this experiment clearly showed that the problem of BLIIRA can be circumvented to some extent by going to higher temperatures, the table above told us, that the major limitation of the squeezing still was the OPO escape efficiency and consequently BLIIRA. The reason, why we could not simply use an output coupler with a higher transmission, was that the nonlinearity of the OPO crystal was low. In this experiment the nonlinearity was only about 0.5%/W as opposed to the 2%/W reported in ref. [7] for the same type of material. With a higher nonlinearity we could have reached the same gain with a smaller amount of pump power and consequently with less BLIIRA and a higher escape efficiency. Towards this end, the relative new technique of Quasi Phase Matching seems promising[43][44][45]. Having the phasematching conditions inherently present in the crystal design, it is possible to have nonlinear interaction when the harmonic and the fundamental have parallel polarizations. This means that it is possible to exploit the generally larger diagonal elements in the nonlinear tensor for parametric processes. For comparison, a 10 mm sample of periodically poled Lithium Niobate can display a single pass nonlinearity of as much as 8%/W, which is 4 times larger than the best KNbO<sub>3</sub> crystals provide.

## 4.4 Summary

In summary the squeezing experiment described in this chapter was very valuable in terms of gained experience with nonlinear optics and nonclassical light. We demonstrated doubling efficiencies exceeding 80% in our  $\text{KNbO}_3$  frequency doubler. This resulted in second harmonic powers in the vicinity of 300 mW, sufficient for pumping out sub-threshold OPO. In the latter we observed a phase sensitive gain as high as 17 and thresholds ranging from 300 mW to 350 mW. The threshold was found to be depending on the pump power because of the BLIIRA. This is also the reason why the maximum gain not necessarily gives the best squeezing. We found our best squeezing to be about -5 dB with a parametric gain of 11.5 dB. Within the uncertainties the loss of squeezing was accounted for, and the biggest contribution to this loss was found to be the OPO intracavity absorption. This limited the escape efficiency to be around 88%, which is still larger than the anticipated efficiency at room temperature. Taking the BLIIRA at room temperature from ref. [7] to be 1.5% with 200mW pump together with our output coupler transmission of 7.3% and residual intracavity losses of 0.3%, we predict an escape efficiency at room temperature of only 80%. This shows clearly that we gained in the degree of squeezing by heating the  $\text{KNbO}_3$  crystal above  $100^\circ\text{C}$  as compared to a similar experiment at room temperature. The rather poor nonlinearity of the OPO  $\text{KNbO}_3$  crystal prevented us from increasing the escape efficiency by employing an output coupler with a higher transmission. The loss of nonlinearity should most likely be attributed to aberrations in the OPO mode.

Although desired, more than 5 dB of squeezing was not necessary for the experiment described in the next chapter. Here we wanted to demonstrate sub-shot noise performance of a Polarization Interferometer by employing a so called Polarization Squeezed State of light.

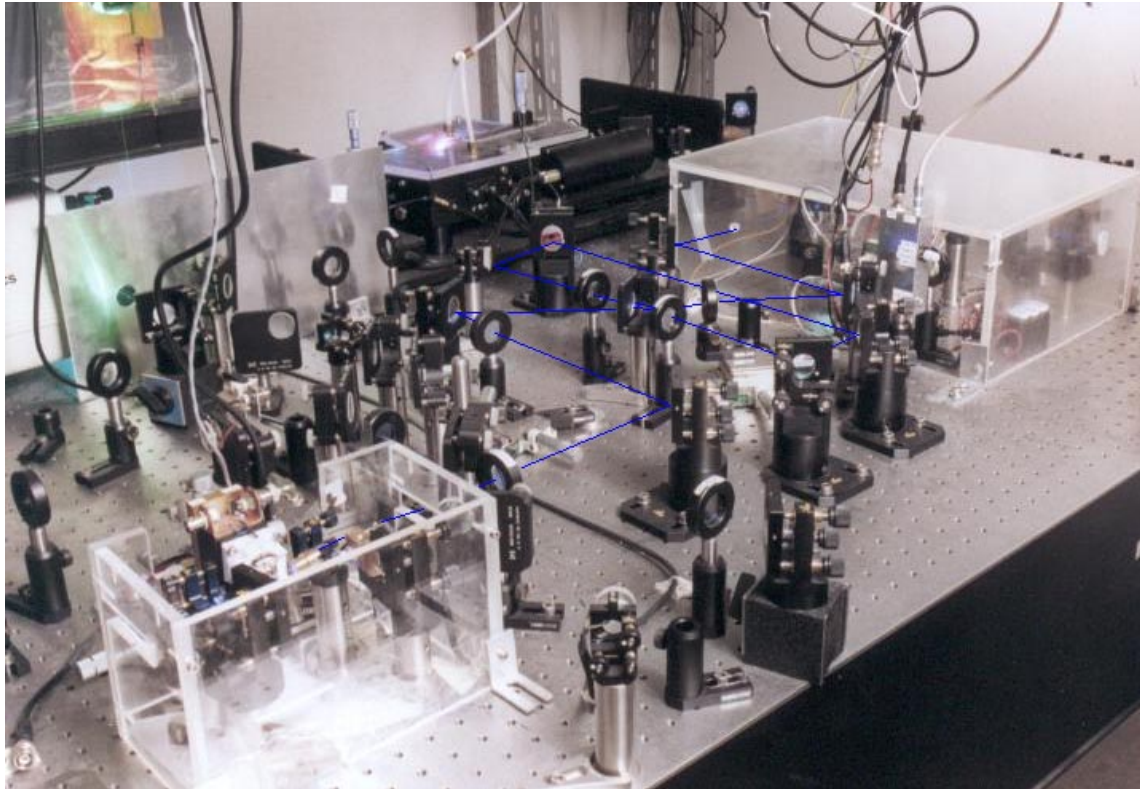


Figure 4.6: The frequency tunable squeezed light source. In the background the Argon Ion laser pumped Ti:Sapphire is seen. This is pumping the doubling cavity in the box on the right. The 458nm output from the doubling cavity is indicated with the line. This is used to pump the subthreshold OPO in the box on the left, resulting in the squeezed vacuum output.

## Chapter 5

# Nonclassical Polarization Spectroscopy

In the last chapter the construction and performance of our squeezed light source was described. This source was operated to produce quantum correlated light at 917 nm, but due to the wide tunability of the Ti:Sapphire laser driving the source, in principle any wavelength between 840 and 1000 nm could be reached. This range was limited by the phasematching temperature of the KNbO<sub>3</sub> crystals responsible for the nonlinear interaction, since these fragile crystals undergo phase transitions at -50°C and 223°C. Needless to say that the tunability was of great importance when the squeezing should be applied to address certain atomic transitions.

In the following three chapters our attempts to perform highly sensitive measurements on the collective spin of an atomic ensemble will be described. The first of these attempts utilized our frequency tunable squeezed light source to probe a Polarization Interferometer. This served as our tool for probing the atomic spin and in the first section of this chapter we will describe the details of our polarization interferometer. Then we will move on to address our atomic target, which in this case was cold, trapped atoms in a Magneto Optical Trap. This device will be presented and characterized in greater detail below. In order to achieve sub-shot noise sensitivity in the Polarization Interferometer, a Polarization Squeezed state had to be produced, and in the third section it will be outlined how to convert the OPO output into this nonclassical state. Finally the details and the results of the experiment will be presented and our conclusions will be drawn.

### 5.1 The Polarization Interferometer

In ultrasensitive optical measurements, the Polarization Interferometer (PI) has proven to be a valuable tool. Noteworthy examples are a precise measurement of the Rydberg constant[46] and the observation of parity nonconservation effects due to the electroweak interaction in atoms[47]. More everyday applications of the PI span from atomic spectroscopy[48] through measurements of molecular rotational relaxation of excited electronic states[49] to the stabilization of lasers and optical resonators[50]. In this section we will describe the PI used in our experiments and in this context derive the lineshapes when macroscopic atomic orientation and alignment is probed with this device.

#### 5.1.1 The setup

Our PI consisted of two polarizing beamsplitters (PBS1/2) rotated 45° relative to each other by means of a half wave retarder ( $\lambda/2$ ). This is illustrated in figure 5.1. The first polarizer served to clean the polarization of the probe beam entering the PI as well as for mixing the orthogonally squeezed vacuum

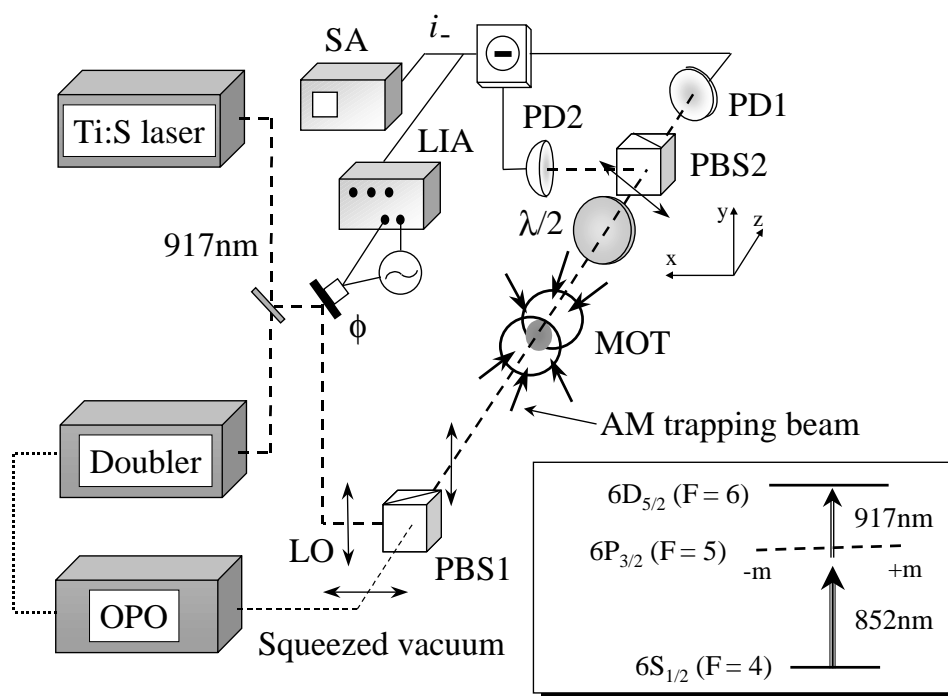


Figure 5.1: The polarization interferometer setup. Squeezed vacuum from the OPO is mixed with the local oscillator on PBS1. The resulting polarization squeezed state is probing the magneto optical trap (MOT) and the polarization rotation is being analyzed by PBS2. An RF spectrum analyzer (SA) is recording the noise power of the differential photocurrent from the photodiodes PD1/2.

with the local oscillator. The latter was an ordinary coherent state produced by our Ti:Sapphire laser. In the absence of an optically active medium in the path of the probe beam, an equal amount of optical power was directed to the photodiodes PD1 and PD2 by the second polarizer PBS2. As a result the differential photocurrent  $i_-$  would be zero in this case. If however, an anisotropic medium was placed between the two polarizers, the polarization would be rotated, and the symmetry between the photocurrents from PD1 and PD2 would be broken. Now the differential photocurrent would be given by  $i_- = 2i_0\theta$ . Where  $i_0$  is the sum of the photocurrents coming from the two PD's and  $\theta$  is the polarization rotation angle.

The prism polarizers commercially available today are usually of very good quality. This means that they have very small extinction ratios, it is not unusual to have this number less than  $10^{-6}$ . Having such two polarizers crossed at  $90^\circ$  the major limitation to the sensitivity, with which one can measure polarization rotation, would be the quality of the photodetector used. Provided that the dark current of this device can be kept low, ultrahigh precision in the measurement can readily be obtained. If however the detector noise is realistic high, our strategy with  $45^\circ$  crossed polarizers turned out to give a better signal to noise ratio, since the signal grew linear in the polarization rotation angle in contrast to the  $90^\circ$  case, where the signal would grow quadratic in  $\theta$ . Keeping in mind that we wanted to apply squeezed vacuum in our PI, the  $45^\circ$  setup had the additional advantage that almost all the light in the probe beam reached the detectors, meaning that the measurement was limited by optical noise instead of electronic noise and that almost no correlations were lost.

### 5.1.2 The lineshape

With the goal of obtaining the parameters relevant to the polarization rotation in the PI, we now apply the Jones formalism to our probe electric field. In general having an electromagnetic wave propagating along the  $z$  axis in an anisotropic medium with the electric field  $\vec{E}(z)$ , we can obtain the effect of the medium on the field from the equation

$$\ell \frac{d\vec{E}(z)}{dz} = [\mathbb{A} - \mathbb{I}(\alpha/2 - i\delta)] \vec{E}(z) \quad (5.1)$$

Here the matrix  $\mathbb{A}$  contains the information about the specific state of the medium, and its elements are assumed to be small, meaning that the anisotropy is small. We have pulled out the optical depth,  $\alpha$ , and phaseshift,  $\delta$ , common for the two components of  $\vec{E}$ , and  $\ell$  is the interaction length of the anisotropic medium. The electric field is assumed to be oscillating in the plane orthogonal to the  $z$  axis. Keeping in mind that the elements of  $\mathbb{A}$  are small, we expand the solution (5.1) to first order in these, to obtain

$$\vec{E}(\ell) = (\mathbb{I} + \mathbb{A}) e^{i\delta - \alpha/2} \vec{E}(0) \quad (5.2)$$

We now choose to work in the basis of the eigenpolarization of PBS2. Here we define horizontal and vertically polarized light to be oscillating along the  $x$  and  $y$  axes respectively (see fig. 5.1). In this basis, we write  $\mathbb{A}$  and the  $45^\circ$  polarized incident light as

$$\mathbb{A} = \begin{pmatrix} a_{xx} & a_{xy} \\ a_{yx} & a_{yy} \end{pmatrix}, \quad \vec{E}(0) = \frac{E_0}{\sqrt{2}} \begin{pmatrix} 1 \\ 1 \end{pmatrix} \quad (5.3)$$

The electric field transmitted/reflected by PBS2 will then be given by

$$\begin{pmatrix} E_x \\ E_y \end{pmatrix} = \frac{1}{\sqrt{2}} E_0 e^{i\delta - \alpha/2} \begin{pmatrix} 1 + a_{xx} + a_{xy} \\ 1 + a_{yx} + a_{yy} \end{pmatrix} \quad (5.4)$$

and the differential photocurrent is

$$i_- = \varepsilon(i_y - i_x) = \varepsilon i_0 e^{-\alpha} \left[ \text{Re}\{a_{yy} - a_{xx}\} + \text{Re}\{a_{yx} - a_{xy}\} + \frac{1}{2}|a_{yx} + a_{yy}|^2 - \frac{1}{2}|a_{xx} + a_{xy}|^2 \right] \simeq 2\theta \varepsilon i_0 e^{-\alpha} \quad (5.5)$$

where we have used the detector quantum efficiency  $\varepsilon$  and the initial probe photon flux  $i_0$ . The rotation angle relative to the original  $45^\circ$ ,  $\theta$ , of the linearly polarized part of the probe field is found to be

$$\theta \simeq \text{Re} \left\{ \frac{E_y(\ell) - E_x(\ell)}{E_y(\ell) + E_x(\ell)} \right\} \simeq \frac{1}{2} (\text{Re}\{a_{yy} - a_{xx}\} + \text{Re}\{a_{yx} - a_{xy}\}) \quad (5.6)$$

The first term in (5.5) is obviously related to the different absorption of light polarized along the  $y$  axis and along the  $x$  axis. This effect is called *linear dichroism*. As it will be indicated below, the second term is related to a different phaseshift of the  $\sigma^+$  and  $\sigma^-$  polarized components of the linearly polarized probe, which is called *circular birefringence*[51]. The last two terms are of higher order in the  $a_{ij}$  coefficients and will therefore be ignored here.

To analyze our signal further it is instructive to switch to a  $\sigma^\pm$  polarized basis with the  $x'$  axis rotated  $45^\circ$  relative the original  $x$  axis. Here our anisotropy matrix  $\mathbb{A}'$  and initial field looks like

$$\mathbb{A}' = \frac{1}{2} \begin{pmatrix} [(a_{xx} + a_{yy}) + i(a_{xy} - a_{yx})] & [i(a_{xx} - a_{yy}) + (a_{xy} + a_{yx})] \\ [-i(a_{xx} - a_{yy}) + (a_{xy} + a_{yx})] & [(a_{xx} + a_{yy}) - i(a_{xy} - a_{yx})] \end{pmatrix}, \quad \vec{E}'(0) = \frac{E_0}{\sqrt{2}} \begin{pmatrix} 1 \\ 1 \end{pmatrix} \quad (5.7)$$

Since the imaginary parts of the diagonal matrix elements control the relative phase between the  $\sigma^+$  and  $\sigma^-$  fields, we see from the form of  $\mathbb{A}'$ , that  $\text{Re}\{a_{yx} - a_{xy}\}$  is responsible for the circular birefringence of

our medium. Another contribution could come from  $\text{Im}\{a_{xx} + a_{yy}\}$  in the diagonal, but since this term appear with the same sign in both diagonal elements, it can only cause an overall phaseshift.

In summary we find the rotation angle to the lowest order in the anisotropy matrix elements to be

$$\theta = \pi \frac{\ell}{\lambda} (n_+ - n_-) + \frac{1}{2} (\alpha_y - \alpha_x) \quad (5.8)$$

Here  $\lambda$  is the wavelength of the probe light in vacuum,  $n_{\pm}$  are the indices of refraction for  $\sigma^{\pm}$  polarized light respectively and  $\alpha_{x/y}$  are the optical depths for light polarized linearly along the  $x$  and  $y$  axes of PBS2 respectively (see figure 5.1).

In order to perform a quantum noise limited measurement, the photocurrent  $i_-$  was recorded at the RF frequency  $\Omega/2\pi = 3$  MHz. In this case we did not measure the angle (5.8) but rather its noise. This is given by

$$\delta i_-^2 = 4i_0^2 \delta\theta^2 + 4\theta^2 \delta i_0^2 \quad (5.9)$$

Obviously the first term describes the noise in the polarization rotation angle and the last is the intensity noise of the probe beam. In our case, the balanced detection scheme together with a quiet laser and a small DC rotation angle meant, that we could ignore the last term. The first term has several contributions, so we write it as

$$\delta i_-^2 \simeq 4i_0^2 (\delta\theta_{sig}^2 + \delta\theta_{ShN}^2 + \delta\theta_{SpN}^2) \quad (5.10)$$

Here  $\delta\theta_{sig}^2$  is the polarization noise due to our modulated atomic sample, and this is what we want to address in this section.  $\delta\theta_{ShN}^2$  is the polarization jitter set by the quantum noise of our probe. Later in this chapter we will show how this contribution can be reduced by means of squeezed light. Finally  $\delta\theta_{SpN}^2$  is the quantum spin noise associated with the macroscopic longitudinal orientation and transverse alignment of our atomic sample. This contribution becomes important when the optical depth of our target is high. In this experiment a high optical depth would result in a high absorption of the probe, and consequently a serious loss of squeezing. For this reason we kept the optical depth of our target low in the experiment and consequently the last term in (5.10) will be ignored here. In chapter 7 we will consider atomic media with high densities, and the spin noise term will be treated in greater detail. It should be noted that we in general assume that our detectors have almost 100% quantum efficiency ( $\varepsilon \simeq 1$ ), such that  $i_0$  describes the photocurrent in units of the elementary charge as well as the photon flux of the probe beam within the bandwidth of our measurement.

As mentioned earlier our probe medium was a sample of cold Caesium atoms trapped in a Magneto Optical Trap. In this section it will suffice to treat these atoms as an effective three level system in a ladder configuration. As illustrated in the insert in figure 5.1, the atoms are trapped on the lower transition corresponding to a wavelength of 852 nm, and the population in the intermediate level is probed on the upper transition at 917 nm.

In order to generate a signal at our probe frequency  $\Omega$ , the atomic population in the intermediate level was modulated by intensity modulating one of the trapping laser beams, which was almost copropagating to the probe. The angle between the two beams was approximately  $20^\circ$ . As a result of the modulation, the index of refraction and the absorption were also modulated, and hence the differences in (5.8) were modulated. From (5.8) it is now clear that if the differences were modulated, the polarization angle of the probe was being modulated as well. In the limit of weak fields on both transitions of our ladder system, the absorption profile of the probe on the upper transition is nothing but a Lorentzian with the width  $\Gamma = (\gamma_1 + \gamma_2)/2$ , where  $\gamma_1$  and  $\gamma_2$  are the FWHM's of the intermediate and excited states respectively. The index of refraction and hence the difference between two indices of refraction varies like the derivative of a Lorentzian with the same width  $\Gamma$ , as the probe detuning is changed. The modulation of the population in the intermediate level would result in a modulation of the sizes of the two lineshapes, and since the noise *power* was recorded on the SA, the resulting signal shape would vary like the square of the sum of the two contributions. In summary this is written like

$$\delta\theta_{sig}^2 |_{\Omega} = \left( \xi_1 \frac{\Gamma^2/4}{\delta^2 + \Gamma^2/4} + \xi_2 \frac{\delta\Gamma}{\delta^2 + \Gamma^2/4} \right)^2 \quad (5.11)$$

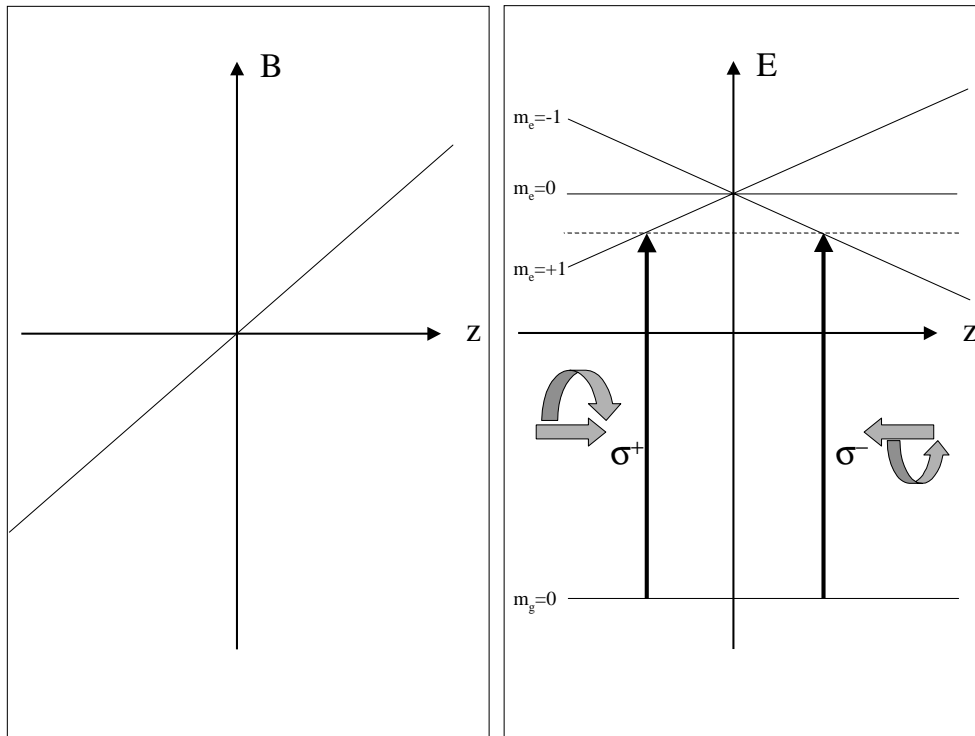


Figure 5.2: The Doppler theory of the MOT. The magnetic field  $B$  is changing sign a  $z = 0$ . Consequently the Zeeman shifts changes sign as the zero field region is crossed and the  $\sigma^+$  and  $\sigma^-$  polarized red detuned cooling lasers come into resonance with the atomic transition and kicks the atom towards the zero field region.

where  $\delta$  is the probe detuning from the two photon resonance in the ladder system, and  $\xi_1$  and  $\xi_2$  are parameters containing the information on how efficient the modulation was transferred from the pump to the probe via the atoms. Since the process described above is nothing but four wave mixing in an atomic medium, the  $\xi$  coefficients are closely related to the third order nonlinearity,  $\chi^{(3)}$ , of the atomic medium. A more elaborate theory for the atomic signal will be given in the following chapters, but for this experiment our simple arguments above will suffice.

## 5.2 The Magneto Optical Trap

As mentioned above, the optically active medium for the PI was provided by a Magneto Optical Trap (MOT). In this Ph. D. work the MOT was used only as a tool, and therefore only a minimum of time was spent on characterizing this device. However, since it was used to provide the target to be probed in the experiments described in this and the following chapters and because the trapping mechanisms turned out to be important to some of our later experiments, a brief description of our MOT setup will be given in the following.

The first demonstration of atoms trapped in a MOT came as early as 1987[52], and since then the MOT has been developed and simplified to become a standard ingredient in various spectroscopic and Quantum Optics experiments[53][54][55][56][8]. Typical temperatures of the atoms in a MOT are well

below 1 mK and the densities can be as high as  $10^{11} \text{ cm}^{-3}$ [57], which means, that they provide dense, Doppler free targets well suited for high precision measurements. Optical depths in a MOT as high as 40 on the trapping transition has been reported[58], but in this work the optical depths were typically well below 10. In the experiment described in this chapter, the optical depth was kept particular low, since nonclassical probe light was involved and hence the absorption should be kept at a minimum.

### 5.2.1 Theory

The mechanism responsible for the trapping of atoms in a MOT is usually visualized as follows. In one dimension a magnetic field varying linearly with position and changing direction as the zero point is crossed is Zeeman shifting the magnetic sublevels of the  $J = 1$  excited state of an atom with a  $J = 0$  ground state. The magnetic field is assumed to be weak, so that the Zeeman shift is linear in the field strength and hence the position. To provide the force, we apply a  $\sigma^+$  polarized red detuned laser beam is propagating in the positive direction and a  $\sigma^-$  polarized laser beam in the opposite direction. Now an atom positioned in the positive half of the quantization axis will become resonant with the  $\sigma^-$  polarized laser due to the Zeeman shift and receive a kick towards the zero field region. The reversed argument applies for an atom in the negative half of the quantization axis. Furthermore an atom located in the zero field region, which has a positive velocity will become resonant with the  $\sigma^-$  polarized laser due to the Doppler shift and hence become decelerated. Similarly an atom moving in the negative direction will become stopped. This is illustrated in figure 5.2. The slope of this Doppler force vs. velocity is basically set by the linewidth of the cooling transition,  $\gamma_1$ , and this sets the Doppler limit  $T_D = \hbar\gamma_1/2k_B$  on how low temperatures one can achieve in a MOT[59]. For  $^{133}\text{Cs}$  this limit is about  $125 \mu\text{K}$ .

It has turned out that the MOT offers the possibility of reaching temperature smaller than the Doppler limit[60][61]. These sub Doppler temperatures obtained in a circular polarized MOT, like we used, are typically explained by means of a velocity dependent orientation in the ground state[62]. This of course means that the ground state must have an angular momentum larger than the  $J = 0$ , we used above. Suppose we have counterpropagating cooling beams  $\sigma^+$  polarized with respect to their propagation axis. This means that with respect to the quantization axis chosen along one of the beams, an atom will see  $\sigma^+$  polarized light propagating in the positive direction and a  $\sigma^-$  polarized beam propagating in the negative direction. If the atom is moving in the positive direction along the quantization axis, the population in the magnetic substates with negative magnetic quantum number,  $m_g$ , will become larger than the population of the positive  $m_g$  states, provided the cooling lasers are red detuned. Consequently an atomic orientation in the negative direction is built up, and due to the difference in the Clebsch Gordan coefficients, the atom is more likely to absorb a photon from the  $\sigma^-$  polarized beam propagating in the negative direction, and as a result receive a momentum kick in the negative direction. The reversed argument can be applied to an atom moving in the negative direction. The net result of this dynamics is, that a moving atom always will experience a force directed opposite to the velocity similar to a friction force. This is why such an arrangement of laserbeams is called *optical molasses*. The velocity dependence of the light force is much stronger than the simpler Doppler force, meaning that the atoms in principle can be cooled as low as the single photon recoil limit. For  $^{133}\text{Cs}$  this limit is around  $100 \text{ nK}$ . In practice radiation trapping in the resulting dense atomic media usually puts a lower limit on the temperature of a few  $\mu\text{K}$ [57].

### 5.2.2 Characterization

The element used in our MOT was Caesium. This was captured from the back ground vapor in our vacuum chamber, in which the Cs pressure typically was about  $10^{-8}$  torr. The atoms were trapped on the  $6S_{1/2}(F = 4) \rightarrow 6P_{3/2}(F = 5)$  transition at 852 nm and probed on the  $6P_{3/2} \rightarrow 6D_{5/2}(F = F')$  transition at 917nm. The hyperfine splitting in the  $6D_{5/2}$  state is so small in Cs, that all accessible hyperfine levels were addressed as the probe laser was scanned across resonance. The finite overlap of the  $6P_{3/2}(F = 5)$  level with the  $6P_{3/2}(F = 4)$  level resulted in a loss of atoms from the cooling cycle due to

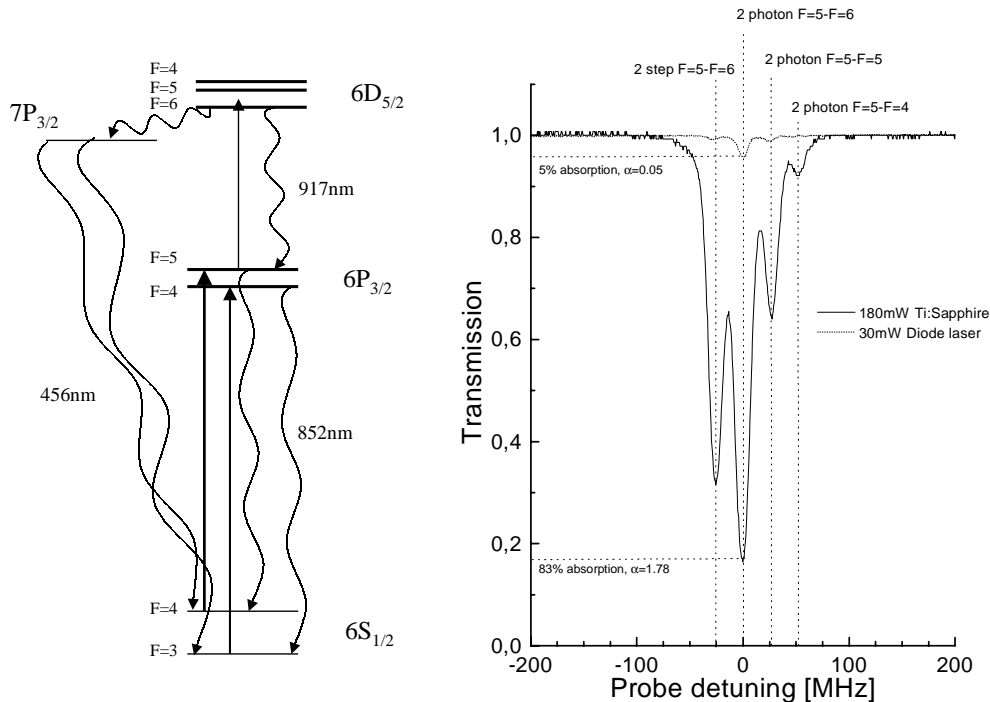


Figure 5.3: The relevant energy levels in atomic Cs. The curves show the transmitted power of the 917nm probe for two different trapping lasers. The multiple peaks are due to the AC Stark splitting of the  $6P_{3/2}(F=5)$  level and the hyperfine splitting of the  $6D_{5/2}$  level.

the decay from  $6P_{3/2}(F=4)$  state to the  $6S_{1/2}(F=3)$  ground state. As a result we needed a designated repumping laser resonant with the  $6S_{1/2}(F=3) \rightarrow 6P_{3/2}(F=4)$  transition in order to keep the trapped atoms in the cooling cycle. The relevant energy levels in Cs are shown in figure 5.3. The repumping laser was a 100 mW diode laser stabilized with an external grating and locked to the Cs transition using standard FM saturation spectroscopy[41]. The light driving the trapping transition was provided by another diode laser when no particular high optical depth was required, and by a homebuilt Ti:Sapphire laser when a large number of trapped atoms was needed. In both cases the laser line was locked to the cross over resonance between the  $6S_{1/2}(F=4) \rightarrow 6P_{3/2}(F=4)$  and the  $6S_{1/2}(F=4) \rightarrow 6P_{3/2}(F=5)$  transitions by using a probe beam which was frequency shifted by means of an acousto optical modulator (AOM). In this way the detuning of the trapping laser could be optimized to give the highest atomic density by adjusting the AOM frequency. Depending on the power available for trapping, the detuning was varied between 6 and 15 MHz. The diode laser provided around 30 mW for trapping whereas the Ti:Sapphire gave around 200 mW.

In the small MOT the atoms were cooled by means of five  $\sigma^+$  polarized laser beams coming from the diode laser. Three of these were propagating in a  $120^\circ$  angle relative to each other towards the center of the vacuum chamber. This happened in a plane orthogonal to the axis of the last two trapping beams, which were counterpropagating. In the case where a Ti:Sapphire laser was used for trapping, we used a six beam configuration, where the  $\sigma^+$  beams were pairwise counterpropagating. In both cases all beams were overlapping in the center of our vacuum chamber. In order to provide confinement in addition to

the cooling a quadrupole magnetic field with a gradient of about 10 Gauss/cm around the zero field region had to be applied. This was provided by two coils in anti-Helmholtz configuration. To obtain trapping, the cooling beams had to be aligned so that they crossed in the zero field region. When the laser diode was used for trapping, the beam diameter was around 4 mm and when the Ti:Sapphire was used, the beam diameter was about 25 mm.

The number of trapped atoms in our MOT was inferred by monitoring the absorption of our 917 nm probe. The traces taken as the probe was scanned across resonance are shown in figure 5.3 for the diode laser setup and the Ti:Sapphire laser setup. This reveals several features. First we notice that the intermediate  $6P_{3/2}$  level was AC Stark splitted, and as a result we observed two resonances for every final state. In the limit of large splitting one of these resonances can be considered to arise mainly from the two step process, where the intermediate level is populated by that trapping laser and then probed. The other resonance is of 2 photon nature, where the final level is excited mainly by the two photon absorption[63]. The former resonance is incoherent in nature and will henceforth be denoted the 'incoherent resonance' whereas the latter is coherent and will be called by this name in the following. We were also able to resolve the hyperfine structure of the  $6D_{5/2}$  state, and indicated on the figure are the  $F = 5 \rightarrow F' = 4, 5, 6$  hyperfine transitions. Because of the large AC Stark splitting the 2 step peaks of the  $F' = 4, 5$  transitions merged together with the two photon peaks of the  $F' = 5, 6$  transitions. Finally using the cross section for absorption of light on resonance estimated by  $\sigma = \lambda^2/2\pi$ , where  $\lambda$  is the wavelength of light, together with the size of our trap, which could be measured with our CCD cameras, we could obtain an estimate of the density of atoms in our trap from the optical depths of figure 5.3. This was done using the definition of the optical depth,  $\alpha = \sigma\rho\ell$ , where  $\ell$  is the size of our trap and  $\rho$  is the density of atoms in the  $6P_{3/2}(F = 5)$  state, and the results are shown in the table below

Trapping laser	Diode	Ti:Sapphire
Optical depth	0.05	1.78
Size [mm]	1.5	7
Density [ $\text{cm}^{-3}$ ]	$2 \times 10^8$	$2 \times 10^9$
Number of atoms	$4 \times 10^5$	$4 \times 10^8$

From the table it is clear that we gained tremendously in terms of optical depth by increasing the power of the trapping laser an order of magnitude together with going to the more economical six beam configuration.

No attempts were made to measure the temperature in the MOT, since it was virtually irrelevant to the experiments presented in this thesis. All we required from the MOT was a Doppler free target, and this is certainly fulfilled to a very good extent at typical MOT temperatures.

As a final curiosity to conclude our trap characterization, we discovered that even though our atoms were pumped only with infrared light, the MOT emitted a faint blue light. This was attributed to the small branching ratio ( $\sim 0.1\%$ ) of the decay from the  $6D_{5/2}$  level to the  $7P_{3/2}$  level. The latter could freely decay to the ground state emitting light at 456nm. For a color picture of this feature the reader is referred to figure 7.9 or to the front page of *Optics Express* Vol. 2 No. 3 (1998). This can be found on the WWW at <http://epubs.osa.org/opticsexpress/v2n3cvr.htm>. The picture is in true colors and was taken with 10 minutes exposure of a standard photographic film, while the probe laser was locked on the two photon resonance.

### 5.3 Polarization Squeezing

With the goal of resolving how to achieve sub-shot noise performance of the PI, we now turn towards the contribution  $\delta\theta_{ShN}^2$  in eq. (5.10). In order to reduce this quantity we needed to apply a nonclassical polarization state in our PI. Several proposals on how to produce such a state has been put forward. These include  $\chi^{(3)}$  mixing processes[64][65], but the higher nonlinearity makes the  $\chi^{(2)}$  processes more attractive[66][67]. Having our tunable squeezed light source available, we chose to follow the example of ref. [68], where more control on the parameters, governing the quantum noise reduction, is possible.

In the basis of PBS1 (figure 5.1) we measured the intensity difference between light polarized  $+45^\circ$  and  $-45^\circ$  relative to the horizontal axis of this polarizer. From classical optics we find that this quantity is described by means of the Stokes parameter  $s_1$ [29]. It turns out that a set of Stokes operators analogous to the classical quantities can be defined in terms of the quantum mechanic field operators. Describing the horizontally polarized part of the probe field with the operator  $c_x$  and the vertically polarized part by  $c_y$ , the Stokes operators can now be written as[69]

$$\begin{pmatrix} s_1 \\ s_2 \\ s_3 \end{pmatrix} = \begin{pmatrix} c_x^\dagger c_y + c_y^\dagger c_x \\ -i(c_x^\dagger c_y - c_y^\dagger c_x) \\ c_x^\dagger c_x - c_y^\dagger c_y \end{pmatrix} \quad (5.12)$$

As mentioned above  $s_1$  describes the intensity difference between light polarized  $\pm 45^\circ$  relative to our polarization analyzer.  $s_2$  is describing the intensity difference between  $\sigma^-$  and  $\sigma^+$  polarized light, which is a measure of the ellipticity of the polarization state, and obviously  $s_3$  is the intensity difference between horizontal and vertical linearly polarized light. The operator triplet (5.12) is closely related to the photon spin, and obey the angular momentum algebra

$$\left[ \frac{1}{2}s_j, \frac{1}{2}s_k \right] = \frac{1}{2}i\varepsilon_{jkl}s_l, \quad j, k, l = \{1, 2, 3\} \quad (5.13)$$

where  $\varepsilon_{jkl}$  is the Levi-Civita symbol. For  $c_y$  being a strong coherent state, we ignore the quantum properties of this field and furthermore choose it as our phase reference. In this case the Stokes operators simplify to

$$\begin{pmatrix} s_1 \\ s_2 \\ s_3 \end{pmatrix} = \begin{pmatrix} CX(\phi) \\ CX(\phi - \pi/2) \\ c_x^\dagger c_x - C^2 \end{pmatrix} \quad (5.14)$$

where  $C = \langle c_y \rangle = \langle c_y^\dagger \rangle$  is the coherent amplitude of our probe and  $X(\phi) = ae^{-i\phi} + a^\dagger e^{i\phi}$  is the quadrature phase component horizontally polarized input to PBS1, which is in phase with  $c_y$ . For a vacuum state the phase  $\phi$  is uninteresting, since such a state is symmetric in phase space. If however the field  $a$  is a squeezed state, as we will see, the phase  $\phi$  controls whether our PI is performing better or worse than the standard quantum limit. In our case only the expectation value of  $s_3$  is nonzero, and in terms of our photon flux, we find it to be  $\langle s_3 \rangle = -C^2 = -i_0$  for a vacuum input along the  $x$  axis. Having the commutator (5.13) at hand we can now write up the Heisenberg uncertainty relation for the variances of the Stokes operators  $s_1$  and  $s_2$

$$\langle \delta s_1^2 \rangle \langle \delta s_2^2 \rangle \geq i_0^2 \quad (5.15)$$

Here we note that (5.15) is consistent with the Heisenberg uncertainty relation (2.5) for the quadrature phases  $X(\phi)$  and  $X(\phi - \pi/2)$ , since  $\langle \delta s_1^2 \rangle \langle \delta s_2^2 \rangle = i_0^2 \langle \delta X^2(\phi) \rangle \langle \delta X^2(\phi - \pi/2) \rangle$ . This implies that if the quantum state of our probe is a minimum uncertainty state, the equality sign in (5.15) applies. Equation (5.15) tells us that for a classical state we cannot define the direction of the polarization vector better than the standard quantum limit, which is set to 1 in our case. Since  $s_2$  describes the ellipticity of our polarization, we can draw the same conclusion for this quantity. However if we inject a squeezed state polarized along the  $x$  axis through PBS1, we can, by controlling the phase of this state relative to the phase of the coherent state reduce the quantum fluctuations in the probe polarization angle at the expense of a strongly fluctuating ellipticity of the probe polarization. Fortunately our balanced detection method is insensitive to the ellipticity of the polarization, and we can obtain a performance better than the standard quantum limit in our PI. If a quarter wave retarder was inserted after PBS1, we would become sensitive to the ellipticity of the probe polarization, and consequently the phase,  $\phi$ , of our squeezing would have to be shifted  $\pi/2$  in order to achieve quantum noise reduction.

To summarize, the contribution to our signal noise from the polarization angle jitter is given by

$$4i_0^2 \delta\theta_{ShN}^2 = 4i_0^2 \frac{\langle \delta(c_x + c_x^\dagger)^2 \rangle}{\langle c_y + c_y^\dagger \rangle^2} = \langle \delta s_1^2 \rangle = i_0 \langle \delta X^2(\phi) \rangle = i_0 (1 - S) \quad (5.16)$$

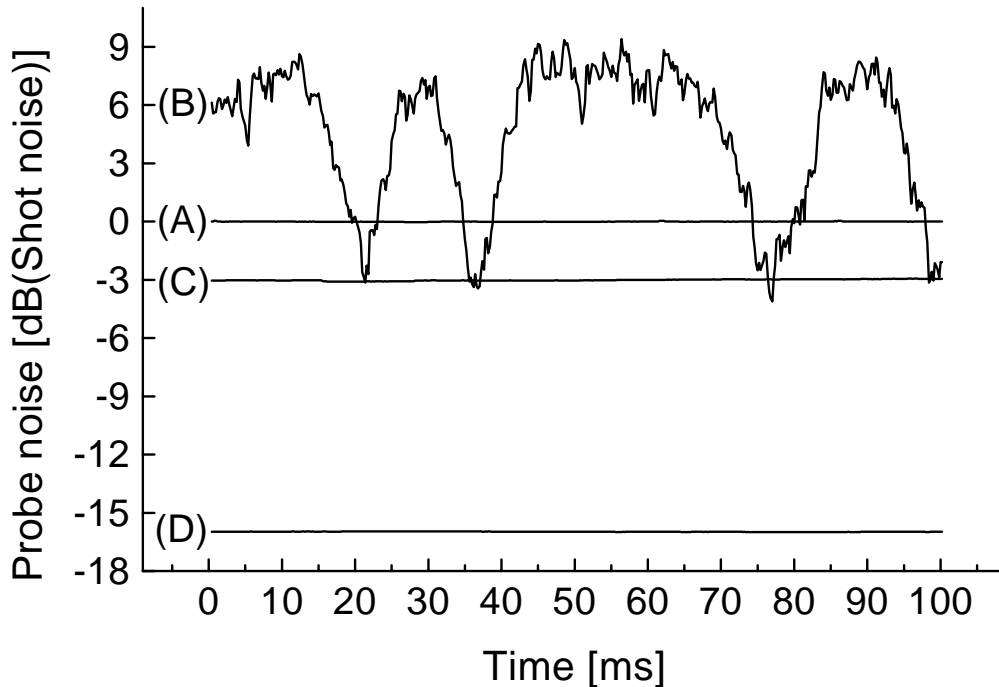


Figure 5.4: The noise of the PI. (A) With blocked OPO. (B) With squeezed input and scanned phase. (C) With squeezed input and locked phase. (D) With blocked probe. The phase was scanned at a 17 Hz rate and the probe contained 1.5 mW of optical power.

where  $S$  is the degree of squeezing left in the probe in front of the detectors.

## 5.4 Sub- Shot noise polarization spectroscopy

With our polarization interferometer ready together with our cold atoms in the MOT, we now combined the two setups with the tunable squeezed light source, described in the previous chapter, with the goal of demonstrating polarization spectroscopy with nonclassical light. The entire experimental setup used for this purpose is shown in figure 5.1. For this experiment we used the diode laser to provide the trapping beams, and consequently the optical depth of the MOT was much less than 1.

As mentioned earlier our atomic signal was enhanced by modulating the intensity of one of the trapping beams and thereby the atomic properties. This complicated the stabilization of the relative phase,  $\phi$ , between the squeezed vacuum and the LO as they were merged together on PBS1. We wanted to lock  $\phi$  to the point where the quantum noise of the probe was minimized, however this required that only this noise was observed, which was not the case when the probe was resonant with the atomic transition. This problem was overcome by monitoring the noise of the photocurrent a few hundred kHz away from the atomic modulation frequency. Since the modulation bandwidth of the atoms was narrow, only probe quantum noise was observed at this frequency, and a voltage proportional to the noise power could be generated. By means of a lock-in amplifier (LIA) and standard dither and lock technique, the phase could now be locked and a polarization squeezed state obtained.

In figure 5.4 the noise characteristics of the polarization interferometer in the absence of atoms is displayed. Trace (A) marks the shot noise level, which was obtained by blocking the squeezed input to PBS1. In (B) the phase  $\phi$  was scanned and we observed the transition from a quantum state with a well defined polarization angle to a state with a well defined ellipticity corresponding to sub- and super shot noise performance respectively. Trace (C) is the probe noise with the phase locked to the minimum, this was 3 dB below the shot noise level, corresponding to 50% quantum noise reduction. Finally trace (D) indicates where the electronic noise level was located. With the 1.5 mW probe power used for these traces, we observed that the shot noise level was 16 dB above the electronic noise, meaning that our measurement was indeed limited by the optical noise of the probe. Unfortunately our squeezing was worse in this experiment than in the experiment described in the last chapter. The reason for this was lack of nonlinearity in the OPO probably due to deterioration of the crystal, which was kept at the high temperature of 130°C over several months. The squeezing balance of this experiment was as follows

Finite frequency of the measurement	0.94
Quantum efficiency of the photodiodes	0.995
Propagation losses from OPO to detectors	0.90
Homodyne efficiency on PBS1	0.98 <sup>2</sup>
OPO escape efficiency	0.88
Finite OPO gain of the OPO	0.80
Finite bandwidth of the phase lock	0.90
<b>TOTAL</b>	<b>0.51</b>

The total noise reduction amounted to 0.51 corresponding to -3.1 dB, which is in good agreement with the observed -3 dB in figure 5.4.

Now the trapping laser was turned on and the MOT formed in the path of our PI. The probe frequency was scanned across the 917 nm atomic resonance in order to observe the polarization noise due to the modulated atoms. According to the theory from the previous sections, our spectrum analyzer signal,  $\Psi$ , around the RF frequency  $\Omega$  would look like

$$\Psi(\Omega) = 2i_0B(1 - S) + 4i_0^2 \left( \xi_1 \frac{\Gamma^2/4}{\delta^2 + \Gamma^2/4} + \xi_2 \frac{\delta\Gamma}{\delta^2 + \Gamma^2/4} \right)^2 \quad (5.17)$$

Here we have assumed that the bandwidth of the atomic modulation is much smaller than the RF bandwidth of the spectrum analyzer,  $B$ , which in turn has been assumed to be much smaller than the bandwidth of squeezing. This means that the latter can be assumed to be constant over the frequency span  $B$ . In figure 5.5 the observed signals are shown (A) with a polarization squeezed probe and (B) with a probe in the coherent state. The noise floor limiting the polarization squeezed trace was 2.3 dB below the shot noise level corresponding to a value of  $S = 0.41$ . This was a bit less squeezing than without the atoms present, but due to the complexity of the experiment it was difficult to keep all the parameters constant over several hours. With the coherent state probe, we found the signal peak to be located 2.3 dB above the shot noise level, this corresponds to a signal to noise ratio of 0.7. By applying our polarization squeezed state in the PI, the probe noise level was reduced and consequently the signal peak was now 3.8 dB above the noise floor and as a result the signal to noise was increased to 1.4, that is, a factor of 2. Ideally the improvement in the signal to noise should be  $(1 - S)^{-1} = 1.7$ , but again due to a fluctuating atomic signal we found an 18% discrepancy.

The resolution bandwidth,  $B$ , of the SA was 100 kHz, and adapting our theory (5.17) to the squeezed trace, we found the values  $i_0\xi_1^2 = (3.8 \pm 1.0)$  kHz and  $i_0\xi_2^2 = (30 \pm 4)$  kHz. Clearly the modulation of the refractive index associated with  $\xi_2$  was transferred more efficient to the probe than the modulation of the absorption, described by  $\xi_1$ . This can be understood by means of a symmetry argument. The modulated trapping beam was almost copropagating with the probe (there was about a 20° angle between them). According to the discussion above, the probe was sensitive to linear dichroism and circular birefringence, but since the trapping beam was  $\sigma^+$  polarized, no preferred transverse direction was available, and the induced transverse linear dichroism due to this beam had to be small. On the other hand the atomic

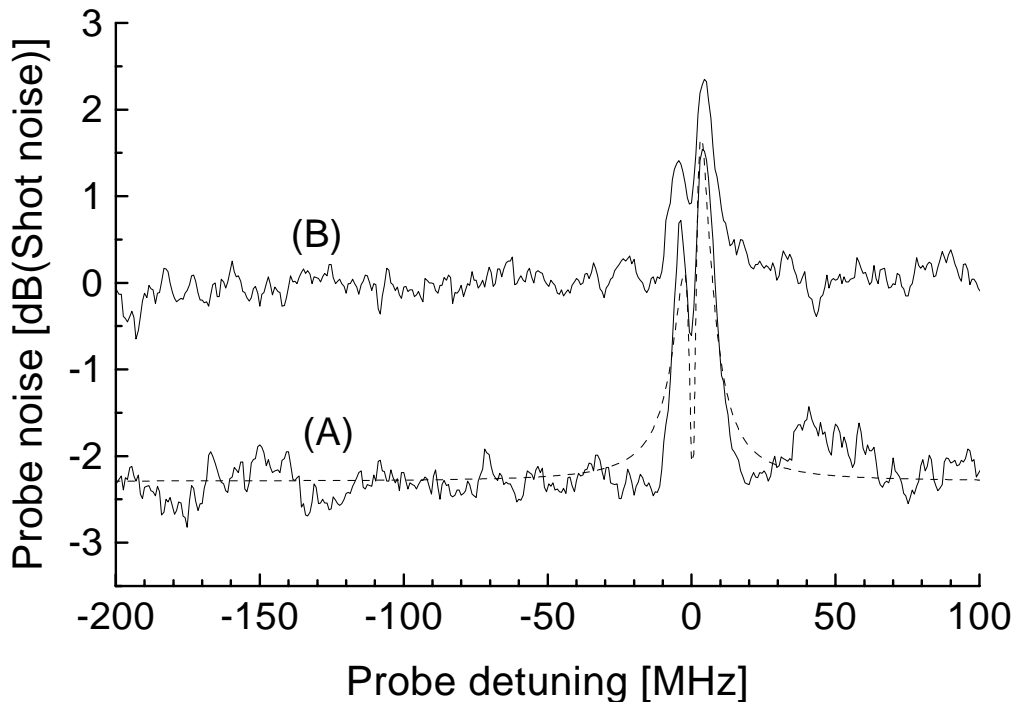


Figure 5.5: The polarization spectroscopy traces. (A) With a 2.3 dB squeezed probe and (B) with a coherent state probe. The best fit to our theory is shown as the dashed line. The improvement in signal to noise due to the reduced quantum noise was found to be a factor of 2.

orientation due to this trapping beam was large, and so was the induced circular birefringence associated with  $\xi_2$ . The tails of the theoretical atomic signal shown as the dashed curve in fig. 5.5 are seen to be too long, which is because our theoretical model is somewhat oversimplified. A more detailed treatment of the modulated two photon transition will be given in the next chapter.

## 5.5 Conclusions

In summary we have characterized our Magneto Optical Trap, and found the optical depth on the probe transition to improve drastically from 0.05 to 1.8 when the stronger Ti:Sapphire laser was used for trapping instead of our diode laser. The density obtained was about  $10^9 \text{ cm}^{-3}$ , which for a cloud of 7 mm diameter corresponded to about  $10^8$  trapped atoms. The strong absorption in the MOT using the Ti:Sapphire laser turned out to become important for a later series of experiments, however when a squeezed probe was applied, a small absorption was desirable in order to preserve the quantum correlations.

In terms of the polarization spectroscopy on our trapped atoms, we saw that the polarization interferometer is sensitive to linear dichroism and circular birefringence. We derived a simple theory describing how to achieve sensitivity beyond the standard quantum limit in the Polarization Interferometer. This required the overlapping of a coherent beam with squeezed vacuum of a polarizing beamsplitter. Choosing an appropriate phase between the two beams, we showed that either the fluctuations in the polarization

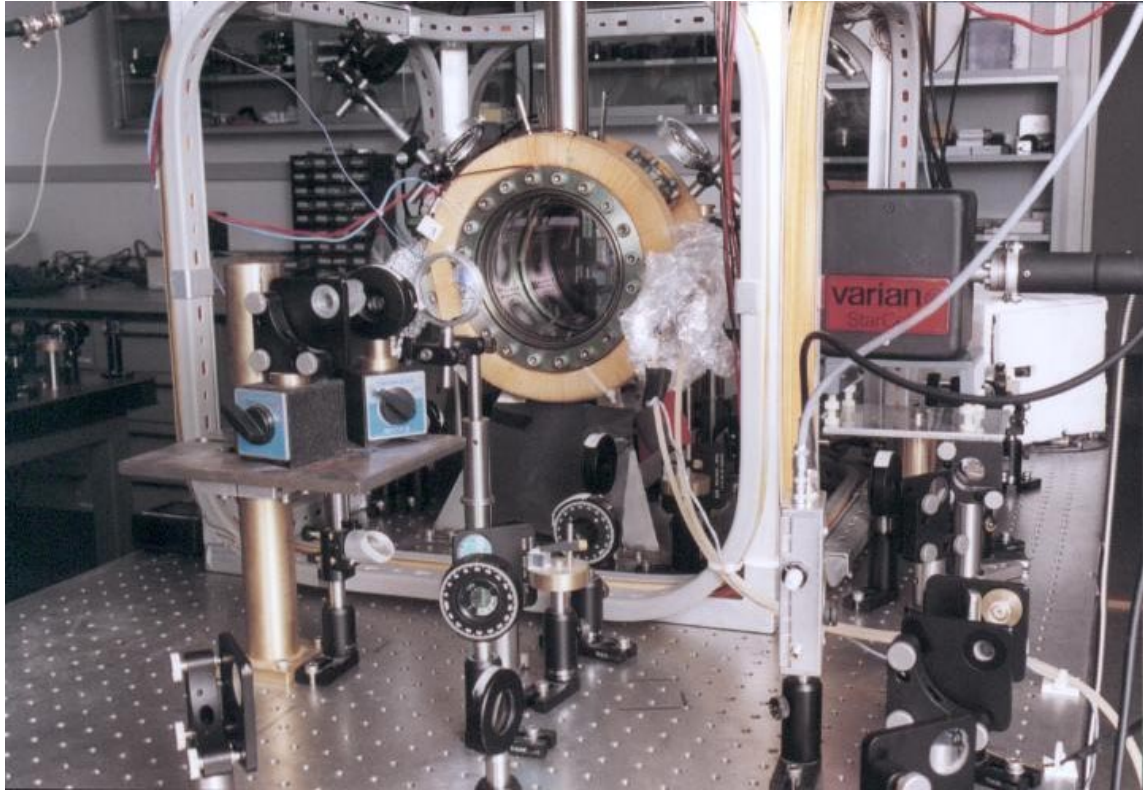


Figure 5.6: The setup used for magneto optical trapping. In the center is the vacuum chamber with the ion pump on the right maintaining a vacuum around  $10^{-8}$  torr. Around the chamber the anti Helmholtz coils can be seen. These are producing a quadrupole magnetic field with a gradient around 10 Gauss/cm in the center. Two trapping beams are entering the chamber perpendicular to the large viewports and the residual four trapping beams are going diagonally through the chamber in the plane orthogonal to the first two beams.

angle or in the ellipticity of the polarization could be reduced. Assuming that our trapped atoms could be described as a simple three level ladder system, we worked out an expression for the shape of the atomic signal, which could be fitted to our traces with a reasonable agreement.

The degree of squeezing achieved in this experiment was not as convincing as in the last chapter. This was mainly due to a worse performance of our OPO as a result of reduced nonlinearity in the nonlinear medium. A quantum noise reduction of -3 dB was achieved in the PI without any atoms present. At the time of the spectroscopy experiment, only -2.3 dB squeezing was left in the probe, however this was sufficient to demonstrate atomic polarization spectroscopy with a nonclassical probe for the first time[11][10]. The signal to noise ratio was increased with a factor of 2 due to the reduced quantum noise of the probe. Finally we found that due to the geometry of the experiment, the modulation of the index of refraction was about 8 times more efficient than the modulation of the extinction coefficient.

This chapter has dealt with the quantum noise associated with the spectroscopy on an optically thin medium. Here we benefitted a lot from squeezing the quantum fluctuations of the probe. In the chapters to follow we will investigate the quantum as well as classical noise associated with the spectroscopy on denser media. In this case intrinsic quantum noise of the atoms becomes important, and hence we will focus our attention on the atomic fluctuations in chapter 7 and ways to reduce this noise will be indicated.

## Chapter 6

# Modulation spectroscopy on a MOT

So far we have considered mainly the noise contribution to our spectroscopic signal coming from quantum noise of our probe. The next two chapters will be devoted to describing experiments, in which the atomic noise contributions to our signals were explored. In this first chapter we will focus on classical atomic noise arising as a result of the interaction of the atoms with miscellaneous external modulation sources. These could for instance be the modulation of the atomic dipole moments due to an amplitude or frequency modulated driving field, or the effect of an oscillating external magnetic field causing modulation of the Larmor precession of the atomic spins. Common for these kinds of modulation is that all atoms in the ensemble experience the same external modulation, that is, the modulation effect is collective and coherent and henceforth we will call the noise from these processes *technical*. This stands in contrast to the *quantum* noise of the atoms, which in general is individual and uncorrelated fluctuations of the relevant atomic parameters. In analogy with the quantum noise of light the quantum noise of atoms can be considered to be the effect of a set of Heisenberg uncertainty relations imposing certain restrictions on the precision with which one can measure two noncommuting atomic observables such as different angular momentum components.

First the motivating issues underlying this experiment will be outlined, then the experimental setup will be presented. Then the results of the absorption spectroscopy of the MOT will be presented together with a comparison to a three level model. This will be followed by the results of the modulated polarization rotation spectroscopy on the MOT, which again will be compared to the three level theory. Finally modulation spectroscopy utilizing the phase noise of a semiconductor laser will be demonstrated and the chapter will be summarized.

### 6.1 Motivation

In order to achieve high sensitivity in atomic spectroscopy it is common to use a modulated probe containing either AM or FM sidebands at some radio frequency  $\Omega$ [41][70]. This technique is useful when the signal to noise ratio is limited by white or broadband noise sources such as the shot noise of light, thermal noise of the detector electronics etc. The contribution of such noise sources to the signal is basically set by the bandwidth of the measurement,  $B$ . The externally applied modulation can have a very narrow bandwidth, meaning that the atomic signal can be compressed into a small frequency window. Since the noise picked up in a measurement is proportional to  $B$ , the signal to noise ratio is easily shown to be proportional to  $i_0 M^2 / 2B$ , where  $i_0$  is the probe photon flux and  $M$  is the modulation index. Taking the photon flux to be  $10^{14} \text{ s}^{-1}$ ,  $M = 0.1$  and  $B = 100 \text{ kHz}$ , we find the signal to noise to be enhanced by  $10^2$  as compared to the DC measurement with the same bandwidth. For the latter the signal to noise will go as  $\sqrt{i_0 / 2B}$ . More important is that the massive  $1/f$  technical noise, which has been ignored so far, will contribute to the DC measurement, whereas it becomes insignificant if

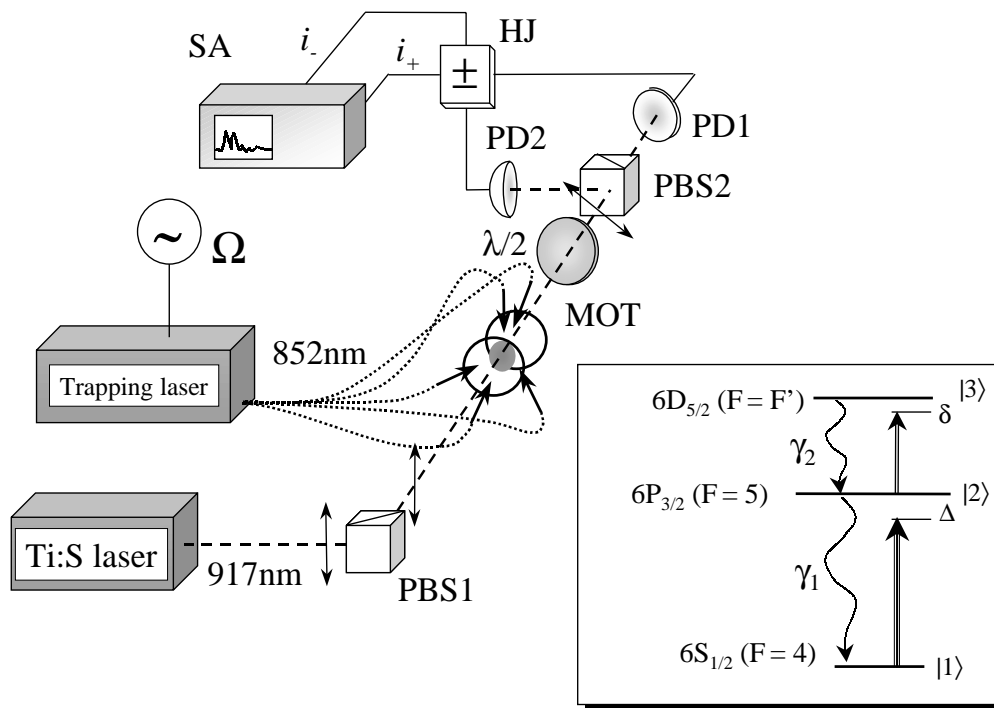


Figure 6.1: The setup used for modulation spectroscopy in a MOT. A diode laser was providing the trapping beams for the MOT and the modulation was produced by modulating the diode laser current. A standard polarization interferometer was used to probe the upper transition and the photocurrents could be either summed or subtracted by a hybrid junction. The noise power of the resulting current at the modulation frequency  $\Omega$  was analyzed in a spectrum analyzer. The polarization interferometer was driven by a Ti:Sapphire laser. The insert shows the three level model used to describe our results.

the frequency  $\Omega$  is chosen sufficiently high. These issues make modulation spectroscopy very attractive whenever weak signals of any kind are to be detected.

In spite of this beauty and simplicity of modulation spectroscopy there are still some pitfalls to avoid when using this technique. In general the modulators needed for such experiments are expensive devices which may reduce the attractiveness of the scheme. Furthermore it is not a trivial task to make for instance an electro optical modulator produce only FM and no AM[71], and if one succeeds thermal drifts of the modulator crystal will probably cause the need for adjustments after a few hours. At best the AM component of the modulation will enter the spectroscopic signal as a broad background making it impossible to reach the shot noise limit and at worst it will obscure the atomic signal itself and cause additional complications when one has to extract the information from this signal. The same effect is also encountered if the probe has to propagate through dispersive elements such as beamsplitters, windows, retarders etc. all of which are common in optical experiments.

In the experiment described below, modulation spectroscopy was performed on the two photon transition  $6S_{1/2}(F=4) \rightarrow 6P_{3/2}(F=5) \rightarrow 6D_{5/2}(F=F')$  in Caesium. The Cs atoms were trapped in a MOT, and in contrast to conventional modulation spectroscopy, as indicated above, the cooling laser resonant with the  $6S_{1/2}(F=4) \rightarrow 6P_{3/2}(F=5)$  transition was modulated instead of the optical probe resonant with the  $6P_{3/2}(F=5) \rightarrow 6D_{5/2}(F=F')$  transition. As a result the atoms themselves were

modulated via the dipole moment induced by the trapping laser, and this modulation was transferred to the probe by means of the atomic third order nonlinearity. Obviously this technique would not suffer from the above mentioned deleterious problems in standard FM spectroscopy, however we had to pay the price of understanding the somewhat more complicated atomic lineshape arising from the indirect way of modulating. This type of spectroscopy lent us excellent insight to the noise properties of our trapping laser and the influence of this laser noise on the atomic quantum noise. This issue will be treated in higher detail in the next chapter.

## 6.2 The setup

The setup used in this experiment resembled the scheme used in the previous chapter quite a lot. The major difference was that no nonclassical light was needed for this experiment and hence the optical part of the setup was somewhat simplified. The MOT was made up by 5 trapping beams of which 2 were counterpropagating and the remaining 3 beams were propagating in a direction  $120^\circ$  relative to each other in the plane orthogonal to the two counterpropagating beams. The trapping beams were provided by an SDL 5401 semiconductor laser stabilized by an external grating and frequency locked to the  $6S_{1/2}(F=4) \rightarrow 6P_{3/2}(F=4,5)$  crossover resonance. The detuning of the trapping laser relative to the transition frequency could be tuned by means of an acousto optic modulator inserted in the path of the light for the frequency lock. As shown in the last chapter the trap parameters in this configuration was a density about  $10^8 \text{ cm}^{-3}$  with a total of about  $10^6$  atoms in the cloud. The modulation yielding the spectroscopic signal was produced by modulating the trapping laser driving current with a  $\Omega/2\pi = 3$  MHz sine wave. In fact the same modulation was used to lock the laser to the Cs transition by means of FM absorption spectroscopy. Like in the last chapter the trapped atoms were probed with a polarization interferometer made up by two Glan Thompson prism polarizers (PBS1/2) and a half wave retarder ( $\lambda/2$ ). The probe beam was produced by a single frequency Ti:Sapphire laser (Microlase MBR-110), which could be scanned up to 1 GHz around 917nm at a 3 Hz repetition rate. The two photocurrents coming from the pin silicon photodiodes (PD1/2) could be either added or subtracted in a hybrid junction (HJ) and the resulting RF current was fed into a spectrum analyzer (SA) where the noise power at  $\Omega$  was monitored. In the case of subtraction of the photocurrents the balancing of the detectors was typically better than 30 dB. The probe intensity was around  $10 \text{ mW cm}^{-2}$  and with the corresponding power the probe was shot noise limited at frequencies higher than 2.5 MHz. Depending on whether the sum ( $i_+$ ) or the difference ( $i_-$ ) of the photocurrents was monitored we gained information about different properties of the ensemble of trapped atoms. The sum,  $i_+$ , simply gave us information about the absorption of the 917 nm probe whereas latter described the deviation from a spherical state of the collective atomic angular momentum according to the discussion in section 5.1.2. The setup is shown in figure 6.1. Two types of modulation experiments were performed. In the first kind the modulation was applied externally to the diode laser drive current and in the second kind the intrinsic phase noise of the diode laser was used directly to modulate the atoms.

## 6.3 Modulated absorption

### 6.3.1 Experiment

When modulating the driving current of a diode laser operating in a stable mode well above threshold, the main impact is a resulting modulation of the laser frequency rather than the amplitude[72]. However the laser amplitude is also modulated at bit. In our case the strength of the FM was measured by sending the laser output through a scanning cavity and measuring the size of the 3 MHz sidebands relative to the carrier. This ratio was found to be 15%, which can be converted into the phase modulation index,  $M$ , by inverting the Bessel function  $J_1(M)$ [73], to give  $M = 0.31$  rad. The corresponding frequency modulation index is 0.15 MHz. The AM of the laser output was measured to be smaller than 5%, but this was of

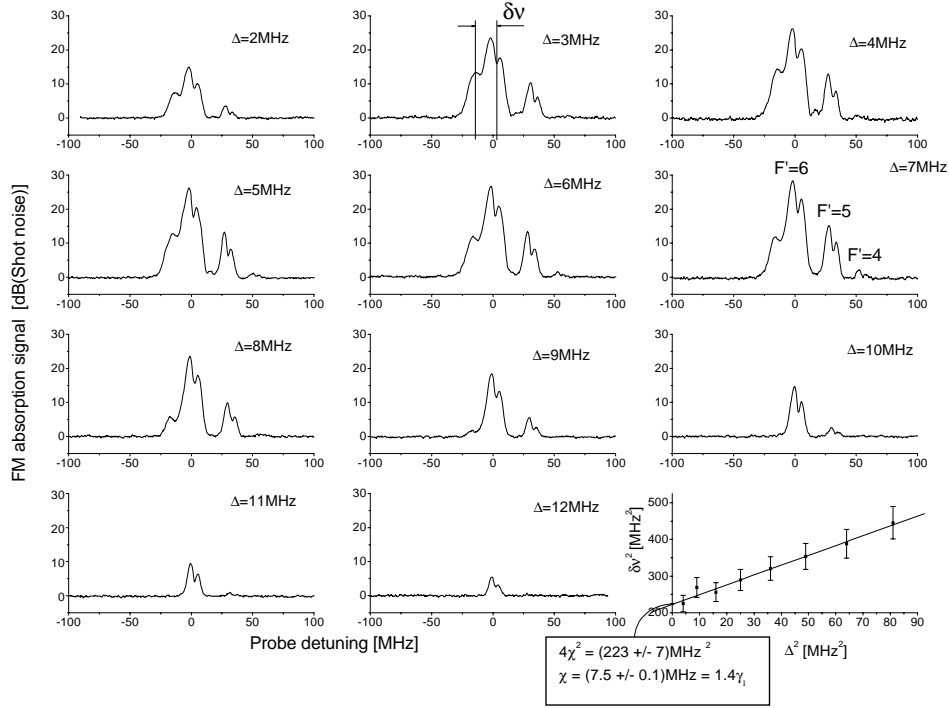


Figure 6.2: The MOT absorption signal for various trapping laser detunings,  $\Delta$ . The AC Stark splitting  $\delta\nu$  is measured for each detuning and the crossing of the straight line of  $\delta\nu^2$  vs.  $\Delta^2$  with the vertical axis yields  $4\chi^2$ , where  $\chi$  is the Rabi frequency. The traces were taken with Resolution BW of 100 kHz and Video BW of 100 Hz.

less importance since the trapping transition was heavily saturated, meaning that small changes in the trapping laser power would mean very little to the atomic dynamics.

Let us first focus on the absorption signal obtained by recording  $i_+$ . Typical traces for various values of the trapping laser detuning,  $\Delta$ , are shown in figure 6.2. Looking first at the  $\Delta = 7$  MHz trace, we clearly see the hyperfine splitting of the  $6D_{5/2}$  state. The transition to the  $F'' = 6$  state is seen to be the strongest in agreement with standard theory[74]. This tells us that the ratio of the transition probabilities for exciting from  $6P_{3/2}(F = 5)$  to  $6D_{5/2}(F')$  and  $6D_{5/2}(F'')$  is given by

$$\frac{W(F \rightarrow F')}{W(F \rightarrow F'')} = \frac{(2F' + 1) \begin{Bmatrix} F' & 1 & F \\ 3/2 & 7/2 & 5/2 \end{Bmatrix}^2}{(2F'' + 1) \begin{Bmatrix} F'' & 1 & F \\ 3/2 & 7/2 & 5/2 \end{Bmatrix}^2} \quad (6.1)$$

where we have used that  $^{133}\text{Cs}$  has nuclear spin  $7/2$  and we have neglected the relatively small energy splitting between the hyperfine levels in the final state. For  $F' = 5$  and  $F'' = 6$ , this ratio is  $77/325$ , which must be squared since we record the noise *power*. Finally we end up finding that the  $F' = 5$  peak must be 12.5 dB lower than the  $F'' = 6$  peak in good agreement with fig. 6.2. Similarly we find the  $F' = 4$  peak to be located 29.8 dB below the  $F'' = 6$  peak. In order to check this ratio a better signal to noise ratio than provided by fig. 6.2 is needed.

Because of the strong pumping field coming from the trapping laser, the intermediate  $6P_{3/2}$  state displayed Autler Townes splitting. In this case we could consider the total transition from the  $6S_{1/2}(F = 4)$  ground state to the  $6D_{5/2}$  final state to have two contributions, one coming mainly from the coherent two photon excitation and another coming from the incoherent two step excitation[63]. This distinction between coherent and incoherent excitation can only be made unambiguously in the limit of large trapping laser detuning. The two processes corresponds to different resonance frequencies of the probe, and hence we see the incoherent peak at negative probe detunings and the coherent double peak can be seen close to zero probe detuning. It should be mentioned here that the absolute probe detuning has been chosen to be zero at the  $F'' = 6$  coherent peak in all the traces. Intuitively we expect the coherent peaks to be centered around zero two photon detuning,  $\Delta + \delta = 0$ , whereas the incoherent peaks are expected to be found at zero probe detuning,  $\delta = 0$ . Because the role of the FM of the trapping laser is mainly to modulate the detuning on the lower transition, the coherent peak splits into two peaks analogous to standard FM absorption spectroscopy. However the incoherent peak is shifted much less from its unperturbed position due to the detuning and hence the splitting of this peak is less pronounced.

By measuring the Autler Townes splitting,  $\delta\nu$ , as indicated on the  $\Delta = 3$  MHz trace, and doing this as function of the trapping laser detuning, we were able to infer the Rabi frequency,  $\chi$ . Again standard theory[63] tells us that plotting  $\delta\nu^2$  vs.  $\Delta^2$  should give us a straight line with a crossing of the vertical axis at  $4\chi^2$ . This is shown in the last plot of fig. 6.2. From this we find the Rabi frequency to be  $\chi = (7.5 \pm 0.1)$  MHz corresponding to 1.4 linewidths ( $\gamma_1 = 5.3$  MHz) of the  $6S_{1/2} \rightarrow 6P_{3/2}$  transition. The variation of the size of the absorption signals as the detuning was increased was simply due to the change in the cooling force confining the atoms in the MOT. Given the intensity of the trapping beams there exist a detuning which optimizes the number of trapped atoms, and in this particular trap configuration the best detuning was around 7 MHz.

### 6.3.2 Modelling

In order to simplify the description of our physical system, we neglect the Zeeman degeneracy and consider it to be a three level ladder configuration. Labeling the ground state  $|1\rangle$ , the intermediate state  $|2\rangle$  and the final state  $|3\rangle$ , we seek to find the density matrix element  $\rho_{32}$  governing the absorption of the probe. Following ref. [63] we find first  $\rho_{21}$  and  $\rho_{22}$  to first order in the Rabi frequency of the lower transition,  $\chi_1$ , and then we use these to obtain  $\rho_{32}$  to second order in  $\chi$  and first order in the upper transition Rabi frequency. With  $\rho_{32}$  at hand we easily find the complex linear susceptibility,  $X$ , around the probe frequency to be

$$X = X_r + iX_i = C\chi_1^2 \frac{\frac{i}{2}(\gamma_1 + \gamma_2) - \delta}{[\Delta^2 + \frac{1}{4}\gamma_1^2 + 2\chi^2] \left[ \left( \frac{i}{2}\gamma_2 - \Delta - \delta \right) \left( \delta - \frac{i}{2}(\gamma_1 + \gamma_2) \right) + \chi^2 \right]} \quad (6.2)$$

Here we have assumed collisional decay to be negligible as compared to the spontaneous decay rate.  $\gamma_1$  is the decay rate of level 2 and  $\gamma_2$  is the decay rate of level 3 to level 2 as illustrated in the insert of fig. 6.1. The decay from level 3 to level 1 has been assumed to be forbidden. Finally we have defined  $\delta$  as the probe detuning and  $C$  as a scaling factor depending on the detection system. The absorption is described by the imaginary part of  $X$  whereas the dispersion is described by the real part. As we shall see in the next section,  $X_r$  will dominate the lineshape of the polarization rotation traces. Equation (6.2) applies only to the DC absorption, however in the limit of a low modulation frequency the atoms will follow the modulation adiabatically and we can readily find the lineshape from (6.2) in this limit. In our situation the modulation frequency of  $\Omega/2\pi = 3$  MHz was indeed comparable to the atomic decay rate of 5.3 MHz, but the full density matrix calculation including all 33 levels involved in the transition[75] has shown that the main effect of the breakdown of the adiabaticity is to broaden the line. For a weak modulation the optical power transmitted through the MOT,  $i_t$ , is given by

$$i_t = i_0 (1 - AX_i) \simeq i_0 \left( 1 - A \left[ X_i + \frac{\partial X_i}{\partial \Delta} M \Omega \cos \Omega t \right] \right) \quad (6.3)$$

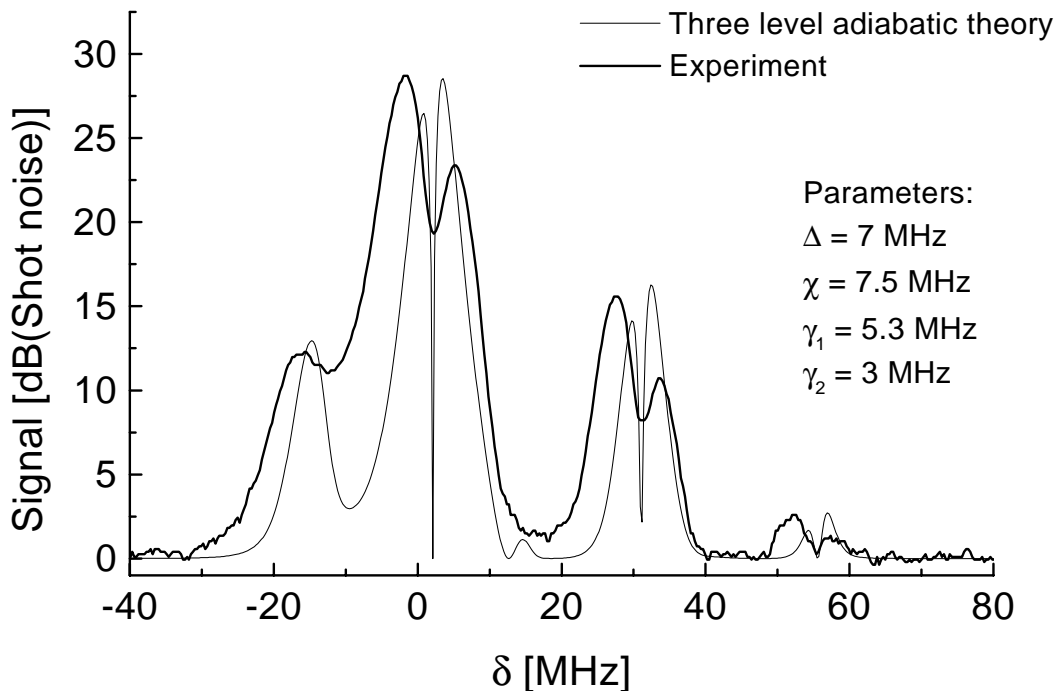


Figure 6.3: Comparison of our three level theory with the experimental trace for  $\Delta = 7$  MHz. The main difference is found in the linewidths. The (thin) theoretical line is about 2.5 times more narrow than the (thick) experimental line.

where  $i_0$  is the initial power,  $A$  is a constant,  $M$  is the phase modulation index and  $\Omega$  is the modulation frequency. The signal,  $\Psi$ , recorded by the spectrum analyzer is the square of the component of (6.3) oscillating at the frequency  $\Omega$ , that is

$$\Psi(\Omega) = \delta i_t^2 |_{\Omega} = \frac{1}{2} \left( A \frac{\partial X_i}{\partial \Delta} M \Omega \right)^2 \quad (6.4)$$

Taking the imaginary part of (6.2), differentiating it with respect to  $\Delta$  and squaring we obtain the thin curve in figure 6.3. The analytical form of the curve is rather lengthy and will not be given here. In fig. 6.3 we have used equation (6.1) together with the hyperfine splitting measured in ref. [56] to include the  $F = 4, 5, 6$  hyperfine levels in the  $6D_{5/2}$  state. We find a good qualitative agreement between the theory and the experiment, the relative size of the hyperfine resonances is obviously well described by (6.1). We find however serious discrepancies in the linewidths of the two traces. The experimental trace is about 2.5 times broader than our theory. According to the more elaborate calculations presented in ref. [75], the breakdown of our adiabaticity assumption results in a linebroadening of a factor 1.8. The physical reason for this is simply that the atomic dynamics cannot follow the fast fluctuating laser frequency. As a result the linewidth of the two photon excitation will acquire a contribution from the trapping laser frequency fluctuations and hence broadening occurs. In general linebroadening is often encountered in MOT spectroscopy. This includes DC absorption spectroscopy[76] as well as modulation spectroscopy[54]. There could be various reasons for this, such as Zeeman broadening due to the finite size of the trap, inhomogeneous strength of the trapping laser field across the trap etc. To reach the

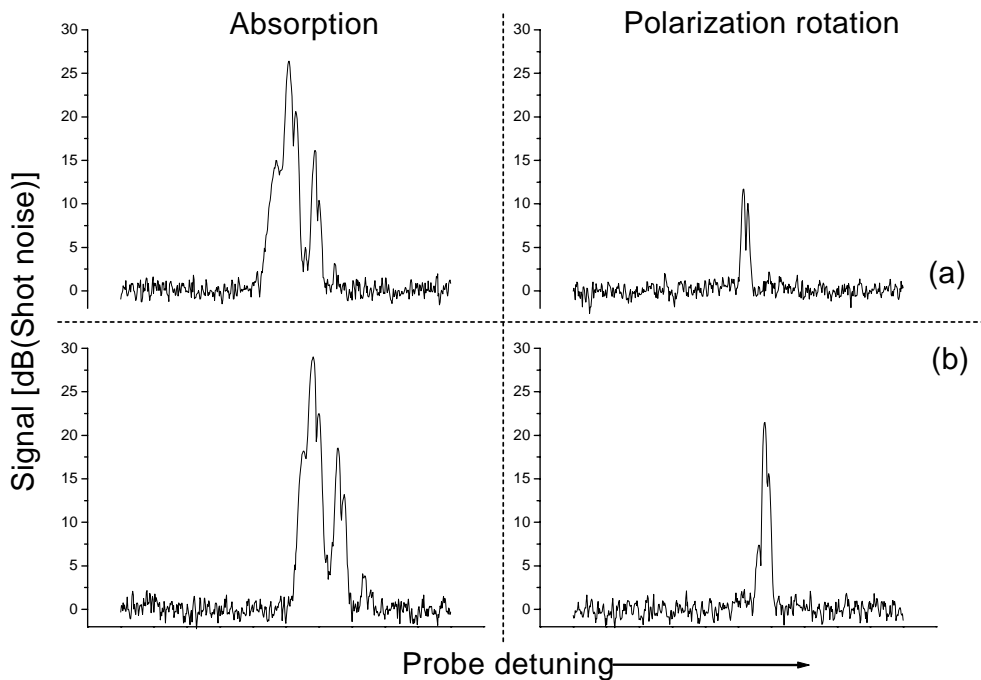


Figure 6.4: (a) The polarization rotation signal for a well balanced MOT and (b) for the unbalanced MOT. The modulated absorption signals shows that the number of trapped atoms in the two cases are approximately the same. The polarization rotation signal is found to be 10 dB larger for the poorly balanced trap than for the 'good' trap.

natural atomic linewidth in MOT spectroscopy it is necessary to turn off the trapping lasers as well as the magnetic field while probing the atoms.

Another discrepancy between the experiment and theory is found in the relative size of the two peaks making up the coherent resonance. Again this is attributed to the limitations of our simple model, which does not include the rapid modulation and the Zeeman degeneracy.

To summarize, we have been able to perform probe shot noise limited modulation absorption spectroscopy on a MOT, but have paid a price in terms of complicated lineshapes and significant linebroadening. No effects of additional background noise as a result of the modulation were found. This could easily be checked by comparing the probe noise with the trap present to the noise when the trapping laser was blocked. The signal to noise of our spectroscopy was about 500 and could be improved by increasing the probe power and/or the modulation index of the trapping laser. This ratio should be compared to the DC absorption, which for this particular trap configuration was about 3% with a signal to noise ratio close to 1. Using our estimate of  $10^6$  atoms in the trap, we can infer that we were sensitive to about  $10^4$  atoms, since this number would give us a signal to noise ratio around 1. Our frequency resolution in this experiment was about 0.5 MHz, however this could easily be improved to a few kHz by locking the probing laser to the two photon transition and scanning its frequency by means of an acousto optical modulator. Because of the relatively broad resonances encountered in this experiment probe laser stabilization was not relevant here, but in the experiment described in the next chapter stabilization of the probe frequency as well as its amplitude was crucial.

## 6.4 Modulated polarization rotation

We will now turn to look at the modulated polarization rotation signal obtained when analyzing the differential photocurrent  $i_-$ . In general this signal was found to contain much more structure than the absorption signals and this complicated the interpretation somewhat. Further complication was added because the signal depended on the deviation from an isotropic distribution of atomic spins and hence the lineshape turned out to be very sensitive to magnetic field gradients, trapping light polarizations and the relative intensities of the different trapping beams.

In order to have the MOT working, the trapping laser beams necessarily had to be balanced carefully in intensity and polarizations. As a result the collective state of the trapped atoms was rather close to being spherical and hence the polarization rotation signals of a well aligned trap were orders of magnitude smaller than the modulated absorption signals. The rapid varying polarization of the trapping beams across the trap size made a transverse aligned atomic ensemble unlikely, and henceforth we will assume the polarization rotation signals to be caused by the longitudinal orientation. As it was shown in section 5.1.2 only these two effects can give contributions to the polarization rotation to the lowest order in the anisotropy.

Figure 6.4 shows the modulated polarization rotation signal with a well aligned and well balanced trap (a) and the corresponding signal with a trap where the trapping beams (almost) copropagating with the probe were given different optical powers (b). On the left we find the modulated absorption signals, which are used as a measure of the number of trapped atoms. These two signals differ in size only by 2 dB indicating that the number of atoms for the two trap configurations is the same within 25%. However the polarization rotation signal for the unbalanced trap was found to be 10 dB larger than for the balanced trap. The reason for this drastic change is the following. If the atoms are trapped they must scatter an equal amount of the  $\sigma^+$  and  $\sigma^-$  polarized photons from the two trapping beams of interest. If these have different intensities the trap necessarily has to move a bit away from the region with zero magnetic field in such a way that the Zeeman splitting cancels the intensity imbalance and the atoms again scatter the same amount of photons from the two beams. When the Zeeman splitted upper state of the trapping transition is probed, the detuning and hence the index of refraction seen by the  $\sigma^+$  and  $\sigma^-$  polarized components of the linearly polarized probe will be different. According to the discussion in section 5.1 this will cause a net rotation of the probe polarization. In terms of the modulated polarization rotation, the Zeeman splitting would result in a different modulation strength of the  $\sigma^+$  and  $\sigma^-$  polarized components which caused a modulated polarization angle of the probe. This situation closely resembles the Faraday effect in atoms, where an external magnetic field induces optical activity in the atomic medium. Although this effect has been thoroughly investigated over the years [77][78][79][80] our situation is somewhat complicated by the strong trapping beams with a polarization which is not very well defined.

Since our signal is given by the modulated difference between two indices of refraction, we again turn to the three level result (6.2), where we now focus on the real part of the susceptibility,  $X_r$ , which is responsible for the probe phaseshift. Following the same procedure as for the modulated absorption signal, we take the derivative of  $X_r$  with respect to the trapping laser detuning,  $\Delta$ , to get the modulated signal and square this to obtain the noise power at the modulation frequency. The comparison of our result with the experimental trace is shown in figure 6.5. Like with the absorption signals we find a good qualitative agreement between theory and experiment, but again the experimental line is broadened with approximately a factor of 2 relative to the natural linewidth. Best agreement between theory and experiment is found around  $\chi = 5.3$  MHz and  $\Delta = 9.5$  MHz. Qualitatively the lineshape can be understood in the following way. The DC coherent resonance has the shape of the derivative of a Lorentzian, when we take the derivative of this curve to model the FM of the trapping laser, we obtain a 'M' shaped resonance. The incoherent resonance is found from the theory to be single peaked, and hence the derivative is dispersive like shaped. The 'M' and the dispersive shaped signals can interfere in various ways depending on the Autler Townes splitting before the total signal is squared by the spectrum analyzer. This results in a variety of complicated signal shapes, which depend critically on

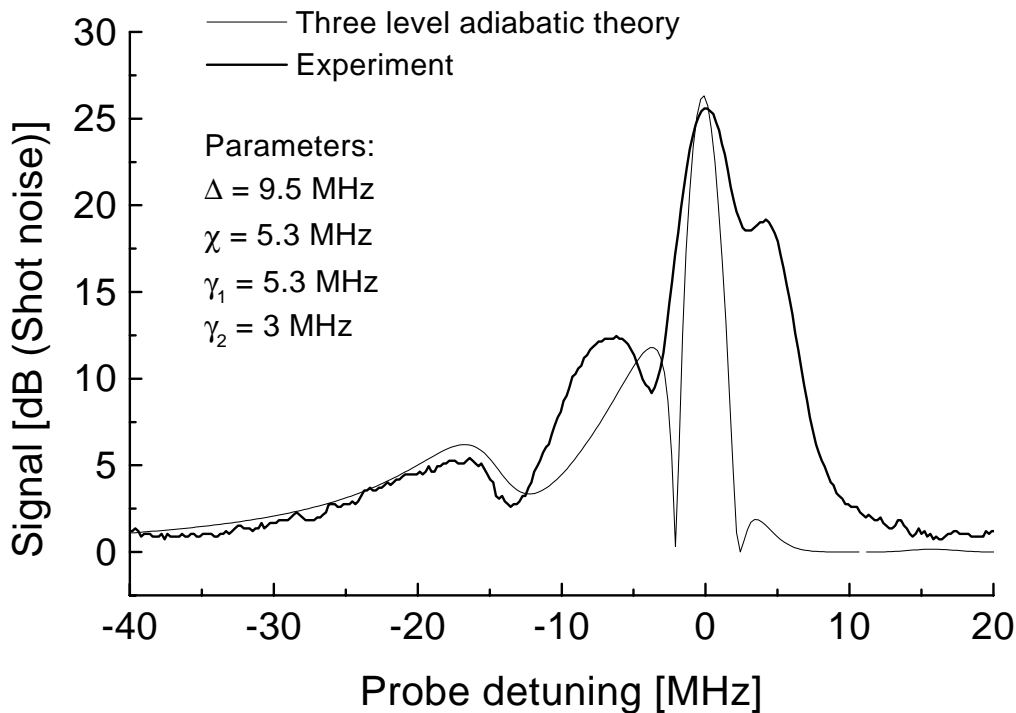


Figure 6.5: The modulated polarization rotation signal. The experimental trace is plotted with the thick line and the three level theory is displayed with a thin line. The spectrum analyzer settings were: Res. BW 100 kHz, Video BW 300 Hz.

the trap parameters. If we take into account the complexity added by the Zeeman degeneracy of the energy levels involved in the two photon transition and the high modulation frequency, we cannot justify to use our simple theory for anything but a qualitative comparison. However the similarity of the two lineshapes in fig. 6.5 confirms our initial assumption that the linear dichroism is indeed a smaller effect in atoms trapped in a MOT.

The highly sensitive polarization rotation signals may prove useful in future studies of trap dynamics. For instance one could imagine a tightly focused probe, which could be used to analyze the orientation of the atoms in different regions of the trap.

## 6.5 Diode laser phase noise spectroscopy

The compactness and simplicity of semiconductor lasers make them attractive for many applications. Hence the growth and purification of these devices is a well developed field and consequently it is today possible to commercially purchase diode lasers covering virtually the whole spectrum from far infrared to visible light. The output of diode lasers in general possess a very stable amplitude and it has turned out that it is relatively easy to reduce the fluctuations of this amplitude below the shot noise limit[81]. The applicability of the diode lasers is however limited by the massive amount of noise present in the phase of the laser output[82][83], which requires rather extensive stabilization systems to reduce[84]. It has however turned out that this phase noise can be utilized for FM spectroscopy on cavities and atomic

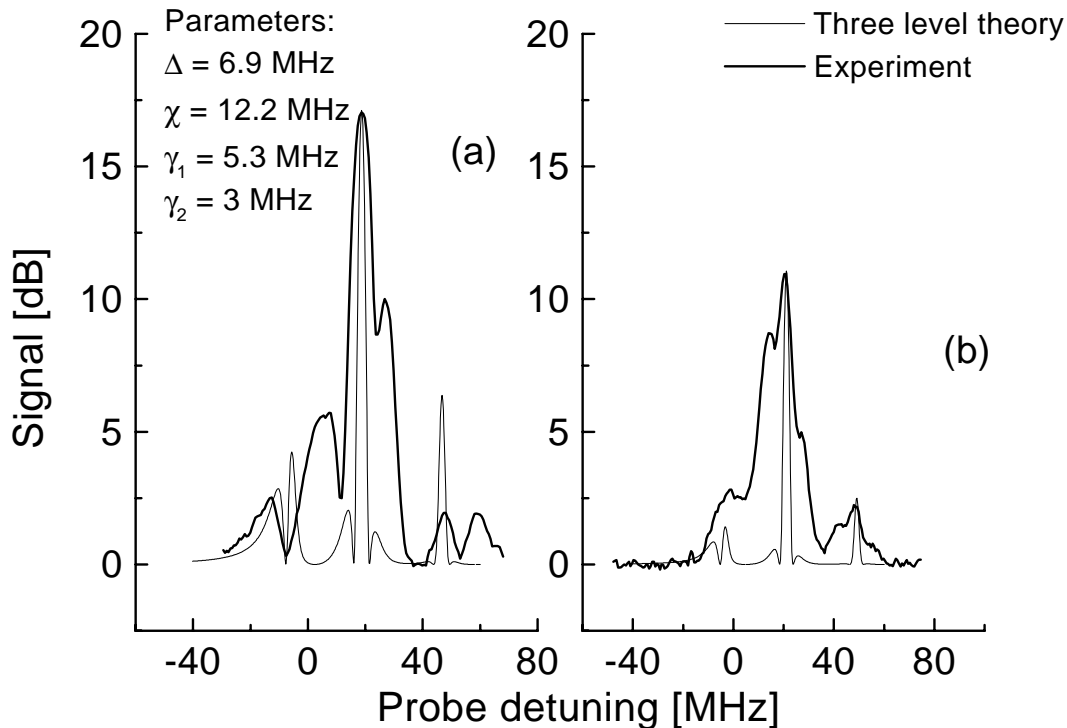


Figure 6.6: (a) Modulated polarization rotation trace. (b) Polarization rotation with modulation from the trapping laser phase noise. The thin lines are the results of the three level theory. The traces were taken with spectrum analyzer settings: Res. BW 100 kHz and Video BW 300 Hz.

systems[85][86][87], so it seemed natural for us to utilize the phase noise of our trapping laser to generate the modulation for our polarization interferometer.

The phase noise of a diode laser similar to our trapping laser has been characterized in ref. [83], and here it was found to extend way above 40 MHz (this was the limit of the detector) and probably into the GHz region. For optical powers of tens of mW the phase noise was typically 60-80 dB above the shot noise limit in the MHz region, this was certainly comparable to the power of the externally applied modulation.

The experiment was performed like the above described modulated polarization spectroscopy except now the external modulation was tuned away from the detection frequency of 3 MHz. A trace recorded with the diode laser phase noise is shown in figure 6.6 (b) and in (a) is shown a trace taken with external modulation for comparison. Looking at the two traces we immediately see that they have the same shape, meaning that our diode laser phase noise indeed has the same effect on our signal as the externally applied FM. The phase noise was however not as strong as the external modulation, and hence the phase noise signal is seen to be 6 dB smaller than trace (a). In order to identify the peaks, the three level theoretical trace has been added to both plots and we find a reasonable qualitative agreement. As usual the MOT signals are about a factor of 2 broader than the natural linewidth, but it is still possible to compare the theory to the experiment. Both theoretical traces have been generated using the parameters  $\Delta = 6.9$  MHz,  $\chi = 12.2$  MHz,  $\gamma_1 = 5.3$  MHz and  $\gamma_2 = 3$  MHz, but the overall amplitude of trace (a) is 4 times larger than for trace (b). In both traces we easily recognize the triplet from the coherent excitation to the  $6D_{5/2}(F = 6)$  state around 20 MHz and at -5 MHz we find the incoherent doublet associated with

the same transition. At 50 MHz probe detuning we find the coherent resonance from the excitation to the  $6D_{5/2}(F = 5)$  level, however the size of this is too small to allow us to resolve its structure. A general problem encountered when applying the three level theory to the polarization rotation case was that the smaller hyperfine resonances differed substantially in size from the ones experimentally observed. The reason for this could be that the difference in the modulation of the refractive indices for  $\sigma^+$  and  $\sigma^-$  polarized light depends on the hyperfine level of interest. In our three level theory we have assumed that response of the different hyperfine transitions to the modulation is simply proportional the transition probability as described by (6.1).

## 6.6 Summary

In this chapter we have shown how to perform highly sensitive modulation spectroscopy on a MOT by modulating the trapping laser sustaining the MOT instead of the probe. This had the advantage over modulating the probe that we easily became probe shot noise limited without the complication of eliminating background noise due to dispersion in optics and AM components in the modulation. However we had to pay the price of understanding the more complicated spectroscopic signals arising from a modulated two photon transition with one strong and another weaker field. Towards this end our oversimplified three level theory was successful on a qualitative level, but it failed to describe the excessive linewidth observed in the experiment. By comparing to the more elaborate theory including the Zeeman sublevels we found the increased linewidth to partly due to the high modulation frequency, which was comparable to the natural atomic linewidth. As a result the atomic dipole moment was unable to follow the frequency modulation adiabatically as it was assumed in our theory and hence the line was broadened relative to the natural linewidth.

Our setup with a polarization interferometer around the MOT gave us the possibility of measuring both the modulated absorption and the polarization rotation due to the trapped atoms. Both signals were limited by the quantum noise of the probe together with the electronic noise of the detectors.

The absorption signals were typically 25-35 dB above the noise floor whereas the polarization rotation signal never became larger than 20 dB above the background. This was found to be due to the symmetry of the MOT which ideally did not allow for deviations of the collective atomic state from a spherical state. Hence if highly sensitive spectroscopy should be performed on a MOT, the modulated absorption must be preferred over the polarization spectroscopy. In our setup we were sensitive to the absorption coming from roughly  $10^4$  trapped atoms. The polarization spectroscopy may however prove useful in other areas of laser cooling and trapping. The signal size and shape of the latter was found to be highly sensitive to the alignment and intensity balance of the trapping beams and hence it could be used in studies of trap dynamics.

Finally we demonstrated how the intrinsic phase noise of the semiconductor trapping laser could be used to generate the same kind of modulated polarization rotation signal as the externally frequency modulated laser. Although this phase noise was observed to be very strong it did not produce the same signal size as when an externally modulated trapping laser was used.

The trapping laser noise turned out to become very important for the outcome of the experiment described in the following chapter. Here the quantum noise of the atomic spin in the intermediate  $6P_{3/2}(F = 5)$  state was investigated and found to be very sensitive to the stability of the trapping laser.

## Chapter 7

# Quantum noise of the Atomic Spin

In the previous chapter the behavior of the technical atomic spin noise was investigated through the modulated polarization rotation spectroscopy in an optically thin medium of trapped atoms. In this chapter we will take this investigation one step further. Whereas the spin noise was used before in spectroscopy to infer intrinsic properties of the trapped atoms, we will in this chapter address the properties of the spin noise itself. Our investigation will include the more fundamental quantum spin noise as well as the technical spin noise. As we shall, see the atomic spin noise can become an important limiting factor to the sensitivity when one is probing optically thick media where the noise power can become comparable to the probe shot noise.

In an optical probe experiment the atomic spin noise can be considered to have two contributions, one coming from the fluctuating number of atoms inside the probe volume and another coming from the decay of the spin. Obviously the first contribution depends on the atomic mean velocity and hence it is temperature dependent. Therefore these fluctuations are usually called thermal but they are indeed fluctuations of the probed atomic spin and they display the same signatures as the second contribution which will be described in more detail below. The thermal fluctuations have been examined experimentally in ref. [88] as well as theoretically in refs. [89],[90]. Typically the frequency of the thermal fluctuations is in the kHz regime for a vapor at room temperature and for an ensemble of cold trapped atoms these fluctuations were unimportant at the frequency where we were observing.

In the following we will focus on the second contribution arising from the decay of atoms present in the probe volume. The spectrum of this kind of spin noise depends on the lifetime of the spin state being probed. If the spin of the ground state or a metastable state is probed, the spectrum of spin fluctuations will typically be set by the rate of spin flipping collisions or inelastic collisions respectively. In a hot vapor or an atomic beam, these fluctuations give rise to a spectrum falling off in the kHz region, whereas in a MOT the spectrum can become very narrow due to the low collision rate. The spin noise considered in this work is the noise of the  $6P_{3/2}(F = 5)$  excited state in Cs. This state can decay directly to the ground state and has a width of 5.3 MHz hence we expect the spin of the state to have a spectrum with a width of the same order of magnitude. A several MHz broad spectrum of spin fluctuations was important in our particular setup because we relied on the fact that the technical noise of our lasers was small at the frequency of the measurement. Throughout the experiment this frequency was 3 MHz.

So far the spin noise of the ground state has been observed in ref. [91], whereas the excited state spin noise has been treated theoretically in ref. [92] and examined experimentally in a supersonic atomic beam[93][94] and in an ion trap[95]. Our experiment with trapped neutral atoms had the advantage over the atomic beam experiment that we only probed the spin fluctuations due to decay, whereas the beam experiment was sensitive to fluctuations due to the decay as well as the finite transit time of the atoms through the interaction region. As it will be shown in the next section the quantum spin noise differ from the technical spin noise in the dependence on the number of probed spins,  $N$ . The quantum spin noise grows like  $N$  in contrast to the technical noise which grows like  $N^2$ . The  $N$  dependence was

shown in the ion trap experiment but with rather poor statistics. A MOT is capable of confining much more atoms than an ion trap, and hence our experiment held the potential of producing data with better statistics than the ion trap experiment.

In this chapter we will first outline a simplified model describing the spin noise in a three level V system. This will serve as to illuminate the most important physics underlying the experiment and furthermore clarify exactly what spin we were probing in our experiment. Then the experimental procedure will be explained and the results presented and interpreted. Finally we will demonstrate an experimental situation in which the achieved signal to noise ratio was limited by the atomic quantum spin noise and the chapter will be concluded by a summary.

## 7.1 The physics of the Spin Noise

As in the previous chapters the atomic system under consideration here is the  $6S_{1/2}(F=4) \rightarrow 6P_{3/2}(F=5) \rightarrow 6D_{5/2}(F=6)$  transition coupled by a strong field on the lower transition and a weaker field on the upper transition. As we saw in section 5.1.2 the polarization rotation of the probe around the resonance frequency of the upper transition had two contributions. One coming from circular birefringence in the trapped atoms and another from linear dichroism. In the experiment described below, the probe laser was locked to the incoherent resonance of the two photon transition and hence we expected only the linear dichroism contributed significantly to the polarization rotation. Keeping in mind our detection scheme where the difference in power between the probe light polarized  $+45^\circ$  and  $-45^\circ$  was measured, we obtain the differential photocurrent[11]

$$i_- = i(+45) - i(-45) = i \frac{\sigma}{A} N i_t (T_2^2 - T_{-2}^2) \quad (7.1)$$

where  $\sigma$  is the atomic absorption cross section for unpolarized light,  $A$  is the area of the probe cross section at the target and  $N$  is the number of atoms inside the probe volume.  $i_t = i_0 e^{-\alpha}$  is the transmitted power of the probe which is depending on the optical depth of the probe transition,  $\alpha$ , and the initial probe power,  $i_0$ . The irreducible spherical tensor operators  $T_{\pm 2}^2$  describe the transverse atomic alignment along the axes oriented  $\pm 45^\circ$  relative to the  $x$  axis. The  $z$  axis is taken to be the propagation axis of the probe. In terms of the atomic angular momentum in the intermediate  $6P_{3/2}(F=5)$  state the tensor operators are given by  $T_{\pm 2}^2 \propto (F_x \pm iF_y)^2$ [96].

In a transition from the ground state, the relation between the polarization rotation angle,  $\theta$ , and  $T_{\pm 2}^2$  for a multilevel system with Zeeman degeneracy can be found in ref. [97] but for our double optical resonance finding this relation is nontrivial. With the goal of understanding the origin of the spin noise we will instead consider the simplified system of a lower transition from a  $F=0$  ground state to a  $F=1$  intermediate state. All optical fields are assumed to be weak so that the population in the intermediate state is small and the probe resonant with the transition between the intermediate state and the upper state simply reads out the fluctuations of the former. In terms of the density matrix elements  $\rho_{m,m'}$  ( $m$  is the magnetic quantum number) of a  $F=1$  state, the difference between the alignment tensors is simply  $T_2^2 - T_{-2}^2 \propto (\rho_{1,-1} - \rho_{-1,1})$ . If we now define a pseudospin  $\vec{J}$  with the components  $J_x = \frac{1}{2}(\rho_{+,-} + \rho_{-,+})$ ,  $J_y = -\frac{i}{2}(\rho_{+,-} - \rho_{-,+})$  and  $J_z = \frac{1}{2}(\rho_{+,+} - \rho_{-,-})$ , where we have used the abbreviations  $\rho_{+,-} = \rho_{1,-1}$ ,  $\rho_{-,-} = \rho_{-1,-1}$  etc., we find that our polarization interferometer setup with the probe being resonant on the incoherent part of the two photon transition, simply is sensitive to the fluctuations of the pseudospin component  $J_y$ . If the linear probe polarization had been rotated  $90^\circ$  to lie along the  $y$  axis, we would have been sensitive to  $J_x$  and if the probe had been detuned off resonance, we would have become increasingly more sensitive to the fluctuations in the atomic orientation along the  $z$  axis described by  $J_z$ . It is however only in the  $F=1$  case that the  $J_z$  and  $F_z$  operators almost are identical. It should be stressed here that the spin noise treated throughout this chapter is in fact the fluctuations of the pseudospin  $\vec{J}$  and not the real spin  $\vec{F}$  as one could be led to believe from our terminology. The results derived below can in principle be generalized to an intermediate state with an arbitrary  $F$ , however this will not be pursued further in this work.

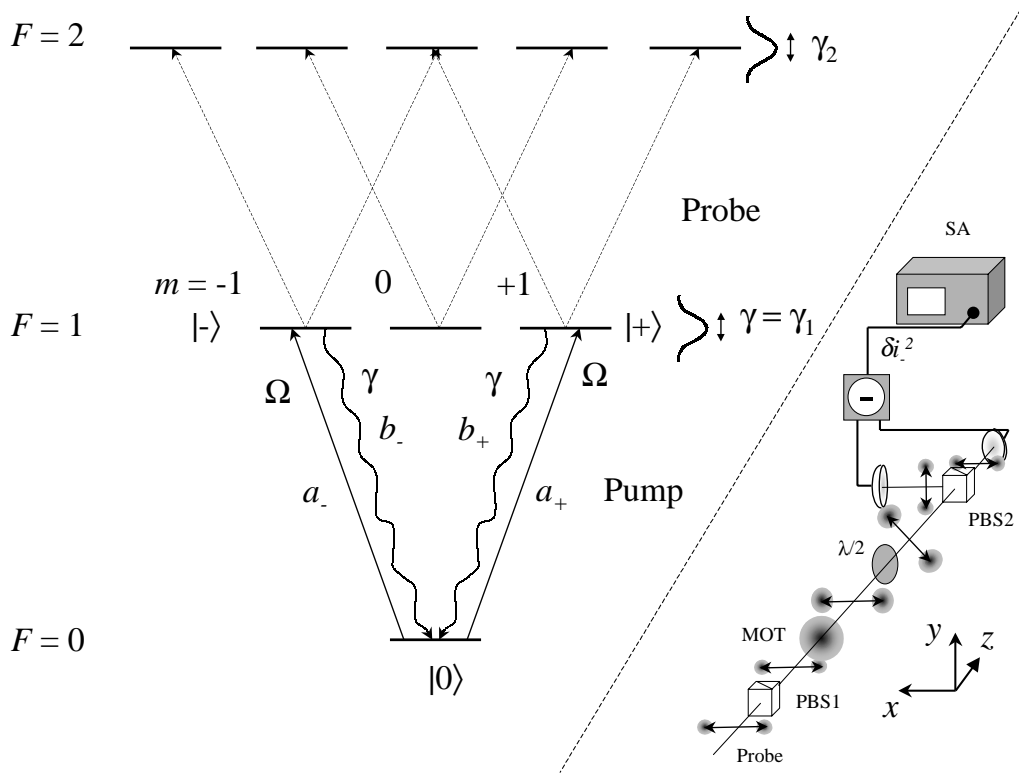


Figure 7.1: On the left is shown the effective V system under consideration. The pseudospin,  $\vec{J}$ , of the intermediate  $F = 1$  state is excited by the  $a_{\pm}$  pump fields. In the limit of weak pump and probe fields this spin is read out by the probe resonant on the upper transition. The spontaneous decay of the intermediate state couples the spin to the vacuum modes  $b_{\pm}$ . On the right the polarization interferometer is illustrated.

### 7.1.1 Modelling spin noise in a V system

We will now seek to derive the spin noise in our V system by deriving Langevin equations for the density matrix elements.. For simplicity we assume in our model that no  $\pi$  polarized light is present so that the  $m = 0$  intermediate state is not populated. The starting point of the calculation is the interaction Hamiltonian

$$\mathcal{H} = \hbar\Omega \left( a_+ e^{i\theta_+} \rho_{+0} + \rho_{0+} e^{-i\theta_+} a_+^\dagger \right) + \hbar\Omega \left( a_- e^{i\theta_-} \rho_{-0} + \rho_{0-} e^{-i\theta_-} a_-^\dagger \right) \quad (7.2)$$

which describes the coupling of the  $m = 0$  ground state  $|0\rangle$  to the two excited states  $|+\rangle$  and  $|-\rangle$  having  $m = 1$  and  $m = -1$  respectively. The ground state and the excited state  $|+\rangle$  is coupled by the quantum field  $a_+$  having the phase  $\theta_+$  and analogous the other excited state  $|-\rangle$  is coupled to the ground state by the '-' field. The decay of the excited states is assumed always to be into the continuum of vacuum modes  $b_{\pm}$ , and the decay rate is denoted  $\gamma$  whereas the coupling constant to the exciting fields is labeled  $\Omega$ . Our system is illustrated in figure 7.1. We now obtain the Langevin equations for our V system to

be

$$\begin{aligned}\frac{d\rho_{\pm 0}}{dt} &= -\frac{1}{2}\gamma\rho_{\pm 0} + i(2\rho_{\pm\pm} + \rho_{\mp\mp} - 1)\left(\Omega a_{\pm}^{\dagger}e^{-i\theta_{\pm}} + \sqrt{\gamma}b_{\pm}^{\dagger}\right) + i\rho_{\pm\mp}\left(\Omega a_{\mp}^{\dagger}e^{-i\theta_{\mp}} + \sqrt{\gamma}b_{\mp}^{\dagger}\right) \\ \frac{d\rho_{\pm\pm}}{dt} &= -\gamma\rho_{\pm\pm} + i\left[(\Omega a_{\pm}e^{i\theta_{\pm}} + \sqrt{\gamma}b_{\pm})\rho_{\pm 0} - h.c.\right] \\ \frac{d\rho_{+-}}{dt} &= -\gamma\rho_{+-} + i\left(\Omega a_{-}e^{i\theta_{-}} + \sqrt{\gamma}b_{-}\right)\rho_{+0} - i\left(\Omega a_{+}^{\dagger}e^{-i\theta_{+}} + \sqrt{\gamma}b_{+}^{\dagger}\right)\rho_{0-}\end{aligned}\quad (7.3)$$

In (7.3) it has been used that  $\rho_{++} + \rho_{--} + \rho_{00} \simeq 1$  to eliminate  $\rho_{00}$ . The Langevin equations are only valid if the individual atoms behave in an uncorrelated way, that is, the light exciting the atoms must be uncorrelated and the atoms do not interact. In the following we will assume that the fields  $a_{\pm}$  are in coherent states. If we take these fields to have the real expectation values  $\langle a_{\pm} \rangle = \alpha_{\pm}$  and defining the saturation parameters

$$s_{\pm} = \left(2\frac{\Omega}{\gamma}\right)^2 \alpha_{\pm}^2 \quad (7.4)$$

we find the steady state solutions of (7.3) to be given by

$$\begin{aligned}\bar{\rho}_{\pm 0} &= -ie^{-i\theta_{\pm}} \frac{\sqrt{s_{\pm}}}{1+2(s_{+}+s_{-})} \\ \bar{\rho}_{\pm\pm} &= \frac{s_{\pm}}{1+2(s_{+}+s_{-})} \\ \bar{\rho}_{\pm\mp} &= e^{-i(\theta_{\pm}-\theta_{\mp})} \frac{\sqrt{s_{+}s_{-}}}{1+2(s_{+}+s_{-})}\end{aligned}\quad (7.5)$$

where we have used that  $\langle b_{\pm} \rangle = \langle b_{\pm}^{\dagger} \rangle = 0$ . The mean pseudospin is now found to be

$$\begin{pmatrix} \bar{J}_x \\ \bar{J}_y \\ \bar{J}_z \end{pmatrix} = \frac{1}{1+2(s_{+}+s_{-})} \begin{pmatrix} \sqrt{s_{+}s_{-}} \cos(\theta_{-}-\theta_{+}) \\ \sqrt{s_{+}s_{-}} \sin(\theta_{-}-\theta_{+}) \\ \frac{1}{2}(s_{+}-s_{-}) \end{pmatrix} \quad (7.6)$$

It can now be seen that the transverse direction of the mean spin is controlled by the relative phase between the  $\sigma^{+}$  and  $\sigma^{-}$  polarized optical fields. For two independent fields this phase difference is stochastic and hence the mean transverse spin average to zero. If on the other hand the two fields are equally strong and come from the same source, for instance a linearly polarized laserbeam, our spin will be exactly orthogonal to the propagation axis. This is because the pseudospin components  $J_x$  and  $J_y$  in fact describe the transverse alignment of the atomic medium, and naturally the atoms will align themselves to the polarization of the pump field with the angle  $\theta_{-}-\theta_{+}$  relative to the  $x$  axis. To achieve a mean spin along the  $z$  axis different intensities in the two fields are required to produce the longitudinal orientation as it is seen from the  $s_{+}-s_{-}$  term.

Having solved the steady state problem we now assume that the fluctuations of the atomic parameters and the coherent fields are small as compared to the mean values. In this case we can linearize the fluctuations of the density matrix elements and the fields around the mean values. Now we Fourier transform the equations (7.3) to obtain the spectrum of fluctuations. For the dipole moments we furthermore assume the atomic excitation to be small so that we can ignore the fluctuations in the upper state populations relative to the field fluctuations. As a result we find the following fluctuating part of the atomic dipole operators to the first order in the saturation parameters

$$\begin{aligned}\delta\rho_{\pm 0} &= -\frac{i}{i\omega + \frac{1}{2}\gamma} \left[ \frac{1+s_{\pm}}{1+2(s_{+}+s_{-})} \left( \Omega e^{-i\theta_{\pm}} \delta a_{\pm}^{\dagger} + \sqrt{\gamma} \delta b_{\pm}^{\dagger} \right) - \right. \\ &\quad \left. - \frac{\sqrt{s_{+}s_{-}}}{1+2(s_{+}+s_{-})} e^{-i(\theta_{\pm}-\theta_{\mp})} \left( \Omega e^{-i\theta_{\mp}} \delta a_{\mp}^{\dagger} + \sqrt{\gamma} \delta b_{\mp}^{\dagger} \right) \right]\end{aligned}\quad (7.7)$$

The dipole fluctuations together with the field fluctuations are now inserted in the Fourier transforms of the equations of motion for  $\delta\rho_{\pm\pm}$  and  $\delta\rho_{\pm\mp}$  as the driving noise terms, and by using (7.5) we find the fluctuations in the upper state populations and coherences to lowest order in the saturation parameters ( $s_{\pm} \ll 1$ ). For fluctuation frequencies smaller than the decay rate ( $\omega \ll \gamma$ ) these are given by

$$\begin{aligned}\delta\rho_{\pm\pm} &= 2\sqrt{s_{\pm}} \left[ \frac{\Omega}{\gamma} \delta X_{\pm}(0) + \frac{1}{\sqrt{\gamma}} \delta Y_{\pm}(\theta_{\pm}) \right] \\ \delta\rho_{\pm\mp} &= 2e^{-i\theta_{\pm}} \sqrt{s_{\pm}} \left( \frac{\Omega}{\gamma} e^{i\theta_{\mp}} \delta a_{\mp} + \frac{1}{\sqrt{\gamma}} \delta b_{\mp} \right) + 2e^{i\theta_{\mp}} \sqrt{s_{\mp}} \left( \frac{\Omega}{\gamma} e^{-i\theta_{\pm}} \delta a_{\pm}^{\dagger} + \frac{1}{\sqrt{\gamma}} \delta b_{\pm}^{\dagger} \right)\end{aligned}\quad (7.8)$$

where we have used the quadrature phase operators

$$\begin{aligned}\delta X_{\pm}(\phi) &= \delta a_{\pm} e^{-i\phi} + \delta a_{\pm}^{\dagger} e^{i\phi} \\ \delta Y_{\pm}(\phi) &= \delta b_{\pm} e^{-i\phi} + \delta b_{\pm}^{\dagger} e^{i\phi}\end{aligned}\quad (7.9)$$

With the fluctuations at hand we now use our definition of the pseudospin operators to write up the variances of the spin components. These are

$$\begin{aligned}\langle \delta J_x^2 \rangle &= s_+ + s_- + \left(\frac{\Omega}{\gamma}\right)^2 [s_+ \langle \delta X_-^2(\theta_+ - \theta_-) \rangle + s_- \langle \delta X_+^2(\theta_- - \theta_+) \rangle] \\ \langle \delta J_y^2 \rangle &= s_+ + s_- + \left(\frac{\Omega}{\gamma}\right)^2 [s_+ \langle \delta X_-^2(\theta_+ - \theta_- + \pi/2) \rangle + s_- \langle \delta X_+^2(\theta_- - \theta_+ - \pi/2) \rangle] \\ \langle \delta J_z^2 \rangle &= s_+ + s_- + \left(\frac{\Omega}{\gamma}\right)^2 [s_+ \langle \delta X_+^2(0) \rangle + s_- \langle \delta X_-^2(0) \rangle]\end{aligned}\quad (7.10)$$

Arriving at these expressions we have used that the bandwidth within which the atoms pick up quantum noise from the vacuum modes is the atomic linewidth  $\gamma$ , and we have normalized the power of our fluctuations to the vacuum level. It is noted that  $\Omega$  is the Rabi frequency due to the presence of a single photon and hence in free space the factor  $(\Omega/\gamma)^2$  is a very small number. This means that if the  $a_{\pm}$  fields would possess nonclassical features such as squeezing, it would have very little impact on the spin noise of the atoms unless the coupling is enhanced for instance by making use of high Q cavities[98][99]. Another possibility of altering the spin noise, which is not evident from this treatment, is by absorbing a squeezed field completely in an atomic medium and thereby transferring the correlations of the light to the excited state of the atoms[100]. As a result it may prove to be possible to reduce the fluctuations of for instance  $J_x$  at the expense of increased fluctuations in  $J_y$  or vice versa and create a so called spin squeezed state[101][102].

The  $s_+ + s_-$  terms appearing in (7.10) before the variance of the pumping fields are arising from the coupling of the excited states to the free space vacuum modes and hence they describe the spin noise resulting from the stochastic process of spontaneous decay of the excited states. Keeping only these terms we find the noise of our pseudospin to be isotropically distributed around the mean spin with the variances

$$\langle \delta J_x^2 \rangle = \langle \delta J_y^2 \rangle = \langle \delta J_z^2 \rangle = s_+ + s_- \quad (7.11)$$

Due to the isotropy of the spin noise we will henceforth denote the spin state derived above the *Spherical Spin State*. The spin state encountered in a MOT has properties closely resembling this state. Since our pseudospin obey the angular momentum algebra  $[J_j, J_k] = \varepsilon_{jkl} J_l$ , ( $j, k, l = x, y, z$ ), we can now check that the associated three Heisenberg uncertainty relations are obeyed. Using (7.11) and (7.6) in the limit of weak excitation we find these to be

$$\begin{aligned}\langle \delta J_x^2 \rangle \langle \delta J_y^2 \rangle &\geq \frac{1}{4} \langle J_z \rangle^2 \rightarrow (s_+ + s_-)^2 \geq \frac{1}{16} (s_+ - s_-)^2 \\ \langle \delta J_y^2 \rangle \langle \delta J_z^2 \rangle &\geq \frac{1}{4} \langle J_x \rangle^2 \rightarrow (s_+ + s_-)^2 \geq \frac{1}{4} s_+ s_- \cos^2(\theta_- - \theta_+) \\ \langle \delta J_z^2 \rangle \langle \delta J_x^2 \rangle &\geq \frac{1}{4} \langle J_y \rangle^2 \rightarrow (s_+ + s_-)^2 \geq \frac{1}{4} s_+ s_- \sin^2(\theta_- - \theta_+)\end{aligned}\quad (7.12)$$

It is easy to see that these three uncertainty relations all are fulfilled for any choice of  $s_{\pm} \geq 0$ . In fact we note that with our configuration of the pump fields it is only possible to achieve the equality in the trivial case when all fields are zero.

### 7.1.2 Dependencies

Equation (7.11) describes the atomic contribution to the quantum noise of the polarization interferometer, however if a massive amount of technical noise is present in the trapping laser or the probe, reaching the quantum noise limit is impossible. Technical noise in the lasers will result in a coherent modulation of all the trapped atoms. Hence the net atomic noise given by

$$\langle \delta J_y^2 \rangle = \left\langle \delta \left( \sum_{\mu} j_y^{\mu} \right)^2 \right\rangle \quad (7.13)$$

will be proportional to the *square* of the number of atoms because the sum over all atoms of their individual spin,  $j_y^\mu$ , is proportional to the number of atoms,  $N$ . In the case of quantum spin noise the noise of the individual spins is uncorrelated and as a result the variance of the sum (7.13) breaks down to  $N$  identical variances so that the quantum spin noise simply is proportional the number of atoms. In the section to follow this difference in the  $N$  dependence is used to distinguish the quantum noise from the technical noise. In general both types of noise are present in the atomic system, and as the number of atoms grows larger the technical noise will always dominate over the quantum noise. In fact this happened already for a few hundreds of atoms in the ion trap experiment[95]. In our experiment the number of trapped atoms were in the vicinity of  $10^8$  and consequently it was vital to have quiet lasers in order to be able to observe the quantum spin noise. It should be noted that although the spin noise derived above is an atomic quantum noise it will add to the probe noise as a technical noise. Hence the amount of spin noise carried by the probe to the detectors will be proportional the probe power at the detectors *squared* in contrast to the probe quantum noise which of course is linear in the probe power.

We are now in a position where it is possible to collect the knowledge obtained in the previous chapters and combine it with the considerations above to write up the net noise power in the differential photocurrent of the polarization interferometer. In units of the elementary charge and normalized to the shot noise of the unattenuated probe this is given by

$$\Psi(\Omega) = \frac{\delta i_-^2}{2B i_0} = e^{-\alpha} (1 - S e^{-\alpha}) + i_0 e^{-2\alpha} \left[ \frac{k_t}{4B} \left( \Omega M \alpha \frac{\partial X_r}{\partial \Delta} \right)^2 + \frac{k_q}{i_0^{sat}} \alpha \right] \quad (7.14)$$

where we remind ourselves that  $B$  is the spectrum analyzer resolution bandwidth,  $S$  is the degree of squeezing in the probe,  $i_0$  is the probe photon flux before the trap,  $\alpha$  is the optical depth of the trap on the probe transition,  $\Omega$  is the detection frequency,  $M$  is the phase modulation index of the trapping laser,  $X_r$  is the real part of the atomic susceptibility at the probe frequency,  $\Delta$  is the trapping laser detuning and  $k_t$  is a scaling constant depending on the detection efficiency, balancing etc. For a coherent spin state[101] and weak fields the proportionality constant  $k_q$  governing the amount of quantum spin noise relative to the shot noise can be shown to depend on the atomic decay rates of the populations and the spin  $k_q = \pi^{-1}(\gamma_1 + \gamma_2)/2\gamma_{spin}$ , and the saturation flux  $i_0^{sat}$  is given by  $i_0^{sat} = A(\gamma_1 + \gamma_2)/2\sigma$ . Here  $\gamma_1$  and  $\gamma_2$  are the decay rates of the populations of the intermediate and upper state respectively,  $A$  is the area of the probe beam cross section and  $\sigma$  is the atomic absorption cross section for unpolarized light. From this we see that in order to have an large amount of quantum spin noise a strong probe transition and a long living spin are required. This is why the spin noise usually is easy to observe in nuclear magnetic resonance experiments, where the long living ground state spin is probed[103]. Even though the symmetry of the MOT is resulting in a spherical spin state rather than a coherent state, and even though the pump fields are not weak, we still expect our estimate of  $k_q$  to be on the right order of magnitude.

The first term in (7.14) describes the shot noise of the probe, which is reduced by the degree of squeezing,  $S$ . In case of an optically thick atomic medium the shot noise is attenuated by the transmission  $e^{-\alpha}$  and furthermore the squeezing is reduced yet another time by the transmission due to the coupling to the vacuum as a result of the attenuation. The first term in the second brackets describes the technical spin noise as we derived it in (6.4) and the second term describes the quantum spin noise. Apart from the obvious fact that the two terms yield different lineshapes as the probe frequency is scanned across resonance, we find that they differ mainly in the dependence on the optical depth,  $\alpha = N\sigma/A$ . Clearly the quantum noise has the spectral shape of the DC absorption entering via the cross section  $\sigma$ , whereas the technical noise has the more complicated structure described in the last chapter.

## 7.2 Experimental setup

After having dealt with the necessary physical considerations we will now address the actual experiment. Although we allowed for squeezing in the probe in eq. (7.14), the entire experiment was in fact performed

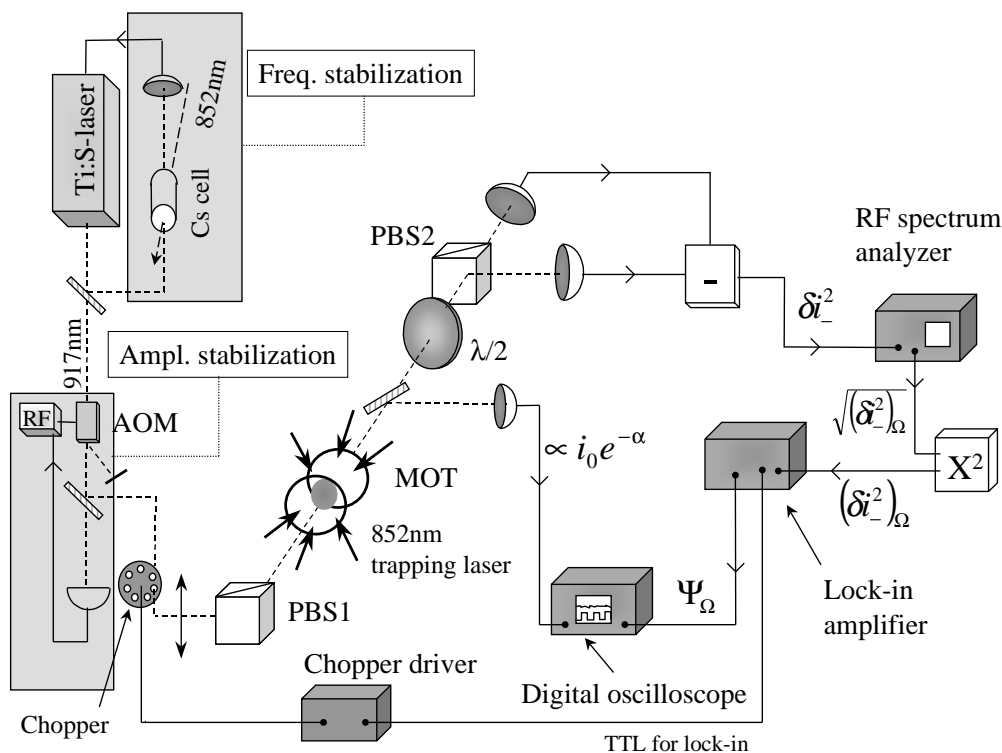


Figure 7.2: The setup used for the measurements of the quantum spin noise. The Ti:Sapphire laser providing the probe light for the polarization interferometer was stabilized in frequency as well as power. The probe was chopped and lock-in detection ensured that only the probe noise was recorded on the digital scope.

with a probe in a coherent state. As it was shown in the last chapter the phase noise of the trapping diode laser turned out to be deleterious to our attempts to reach the quantum spin noise. Figure 6.6 shows a modulation signal made up of technical noise which is 10 times the probe shot noise leaving little room for the quantum noise. Another issue is that the ratio of spin noise to shot noise is proportional to  $\alpha e^{-\alpha}$ . This is maximum for  $\alpha = 1$  and the absolute power of the spin noise, described by  $\alpha e^{-2\alpha}$ , is maximum for  $\alpha = 1/2$ . In the MOT used up to this stage of our investigations, only 20-30 mW of trapping power coming from a diode laser gave us an optical depth around 0.03 far from the optimum value. In order to reach higher optical depths and avoid the phase noise we built a Ti:Sapphire laser providing around 200 mW of light at 852 nm for trapping. Being well locked to the Cs  $D_2$  line the trapping laser phase possessed only a small amount of technical noise above a couple of MHz, which should reduce the technical spin noise substantially. Furthermore we rebuilt our trap from a 5 beam to a 6 beam configuration in which the power of each beam was retroreflected to be recycled. With 60 mW in each beam we were able to obtain an optical depth as high as 1.8 on the probe transition and with a size of the trap around 7 mm in diameter, we can estimate the density of atoms to be around  $10^9 \text{ cm}^{-3}$  and the overall number of atoms to be around  $10^8$ . As it can be seen from (7.14), the ratio of spin noise to shot noise grows proportional with  $i_0$  hence it was advantageous to use a somewhat saturating probe. In the rest of the experiment we used  $i_0/i_0^{sat} = 0.72$ , and the highest achievable optical depth was around 1 with this probe power.

If we use (7.14) to estimate the ratio of spin noise to the unattenuated shot noise ( $\alpha = 0$ ), we find

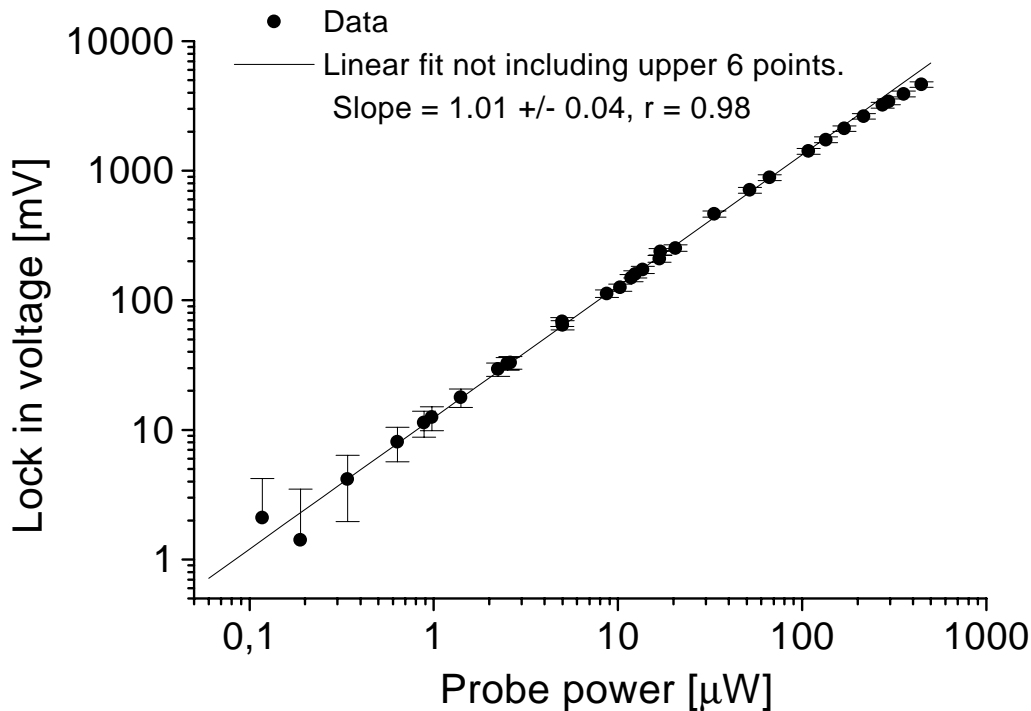


Figure 7.3: Testing the sensitivity and linearity of our lock-in detection of the probe noise. The fit shows that our scheme was linear within 1%. Optical powers between 400 nW and 200  $\mu\text{W}$  could be detected before electronic noise dominated in the lower end and the detectors saturated in the high end.

this ratio to be 4.9% with  $\alpha = 1$ ,  $\gamma_1 = 5.3$  MHz,  $\gamma_2 = 3$  MHz and  $\gamma_{spin} = 5.3$  MHz. Typical probe powers were around 340  $\mu\text{W}$ , which gave a shot noise level about 5-6 dB above the electronic noise level. Since the spin noise only was expected to be a few percent of the shot noise, we clearly needed some method of reducing the significance of the electronic noise. This was done by chopping the probe at a 1 kHz rate. The balanced detector output was sent into a RF spectrum analyzer (SA) which returned a voltage proportional to the RMS noise of the detector current at  $\Omega/2\pi = 3$  MHz. With the goal of sending this output into a lock-in amplifier being gated by the chopper TTL pulse, we first had to square the voltage to get a signal proportional to the variance of the probe fluctuations. With a zero degree mixing phase of the lock-in amplifier we got an output that only was proportional to the chopped probe noise. With the lock-in amplifier averaging on a 30 seconds timescale, the output was sent into a digital scope where it was averaged even more. The setup is shown in figure 7.2.

From (7.14) we see that the ratio of spin noise to shot noise is linear in the probe power. Our Ti:Sapphire laser that provided the light for the probe showed fluctuations in the power on the order of 10% at frequencies around 1 kHz. Hence our spin noise to shot noise ratio would fluctuate with this amount, and since the spin noise only was a rather small fraction of the shot noise, we had to stabilize the probe power in order to achieve a stable signal. This was done by placing an acousto optic modulator (AOM) in the probe path and filtering out the first order diffraction. A photodiode measured the probe power and a servoloop stabilized this power to a fixed internal voltage of the loop by varying the RF power driving the AOM. As a result the power fluctuations were reduced from 10% to less than 1% in the 10 kHz bandwidth that the servoloop provided.

In part of the experiment we also needed to lock the probe laser frequency to the atomic resonance. This was done by using standard two photon (almost) Doppler free spectroscopy in an external Cs cell. Towards this end we used a 852 nm pump beam with FM sidebands counterpropagating to a 917 nm probe. The resulting modulated two photon absorption signal was now used to derive an error signal by means of standard phase sensitive RF technique. Because of the different wavelengths the cancellation of the Doppler broadening was not perfect, however the residual effect was only 7% and hence insignificant.

Finally we needed to know the DC absorption of the probe in the trap to infer  $\alpha$ . This was measured by splitting off 2% of the transmitted probe power to a DC detector and measuring the detector voltage on a digital oscilloscope.

### 7.3 Measurements and results

In order to prove that we really detected spin noise, we had to demonstrate that this was linear in the number of trapped atoms. Hence we had to vary the optical depth over as large a range as possible without changing the trap parameters (magnetic fields, detunings, alignment etc.). This was done by attenuating the power of the MOT repumping laser. Up to this point this laser has been ignored since it has had no importance to the experiments. The repumping laser was a diode laser resonant with the  $6S_{1/2}(F=3) \rightarrow 6P_{3/2}(F=4)$  transition in the trapped Cs atoms. This laser was required because Cs has a double ground state made up by the  $F=3$  and  $F=4$  hyperfine components. The trapping laser was resonant with the  $6S_{1/2}(F=4) \rightarrow 6P_{3/2}(F=5)$  transition and due to the finite overlap of the Lorentzian tails of the  $6P_{3/2}(F=5)$  state with the  $6P_{3/2}(F=4)$  state there was about 0.05% probability that the decay of the  $6P_{3/2}(F=5)$  state went to the  $F=3$  ground state and hence left the cooling cycle. These atoms decaying to the 'wrong' ground state were pumped back into the cooling cycle by the repumping laser. By changing the power of this laser we were able to control the number of atoms in the cooling cycle and thereby in the probed  $6P_{3/2}(F=5)$  state relative to the number of atoms in the  $6S_{1/2}(F=3)$  state without changing any other trapping conditions.

With a varying optical depth the shot noise of the transmitted probe varied as well. The spin noise was observed as the excess noise relative to the predicted shot noise inferred by measuring the transmitted DC power. Hence we needed to know how the shot noise was transmitted through our lock-in detection system as the probe power was varied. For this measurement no trapped atoms were present and the probe power was simply attenuated by a half wave retarder and a polarizer. The measurement also served to test the linearity of our somewhat complicated data acquisition procedure. As it is shown in figure 7.3, where the lock-in voltage vs. probe power is plotted, our detection system was linear within 1% and we managed to discriminate the shot noise against the electronic noise for probe powers as low as a few hundred nanoWatts. With an initial probe power of 340  $\mu\text{W}$  this corresponds to an optical depth around 7, which is much higher than we could achieve in our MOT. The deviation from the straight line in the upper end was caused by saturation of the RF amplifiers in our detectors. Reducing the gain of these amplifiers would make it possible for us to reach higher powers, however this was not necessary in this experiment since the 340  $\mu\text{W}$  probe power already was saturating the atomic transition. If we compare our results to ref. [104] where shot noise was detected in a similar scheme, we find that our detectors allowed us to detect smaller powers, but we paid the price of saturation at smaller powers.

Now that we understood our detection system we started our MOT and observed the probe noise power at 3 MHz as it was scanned across the atomic resonance. A typical trace is shown in figure 7.4. Here the dashed line is the probe noise measured by adding the photocurrents of the two detectors and the full line is the balanced detection signal. Focusing on the latter it is clear why it would have been impossible to detect the quantum spin noise using semiconductor lasers for trapping. The peak 7 dB above the shot noise level corresponds to the two photon transition made by the probe and the semiconductor repumping laser. Clearly this looks like a modulated polarization rotation signal and hence we attribute this to be the signature of strong technical spin noise caused by the phase noise of the repumping laser. The transition is shown in the insert of fig. 7.4, which shows that the resonance is shifted about 280 MHz

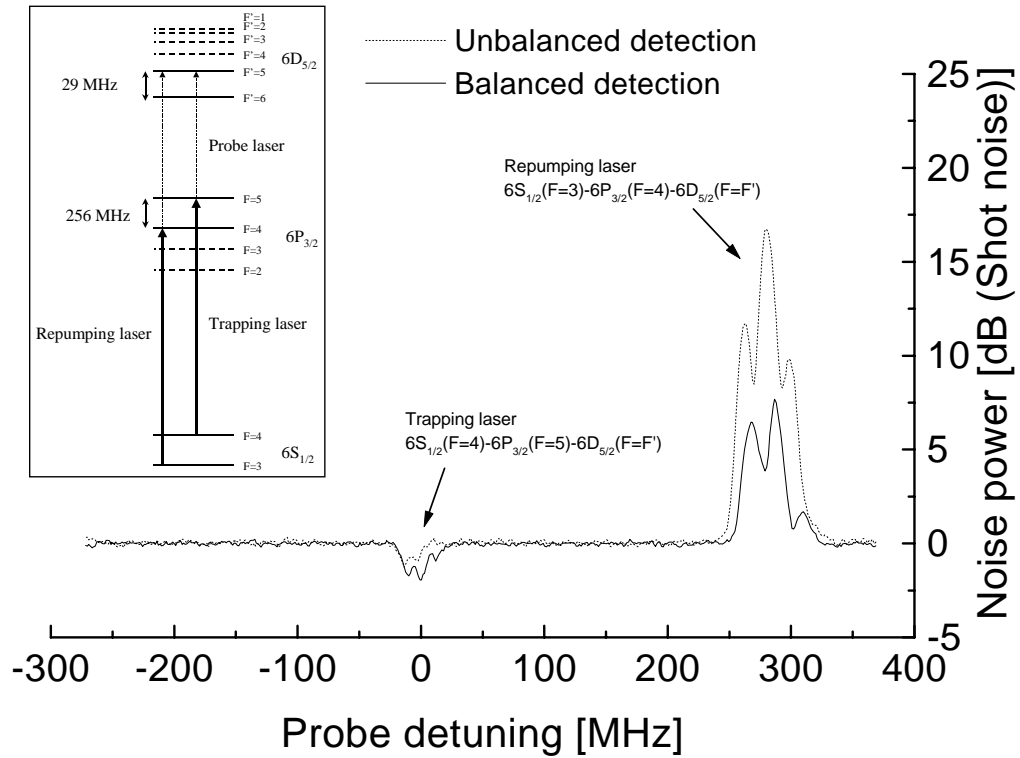


Figure 7.4: The SA traces at 3 MHz derived from analyzing the sum of the photocurrents (dotted line) and the difference of the photocurrents (full line). The dips are due to the DC absorption and the accompanying reduction of shot noise. In contrast to this the peaks are modulated signals due to the modulated two photon transition made by the probe with the phase noise of the repumping laser. The insert shows the relevant transitions.

relative to the two photon transition with the trapping laser as a result of the hyperfine splittings in the  $6P_{3/2}$  and the  $6D_{5/2}$  states. Because our trapping laser now was a relatively quiet Ti:Sapphire, we did not observe any noise peaks at the two photon transition frequency with trapping laser. Instead we saw a dip as a result of the absorption of probe power and the associated reduction of shot noise. According to our discussion in section 1 of this chapter this dip should reflect the DC absorption profile of the transition and this is also what we observe in fig. 7.4. When comparing the balanced to the unbalanced detection we see the importance of balancing the detectors. By making use of the knowledge gained in the last chapter we know that the modulation spectroscopy signals and hence the technical atomic noise was by far stronger in  $i_+$  corresponding to the absorption measured with unbalanced detectors. In contrast to this, the polarization rotation signals were smaller as a result of the balanced detection leading to  $i_-$  and the small rotation angle, which left most of the modulation balanced out. The quantum spin noise however is stochastic in nature and cannot be balanced out by the detectors. As a result we should expect to see the same amount of atomic quantum noise in the absorption and the polarization rotation signals. This was the reason why we in the rest of this experiment chose to analyze only  $i_-$  coming from the balanced detectors.

By measuring the DC absorption of the probe by a photodiode as we scanned the probe across resonance and comparing the DC absorption to the reduction of shot noise, we were able to identify the atomic spin noise as the discrepancy between the two. As shown in figure 7.5(a), the shot noise did

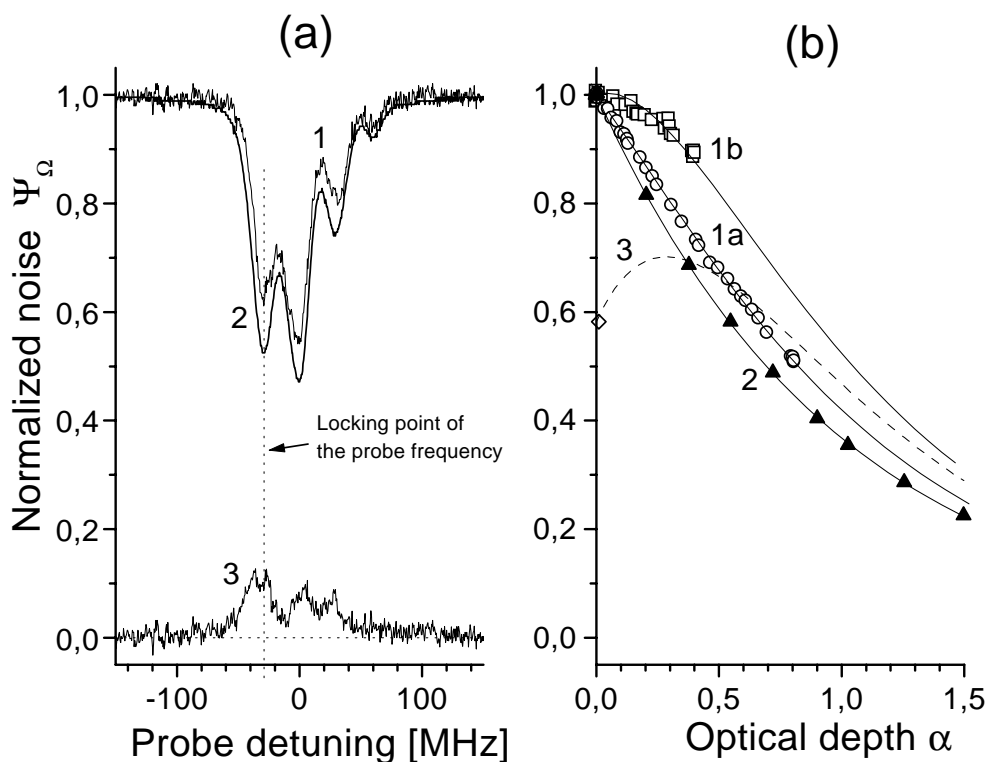


Figure 7.5: (a) Curve 1 shows the transmitted DC power as the probe was scanned across resonance. Curve 2 shows the transmitted noise power at 3 MHz and curve 3 is the difference between curve 1 and 2 reflecting the spin noise. (b) Curve 1a is the combined shot noise and spin noise with a  $340 \mu\text{W}$  probe. The line is the theoretical prediction with  $i_0/i_0^{\text{sat}} = 0.72$  and the value of  $k_q$  obtained experimentally later in this chapter. Curve 1b is the same as 1a but with  $950 \mu\text{W}$  probe power corresponding to  $i_0/i_0^{\text{sat}} = 2$ , again the line is the theory. Curve 2 shows the transmitted shot noise when the probe is attenuated by a passive absorber and curve 3 shows the predicted shot noise and spin noise for the squeezed probe in chapter 5. The diamond corresponds to the optical depth of this experiment.

not reduce as much as we would expect the atoms merely were passive absorbers. The additional noise, which is shown in curve 3, is the atomic spin noise. From the curve we see that the spin noise was about 10% of the unattenuated shot noise. Although it is rather noisy, we note that curve 3 resembles the DC absorption in shape and hence it is likely to be the quantum spin noise. In this case we find that our initial estimate for a coherent spin state of 4.9% was indeed within the right order of magnitude. In order to investigate whether this noise was of technical or quantum origin we locked the probe laser to the incoherent resonance farthest on the left of fig. 7.5(a). Then we started our chopper to begin our sensitive lock-in detection and measured the lock-in voltage  $[e^{-\alpha} + i_0 k_q \alpha e^{-2\alpha} / i_0^{\text{sat}}]$  from (7.14) as the optical depth of the trap was varied by attenuating the repumping laser. This is shown for two different probe powers as the circles and the squares in fig. 7.5(b). In parallel to this we also recorded the transmitted probe power  $i_0 e^{-\alpha}$  by means of the DC detector in order to infer the optical depth. After this series of measurements we blocked the trapping laser and simply varied the probe power to get the noise level in the case of passive absorption. The simultaneous recording of the DC detector allowed us to infer the shot noise level as function of the optical depth. This is shown as triangles in fig. 7.5(b). If we keep in mind that our spin noise is the difference between curves 1 and 2, we can confirm that

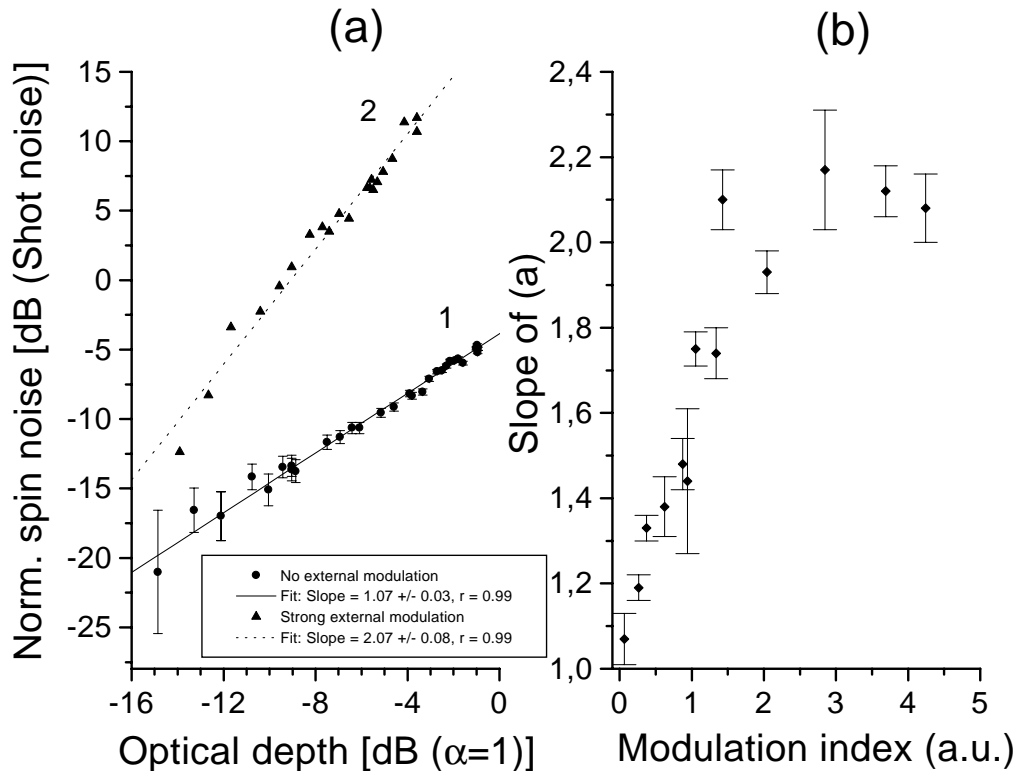


Figure 7.6: (a) The dependence of the spin noise normalized to  $e^{-2\alpha}$  on the optical depth  $\alpha$ . The spin noise is in units of the shot noise of the unattenuated probe. Curve 1 is with no external modulation and curve 2 is with external FM of the trapping laser. (b) The transition of the slopes from (a) as the modulation index of the FM is increased. The change from 1 to 2 in the slopes reflect the transition from dominating quantum noise to dominating technical noise.

this is maximum around an optical depth of 0.5 as it was predicted in section 7.2. When both of these curves were normalized to perfect transmission of the probe (zero optical depth), we could directly find the spin noise  $i_0 k_q \alpha e^{-\alpha} / i_o^{sat}$  as the ratio of curves 1 to curve 2. This ratio was normalized to the MOT transmission  $e^{-\alpha}$  in order to test whether it was proportional to  $\alpha$  if quantum noise was observed or  $\alpha^2$  in the case of technical noise. The result is shown on a Log-Log plot in curve 1 of figure 7.6(a). Here the slope of  $1.07 \pm 0.03$  clearly indicates that our atomic spin noise was predominantly of quantum nature. By applying FM to the trapping laser we obtained curve 2 with the slope of 2. This was reflecting the transition of the spin noise dominated by quantum noise to almost pure technical spin noise. The slopes of curves similar to fig. 7.6(a) are shown in fig. 7.6(b) as function of the trapping laser modulation index,  $M$ . This was found by measuring the size of the modulated absorption signal at a fixed optical depth. From (7.14) we find the size of this signal to be proportional to  $M^2$ . The figure clearly shows the transition from the dominating quantum noise growing linear in the number of atoms to the dominating technical noise growing like the square of the number of atoms and hence giving a slope of 2. Due to a fluctuating modulation index of our rather primitive electro optical modulator, the points on fig. 7.6(a) curve 2 fluctuate somewhat. This is also the cause of the scattering of the points in (b).

By the use of (7.14) we are now also in a position to see the effect of squeezing in the probe. This is shown as the diamond on curve 3 of fig. 7.5(b). Extrapolating this point by means of our theory and the value of  $k_q$  obtained below, we see that as the optical depth increases above 0.6 nothing is gained

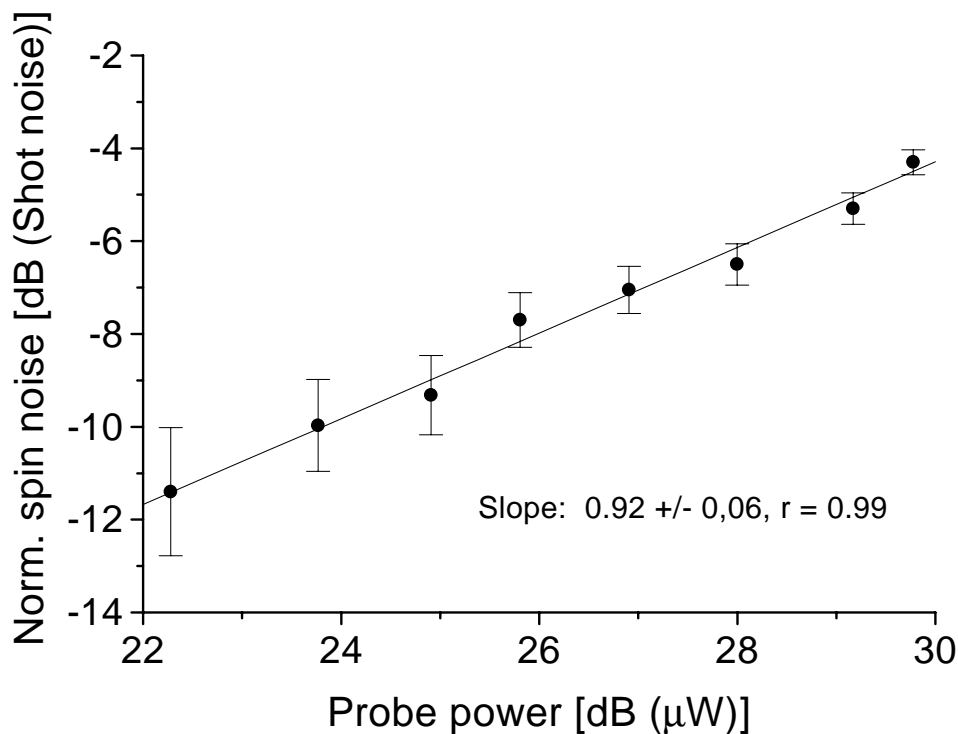


Figure 7.7: The log-log plot of the spin noise dependence on the probe power. The spin noise is normalized to  $e^{-2\alpha}$ . The slope of  $0.92 \pm 0.06$  confirms our theory predicting a linear dependence.

in terms of noise reduction by squeezing the probe. If quantum noise reduction in an optically thick medium should be obtained it is instead necessary to squeeze the atomic spin for instance by exciting the intermediate  $6P_{3/2}$  state with quantum correlated light as proposed in ref. [100].

To conclude these measurements we finally tested the dependence of the spin noise on the probe power. Equation (7.14) tells us that the spin noise normalized to the probe shot noise should grow linearly as the probe power is increased. For this purpose we fixed the optical depth at 0.32 corresponding to -5 dB on fig. 7.6(a). Now the probe power was varied from about  $150 \mu\text{W}$  to  $800 \mu\text{W}$  and the spin noise was recorded in a similar fashion as before. The results are shown in figure 7.7, from which we find the slope of the Log-Log plot of the spin noise versus probe power to have a slope of  $0.92 \pm 0.06$ . This clearly shows the linear relationship and provides us with yet another indication that we have a reasonable understanding of the atomic spin noise.

We can find the experimental value of the parameter  $k_q$  in (7.14) by reading out the spin noise of curve 1 in fig. 7.6(a) at  $\alpha = 1$ . From (7.14) we find that this number is  $k_q i_0 / i_0^{sat}$  since the  $e^{-2\alpha}$  has been normalized away. The number is found to be -3.85 dB corresponding to 0.41, and by using that  $i_0 / i_0^{sat}$  in the experiment was 0.72, we find  $k_q^{ex} = 0.58$ . The theoretical value of this parameter assuming a coherent spin state with  $F = 1$  is found to be  $k_q^{theo} = 0.25$  with  $\gamma_1 = \gamma_{spin} = 5.3 \text{ MHz}$  and  $\gamma_2 = 3 \text{ MHz}$ . Our discrepancy of a factor of 2 should be found from the fact that the MOT spin state is not a collective coherent spin state as defined in [101], rather it is a spherical spin state made up by uncorrelated individual spins pointing in random directions. In comparison the coherent spin state is made up by uncorrelated spins pointing in the same direction. Intuitively the oriented coherent spin state has smaller fluctuations in the transverse collective spin components than the totally symmetric

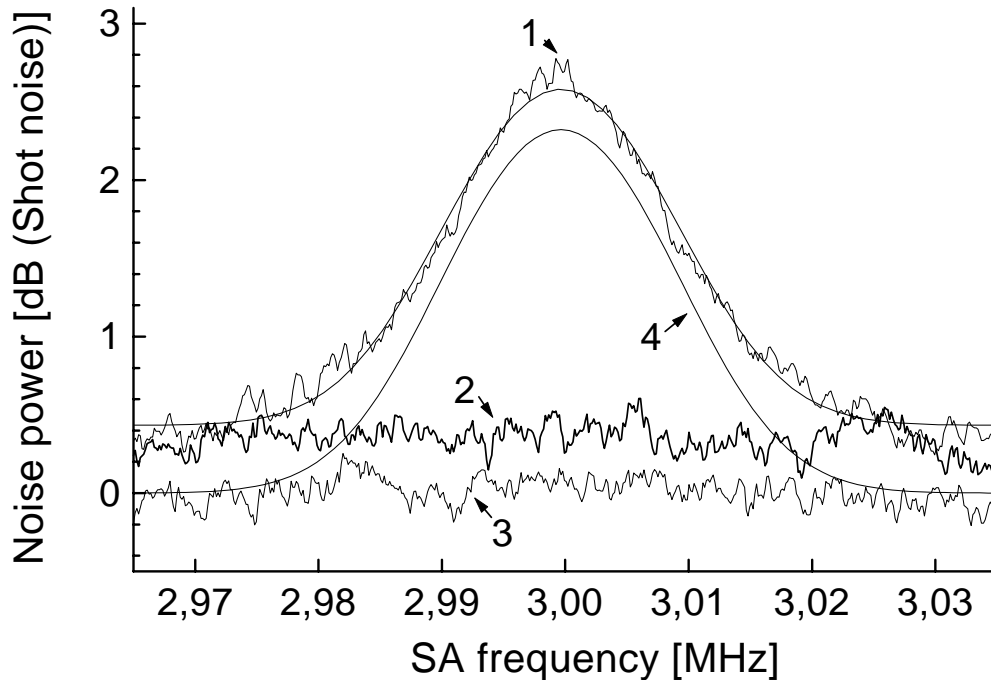


Figure 7.8: The recorded noise power in the spin noise limited experiment. Curve 1 shows the modulation signal limited by probe shot noise and spin noise. The line accompanying curve 1 is a best fit to a Gaussian. Curve 2 shows the level of spin noise and shot noise and curve 3 shows the level of shot noise. Curve 4 is the achieved signal in the absence of spin noise with the parameters obtained from the fit to curve 1.

spherical spin state and hence we expect  $k_q$  to be larger for the latter. The value of  $k_q^{ex} = 0.58$  has been used to generate the theoretical curves in fig. 7.5(b).

## 7.4 Being limited by the quantum spin noise

For the sake of demonstration we will now look at a simple experiment in which the sensitivity was limited by the quantum noise of the atomic spin. For this purpose we used the same setup as in fig. 7.2 but with the chopper and the electronics for lock-in detection removed. The spectrum analyzer span was changed from zero to 70 kHz and the noise power of the transmitted probe was observed in this range centered around 3 MHz. Now FM was applied to the trapping laser at the detection frequency and we wanted to observe the modulation transferred from this laser to the probe via the trapped atoms. This is similar to the experiments from chapter 6 but now with a much larger trap in which the atomic quantum noise played a bigger role. The modulation was so weak that the effect on the probe only was a peak 2 dB above the background noise as shown in figure 7.8 curve 1. The background noise level is shown in curve 2. This was detected by turning off the modulation and from our discussion in the last section we know that it was made up by quantum spin noise, probe shot noise and electronic noise. Like in the previous experiment the probe power in this experiment was about  $340 \mu\text{W}$ . This gave 5-6 dB of shot

noise above electronic noise and hence we disregard the latter in the rest of this discussion. To find the level of the shot noise only we blocked the trapping beams and reduced the probe power to compensate for the lack of absorption from the MOT. This level is shown as curve 3 in fig. 7.8. Comparing curves 2 and 3 we find the combined spin noise and shot noise to be located 0.35 dB above the shot noise level corresponding to the amount of spin noise being 8% of the shot noise. The line on top of curve 1 is a Gaussian fit to the modulation and the parameters from this fit was used to generate curve 4 which describes the modulation signal in the absence of spin noise, that is if we had perfect spin squeezing. Curve 1 is found to be peaked 2.23 dB above the noise floor comprised of shot noise and spin noise and the corresponding signal to noise ratio is 0.67. In comparison curve 4 peaks 2.32 dB above the shot noise floor yielding signal to noise ratio of 0.71. This shows that our quantum spin noise was indeed limiting the achieved signal to noise ratio in this simple experiment. Of course the limitation by spin noise could be avoided in this experiment by increasing the modulation index, but in other branches of physics such as the investigation of electroweak interactions in atoms[47] and ultrasensitive magnetometry[105] the quantum spin noise may well prove to become a limiting factor of the achievable sensitivity.

## 7.5 Summary

In this chapter we have seen how the stochastic process of atomic decay cause fundamental fluctuation of the atomic spin. Our simple theory for a V system with weak fields on the two transitions showed that it was in particular the coupling to the vacuum modes of the electromagnetic field that caused the spin fluctuations rather than the coupling to the pump fields. It turned out that in order to have the latter coupling dominating the spin noise, a single photon Rabi frequency on the order of the atomic decay rate is needed. Such strong coupling typically require the pump fields to be modes of a high Q cavity. Because our theory assumed an optically thin medium we were not able to show that the fluctuations of the atomic spin could indeed be reduced by absorbing quantum correlated fields completely in the atomic medium as it was shown in a recent publication[100]. Our argumentation led us to the fact that the quantum spin noise could be distinguished from the technical spin noise from the dependence on the number of spins,  $N$ . The quantum noise grows linear in  $N$ , whereas the technical noise grows quadratic.

By building a setup in which the probe noise was discriminated against the electronic noise of the detection system we demonstrated shot noise limited measurements with probe powers as small as a few hundred nanoWatts. This was crucial for the following spin noise measurements since our theory predicted spin noise on the order of a few percent of the shot noise at the optimum conditions. These were shown to be at an optical depth of 0.5, where the absolute spin noise was maximum, and with a somewhat saturating probe.

By comparing the DC absorption of the probe to the absorption at 3 MHz, we were able to detect the spin noise at the latter frequency. This was seen to follow the DC absorption profile indicating that it was indeed quantum noise. As a further test of the spin noise we locked the probe laser to the atomic resonance and varied the number of spins by attenuating the MOT repumping laser. After an appropriate normalization to the transmitted probe power, we found the Log-Log plot of spin noise versus the number of spins to be linear with a slope of  $1.07 \pm 0.03$  revealing that the main contribution to this noise was of quantum nature. By applying external FM to the trapping laser we were able to see the transition from the almost pure quantum spin noise to pure technical noise, manifested in a change of the slope in the Log-Log plots from almost 1 to 2 as the modulation depth was increased.

We also tested that the spin noise normalized to the probe shot noise was linear in the probe power and we found the experimental value of the parameter  $k_q$ , describing the strength of the spin noise relative to the probe shot noise, was within a factor 2 of our theoretically predicted value. The discrepancy was attributed to the spin state of the MOT, which was a spherical state rather than a coherent spin state as it was assumed in our theory.

Using the data taken with a squeezed probe in chapter 5, we showed by extrapolation that a gain in signal to noise by employing such squeezed probes only is possible if the probed medium is optically

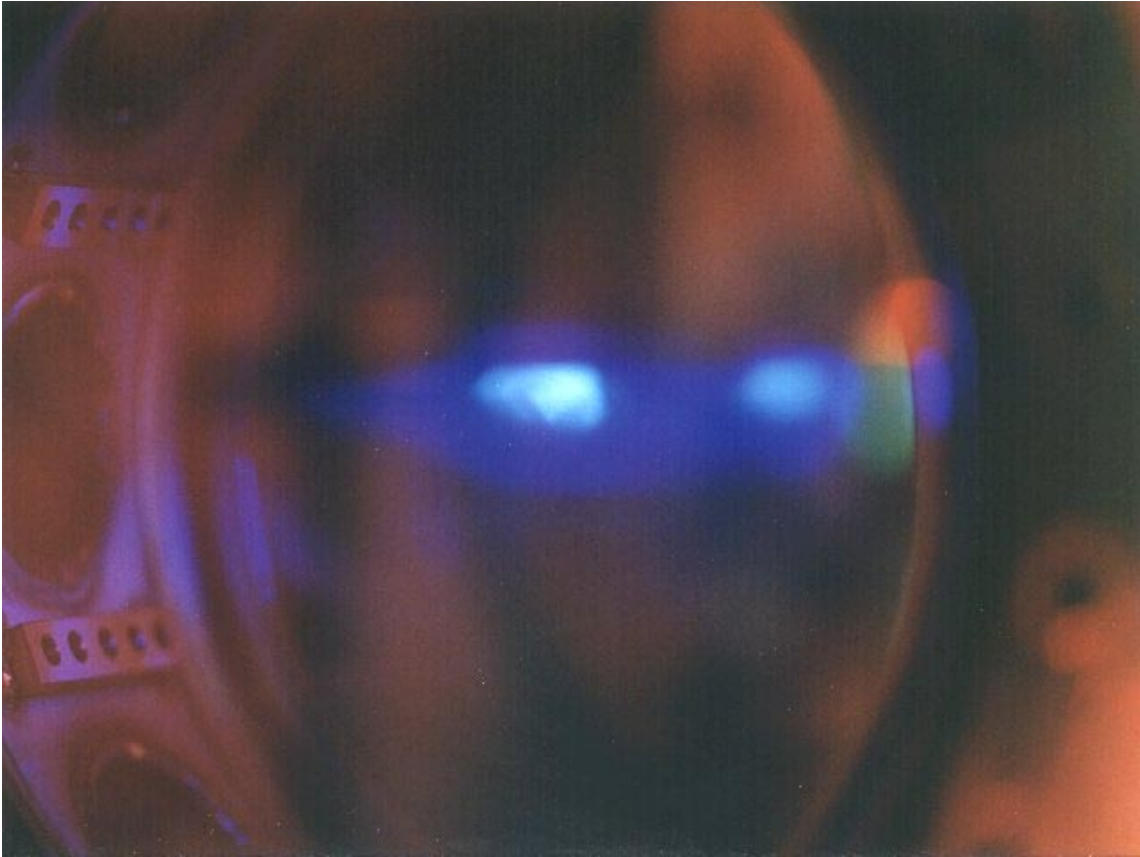


Figure 7.9: The trapped Caesium atoms probed by the polarization interferometer. The atoms were trapped on the 852 nm  $D_2$  line and probed on the 917 nm  $6P_{3/2} \rightarrow 6D_{5/2}$  transition. Here the absorption was around 80%. The density of atoms in the trap was a few times  $10^9$ . The cloud had a diameter around 7mm and the blueish glow was due to the decay of the  $6D_{5/2}$  excited state into the  $7P_{3/2}$  state, which decayed to the ground state emitting blue light at 456nm. The picture was taken with 10 minutes exposure and all the colors are real.

thin. In our setup the improvement in signal to noise due to squeezing would be lost at optical depths higher than 0.6. Improving the signal to noise in this region would instead require a pump field in a squeezed state to produce a squeezed spin state of the trapped atoms.

Finally we demonstrated an experiment in which the spin fluctuations of our trap accounted for a significant amount of the noise limiting the sensitivity. This noise may turn out to become limiting factor in future experiments as the techniques in experimental physics are refined and the sensitivity of the measurements improves.

This chapter concludes the series of experiments based upon the probing of our MOT by a polarization interferometer. In the next chapter it will be demonstrated how squeezed states of light can be used to test fundamental quantum mechanics as well as for the transfer of quantum information over macroscopic distances.

## Chapter 8

# Quantum Teleportation of Continuous Quantum Variables

In the early days of the quantum mechanics as we know it today (1935), Einstein, Podolsky and Rosen put forward the famous paradox, known today as the EPR paradox[106]. Here the nonlocality of quantum mechanics was disputed and the wavefunction description of the physical reality questioned. Later the same year Bohr explained the paradox using the complementarity principle of quantum mechanics, a principle which most people today take for granted[107]. The basic principle in transferring the quantum state of one particle onto another remote particle is exactly to exploit the nonlocality of quantum mechanics manifested in the form of two particles being in an entangled state[108]. This phenomenon is commonly called *Quantum Teleportation* inspired from the science fiction literature. The experimental realization of quantum teleportation is closely related to experiments carried out previously aimed at violating Bell's inequalities[109] and hence confirming quantum mechanics as a theory describing the physical reality[110]. Therefore the outcome of the experiment described below is twofold. A fundamental property of quantum mechanics, namely the nonlocality of the wavefunction, is demonstrated (again) and furthermore it is demonstrated how it is possible to transfer the quantum state of one physical system onto another system. From a more practical viewpoint quantum teleportation may be used in quantum computation for error correction protocols[111] or in optical communication for superdense coding of information[112]. The teleportation scheme presented in this chapter may also prove to provide a quantum cryptography line. Hence we see that quantum teleportation plays a central role in the relatively new, but rapidly growing, field of quantum information science.

The structure of this chapter is as follows. First the theory underlying quantum teleportation of discrete variables is touched briefly. This is helpful for the understanding of the teleportation of continuous variables. Then it is demonstrated how to produce the entangled fields, that are needed for the teleportation of continuous variables and a theoretical foundation of this kind of teleportation is laid. We will then move on to describe the experiment and present the setup, which is followed by a presentation and an interpretation of the results. Finally the chapter will be concluded with a summary of the achieved results together with a brief outlook on how to extend the experiment to cover other interesting aspects of quantum teleportation.

### 8.1 Basic principles in quantum teleportation

As indicated above we mean by quantum teleportation the mapping of the state of one quantum system to another quantum system. The possibility of this was discovered in 1993 by Bennett *et. al.*[113]. They presented a scheme in which two entangled spin 1/2 particles in a singlet state are used to teleport the spin state of a third spin 1/2 particle by means of a Bell measurement and a subsequent broadcasting

of the outcome to the site, where the quantum state is reconstructed. A fundamental principle in quantum mechanics usually referred to as the *No Cloning Theorem*[114] prohibits the copying of the quantum state. Consequently it must be demanded that any information about the initial quantum state of the third particle prior to the detection must be completely destroyed in the detection scheme. This is exactly what happens when the joint state of the teleported particle and one of the entangled particles is expanded on the complete set of Bell states. The authors, coming from the field of quantum communication, labelled the performer of the Bell measurement *Alice* and the receiver of the broadcast signal *Bob*. This nomenclature will be used in this work as well. As we shall see the teleportation scheme of continuous quantum variables is very similar to Bennett's scheme, which is why a brief description of the latter can be found in Appendix B for comparison and clarification.

The quantum teleportation of the polarization state of single photons has already been carried out experimentally[115][116]. Clearly the polarization state of the electromagnetic field is equivalent to a spin 1/2 system and in this fashion Bennett's scheme has already been implemented experimentally. However the two experiments carried out before the one presented here both suffered from extremely low efficiencies ( $\sim 10^{-8}$ ) and in order to complete the teleportation protocol, a certain postselection of the detected events was needed. As it will be seen below, our scheme provided real time, continuous wave quantum teleportation of the continuous quadrature phases of the electromagnetic field. We detected the teleported state only to verify the protocol and to quantify the quality of our scheme.

One year after Bennett's original proposal Vaidman[117] demonstrated the principles of teleporting continuous quantum variables. A recent proposal aimed at teleporting the quadrature phases of the electromagnetic field[118] took Vaidman's idea closer to an experimental implementation. The proposal was based on a Wigner function analysis, whereas the theory presented below will utilize Heisenberg operator picture. This approach tends to lend more insight into the underlying physics but makes it harder to distinguish between manifestly quantum and classical states.

The quadrature phases of the electromagnetic field, denoted  $q$  and  $p$  are analogues of the position and momentum for a quantum particle in a harmonic oscillator potential. Originally the EPR paradox was formulated exactly in terms of the position and momentum of two entangled particles, and hence the teleportation of quadrature phases was performed in the original spirit leading to the EPR paradox.

As a workhorse this teleportation scheme employs entangled quantum *fields* in contrast to the entangled particles used above. The first objective of this section is to demonstrate how to produce two beams of entangled optical fields.

### 8.1.1 Creating EPR correlated fields

In 1992 it was shown by Ou *et. al.*[119] how to produce two independently squeezed fields from the two entangled output fields of a nondegenerate OPO. This was done by splitting the orthogonally polarized twin beams on a polarizing beamsplitter oriented  $45^\circ$  relative to the two polarizations and observing the phase sensitive quantum noise of the two outgoing beams. In our experiment the entangled fields were produced by the time reversed process, namely by mixing two independent but phase coherent squeezed beams on a 50/50 beamsplitter with an appropriate phase difference.

The experiment described below employed a single OPO ring resonator being pumped in the two counterpropagating directions from the same source as shown in figure 8.1. Unfortunately intracavity backscattering always couples the two counterpropagating modes of a ring cavity, meaning that the two resulting squeezed beams were not exactly independent. This mode coupling will be taken into account in the following treatment.

The starting point of our calculation is the two counterpropagating squeezed fields  $a_\pm$  given by a linear transformation of the vacuum fields  $a_\pm^{(0)}$

$$a_\pm = \mu_\pm a_\pm^{(0)} + \nu_\pm a_\pm^{(0)\dagger} \quad (8.1)$$

where the vacuum fields obey standard boson commutation relations  $[a_i^{(0)}, a_j^{(0)\dagger}] = \delta_{ij}$  and the coefficients

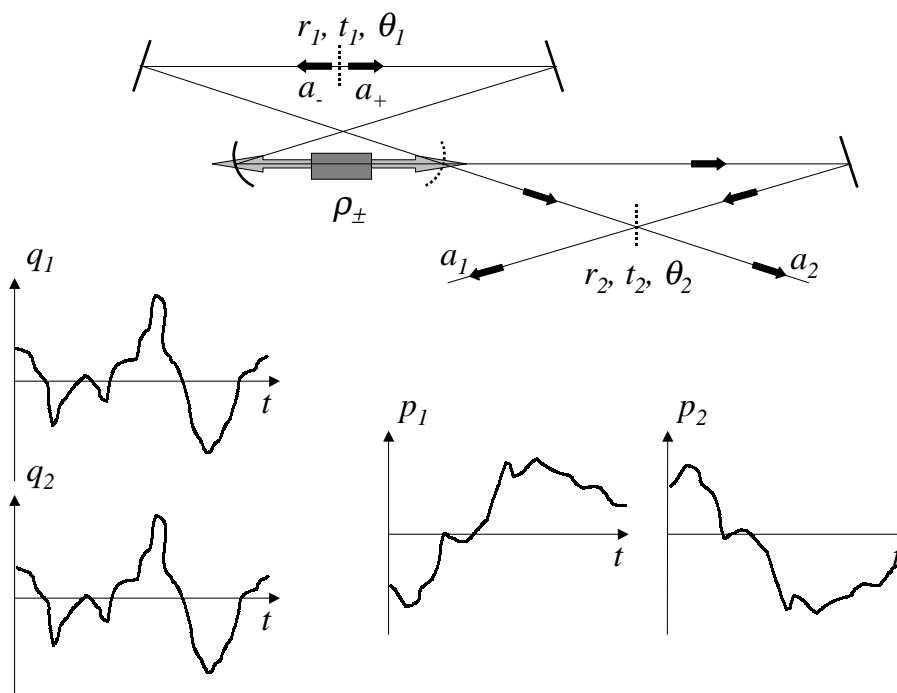


Figure 8.1: The entangled EPR beams created by pumping an OPO in two directions and mixing the resulting squeezed beams with  $\pi/2$  relative phase on a 50/50 beamsplitter. The outgoing fields are found to have correlated amplitudes and anticorrelated phase quadratures.

$\mu_{\pm}$  and  $\nu_{\pm}$  are given by

$$\mu_{\pm} = \cosh \rho_{\pm}, \quad \nu_{\pm} = \sinh \rho_{\pm} \quad (8.2)$$

The parameters  $\rho_{\pm}$  measure the strength of the nonlinear interaction in the two directions and they are assumed here to be real and positive. The OPO's are assumed to have negligible intracavity losses except for the output coupler transmission and the coupling between the two directions of propagation. Forming the quadrature phase operators  $q_{\pm} = a_{\pm} + a_{\pm}^{\dagger}$  and  $p_{\pm} = -i(a_{\pm} - a_{\pm}^{\dagger})$  we find

$$q_{\pm} = e^{\rho_{\pm}} q_{\pm}^{(0)}, \quad p_{\pm} = e^{-\rho_{\pm}} p_{\pm}^{(0)} \quad (8.3)$$

where  $q_{\pm}^{(0)}$  and  $p_{\pm}^{(0)}$  are the vacuum field quadratures.

The interbeam coupling is modelled here as a beamsplitter with nearly 100% transmission inside the OPO resonator. The beamsplitter is assumed to have reflectivity  $r_1$  and transmittivity  $t_1$  and relative optical phase between the two squeezed fields on this beamsplitter is denoted  $\theta_1$ . For a single scatterer being responsible for the coupling,  $\theta_1$  is simply a constant, but in the more general case of a distributed scatterer we have to keep in mind that  $\theta_1$  is an average over all the phases for the scatterers weighted with their individual reflectivities. The second beamsplitter, located outside the OPO resonator, is assumed to have reflectivity  $r_2$  and transmittivity  $t_2$ , both being close to  $2^{-1/2}$ , and the relative optical phase at this point is called  $\theta_2$ .

All in all we find the two fields emerging from the second beamsplitter  $a_1$  and  $a_2$  to be given by

$$\begin{pmatrix} a_1 \\ a_2 \end{pmatrix} = \begin{pmatrix} t_2 & -r_2 e^{i\theta_2} \\ r_2 & t_2 e^{i\theta_2} \end{pmatrix} \begin{pmatrix} t_1 & -r_1 e^{i\theta_1} \\ r_1 & t_1 e^{i\theta_1} \end{pmatrix} \begin{pmatrix} a_+ \\ a_- \end{pmatrix} \quad (8.4)$$

Introducing the quadrature phases for the outgoing fields in analogy to the squeezed fields and performing the algebra, we arrive at

$$\begin{pmatrix} q_1 \\ p_1 \\ q_2 \\ p_2 \end{pmatrix} = \begin{pmatrix} [t_1 t_2 - r_1 r_2 \cos \theta_2] & [r_1 r_2 \sin \theta_2] & [-r_1 t_2 \cos \theta_1 - r_2 t_1 \cos(\theta_1 + \theta_2)] \\ [-r_1 r_2 \sin \theta_2] & [t_1 t_2 - r_1 r_2 \cos \theta_2] & [-r_1 t_2 \sin \theta_1 - r_2 t_1 \sin(\theta_1 + \theta_2)] \\ [r_2 t_1 + r_1 t_2 \cos \theta_2] & [-r_1 t_2 \sin \theta_2] & [-r_1 r_2 \cos \theta_1 + t_1 t_2 \cos(\theta_1 + \theta_2)] \\ [r_1 t_2 \sin \theta_2] & [r_2 t_1 + r_1 t_2 \cos \theta_2] & [-r_1 r_2 \sin \theta_1 + t_1 t_2 \sin(\theta_1 + \theta_2)] \\ [r_1 t_2 \sin \theta_1 + r_2 t_1 \sin(\theta_1 + \theta_2)] & [-r_1 t_2 \cos \theta_1 - r_2 t_1 \cos(\theta_1 + \theta_2)] & \\ [r_1 r_2 \sin \theta_1 - t_1 t_2 \sin(\theta_1 + \theta_2)] & & \\ [-r_1 r_2 \cos \theta_1 + t_1 t_2 \cos(\theta_1 + \theta_2)] & & \end{pmatrix} \begin{pmatrix} q_+ \\ p_+ \\ q_- \\ p_- \end{pmatrix} \quad (8.5)$$

At a first glance this result looks rather complicated, but choosing first no interbeam coupling,  $r_1 = 0$ ,  $t_1 = 1$ , equation (8.5) simplifies to

$$\begin{pmatrix} q_1 \\ p_1 \\ q_2 \\ p_2 \end{pmatrix} = \begin{pmatrix} t_2 & 0 & -r_2 \cos \chi & r_2 \sin \chi \\ 0 & t_2 & -r_2 \sin \chi & -r_2 \cos \chi \\ r_2 & 0 & t_2 \cos \chi & -t_2 \sin \chi \\ 0 & r_2 & t_2 \sin \chi & t_2 \cos \chi \end{pmatrix} \begin{pmatrix} q_+ \\ p_+ \\ q_- \\ p_- \end{pmatrix} \quad (8.6)$$

where we have defined  $\chi = \theta_1 + \theta_2$ . By using that the vacuum fields are completely uncorrelated and normalizing to their noise level, we can now readily write up the cross correlation between the two outgoing fields as

$$\begin{aligned} \langle \delta(q_1 + q_2)^2 \rangle &= (t_2 + r_2)^2 e^{2\rho_+} + (t_2 - r_2)^2 (e^{2\rho_-} \cos^2 \chi + e^{-2\rho_-} \sin^2 \chi) \\ \langle \delta(q_1 - q_2)^2 \rangle &= (t_2 - r_2)^2 e^{2\rho_+} + (t_2 + r_2)^2 (e^{2\rho_-} \cos^2 \chi + e^{-2\rho_-} \sin^2 \chi) \\ \langle \delta(p_1 + p_2)^2 \rangle &= (t_2 + r_2)^2 e^{-2\rho_+} + (t_2 - r_2)^2 (e^{2\rho_-} \sin^2 \chi + e^{-2\rho_-} \cos^2 \chi) \\ \langle \delta(p_1 - p_2)^2 \rangle &= (t_2 - r_2)^2 e^{-2\rho_+} + (t_2 + r_2)^2 (e^{2\rho_-} \sin^2 \chi + e^{-2\rho_-} \cos^2 \chi) \end{aligned} \quad (8.7)$$

From (8.7) it can be seen that choosing the relative phase of the two beams to be  $\chi = \pi/2$ , results in two entangled outgoing fields. These will have the amplitudes, which are correlated, since  $\delta(q_1 - q_2)^2$  is smaller than the standard quantum limit (SQL) when  $r_2 \simeq t_2 \simeq 2^{-1/2}$ . The SQL in this case is 2 units of vacuum noise, because we are considering the cross correlations between two originally independent fields. Furthermore we find the phases to be anticorrelated because  $\delta(p_1 + p_2)^2$  possess reduced fluctuation with respect to the SQL. This is illustrated in figure 8.1.

If we now turn to look at the noise of a single beam emerging from the second beamsplitter, we find, when putting  $t_2 = r_2 = 2^{-1/2}$  and  $\rho_+ = \rho_- = \rho$ , the variances to be

$$\begin{aligned} \langle \delta q_1^2 \rangle &= \langle \delta q_2^2 \rangle = \frac{1}{2} [e^{2\rho} (1 + \cos^2 \chi) + e^{-2\rho} \sin^2 \chi] \\ \langle \delta p_1^2 \rangle &= \langle \delta p_2^2 \rangle = \frac{1}{2} [e^{-2\rho} (1 + \cos^2 \chi) + e^{2\rho} \sin^2 \chi] \end{aligned} \quad (8.8)$$

When  $\chi = 0$  we find the phase sensitive noise associated with the squeezed states, where the  $q$  quadratures are antisqueezed and the  $p$  quadratures are squeezed. That is, if we overlap two squeezed beams in phase on a 50/50 beamsplitter, we just produce two new squeezed fields. However when  $\chi = \pi/2$  we find that the resulting entangled state possess no phase sensitive noise and that all quadratures has the variance given by  $\cosh 2\rho$ , which is roughly 50% of the noise level in the antisqueezed quadratures, obtained with  $\chi = 0$ .

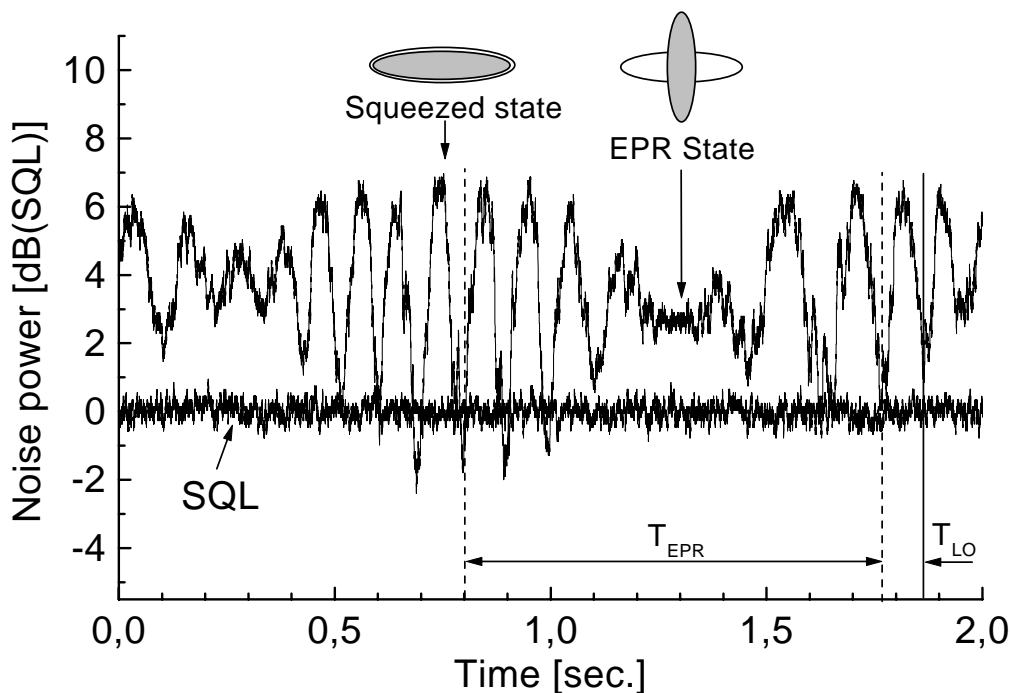


Figure 8.2: Quantum noise of a single EPR beam. The local oscillator phase is scanned at about 10 Hz ( $T_{LO}$ ) and the relative phase between the squeezed fields is scanned at about 1 Hz ( $T_{EPR}$ ) rate. As the two squeezed fields are in phase we observe the characteristic phase sensitive noise for a squeezed phase, whereas when the squeezed fields are in quadrature we observe the phase insensitive noise of the EPR state. SQL marks the single beam shot noise level.

Being now a bit more realistic by taking into account the interbeam coupling, we define  $r_1^2 = \varepsilon$ , so that  $t_1^2 = 1 - \varepsilon$  ( $\varepsilon \ll 1$ ). Furthermore we take again  $t_2 = r_2 = 2^{-1/2}$  and  $\rho_+ = \rho_- = \rho$ , and focus only on the entangled state meaning that  $\chi = \theta_1 + \theta_2 = \pi/2$ . With these parameters we find the cross correlation to be given by

$$\begin{aligned} \left\langle \delta(q_1 + q_2)^2 \right\rangle &= \left\langle \delta(p_1 - p_2)^2 \right\rangle = 2 \left[ (1 - \varepsilon)e^{2\rho} + \varepsilon(\cos^2 \theta_1 e^{2\rho} + \sin^2 \theta_1 e^{-2\rho}) \right] \\ \left\langle \delta(q_1 - q_2)^2 \right\rangle &= \left\langle \delta(p_1 + p_2)^2 \right\rangle = 2 \left[ (1 - \varepsilon)e^{-2\rho} + \varepsilon(\sin^2 \theta_1 e^{2\rho} + \cos^2 \theta_1 e^{-2\rho}) \right] \end{aligned} \quad (8.9)$$

In general we cannot tell much about the scattering phase  $\theta_1$ , but for a uniform scatterer distributed over several optical wavelengths, we can average over the cavity length,  $z$ , to obtain  $\langle \sin^2 \theta_1 \rangle_z = \langle \cos^2 \theta_1 \rangle_z = 1/2$ . If we furthermore insert a realistic value of  $\varepsilon = 0.01$ , and cheat a bit to take into account a real OPO with internal losses. For such a device the product of the squeezing and antisqueezing does not amount to the SQL as indicated throughout this section. Rather it tends to give a larger number than the SQL. To correct for this we use that the  $q$  and  $p$  quadratures are independent degrees of freedom for the electromagnetic field, so that our results above contain no mixed terms of cross correlation between different quadratures. This justifies that we can put  $\langle \delta q_+^2 \rangle \neq (\langle \delta p_+^2 \rangle)^{-1}$  corresponding to having an OPO escape efficiency smaller than 100%. Realistic values for the OPO's used to produce

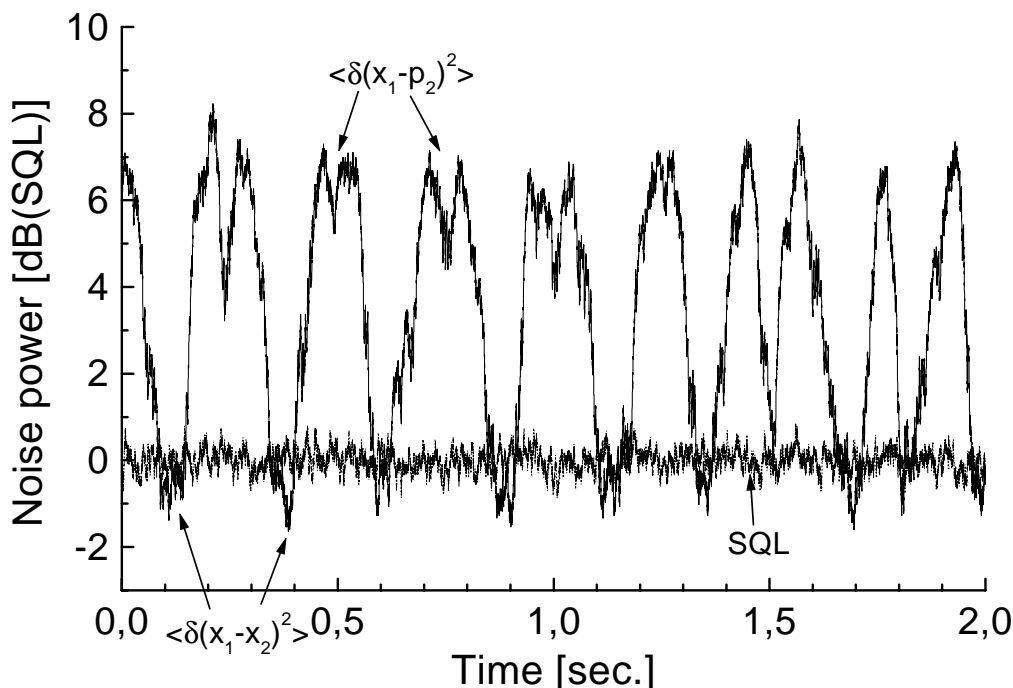


Figure 8.3: The interbeam correlations observed with two balanced homodyne detectors. One detector was measuring  $q_1$  whereas the other was scanned continuously between measuring  $q_2$  and  $p_2$ . The relative squeezing phase was locked to be  $\pi/2$ . The photocurrents from the two detectors were subtracted and analyzed in a RF spectrum analyzer. SQL for this measurement was 2 units of vacuum noise.

the results in this section are  $e^{2\rho} = 5$  and  $e^{-2\rho} = 0.6$ . Inserting our numbers in (8.9), we find the cross correlations to be  $\langle \delta(q_1 - q_2)^2 \rangle = \langle \delta(p_1 + p_2)^2 \rangle = 1.2$  and  $\langle \delta(q_1 + q_2)^2 \rangle = \langle \delta(p_1 - p_2)^2 \rangle = 10$ . This corresponds to -2 dB and +7 dB relative to the SQL respectively.

We will now compare our theory to the experimental results from the characterization of our EPR entangled state. First we simply set up a balanced homodyne detector to analyze the phase sensitive noise of a single beam. In this run the local oscillator phase of the detector was scanned fast (about 10 Hz), while the phase  $\theta_2$  was scanned slowly with about 1 Hz. The observed noise as a result of this procedure is shown in figure 8.2. In this trace we observe the phase sensitive noise associated with the squeezed state, obtained when the two squeezed field were combined in phase. This corresponds to times between 0.5 and 1 seconds. The trace shows only moderate squeezing of about -1 dB and a modest OPO gain of 4-5. Between 1.2 and 1.4 seconds the two squeezed fields are seen to have moved into quadrature and as a result we see no phase sensitive noise. This is the indication of the entangled field state. The phase insensitive noise level is found to be about 3 dB below the noise level of the antisqueezed quadrature. This corresponds to the level set by  $\cosh 2\rho$ , derived above, which is about 50% of the noise level of  $e^{2\rho}$  associated with the antisqueezed quadrature. The SQL noise level in this trace, was obtained as the single beam shot noise, hence it was one unit of vacuum noise.

Of course figure 8.2 reveals no information about the actual degree of the interbeam correlations. In order to measure these, we put up a balanced homodyne detector in each beam and locked the optical

phase between the squeezed fields to keep them in quadrature. One of the local oscillators was then locked to be in phase with the EPR beam, meaning that the noise of the quadrature phase  $q_1$  was measured. The other LO phase was scanned and the two differential photocurrents coming from the homodyne detectors were subtracted and analyzed in a RF spectrum analyzer. As a result of this procedure we went from measuring  $\langle \delta(q_1 - q_2)^2 \rangle$  to  $\langle \delta(q_1 - p_2)^2 \rangle$  depending on the phase of the scanned LO. In the first case our theory tells us that we should observe the noise level -2 dB below the SQL. The latter was obtained by blocking the OPO pump. In the last case we easily find from (8.6) that the noise level is  $2 \cosh 2\rho$ , corresponding to about 7 dB above the SQL according to the estimates above.

The observed trace is shown in figure 8.3. First it should be noted that the SQL of this measurement was two units of vacuum noise as opposed to the single unit of vacuum for the results in fig. 8.2. As the LO phase of our second homodyne detector was scanned, we observed first the 7 dB of excess noise relative to the SQL corresponding to the measurement of the noisy quantity  $\langle \delta(q_1 - p_2)^2 \rangle$ . This was followed by a drop in the noise to about -1 dB below the SQL corresponding to the measurement of  $\langle \delta(q_1 - q_2)^2 \rangle$ . Clearly the interbeam entanglement helped to reduce the relative amplitude fluctuations in the two beams below the standard quantum limit, where the latter is set by the correlations between two independent coherent states. All in all we find a reasonable agreement between the measured degree of correlations and the predictions from our theory. The observed -1 dB corresponds to a noise of 1.59 units of vacuum noise. In comparison our theoretical prediction of -2 dB corresponds to 1.26 units of vacuum. The deviation of 26% could easily be attributed to our crude estimate of the average scattering phase,  $\theta_1$ , inside the OPO.

After this intermezzo on how to produce the entanglement needed for our teleportation experiment, we will now address the theory behind the teleportation of continuous variables.

### 8.1.2 Teleportation of continuous variables

In analogy to the teleportation of discrete variables it is necessary in our scheme to erase all information about the input quantum state to be teleported. In practice this was done by mixing the latter on a 50/50 beamsplitter with one of our entangled beams described in the last section. Assuming that our input quantum state is described by the field operator  $\psi$ , we find the two fields emerging from the 50/50 beamsplitter,  $a_3$  and  $a_4$ , to be given by

$$\begin{aligned} a_3 &= 2^{-1/2} (a_1 - \psi) \\ a_4 &= 2^{-1/2} (a_1 + \psi) \end{aligned} \quad (8.10)$$

where the quadratures of  $a_1$  can be found from (8.6) putting  $\chi = \pi/2$ . It can be shown that Alice's Bell measurement in the case of continuous variables is made by measuring the amplitude quadrature,  $q_3$ , of one beam and the phase quadrature,  $p_4$ , of the other beam. Depending on the outcome of these two measurements, phase space displacements of certain amplitudes are required on the second entangled field,  $a_2$ . In ref. [118] this is done by a so called actuator, which in reality is nothing but an almost perfectly reflecting mirror (99%). By transmitting a coherent state through this mirror and controlling its amplitude and phase according to the method prescribed below, it is possible for Bob to displace the Wigner function describing  $a_2$  in phase space. The teleportation scheme is shown in fig. 8.4.

In order to detect the quadratures, it is ideal to use balanced homodyne detectors. The finite detection efficiency of these devices can be modelled by a weakly reflecting mirror with reflectivity  $\eta$  in front of each detector. The role of this mirror is to mix vacuum noise into the detected signals. The photocurrents from the detectors will then be given by

$$\begin{aligned} i_q &= \eta q_3 + \sqrt{1 - \eta^2} q_3^{(0)} \\ i_p &= \eta p_4 + \sqrt{1 - \eta^2} p_4^{(0)} \end{aligned} \quad (8.11)$$

where  $i_q$  and  $i_p$  are the photocurrents from the detectors measuring  $q_3$  and  $p_4$  respectively, and  $q_3^{(0)}$  and  $p_4^{(0)}$  are vacuum field quadratures.

The amplitude of the displacement beam is now being controlled by  $i_q$  and its phase is controlled by  $i_p$ . The size of the phase space displacements of the field  $a_2$  is assumed to be proportional to the photocurrents, and strength of the feedback is controlled by the gains  $g_q$  and  $g_p$ . As a result the output state,  $\zeta$ , will have the quadratures

$$\begin{aligned} q_\zeta &= q_2 + g_q i_q \\ p_\zeta &= p_2 + g_p i_p \end{aligned} \quad (8.12)$$

By combining (8.10), (8.11) and (8.12) we end up with following quadratures of the output state

$$\begin{aligned} q_\zeta &= 2^{-1/2} \left[ -g_q \eta q_\psi + \left( 1 + \frac{g_q \eta}{\sqrt{2}} \right) q_+ - \left( 1 - \frac{g_q \eta}{\sqrt{2}} \right) p_- \right] + g_q \sqrt{1 - \eta^2} q_3^{(0)} \\ p_\zeta &= 2^{-1/2} \left[ g_p \eta p_\psi + \left( 1 + \frac{g_p \eta}{\sqrt{2}} \right) p_+ + \left( 1 - \frac{g_p \eta}{\sqrt{2}} \right) q_- \right] + g_p \sqrt{1 - \eta^2} p_4^{(0)} \end{aligned} \quad (8.13)$$

Here  $q_\psi$  and  $p_\psi$  are the quadratures of the input state and the squeezed field quadratures  $q_\pm$  and  $p_\pm$  are given by (8.3). From (8.13) it is clear that in order to have good teleportation of  $\psi$  to  $\zeta$ , the detection efficiency must be nearly 100% and the feedback gains  $g_q$  and  $g_p$  must be adjusted to be

$$g_p = -g_q = \frac{\sqrt{2}}{\eta} \quad (8.14)$$

Furthermore we need good squeezing from our OPO's, so that only a small amount energy is present in the  $p_\pm$  quadratures. The opposite polarity of the feedback from the two measurements is needed because the quadratures  $p_1$  and  $p_2$  are *anticorrelated* in contrast to the correlated  $q_1$  and  $q_2$  quadratures.

Since we in our experiment detected the noise of the teleported state, we find this in units of the vacuum state noise to be given by

$$\begin{aligned} \langle \delta q_\zeta^2 \rangle &= \langle \delta q_\psi^2 \rangle + 2e^{-2\rho_-} + 2\frac{1-\eta^2}{\eta^2} \\ \langle \delta p_\zeta^2 \rangle &= \langle \delta p_\psi^2 \rangle + 2e^{-2\rho_+} + 2\frac{1-\eta^2}{\eta^2} \end{aligned} \quad (8.15)$$

where the optimized feedback gain (8.14) have been used. It is clear that the noise of the output state will match the noise of the input state in the limit of perfect squeezing ( $\rho_\pm \rightarrow \infty$ ) and perfect detection efficiency ( $\eta \rightarrow 1$ ). In order to distinguish between quantum and classical teleportation, we find from (8.15) the best performance in classical teleportation by putting  $\rho_\pm = 0$

$$\begin{aligned} \langle \delta q_\zeta^2 \rangle_{Class} &= \langle \delta q_\psi^2 \rangle + \frac{2}{\eta^2} \\ \langle \delta p_\zeta^2 \rangle_{Class} &= \langle \delta p_\psi^2 \rangle + \frac{2}{\eta^2} \end{aligned} \quad (8.16)$$

That is, the best classical teleportation is obtained when  $\eta = 1$ , in which case the output state is given by the input state plus two units of vacuum. The extra vacuum is the price one has to pay when being restricted only to use classical states of light. One unit of vacuum comes from the simultaneous measurement of the noncommuting quadratures  $q_\psi$  and  $p_\psi$  on Alice's homodyne detectors. The other unit of vacuum comes from the actuator, where the vacuum field  $a_2$  is assigned a coherent amplitude. In other words, every time we cross the border from our quantum fields to the classical currents we have to pay the price of one unit of vacuum. The extra vacuum noise added classically is called the *Quantum Duty* or *QuDuty* in the literature[118]. Crossing the border set by the quduty, for instance by using entangled states like in this experiment, opens up for possibilities like dense coding of information[112] and quantum cryptography. Along this line, we will in this thesis, consider the signature of quantum teleportation to be teleportation with a performance better than the quduty in the case of ideal classical teleportation ( $\eta = 1$ ).

In order to be able to quantify the quality of our teleportation we introduce an independent observer, *Victor*, in our scheme. His role is to provide the input state to be teleported and compare the teleported

state to the input state. For this purpose Victor has another homodyne detector with which he can measure the variances of  $q_\zeta$  and  $p_\zeta$ . In the experiment we used a coherent state as the input state, and in general the output state, in the case of nonperfect teleportation, is a statistical mixture of coherent states. As a measure of the quality of the teleportation we now introduce the fidelity  $\mathcal{F} = \left| \langle \psi^\dagger \zeta \rangle \right|^2$ , which for a coherent state input is found to be

$$\mathcal{F} = \frac{2}{\sqrt{(\langle \delta q_\zeta^2 \rangle + 1)(\langle \delta p_\zeta^2 \rangle + 1)}} \exp \left[ -2 \frac{|\langle \zeta \rangle - \langle \psi \rangle|^2}{\sqrt{(\langle \delta q_\zeta^2 \rangle + 1)(\langle \delta p_\zeta^2 \rangle + 1)}} \right] \quad (8.17)$$

Clearly the fidelity is 1 if the output state is a coherent state with amplitude  $\langle \zeta \rangle = \langle \psi \rangle$  and variances  $\langle \delta q_\zeta^2 \rangle = \langle \delta q_\psi^2 \rangle = 1$ ,  $\langle \delta p_\zeta^2 \rangle = \langle \delta p_\psi^2 \rangle = 1$ , corresponding to perfect teleportation of the input state. Classically ( $\rho_\pm = 0$ ) the quantum limits the fidelity to  $\mathcal{F}_{Class}^{Theo} \leq 0.5$ , since the best teleportation is seen from (8.16) and (8.13) to be achieved with  $\eta = 1$  and  $g_p = -g_q = \sqrt{2}/\eta$ . These values yield the variances  $\langle \delta q_\zeta^2 \rangle_{Class} = \langle \delta p_\zeta^2 \rangle_{Class} = 3$  and the amplitude  $\langle \zeta \rangle = \langle \psi \rangle$ , which inserted in (8.17) gives  $\mathcal{F}_{Class}^{Theo} = 0.5$ . Detection efficiencies smaller than 1 would only increase the variances and hence reduce the fidelity below 0.5.

If we take into account the efficiencies,  $\xi_1$  and  $\xi_2$  with which the amplitudes of the two entangled fields are propagating and detected, we find that Victor observes the following variances on his homodyne detector

$$\langle \delta q_\zeta^2 \rangle = \langle \delta p_\zeta^2 \rangle = g^2 + \frac{1}{2} e^{-2\rho} (\xi_2 + g\xi_1)^2 + \frac{1}{2} e^{2\rho} (\xi_2 - g\xi_1)^2 + (1 - \xi_1^2) g^2 + (1 - \xi_2^2) + 2g^2 \frac{1 - \eta^2}{\eta^2} \quad (8.18)$$

Here we have assumed that the two OPO's has the same gain ( $\rho_+ = \rho_- = \rho$ ) and the normalized feedback gain,  $g$ , is measured in units of the optimum  $\sqrt{2}/\eta$ . In (8.18) it has been used explicitly that the polarity of  $g_q$  is opposite to the polarity of  $g_p$ . This equation is important since it enables us to calculate the fidelity, observed by Victor, as function of the feedback gain in the classical channel between Alice and Bob. Hence if we know the efficiencies  $\xi_1$ ,  $\xi_2$  and  $\eta$  together with the parametric gains, we can predict the fidelity of teleportation as  $g$  is varied.

To conclude this section let us compare the teleportation of discrete variables to teleportation of continuous variables. The main difference between the two schemes is, that the discrete teleportation work in a 8 dimensional Hilbert space, whereas the continuous teleportation span an infinite dimensional Hilbert space. As a result of the different number of degrees of freedom, the discrete teleportation employ single pairs of entangled particles where the continuous scheme use entangled fields made up by many particles. Moreover the finite set of unitary transformations needed in the discrete case has to be generalized to a continuum of linear transformations (displacements) in the continuous case. Finally from a practical viewpoint it is difficult to detect single photons with a high efficiency and good signal to noise. This is required in order to perform the discrete teleportation reliably. The continuous teleportation work with standard photodiodes, which can have virtually 100% efficiency. As a result the continuous teleportation holds the potential of becoming very efficient, which is not the case for the discrete teleportation with the current technology.

With the basic principles of quantum teleportation at hand, and having characterized the entangled beams driving our scheme, we now turn towards the actual experiment, which was carried out at California Institute of Technology via the joint effort of the Quantum Optics Group of Professor H. J. Kimble and the Experimental Quantum Optics Group in Aarhus.

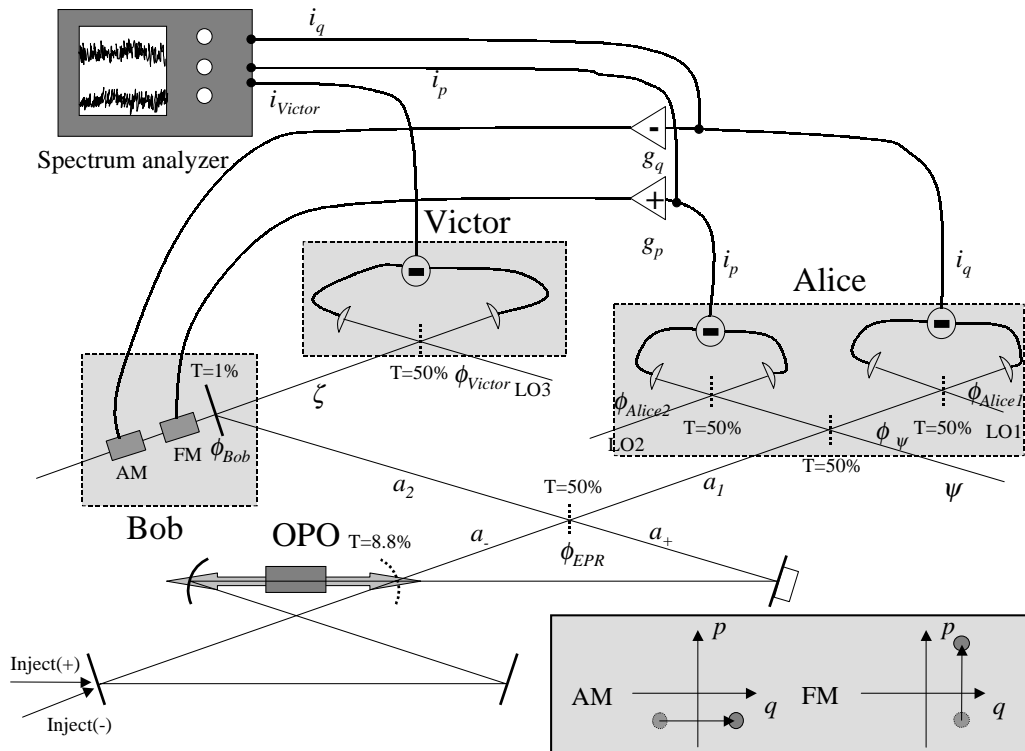


Figure 8.4: The detailed experimental setup used in the teleportation of continuous variables. The OPO is producing two squeezed beams, which are overlapped with the phase  $\phi_{EPR}$  to produce the EPR entangled beams  $a_1$  and  $a_2$ . One of these is used to read out the input state  $\psi$  at Alice, and the other is displaced in phase space by Bob to produce the output state  $\zeta$ . Victor serves the purpose of characterizing the teleported state  $\zeta$ , to verify the teleportation.

## 8.2 Experimental setup

The workhorse of the whole experiment was a homebuilt single frequency Ti:Sapphire laser operating around 860 nm. This laser provided about 1.5 Watts of which 80% was used for second harmonic generation to produce the pump for the two OPO's. The doubling efficiency was typically higher than 40% which gave more than 450 mW output of our doubling cavity. Due to propagation losses and coupling efficiencies into the OPO's only about 150 mW net power was available for each OPO.

As mentioned earlier the two OPO's shared the same optical resonator and the same nonlinear crystal. They were simply obtained by pumping a nonlinear ring resonator in both directions to provide parametric gain for the two counterpropagating modes. The OPO output coupler transmission was  $(8.8 \pm 0.3)\%$  and the  $\text{KNbO}_3$  crystal nonlinearity was  $(1.8 \pm 0.2) \%W^{-1}$ . Passive losses in the OPO resonator were measured to be 0.5% and the coupling between the forward and the backward propagating modes was measured to be about 1%. The 430 nm pump beams were both modematched to the OPO with  $(90 \pm 3)\%$  efficiency and with 150 mW in each beam, a parametric gain of  $5 \pm 1$  was observed in both directions of the resonator. When the resonator was pumped in both directions simultaneously the increased BLIIRA in the  $\text{KNbO}_3$  crystal caused the squeezing to degrade and it was observed that the best squeezing of about -3 dB was obtained with a parametric gain of  $2.0 \pm 0.2$ . Clearly a better performance could have been obtained by pumping two separate nonlinear resonators, since only half

the pump power would be needed to achieve the appropriate gain and hence the BLIIRA could have been reduced. However the construction and assembly of a high performance subthreshold OPO is not a trivial task, and due to time constraints the double OPO was preferred in this experiment. In order to achieve high gain, the OPO resonator was locked to the laser frequency by injecting a weak coherent field in the TEM<sub>00</sub> mode. This field was frequency modulated using an electro optical modulator (EOM), and an errorsignal was derived using a standard RF technique. With the goal of locking several optical phases later in the experiment, we had to inject weak TEM<sub>00</sub> fields into the two counterpropagating modes of the OPO anyway. These fields, denoted  $Inject(\pm)$  in figure 8.4, were locked to be in phase with the squeezed vacuum produced in the OPO's by optimizing their parametric gain using standard lock-in techniques.

By observing the DC interference fringe between  $Inject(\pm)$  after the first 50/50 beamsplitter in fig 8.4, it was possible to stabilize the relative phase between the two squeezed fields ( $\phi_{EPR}$ ) to be  $\pi/2$  and hence produce the EPR state needed for the teleportation. In order to lock the local oscillator (LO) phases  $\phi_{Alice1}$ ,  $\phi_{Alice2}$  and  $\phi_{Victor}$  (indicated on the figure) FM sidebands were added to the fields  $Inject(+)$  and  $Inject(-)$  at frequencies 5 and 7 MHz respectively. With the two squeezed beams locked in quadrature, the amplitude and phase quadratures of the resulting entangled beams could be detected by locking to the side of the RF fringes 5 and 7 MHz respectively. These fringes were generated as a result of the interference between the LO's and the combined fields injected into the OPO and transmitted through the setup. In this way the homodyne detector *Alice1* was locked to measure the  $q_3$  quadrature, meaning that  $\phi_{Alice1} = 0$ . Similarly we achieved  $\phi_{Alice2} = \pi/2$  to measure  $p_4$  and  $\phi_{Victor}$  could be either 0 or  $\pi/2$  depending on which quadrature of the teleported state, Victor wanted to examine. Finally the coherent beam, controlled by Bob, had to be phase locked to the field  $a_2$  in order to produce well defined linear transformations, for this lock we again made use of the RF interference fringe at 5 MHz between Bob's beam and the modulated injected fields. From this fringe  $\phi_{Bob}$  was locked to be 0, meaning that the carrier was in phase with  $a_2$ . When the entire experiment was running, a total of 9 servolocks were in use.

In order to observe quantum noise limited optical fields, we chose to teleport only a single RF sideband of the input state, instead of the full spectrum of the state. As a result the low frequency technical noise, present in any laser, did not play a role in this experiment, and furthermore the phase space displacements turned out to become very simple to perform. By considering only Fourier components of the wavefunctions in a narrow band around the teleportation frequency, we can define the phase space for these components. In this space the role of amplitude modulation (AM) would be displacements along the horizontal ( $q$ ) axis, whereas frequency modulation (FM) would cause displacements along the vertical ( $p$ ) axis. This is illustrated in the insert of fig. 8.4. All of this required of course that the carrier was phase locked to the entangled beam  $a_2$ , and hence we see the importance of locking  $\phi_{Bob}$ .

To ensure a high teleportation efficiency all fields were required to be in the same spatial mode, and hence a high fringe visibility on the 50/50 beamsplitters was needed. In this experiment the fringe visibilities as a result of the interference between the LO's and the input state,  $\psi$ , on the *Alice1* and *Alice2* beamsplitters were both  $0.97 \pm 0.02$ . The entangled fields were interfered with a visibility of  $0.94 \pm 0.04$  with Alice's LO's and the input state. On Victor's 50/50 beamsplitter we had a visibility of  $0.97 \pm 0.02$  between Bob's carrier of modulation and the LO, whereas the entangled field only interfered with the visibility  $0.94 \pm 0.04$  with the LO. Our entangled fields were characterized by  $e^{-2\rho} = 0.5 \pm 0.1$  and  $e^{2\rho} = 2.0 \pm 0.2$ .

### 8.3 Teleportation results

In order to calibrate the feedback gain, the input state  $\psi$  was subjected to FM by means of an EOM. As the phase of the input beam was scanned, the phase sensitive classical noise could be monitored in the photocurrent  $i_q$ . At the same time the teleported classical noise in the same quadrature ( $q_c$ ) was measured by Victor's detector, and the gains could be adjusted so that Victor observed 3 dB more

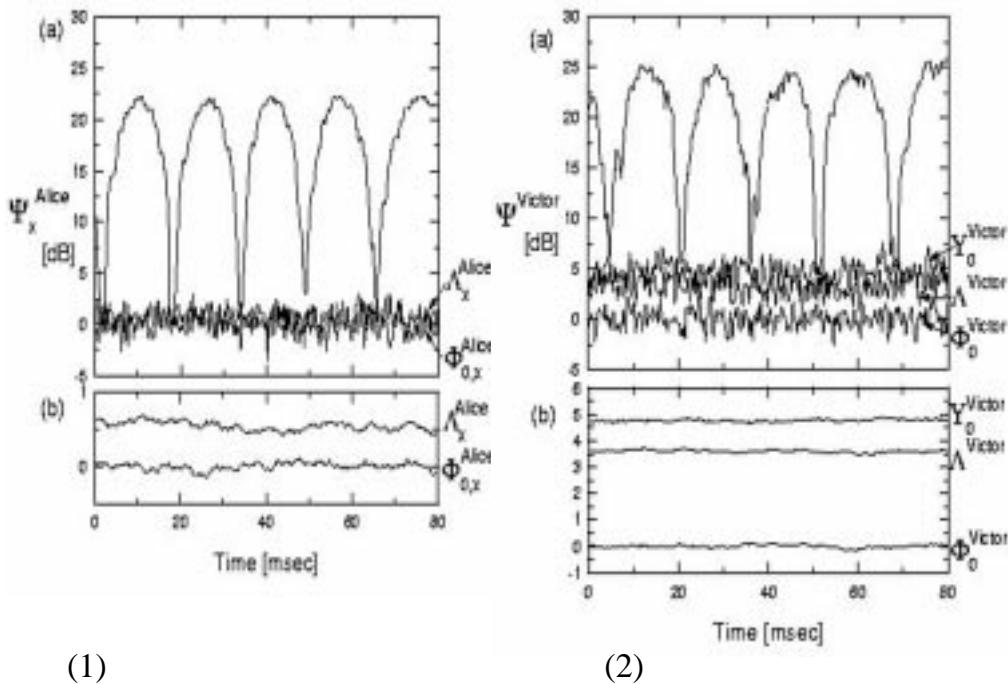


Figure 8.5: (1a) The noise observed in the photocurrent of *Alice1*. The upper curve is with FM sidebands added to the input state.  $\Lambda_x^{Alice}$  is the increased noise seen by Alice as quantum teleportation takes place and  $\Phi_{0,x}^{Alice}$  marks the vacuum noise level. (1b) is the expanded view of the last two levels taken with smaller video bandwidth. (2a) The noise of the the teleported state as observed by Victor. The upper trace is the teleported FM sidebands as the phase of the input state is scanned.  $Y_0^{Victor}$  is the classical noise level 4.8 dB above the vacuum level,  $\Phi_0^{Victor}$ , as a result of the quduty and  $\Lambda^{Victor}$  is the noise observed as quantum teleportation takes place. (2b) shows the expanded view of the last 3 traces. Spectrum analyzer settings: Center frequency 2.9 MHz, resolution bandwidth 30 kHz and video bandwidth 1 kHz in (a) figures and 30 Hz in (b) figures.

classical noise relative to the vacuum level than *Alice1*. It should be remembered that the classical noise on the input state was splitted off to *Alice1* and *Alice2* in equal amounts, hence the difference of 3 dB in the noise levels. Furthermore it was checked that the phase of the teleported classical noise was identical to the phase of the input state by comparing the variances of  $q_3$  and  $q_\zeta$  in real time and observing that they were in phase, as the phase of  $\psi$  was scanned linearly. Finally it was observed that the variances of  $p_4$  (from *Alice2*) and  $q_\zeta$  were in quadrature as they should be. The phase sensitive noise observed by *Alice1* is shown as the upper trace on figure 8.5(1a) and Victor's observation is shown as the upper trace on fig. 8.5(2a). Here the noise power,  $\Psi$ , is displayed as a function of the phase of the input state  $\phi_\psi$ .  $\Phi_0$  marks the vacuum noise levels. Throughout this series of measurements shown on fig. 8.5(2), the phase of Victor's LO was locked to be in phase with the field  $\zeta$ , meaning that  $q_\zeta$  was observed. It was however checked that the phase sensitive noise shifted  $\pi/2$  when  $p_\zeta$  was measured.

So far the entangled beams had been replaced with vacuum, and as a result we were in the classical limit. Hence we see from (8.16) that the quduty should cause the teleported state to contain about three units of vacuum noise with our detection efficiencies close to 1. This corresponds to a minimum noise

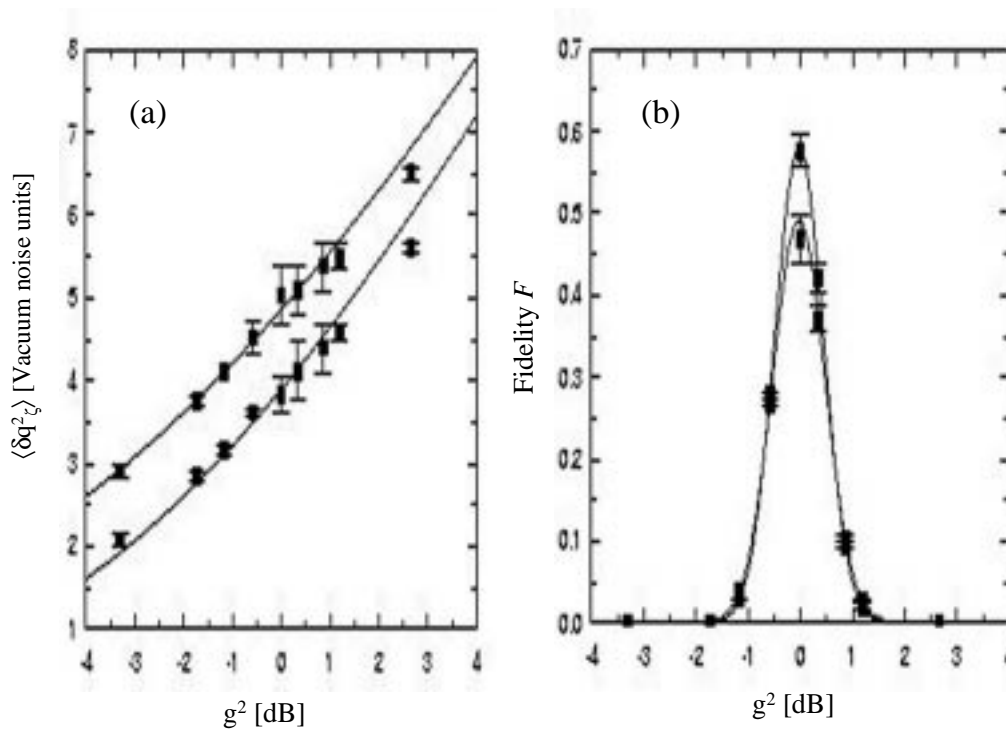


Figure 8.6: (a) The variance of the teleported state observed by Victor as the gain was varied. The upper points were taken without entanglement and the lower points were taken with the entanglement present. The curves are the results of the theoretical predictions based on the measured efficiencies and quantum noise reduction. (b) The fidelity of entanglement between the teleported and the input state as the gain was varied. The lower points are the classical results and the upper points are derived from the corresponding lower points in (a). The maximum fidelity of  $0.58 \pm 0.03$  proves that the teleportation scheme is more efficient than any scheme based on classical states of light. Such a scheme cannot yield higher fidelities than 0.5. Our classical teleportation results yielded a highest fidelity of  $0.48 \pm 0.03$ .

level of the teleported state located about 4.8 dB above the vacuum noise level. The latter could be found by simply blocking the teleported state, so that only vacuum was incident on Victor's detector. To observe the quduty we turned off the FM on the input state and monitored  $\langle \delta q_\zeta^2 \rangle_{Class}$  on Victor's homodyne detector. This can be seen in figure 8.5(2b), which is just the expanded view of the flat noise traces in fig. 8.5(2a) taken with a smaller video bandwidth. Here the level  $Y_0^{Victor} = \langle \delta q_\zeta^2 \rangle_{Class}$  is found to be roughly 4.8 dB above the vacuum noise level  $\Phi_0^{Victor}$ , indicating that our teleportation setup indeed was performing almost as good, as it is classically possible.

Now the entangled beams were allowed to join the game, and as a result the noise level of the teleported state was seen to drop  $1.2 \pm 0.2$  dB corresponding to a 24% reduction. This is shown as  $\Lambda^{Victor}$  in fig. 8.5(2b). In order not to violate the no cloning theorem, Alice could not be allowed to acquire as much information about the input state, as she did classically, and hence the noise level of each of Alice's detectors had to increase by the square root of 1.2 dB, that is 0.6 dB, as Victor's noise level dropped. Fig. 8.5(1b) shows that the noise of the detector *Alice1*, labelled  $\Lambda_x^{Alice}$ , indeed was  $0.55 \pm 0.7$  dB above the vacuum noise level,  $\Phi_{0,x}^{Alice}$ .

Since it was experimentally difficult to adjust the gain,  $g$ , to be exact 1 in units of  $\sqrt{2}/\eta$ , we instead varied this gain and recorded the variance of Victor's detection with and without entangled fields present. Following the same procedure as above, we obtained the series of datapoints displayed in figure 8.6(a), where  $\langle \delta q_\zeta^2 \rangle$  is plotted vs.  $g$ . Here the upper points were taken without entanglement and the lower points with entanglement present. The accompanying curves are generated using (8.18) with the relevant experimental parameters, given in the last section. With the datapoints at hand, we could infer the fidelity by means of (8.17) and this is plotted in fig. 8.6(b) together with the theoretical prediction given our experimental parameters. Now the upper points correspond to entangled beams present and the lower points are the classical results. We find the highest fidelity to be  $\mathcal{F}_{Quant}^{Exp} = 0.58 \pm 0.03$ , which is clearly above the best classical value of 0.5. We can then conclude that the coherent state injected in our teleportation setup was transferred from Alice to Bob more efficient, than it is classically possible, and hence we have performed quantum teleportation of the continuous quadrature phases of the electromagnetic field. Our classical teleportation gave a highest fidelity of  $\mathcal{F}_{Class}^{Exp} = 0.48 \pm 0.03$  in good agreement with the theoretical prediction of  $\mathcal{F}_{Class}^{Theo} = 0.485 \pm 0.010$ , found from the detection efficiency  $\eta = 0.97 \pm 0.02$ . This illustrates again that our teleportation setup was operating close to the ideal classical conditions, which would have resulted in a fidelity of 0.5. The points around  $g = 1$  in fig. 8.6 were generated from numerous independent measurements of  $\langle \delta q_\zeta^2 \rangle$  and  $\langle \delta p_\zeta^2 \rangle$ .

## 8.4 Conclusions

To summarize this chapter, we have outlined the principle of transferring a quantum state from one quantum system onto another system, which is what we mean by quantum teleportation. In the case of teleportation of discrete quantum variables, a finite set of Bell state measurements is needed on the joint system made up by one of a pair of entangled particles and the particle carrying the input state. This is accompanied by a classical broadcasting of the outcome from Alice to Bob. Depending on the outcome of the Bell measurement Bob has to perform one of a discrete set of unitary transformations on the remaining entangled particle. The complete process cannot take place faster than the speed of light. This is a result of the classical communication, which is required to transfer the classical part of the information of the input quantum state. The quantum information can be considered to be transferred instantaneous in the sense that the quantum mechanical wavefunction is projected onto its final state as a result of the detection made by Alice.

The teleportation of continuous variables requires entangled fields instead of single particles, and it was shown how to prepare such fields theoretically as well as experimentally. By inserting realistic parameters from the experiment into our theory, we found the quantum noise reduction in the difference between the amplitudes of the two fields to be -2 dB in fair agreement with the observed -1 dB. The discrepancy is attributed to the unknown phase of the coupling between the two squeezed beams making up the entanglement.

Continuous variables are teleported in a fashion similar to the discrete variables. The Bell state measurement is generalized to a homodyne detection of the  $q$  and  $p$  quadratures of the joint system of the input state and one of the entangled fields. The set of unitary transformations from the discrete case are replaced by a continuum of displacements in phase space in the continuous teleportation.

We then presented the simple theory describing the teleportation of continuous variables and suggested the fidelity,  $\mathcal{F}$  (8.17), as a measure of the quality of the teleportation. In the case of perfect quantum teleportation the fidelity is 1, corresponding to a perfect overlap between the output state and the input state. It was indicated that the highest achievable classical fidelity of 0.5 can be obtained only in the case of perfect detection efficiencies and the feedback gain of  $\sqrt{2}$ . The limitation on the classical teleportation is set by the so called quduty, which is the quantum tariff to be paid every time we cross the border from classical currents to quantum fields. In the ideal case of perfect detection the output state has the same mean amplitude and phase as the input state, but it contains additional two units of vacuum noise in these quadratures as a result of the quduty.

With the theory present, we now focused on the experiment of teleportation of continuous variables. The setup was described and the optical phases relevant to the experiment were pointed out. From an experimental point of view it turned out to be convenient to teleport only a single RF sideband, which made the phase space displacements, required in this experiment, easy to perform. All we needed towards this end was to mix an amplitude or frequency modulated coherent state with one of our entangled beams on a 99/1 beamsplitter.

The experiment clearly revealed the quduty, limiting the classical performance of such a teleportation setup. This manifested itself in an addition of 4.8 dB to the noise level of the teleported state relative to the vacuum noise level. By employing the entangled fields in a nonlocal quantum state, we demonstrated that the quduty was suppressed by about  $-1.2 \pm 0.2$  dB, which clearly was a result of a better performance than the classical setup and hence an indication of quantum teleportation. Further proof of quantum teleportation was delivered by a series of measurements of the variances of the teleported state as the feedback gain from Alice to Bob was varied. From these we inferred the fidelity of  $\mathcal{F}_{Quant}^{Exp} = 0.58 \pm 0.03$ , which is distinctively higher than the highest achievable classical value of 0.5. Similarly the classical teleportation was found to yield the highest fidelity of  $\mathcal{F}_{Class}^{Exp} = 0.48 \pm 0.03$ , indicating that our setup was almost optimized as far as the classical teleportation is concerned.

Our teleportation scheme has the advantage as compared to the previously demonstrated schemes [115] [116], that we teleport the input state with high efficiency in real time. The discrete quantum teleportation relies on the detection of single photons, which is nontrivial to do with a high efficiency and good signal to noise ratio. Furthermore the discrete teleportation schemes utilize the detection procedure to project the teleported state onto the single photon subspace, whereas the detection made by Victor in our scheme only served the purpose of quantifying the quality of our teleportation.

The principles and the experimental setup described in this chapter holds the possibilities of being extended in various directions. The most obvious would be to teleport a nonclassical state of the radiation field instead of a coherent state. By injecting, for instance, a squeezed state, a Fock state or a Schrödinger cat state into our setup, we would truly be able to reveal the quantum nature of the teleportation process. Clearly the quduty would be deleterious to these states and virtually destroy their quantum nature, hence quantum teleportation is needed in order to preserve these characteristics. However the teleportation of the quantum properties of such states would require stronger correlations than demonstrated in this chapter. Given a perfectly squeezed input state, the teleported state would still possess quantum noise reduction provided that the entangled beams display an interbeam quantum noise reduction of 66%, and with a 50% squeezed input state 81% interbeam correlations are needed. Such strong correlations are nontrivial to realize experimentally and hence the teleportation of manifestly nonclassical states is not likely to be seen in the near future.

In section 10.2.2 the possibility of using our setup in other fields of quantum information science is discussed.

## Chapter 9

# The Internally Pumped Optical Parametric Oscillator

The discovery and experimental realization of the squeezed states of light[120][121] has opened a new area in atomic and optical physics. Using these states basic atomic properties may be altered though the interaction with a squeezed reservoir of modes[122][8], atomic properties can be probed with sensitivity better than the standard quantum limit[6][11] or the entanglement inherent in the squeezed states may be used for quantum cryptography[123][124] or teleportation[118] just to mention a few examples. However, as described in chapter 4, the experimental scheme which has been most successful so far in the production of strong squeezing requires a rather extensive optical setup not easily operated[7][38]. This limits the attractiveness of nonclassical light for many applications and hence new, simpler schemes which can be made more compact are desirable. Towards this end the Internally Pumped OPO (IOPO) may prove to become a good alternative to the conventional scheme since, as it will be shown theoretically in this chapter, strong squeezing can be predicted in the output of this device. A threshold well within reach of modern coherent light sources also makes the IOPO above threshold attractive as a compact source of widely tunable coherent light.

This chapter is initiated with a description of the system of interest, followed by a derivation of the equations of motion governing the IOPO fields. Then we will move on to find the stationary solutions of these fields together with the threshold of parametric oscillations. The spectra of quantum fluctuations for the fundamental and the downconverted fields will be derived and the quantum noise around the fundamental frequency in the IOPO reflection will be analyzed. Finally the chapter will be concluded by a summary.

### 9.1 Introduction

The physical system under consideration is made up by a ring resonator with a nonlinear  $\chi^{(2)}$  medium inside. This optical cavity is pumped by light at the fundamental frequency  $\omega$ , which is resonant. Via the interaction with the nonlinear medium part of the fundamental light is converted into the second harmonic at frequency  $2\omega$ . The latter can now again interact with the nonlinear medium either degenerate or nondegenerate to produce two subharmonic fields at frequencies  $\omega_+$  and  $\omega_-$  which in order to preserve energy must fulfill the condition  $2\omega = \omega_+ + \omega_-$ . Alternatively we may think of this system as an external cavity second harmonic generator where the second harmonic is used to pump a nondegenerate OPO inherent in the same cavity. This is why we have chosen to call the scheme the Internally Pumped OPO. As illustrated in figure 9.1 the input coupler for the fundamental also serve as an output coupler to the subharmonics. Consequently the reflection of the IOPO will be a mixture of the reflected fundamental with the subharmonics generated inside the resonator and transmitted through the

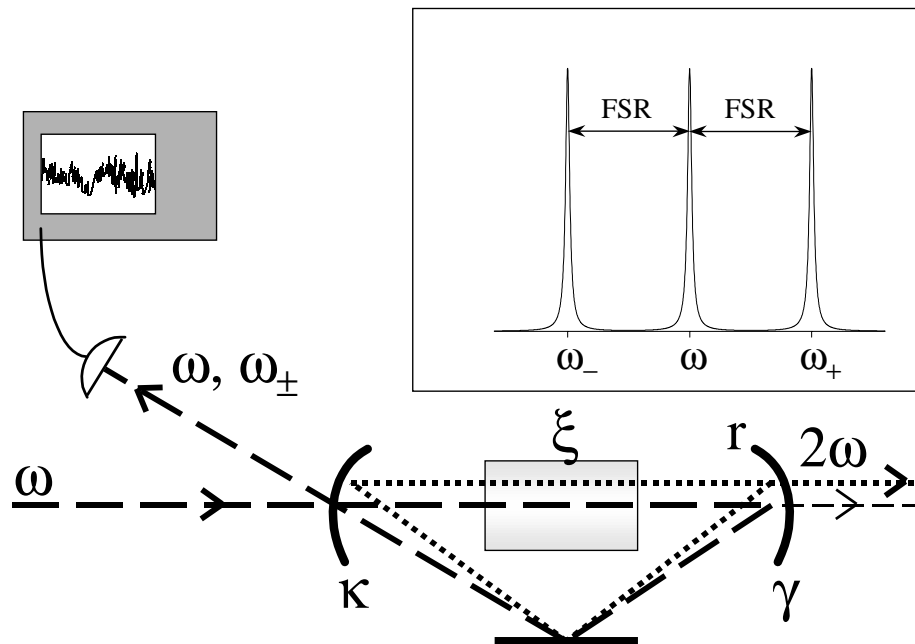


Figure 9.1: The Internally Pumped OPO. Dashed lines illustrate the lower frequencies  $\omega$  and  $\omega_{\pm}$ . Dotted lines illustrate the second harmonic  $2\omega$ . The subharmonics  $\omega_{\pm}$  are considered to be the longitudinal modes symmetrically placed around the fundamental  $\omega$  one FSR away.

coupler. The conventional externally pumped OPO below threshold has proven to work as an efficient source of squeezed vacuum and hence we expect the output of the IOPO below threshold to exhibit similar strong nonclassical correlations.

In principle the second harmonic will be downconverted into all pairs of longitudinal cavity modes placed symmetrically around the fundamental for which the phasematching conditions are fulfilled to a reasonable extent. Below threshold the correlated spontaneously emitted photon pairs of our IOPO will cause these pairs of longitudinal modes to be highly correlated and if we take into account reflected fundamental light assumed here to be in a strong coherent state, this can be made to serve as a local oscillator for a heterodyne measurement so that an ideal photodetector monitoring the IOPO reflection will observe quantum noise reduction at frequencies being an integer times the free spectrum range (FSR) of the cavity. However the FSR of a realistic cavity is typically several hundreds of MHz to a few GHz and hence detection of noise in the subharmonics requires very high frequency detectors unless we restrict ourselves to the set of modes closest to the fundamental.

As it turns out the cascaded nonlinear coupling of four modes makes the IOPO a system being rich on peculiar transient and stationary effects. In the case where the resonator is assumed to have a high finesse for all four modes ( $\omega, 2\omega, \omega_{\pm}$ ) and for the IOPO above threshold, damping of the self pulsing instabilities and twin beam correlated photons in the output has been found theoretically together with sub Poissonian photon statistics of the individual twin beams[125][126][127]. The classical properties of the quadruply resonant[128] and the triply resonant ( $\omega, \omega_{\pm}$ ) IOPO above threshold[129][130] have been examined and optical bistability of the fundamental has been observed in the latter configuration depending on the

phasematching conditions[131]. Experimentally many of the quantum properties of the IOPO are still left to be investigated. Only in refs. [130][132] has squeezing of the nonresonant second harmonic been reported and in ref. [133] the squeezing of the fundamental reflection of a doubly resonant frequency doubler was observed. A detailed classical analysis of the interaction of the four Gaussian modes in the IOPO can be found in [134] together with a discussion of the twin beam correlations of the output.

In the following we will consider the IOPO below threshold in the case where the fundamental and the subharmonics are perfectly resonant in the cavity with no detuning, whereas the second harmonic can be either nonresonant or resonant with an arbitrary detuning. Our treatment is only valid in the region where the finesse of the cavity for the second harmonic is considerably smaller than the finesse for the remaining fields since our approach is equivalent to an adiabatic elimination of the former field from the equations of motion. In contrast to the previous treatments we will here focus our attention on the noise of the quadrature phases of the fundamental as well as the subharmonics in the configuration mentioned above where the fundamental acts as local oscillator for the downconverted fields. The relative phase between the local oscillator and the subharmonics will clearly depend critically on the detuning of the second harmonic which is why the phase of this field is considered in so much detail below. Since it has been shown that the semiclassical approach taken in this treatment with the subsequent adiabatic elimination of the second harmonic does not account for the squeezing in the latter field in an appropriate way[135], we will not derive its spectrum of squeezing here.

## 9.2 Equations of motion

As it was mentioned above we will treat the low frequency modes  $\omega$  and  $\omega_{\pm}$  as perfectly resonant cavity modes with no detuning whereas the second harmonic (SH) can be either nonresonant or resonant with an arbitrary detuning. In ref. [136] it has been shown how to extract a single quantum mode from the continuum and thereby connecting the two extremes of our treatment with a resonant and nonresonant SH quantum field.

Using this as our foundation we now proceed to consider the variation of the SH inside the nonlinear medium. Since the SH field  $b$  not necessarily is resonant in the cavity, we have to take the longitudinal spatial variation of this mode into account. All other fields are assumed to be perfectly resonant and hence we can assign a steady state amplitude these independent of where in the cavity they are observed. Assuming all our modes to be plane waves we now write up the slowly varying envelope of the SH inside the nonlinear medium

$$b(z) = b(0) + i\frac{z}{\ell} (\xi_1 a_1^2 + \xi_2 a_+ a_-) \quad (9.1)$$

where  $z$  is the longitudinal coordinate in the cavity,  $\ell$  is the length of the interaction region and  $a_1$  and  $a_{\pm}$  are the slowly varying intracavity fundamental and subharmonic fields respectively.  $\xi_1$  and  $\xi_2$  are the degenerate and nondegenerate nonlinear coupling constants respectively and close to the degeneracy these are related by  $\xi_2 \simeq 2\xi_1$ . If the subharmonics and the fundamental are adjacent longitudinal modes of the cavity, we are obviously very close to degeneracy and in the rest of this treatment we will use  $\xi_2 = 2\xi_1 \equiv 2\xi$ .

By integrating (9.1) we obtain the SH immediately after the nonlinear medium

$$b(\ell) = b(0) + i\xi (a_1^2 + 2a_+ a_-) \quad (9.2)$$

and the SH before the nonlinear medium  $b(0)$  is related to  $b(\ell)$  by

$$b(0) = b(\ell)e^{i\delta} + \sqrt{1-r^2}e^{i\delta}\sqrt{\tau}b^{in} \quad (9.3)$$

where we have defined the single round trip phaseshift,  $\delta$ , the cavity round trip time,  $\tau$ , and the SH output coupler transmission,  $r$ . The field  $b^{in}$  is the continuum vacuum input on the SH output coupler

which becomes relevant later when we consider the quantum fluctuations in the IOPO. Combining (9.2) and (9.3) we find the SH fields before and after the nonlinear medium to be

$$\begin{aligned} b(0) &= \frac{re^{i\delta}}{1-re^{i\delta}} i\xi (a_1^2 + 2a_+a_-) + \frac{e^{i\delta}\sqrt{1-r^2}}{1-re^{i\delta}} \sqrt{\tau} b^{in} \\ b(\ell) &= \frac{1}{1-re^{i\delta}} i\xi (a_1^2 + 2a_+a_-) + \frac{e^{i\delta}\sqrt{1-r^2}}{1-re^{i\delta}} \sqrt{\tau} b^{in} \end{aligned} \quad (9.4)$$

The three resonant fields are found from the single round trip increments

$$\begin{aligned} \Delta a_1 &= [\sqrt{2\kappa}\mathcal{E} - (\kappa + \gamma) a_1] \tau + 2i\xi \int_0^1 d\left(\frac{z}{\ell}\right) a_1^\dagger b(z) + \tau\sqrt{2\kappa}a_1^{in} + \tau\sqrt{2\gamma}\alpha_1^{in} \\ \Delta a_\pm &= -(\kappa + \gamma) a_\pm \tau + 2i\xi \int_0^1 d\left(\frac{z}{\ell}\right) a_\mp^\dagger b(z) + \tau\sqrt{2\kappa}a_\mp^{in} + \tau\sqrt{2\gamma}\alpha_\mp^{in} \end{aligned} \quad (9.5)$$

where  $\kappa$  is the decay rate of the fundamental through the input/output coupler and  $\gamma$  are the residual cavity losses for the fundamental. The decay rates for the subharmonics and the fundamental have been assumed to be the same which is justified by the small frequency difference of on FSR between the fields. The classical pump field feeding the intracavity fundamental mode has been denoted  $\mathcal{E}$  which is just a c-number and the 'in' fields belong to the reservoir of vacuum modes entering the cavity via the loss mechanisms. By evaluating the integrals in (9.5) using (9.1) and (9.4), we find the following set of equations governing the dynamics of the IOPO

$$\begin{aligned} \frac{da_1}{dt} &= \sqrt{2\kappa}\mathcal{E} - (\kappa + \gamma) a_1 - \frac{\xi^2}{\tau} g a_1^\dagger (a_1^2 + 2a_+a_-) + \sqrt{2\kappa}a_1^{in} + \sqrt{2\gamma}\alpha_1^{in} + 2\frac{\xi}{\sqrt{\tau}} j a_1^\dagger b^{in} \\ \frac{da_\pm}{dt} &= -(\kappa + \gamma) a_\pm - \frac{\xi^2}{\tau} g a_\mp^\dagger (a_1^2 + 2a_+a_-) + \sqrt{2\kappa}a_\pm^{in} + \sqrt{2\gamma}\alpha_\pm^{in} + 2\frac{\xi}{\sqrt{\tau}} j a_\mp^\dagger b^{in} \\ b(\ell) &= h\xi (a_1^2 + 2a_+a_-) - i\sqrt{\tau} j b^{in} \end{aligned} \quad (9.6)$$

Here we have hidden the cavity response to the SH field in the functions  $g$ ,  $h$  and  $j$  defined to be

$$\begin{aligned} g &= (1 + re^{i\delta}) (1 - re^{i\delta})^{-1} \equiv g_R (1 + i\rho) \\ h &= i (1 - re^{i\delta})^{-1} \equiv h_R (1 + iR) \\ j &= ie^{i\delta} \sqrt{1-r^2} (1 - re^{i\delta})^{-1} \equiv j_R (1 + i\Sigma) \end{aligned} \quad (9.7)$$

and the explicit form of  $\rho$  is

$$\rho = -\frac{2r \sin \delta}{1 - r^2} \quad (9.8)$$

Clearly the nonlinear coupled set of equations (9.6) contain a variety of solutions resulting in many interesting effects. However we will restrict ourselves mainly to the IOPO below threshold, meaning that the expectation values  $\langle a_\pm \rangle$  are zero. For the nonresonant SH ( $g = 1$ ,  $h = j = i$ ) it is easy to verify that our equations of motion are equivalent to the Langevin equations obtained when eliminating the SH mode adiabatically from an interaction Hamiltonian of the form

$$\mathcal{H} = \frac{\hbar}{\tau} \left[ \xi_1 \left( a_2^\dagger a_1^2 + \left( a_1^\dagger \right)^2 a_2 \right) + \xi_2 \left( a_+^\dagger a_-^\dagger a_1 + a_1^\dagger a_+ a_- \right) \right] \quad (9.9)$$

This is why we do not expect our treatment to be valid when the losses of the SH become small enough to be comparable to the losses of the low frequency modes, corresponding to  $r \rightarrow 1$ .

Now the single mode quadrature phase operators  $X_1$ ,  $Y_1$ ,  $X_2$  and  $Y_2$  defined as

$$\begin{aligned} X_1 &= a_1 e^{i\theta_1} + a_1^\dagger e^{-i\theta_1}, & X_2 &= a_2 e^{i\theta_2} + a_2^\dagger e^{-i\theta_2} \\ Y_1 &= a_1 e^{i\theta_1} - a_1^\dagger e^{-i\theta_1}, & Y_2 &= a_2 e^{i\theta_2} - a_2^\dagger e^{-i\theta_2} \end{aligned} \quad (9.10)$$

are introduced together with the two mode quadrature phases

$$\begin{aligned} X_\pm &= \frac{1}{\sqrt{2}} \left[ (a_+ \pm a_-) e^{i\phi} + \left( a_+^\dagger \pm a_-^\dagger \right) e^{-i\phi} \right] \\ Y_\pm &= \frac{-i}{\sqrt{2}} \left[ (a_+ \pm a_-) e^{i\phi} - \left( a_+^\dagger \pm a_-^\dagger \right) e^{-i\phi} \right] \end{aligned} \quad (9.11)$$

We let the pump field set the overall phase of the problem, meaning that we henceforth take  $\mathcal{E}$  to be a real number. As a result the phases  $\theta_1$ ,  $\theta_2$  and  $\phi$  are defined relative to the phase of this field. From (2.5) we see that the single mode quadrature phases  $X_j$  and  $Y_j$  ( $j = 1, 2$ ) are complementary operators and it is easy to check that the same applies to the two mode quadrature phases  $X_k$  and  $Y_k$  ( $k = +, -$ ). By using our equations of motion (9.6) together with their Hermitian conjugates and inserting our definitions (9.10) and (9.11), we arrive at the equations of motion for the quadrature phases. However these are rather lengthy and will not be displayed here, but they can be found in appendix C. Here it is also shown that they simplify considerably provided we define the quadrature phases  $\theta_1$ ,  $\theta_2$  and  $\phi$  in a sensible way.

### 9.3 Steady state solutions

With our equations of motion at hand we will now look for the steady state solutions to these. From the steady state fields we can find the threshold of the IOPO operation as the point where the subharmonics start to acquire a nonzero mean value. Furthermore we need the mean values of the fields for our semiclassical treatment of the quantum noise in the next section.

We keep in mind the 'in' fields are in the vacuum state and hence their mean amplitudes are zero. Now we choose the phases  $\theta_1$  and  $\phi$  according to (C.8) and (C.9) so that the steady state quadratures  $\bar{Y}_1 = \bar{X}_- = \bar{Y}_+ = 0$ . In this case the equations of motion for the subharmonic mean fields simplify to

$$\left[ Z^2 + \left( \frac{\kappa + \gamma}{A} \right)^2 \right]^2 + \rho^2 Z^4 = (1 + \rho^2) \bar{X}_1^4 \quad (9.12)$$

according to (C.11). Here we have defined the subharmonic excitation  $Z^2 = \bar{X}_+^2 + \bar{Y}_-^2$  and  $A = \xi^2 g_R / 4\tau$ . Clearly  $Z^2$  is by definition a real number, and from (9.12) it is found that the solution with respect to  $Z^2$  becomes real when  $\bar{X}_1$  exceeds the value

$$X_1^{th} = \sqrt{\frac{\kappa + \gamma}{A\sqrt{1 + \rho^2}}} = \frac{2}{\xi} \sqrt{\frac{(\kappa + \gamma)\tau}{|g|}} \quad (9.13)$$

which defines the intracavity fundamental field required to reach the IOPO threshold. In terms of this value the solution of (9.12) is given by

$$Z^2 = \frac{(X_1^{th})^2}{\sqrt{1 + \rho^2}} \left[ \sqrt{\left( [\bar{X}_1 / X_1^{th}]^4 - 1 \right) (1 + \rho^2) + 1} - 1 \right] \quad (9.14)$$

and for no SH detuning ( $\rho = 0$ ) the subharmonic excitation reduces to

$$Z = X_1^{th} \sqrt{[\bar{X}_1 / X_1^{th}]^2 - 1} \quad (9.15)$$

This is identical to the result from the externally pumped two mode OPO[137] with the modification that our threshold is expressed in terms of the *fundamental* pump whereas the externally pumped OPO threshold usually is expressed through the second harmonic pump. Hence our ratio of  $\bar{X}_1 / X_1^{th}$  must be squared in order to make a comparison possible. By utilizing the symmetry of the parametric downconversion into the two subharmonic fields we can readily deduce these to be  $\bar{X}_+ = \bar{Y}_- = Z / \sqrt{2}$ .

For the fundamental field we employ the equations of motion (C.1). With our choice of phases these reduce in the steady state to

$$\left[ \frac{\sqrt{8\kappa\mathcal{E}} \cos \theta_1}{A\bar{X}_1} - \bar{X}_1^2 - \frac{\kappa + \gamma}{A} \right]^2 - \left( \frac{Z}{\bar{X}_1} \right)^4 = Z^4 (1 + \rho^2) \quad (9.16)$$

where the phase of the fundamental quadrature  $\theta_1$  is given by

$$\sin \theta_1 = A\bar{X}_1 \frac{\rho\bar{X}_1^2 - (\rho C_1 + S_1) Z^2}{\sqrt{8\kappa\mathcal{E}}} \quad (9.17)$$

When the IOPO is exactly on threshold we have that  $Z = 0$ , and by using our value for the intracavity threshold field (9.13) in (9.16) together with our choice of phase (9.17), we find external pump field required to drive the IOPO above threshold

$$\mathcal{E}_{th} = X_1^{th} \frac{\kappa + \gamma}{2\sqrt{\kappa}} \sqrt{1 + \frac{1}{\sqrt{1 + \rho^2}}} \quad (9.18)$$

This corresponds the threshold power of

$$P_{th} = \frac{(\mathcal{T} + \mathcal{L})^3}{2\mathcal{T}E_{NL}} \frac{1}{|g|} \left( 1 + \frac{1}{\sqrt{1 + \rho^2}} \right) \quad (9.19)$$

where the single pass nonlinearity for second harmonic generation has been defined as  $E_{NL} = P(2\omega)/P^2(\omega)$ . This quantity can be found from (9.1) by ignoring the downconverted fields. As in section 2.2 we have defined the fundamental output coupler transmission  $\mathcal{T}$  and the remaining intracavity losses  $\mathcal{L}$ . In the limit of nonresonant SH ( $\rho = 0$ ,  $|g| = 1$ ), we find the functional dependence of our threshold on the cavity parameters to agree with the results derived in ref. [134] for focused beams. The main effect of the resonance properties of the SH in the cavity is hidden in the function  $|g|$  defined in (9.7). This shows that the threshold can be reduced drastically if the SH cavity losses are small ( $r \lesssim 1$ ) and the phaseshift  $\delta$  is zero, since this will result in a large build up of the intracavity SH field. In contrast to this the OPO threshold is found to become very large when the SH losses are small but the phaseshift is appreciable in which case the intracavity SH field interferes destructively with itself.

To minimize the threshold the output coupler transmission should be chosen as  $\mathcal{T} = \mathcal{L}/2$  however from the quantum theory of the externally pumped OPO in section 2.2, we know that this is far from being the optimum choice when the squeezing in the output is considered. In chapter 4 we found that our squeezing was limited mainly by the OPO escape efficiency  $\mathcal{T}/\mathcal{T} + \mathcal{L}$  which for  $\mathcal{T} = \mathcal{L}/2$  is only 33%. To optimize the squeezing the output coupler transmission should be made as large as the available pump power allows for in terms of the increased threshold.

If we estimate typical values of  $\mathcal{L} = 0.5\%$ ,  $\mathcal{T} = 5\%$  and  $E_{NL} = 0.02 \text{ W}^{-1}$  as for a good  $\text{KNbO}_3$  crystal[7], and if we furthermore assume the SH to be nonresonant, we find from (9.19) a threshold power of 166 mW well within reach of modern coherent light sources. Experimentally the threshold power of 120 mW has been reported in a  $\text{LiNbO}_3$  IOPO with the fields  $\omega$ ,  $\omega_{\pm}$  resonating and the SH escaping[129].

It should be emphasized at this point that our treatment only is valid in a plane wave approximation, however the threshold calculation employing the focused Gaussian beams usually do not differ by more than a factor of 2[83].

Having found the threshold of parametric oscillations we will limit ourselves to consider only the subthreshold operation of the IOPO in the rest of this calculation. Using (9.16) with the phase (9.17), we find the steady state intracavity fundamental field below threshold by putting  $Z = 0$ . This is given by

$$\bar{X}_1 = X_1^{th} \Gamma(\sigma, \rho), \quad \sigma \leq 1 \quad (9.20)$$

where  $\Gamma(\sigma, \rho) = \sqrt{z(\sigma, \rho)}$ , and  $z$  is the real solution of the cubic equation

$$\sqrt{1 + \rho^2} z (1 + z^2) + 2z^2 - 2\sigma^2 (1 + \sqrt{1 + \rho^2}) = 0 \quad (9.21)$$

In (9.21) we have defined the IOPO pump parameter  $\sigma = \mathcal{E}/\mathcal{E}_{th} = \sqrt{P/P_{th}}$ . It can be checked that in the limit of no SH detuning ( $\rho = 0$ ), (9.20) reduces to the intracavity fundamental build up found

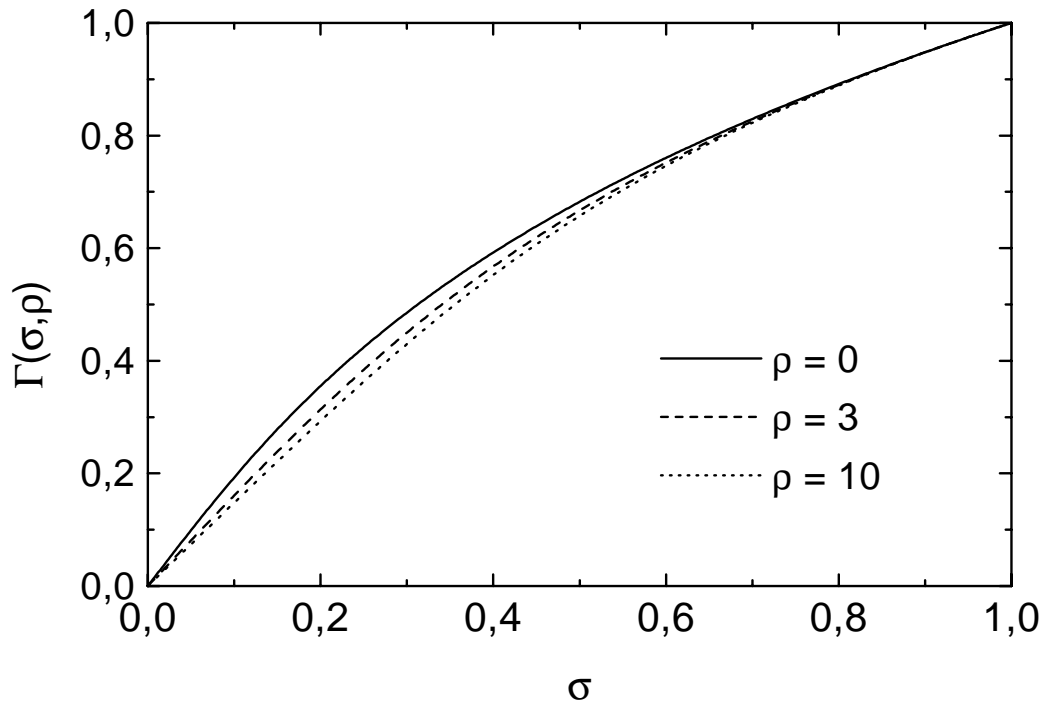


Figure 9.2: The build up of the fundamental mean field  $\Gamma(\sigma, \rho) = \bar{X}_1/X_1^{th}$  as function of the IOPO pump parameter  $\sigma = \sqrt{P/P_{th}}$  for various values of the SH detuning parameter  $\rho$ .

for doubly resonant second harmonic generation. A comparison shows that a replacement of  $\mathcal{E}_{th}$  with the critical pump field required to reach the point of self pulsing yields identical solutions. This would not have been the case if  $\xi_2 \neq 2\xi_1$ , in fact it has been shown that the self pulsations in the doubly resonant frequency doubler can be damped out if the IOPO threshold is reached before the self pulsing threshold [125][127].

The function  $\Gamma$  controlling the fundamental build up is plotted versus  $\sigma$  for different values of the SH detuning  $\rho$  in figure 9.2. From this we see that  $\Gamma$  grows monotonic from 0 when no pump is present to 1 when  $\sigma = 1$  corresponding to the IOPO on threshold. The influence of the SH detuning associated with the different values of  $\rho$  is seen to be of minor importance. In fact we find that in the limit of  $\rho \gg 1$  equation (9.21) reduces to the  $\rho$  independent equation  $z^3 + z - 2\sigma^2 = 0$ . As we saw above, the main impact of the SH detuning is on the threshold power which can become very large or very small.

By inserting our solution (9.20) together with the threshold pump field (9.18) into (9.17) with  $Z = 0$ , we find the natural choice of the fundamental quadrature phase for the IOPO below threshold

$$\theta_1 = \arcsin \left( \frac{\rho \Gamma^3(\sigma, \rho)}{\sigma \sqrt{2\sqrt{1+\rho^2} (1 + \sqrt{1+\rho^2})}} \right) \quad (9.22)$$

In this region the choice of the subharmonic quadrature phase  $\phi$  can be made arbitrarily, but in terms of the quantum noise there exists a natural choice which separates the squeezed from the antisqueezed quadratures.

As it is shown in appendix C the obvious choice of the SH quadrature phase  $\theta_2$  below threshold is

$$\theta_2 = 2\theta_1 + \arctan R^{-1} \quad (9.23)$$

Using this we find the following stationary SH field quadratures after the nonlinear medium

$$\begin{aligned} \bar{X}_2(\ell) &= 0 \\ \bar{Y}_2(\ell) &= Y_2^{th} \Gamma^2(\sigma, \rho), \quad \sigma \leq 1 \end{aligned} \quad (9.24)$$

Here we have defined the intracavity threshold SH field  $Y_2^{th} = \xi |h| (X_1^{th})^2 / 2$ . For nonresonant SH we have  $|h| = 1$  and  $\rho = 0$ , so that the SH threshold field reduces to  $Y_2^{th} = 2(\kappa + \gamma)\tau/\xi$  which is just twice the SH threshold of the externally pumped OPO (2.7) derived in section 2.2. The factor of 2 arise from the fact that in the IOPO the SH field is generated inside the nonlinear medium in which the parametric downconversion takes place, whereas in the externally pumped OPO the SH field is constant throughout the medium. As a result the SH field integrated over the nonlinear medium is a factor of 2 larger in the externally pumped OPO than in the IOPO, and consequently the threshold field is a factor of 2 smaller in a plane wave approximation.

## 9.4 Quantum noise

We will now use our steady state results derived above as the operating points for our field operators. Provided the quantum fluctuations are small compared to the nonzero mean fields we can linearize the fluctuations around the operating points and write up the Langevin equations to be solved. This procedure is usually referred to as the semiclassical approach[18]. As a result of the linearization our results are not valid in regions with strongly fluctuating fields as it is the case close to threshold.

As it was mentioned in the introduction we will focus our attention on the quantum noise of the low frequency modes  $\omega$  and  $\omega_{\pm}$ . For these modes we define the fluctuation operators

$$q_j = X_j - \bar{X}_j, \quad p_j = Y_j - \bar{Y}_j, \quad j = 1, +, - \quad (9.25)$$

which we insert in our equations of motion together with our subthreshold stationary solutions. Keeping only terms linear in the fluctuations we arrive at the Langevin equations for the fundamental quadratures

$$\begin{aligned} \frac{d}{d(\kappa+\gamma)t} \begin{pmatrix} q_1 \\ p_1 \end{pmatrix} &= - \left[ \mathbb{I} + \Gamma^2 \begin{pmatrix} 3 & -\rho \\ 3\rho & 1 \end{pmatrix} \right] \begin{pmatrix} q_1 \\ p_1 \end{pmatrix} + \frac{\sqrt{2\kappa}}{\kappa+\gamma} \begin{pmatrix} q_1^{in} \\ p_1^{in} \end{pmatrix} + \\ &+ \frac{\sqrt{2\gamma}}{\kappa+\gamma} \begin{pmatrix} Q_1^{in} \\ P_1^{in} \end{pmatrix} + \frac{2\Gamma}{\sqrt{(\kappa+\gamma)}} \begin{pmatrix} q_2^{in} \\ p_2^{in} \end{pmatrix} \end{aligned} \quad (9.26)$$

as well as the subharmonics

$$\frac{d}{d(\kappa+\gamma)t} \begin{pmatrix} q_{\pm} \\ p_{\pm} \end{pmatrix} = - \left[ \mathbb{I} + \Gamma^2 \sqrt{1 + \rho^2} \mathbb{S} \right] \begin{pmatrix} q_{\pm} \\ p_{\pm} \end{pmatrix} + \frac{\sqrt{2\kappa}}{\kappa+\gamma} \begin{pmatrix} q_{\pm}^{in} \\ p_{\pm}^{in} \end{pmatrix} + \frac{\sqrt{2\gamma}}{\kappa+\gamma} \begin{pmatrix} Q_{\pm}^{in} \\ P_{\pm}^{in} \end{pmatrix} \quad (9.27)$$

Here  $\mathbb{I}$  describes the  $2 \times 2$  unit matrix and  $\mathbb{S} \equiv \begin{pmatrix} 1 & 0 \\ 0 & -1 \end{pmatrix}$ . In order to obtain (9.26) and (9.27) we have chosen the quadrature phases to be  $\theta_2 = 2\theta_1 + \arctan \Sigma$  and

$$\phi = \theta_1 - 1/2 \arctan \rho \quad (9.28)$$

where  $\theta_1$  is defined in (9.22). From (C.4) these phases are seen to simplify our equations of motion. We assume that all the 'in' fields describe independent uncorrelated vacuum fluctuations only.

With the goal of finding the spectra of fluctuations we now Fourier transform (9.26) and (9.27) to find

$$\left[ (i\Omega + 1) \mathbb{I} + \Gamma^2 \begin{pmatrix} 3 & -\rho \\ 3\rho & 1 \end{pmatrix} \right] \begin{pmatrix} q_1 \\ p_1 \end{pmatrix} = \frac{\sqrt{2\kappa}}{\kappa+\gamma} \begin{pmatrix} q_1^{in} \\ p_1^{in} \end{pmatrix} + \frac{\sqrt{2\gamma}}{\kappa+\gamma} \begin{pmatrix} Q_1^{in} \\ P_1^{in} \end{pmatrix} + \frac{2\Gamma}{\sqrt{(\kappa+\gamma)}} \begin{pmatrix} q_2^{in} \\ p_2^{in} \end{pmatrix} \quad (9.29)$$

for the fundamental and

$$\left[ (i\Omega + 1)\mathbb{I} \pm \Gamma^2 \sqrt{1 + \rho^2} \mathbb{S} \right] \begin{pmatrix} q_{\pm} \\ p_{\pm} \end{pmatrix} = \frac{\sqrt{2\kappa}}{\kappa + \gamma} \begin{pmatrix} q_{\pm}^{in} \\ p_{\pm}^{in} \end{pmatrix} + \frac{\sqrt{2\gamma}}{\kappa + \gamma} \begin{pmatrix} Q_{\pm}^{in} \\ P_{\pm}^{in} \end{pmatrix} \quad (9.30)$$

for the subharmonics, where the frequency  $\Omega$  is measured in units of the IOPO bandwidth  $\kappa + \gamma$ . The field operators in (9.29) and (9.30) are defined in the frequency space as opposed to the field operators in (9.26) and (9.27) which are functions of time. To simplify the notation we have used the same notation to describe both sets of operators, and in the rest of this chapter all of our field operators will be defined in the frequency space.

We infer the fields going out of the IOPO by applying the boundary conditions for a field  $F$  on the input/output coupler

$$F^{out} = \sqrt{2\kappa} F - F^{in} \quad (9.31)$$

where we assume the coupler transmission to be small compared to 1.

### 9.4.1 Fundamental field

By combining (9.31) and (9.29) we find the output field quadratures for the fundamental to be

$$\begin{pmatrix} q_1^{out} \\ p_1^{out} \end{pmatrix} = (2\eta \mathbb{M}^{-1} - \mathbb{I}) \begin{pmatrix} q_1^{in} \\ p_1^{in} \end{pmatrix} + 2\sqrt{\eta(1-\eta)} \mathbb{M}^{-1} \begin{pmatrix} Q_1^{in} \\ P_1^{in} \end{pmatrix} + 2\Gamma \sqrt{2\eta} \mathbb{M}^{-1} \begin{pmatrix} q_2^{in} \\ p_2^{in} \end{pmatrix} \quad (9.32)$$

where we have defined

$$\mathbb{M} = \left[ (i\Omega + 1)\mathbb{I} + \Gamma^2 \begin{pmatrix} 3 & -\rho \\ 3\rho & 1 \end{pmatrix} \right] \quad (9.33)$$

together with the OPO escape efficiency  $\eta = \kappa/(\kappa + \gamma) \simeq \mathcal{T}/(\mathcal{T} + \mathcal{L})$ . The last equality is only valid for  $\mathcal{T}, \mathcal{L} \ll 1$ .

When using (9.32) to find the spectrum of fluctuations we keep in mind that the  $q$  and  $p$  quadratures are independent and that all the 'in' fields are uncorrelated. Furthermore we normalize our fluctuations to the amount of noise power from our white vacuum fluctuations in the bandwidth relevant to our measurement. Hence we have

$$\begin{aligned} \langle q_i^{in}(-\Omega) q_j^{in}(\Omega) \rangle &= \delta_{ij} = \langle p_i^{in}(-\Omega) p_j^{in}(\Omega) \rangle \\ \langle q_i^{in}(-\Omega) p_j^{in}(\Omega) \rangle &= 0 = \langle p_i^{in}(-\Omega) q_j^{in}(\Omega) \rangle \end{aligned} \quad (9.34)$$

from which we find the variances of the fundamental quadratures to be

$$\langle (q_1^{out})^2 \rangle = 1 - \eta \frac{4\Gamma^2 \left[ \Omega^2 + (1 + \Gamma^2)^2 + \rho^2 \Gamma^2 (2 - \Gamma^2) \right]}{[(1 + \Gamma^2)(1 + 3\Gamma^2) + 3\rho^2 \Gamma^4 - \Omega^2]^2 + 4\Omega^2 (1 + 2\Gamma^2)^2} \quad (9.35)$$

and

$$\langle (p_1^{out})^2 \rangle = 1 + \eta \frac{4\Gamma^2 \left[ \Omega^2 + (1 + 3\Gamma^2)^2 + \rho^2 \Gamma^2 (2 + 3\Gamma^2) \right]}{[(1 + \Gamma^2)(1 + 3\Gamma^2) + 3\rho^2 \Gamma^4 - \Omega^2]^2 + 4\Omega^2 (1 + 2\Gamma^2)^2} \quad (9.36)$$

Since the quantum noise reduction is found in the  $q_1^{out}$  quadrature, we will focus on (9.35) here. For zero SH detuning ( $\rho = 0$ ) and at zero frequency ( $\Omega = 0$ ) we find (9.35) to reduce to

$$\langle (q_1^{out})^2 \rangle = 1 - \frac{4\eta \Gamma^2}{(1 + 3\Gamma^2)^2} \quad (9.37)$$

which is the noise reduction found for a two photon absorber[138] and singly resonant second harmonic generation where the second harmonic is adiabatically eliminated[139]. The minimum of (9.37) is found

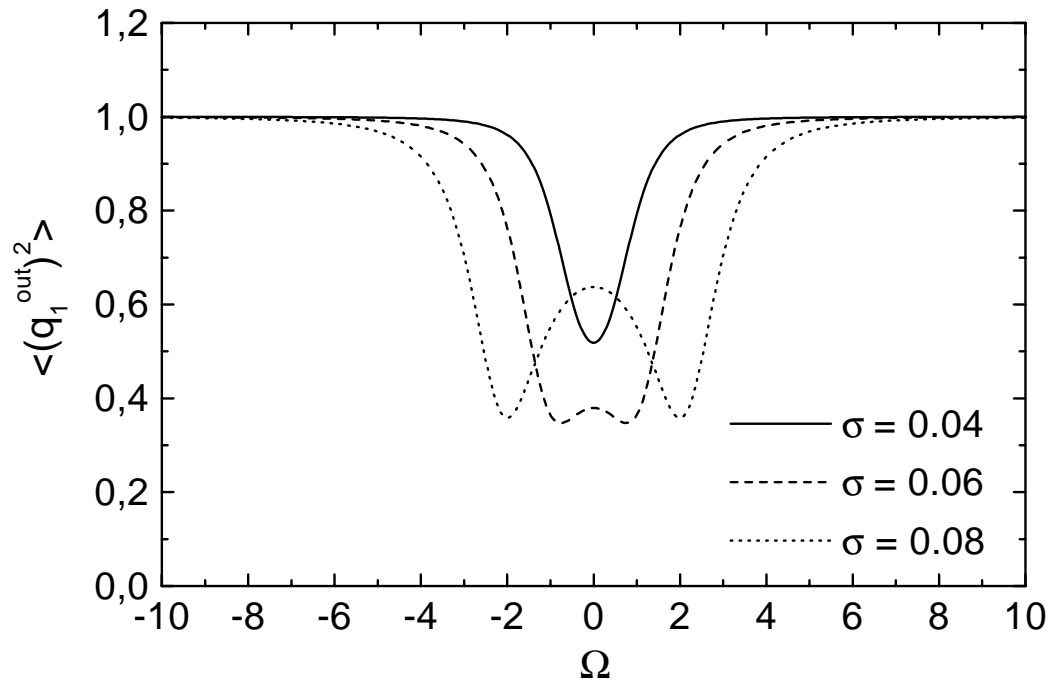


Figure 9.3: Noise spectra of the fundamental field for different pump powers with a detuning parameter of  $\rho = 100$ . Best squeezing is found to approach  $2/3$  corresponding to  $-4.8$  dB.

to be  $2/3$  or  $-1.76$  dB quantum noise reduction. This is found for  $\eta = 1$  and  $\Gamma = 3^{-1/2}$  corresponding to  $\sigma = 0.385$ . For  $\rho = 0$  we see from (9.22) that  $q_1^{\text{out}}$  simply describes the amplitude of the outgoing fundamental and the mechanism responsible for the amplitude squeezing can be visualized as follows. Due to the second harmonic generation the fundamental field is exposed to nonlinear losses. As a result an immediate field with an amplitude larger than the mean will be converted stronger into the SH than a field with the mean amplitude and the reversed argument applies to an immediate field with an amplitude smaller than the mean. This results in a fundamental field with amplitude fluctuations smoothed out on a timescale set by the cavity round trip time.

With a finite SH detuning figure 9.3 reveals more interesting features. As  $\rho$  becomes very large corresponding to almost complete destructive interference of the fed back second harmonic with itself, the noise of our squeezed quadrature, defined with a phase according to (9.22), is found numerically to approach  $1/3$ . This occurs at a frequency around  $\Omega \simeq \sqrt{11}$  as  $\rho \rightarrow \infty$  and  $\sigma \rightarrow 0_+$ . Of course our treatment is not valid in this extreme limit, since we find from (9.8) that  $r$  must approach 1 in order to make  $\rho$  very large. However, as fig. 9.3 shows, quantum noise reduction close to  $2/3$  can be obtained at smaller frequencies with  $\rho$  as small as 100. The mechanism for the improved quantum noise reduction with large SH detuning is related to the resulting negative feedback of the SH as a result of the destructive interference in the cavity. The same mechanism as for zero SH detuning applies here but the large  $\rho$  results in almost perfect cancellation of the SH field having made a single round trip and hence the degenerate downconversion of this field back into the fundamental mode is weak. This is not the case with  $\rho = 0$  where a part of the fundamental fluctuations always return to the fundamental mode as a result of two interactions with the SH, and hence we find stronger squeezing with a finite SH detuning.

From an experimental point of view the stronger squeezing with finite  $\rho$  will not be easy to observe since the IOPO threshold becomes very high as a result of the low losses and strong detuning required to make  $\rho$  large. This means that in order to achieve an appreciable value of  $\sigma$  of 5-10%, a substantial amount of pump power is needed. Furthermore we have found that the phase of the squeezed quadrature is not zero as it would be if squeezing was found in the amplitude of the fundamental. This means that, unless the IOPO cavity is perfectly impedance matched to the pump, the field reflected off the IOPO will be composed by the partially reflected pump and the squeezed field transmitted through the coupler with a different phase. Hence the noise in the amplitude of this combined field will be set by a mixture of the noise of the 'pure' quadratures defined by (9.22).

### 9.4.2 Subharmonics

Using the same approach as in the last section we find the noise spectra for the subharmonics by using (9.30). These are given by

$$\langle (q_+^{out})^2 \rangle = \langle (p_-^{out})^2 \rangle = 1 - \eta \frac{4\Gamma^2 \sqrt{1 + \rho^2}}{\Omega^2 + (1 + \Gamma^2 \sqrt{1 + \rho^2})^2} \quad (9.38)$$

$$\langle (p_+^{out})^2 \rangle = \langle (q_-^{out})^2 \rangle = 1 + \eta \frac{4\Gamma^2 \sqrt{1 + \rho^2}}{\Omega^2 + (1 - \Gamma^2 \sqrt{1 + \rho^2})^2} \quad (9.39)$$

where we have defined the escape efficiency  $\eta$  as for the fundamental. It should be noted here that the above two spectra are centered around the frequency  $\omega - \omega_-$  which in our case is taken to be one free spectrum range of the IOPO cavity.

With a zero SH detuning or a completely nonresonant SH field ( $\rho = 0$ ), we find our results to be equivalent to the squeezing found for the externally pumped OPO provided we make the substitution  $\Gamma^2 \leftrightarrow \sigma$ . Clearly this replacement must be made since our threshold for the IOPO is derived in terms of the fundamental pump whereas the threshold in refs. [137][140][141] is found for the second harmonic pump. In (9.24) the latter was found to be proportional to  $\Gamma^2$  and hence the substitution is required for comparison.

As in the externally pumped OPO we find perfect squeezing with  $\eta = \Gamma = 1$  at zero frequency  $\Omega = 0$ . This corresponds to having an IOPO with no intracavity losses except the output coupler operating exactly on threshold and recording the frequency component at one FSR of the photocurrent of a heterodyne detector.

In analogy with the discussion at the end of chapter 2 the physical mechanism responsible for the squeezing in the subharmonics of the IOPO is the two photon nature of the parametric downconversion as described by the Hamiltonian (9.9). The SH photons are always downconverted into pairs of subharmonic photons. The photons making up each of the pairs are having frequencies  $\omega_+$  and  $\omega_-$  lying symmetrically around the fundamental frequency. Furthermore the phases of the subharmonic fields always add up to a constant set by the phase of the SH field. This argument applies to the mean fields as well as the fluctuations. In the externally pumped OPO the overall phase is set by the SH pump and consequently squeezing is found in the quadrature describing the sum of the subharmonic phases  $p_+$ . Furthermore since the downconverted photons are generated in pairs, the resulting amplitudes of the two subharmonics are almost equally strong and hence squeezing is also found in the quadrature describing the difference between the subharmonic amplitudes  $q_-$ . From (9.1) we find that there is a  $\pi/2$  phaseshift associated with each interaction via the nonlinear medium. In the externally pumped OPO only a single interaction is needed in order to generate the subharmonics, whereas *two* interactions are needed in the IOPO resulting in an additional  $\pi/2$  phaseshift. Hence in the IOPO squeezing is found in the quadratures orthogonal to  $q_-$  and  $p_+$ , namely  $q_+$  and  $p_-$ . This means that a local oscillator in phase with the fundamental pump or the pump itself will produce a squeezed beatnote at the frequency of one FSR when overlapped in

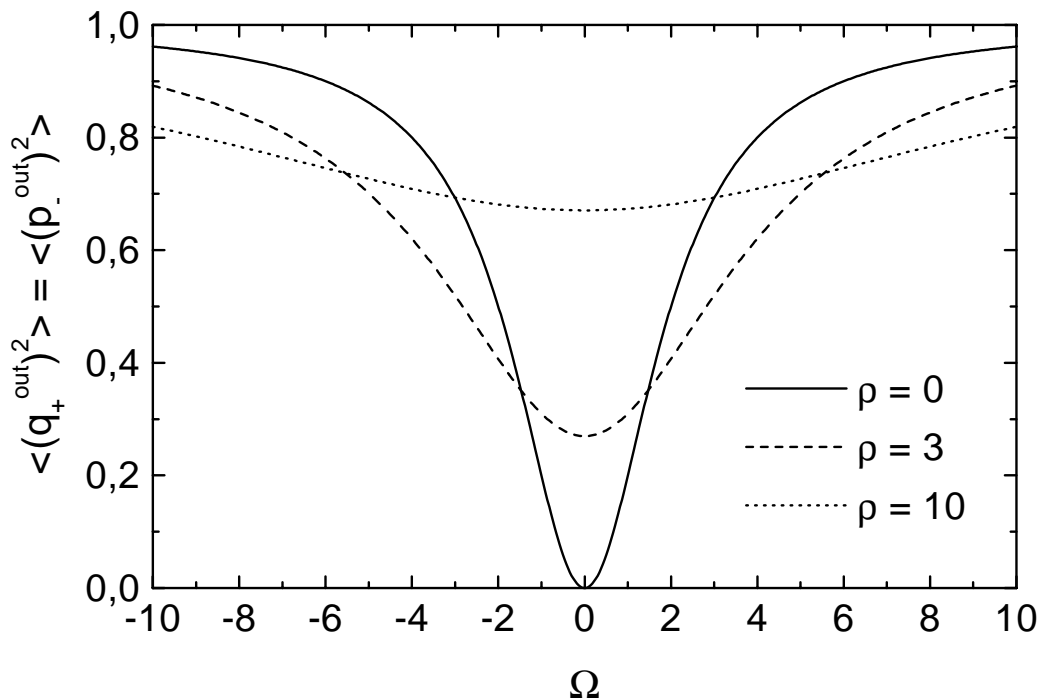


Figure 9.4: The quantum noise reduction around the FSR frequency. The traces correspond to the parameters  $\sigma = 1 = \eta$ . Perfect squeezing is found for no SH detuning ( $\rho = 0$ ) and the spectrum of vacuum fluctuations is approached as  $\rho \rightarrow \infty$ .

phase with the squeezed vacuum emerging from the IOPO. In the next section we will elaborate more on this observation.

Having a finite SH detuning the best squeezing is still found for  $\eta = \Gamma = 1$  around zero frequency. But, as we see from figure 9.4, the perfect squeezed is reduced and the dip is broadened as  $\rho$  increases. The reason for this is that the SH phase change from one cavity round trip to another grows with increasing  $\rho$  and hence the phase of the quadrature, in which the best squeezing of the subharmonics is found, is different for each round trip. If we average the squeezing over many round trips we end up with a mixture of the squeezed and antisqueezed quadratures with an arbitrary phase resulting in nothing but the initial vacuum fluctuations entering the IOPO. This is why we see the spectrum of squeezing approaching a flat line at the vacuum level as  $\rho \rightarrow \infty$  in fig. 9.4.

### 9.4.3 IOPO reflection

Extending the discussion from the last section we now devise an experiment in which the amplitude noise of the field reflected off the IOPO cavity is recorded around the fundamental frequency (fig. 9.1). The measurement is assumed the enough bandwidth to enable the observation of the quantum noise of the fundamental as well as the beatnote of the fundamental carrier against the downconverted fields.

By using the beamsplitter relations on the IOPO coupler assuming the transmission of this to be

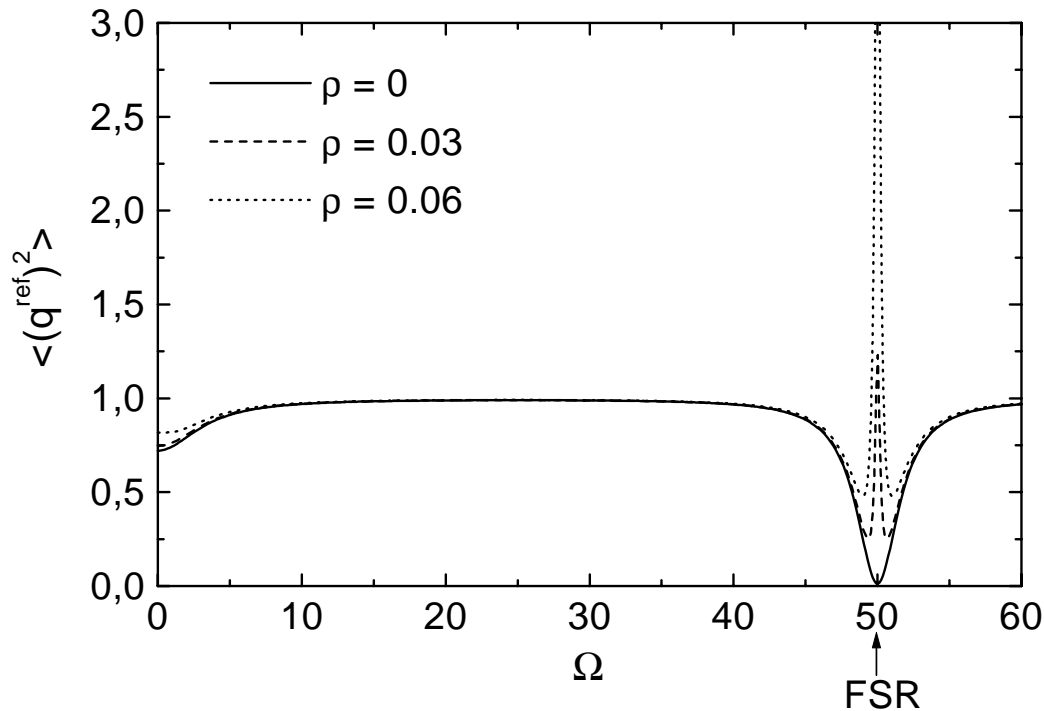


Figure 9.5: The spectrum of amplitude noise in the IOPO reflection. The traces correspond to  $\sigma = 0.8$  and  $\eta = 1$ . The IOPO cavity FSR has been assumed to be 50 linewidths.

small, we find the reflected stationary field to be

$$\bar{X}^{ref} = -2\mathcal{E} + \sqrt{2\kappa}\bar{X}_1 e^{-i\theta_1} \quad (9.40)$$

The phase  $\psi$  of this field is

$$\psi = -\arctan\left(\frac{\sin\theta_1}{\cos\theta_1 - \frac{\sigma}{\sqrt{2}\eta\Gamma}\sqrt{1 + \frac{1}{\sqrt{1+\rho^2}}}}\right) \quad (9.41)$$

from which we now can find the amplitude noise of the field. Towards this end we use (9.22) and (9.28) to project the noise found in the last two sections onto the coherent amplitude of the reflected field (9.40) since this is now acting as a local oscillator to the detection scheme. The resulting spectra of fluctuations are shown in figure 9.5 for three different SH detunings. In the figure the FSR has been taken to be 50 cavity linewidths. For zero SH detuning we find 25% quantum noise reduction around zero frequency as a result of the noise eating second harmonic generation. However, around the FSR frequency, where the IOPO has a high gain due to the cavity build up, we find perfect squeezing due to the nondegenerate parametric downconversion. The same feature would be observed at higher frequencies being an integer times the FSR as long as the phasematching conditions in the nonlinear medium are fulfilled.

With a finite SH detuning we see noise spikes entering the squeezing around the FSR frequency due to the mixing of the squeezed quadrature with the strongly antisqueezed quadrature. This is seen to be a strong effect even at values of  $\rho$  of a few percent, meaning that good control of the SH detuning is

needed if strong squeezing should be observed in the IOPO reflection. Around zero frequency the same effect can be observed, but due to the smaller amount of squeezing here, the mixing of the quadratures is less critical. In order to see better squeezing around zero frequency we found in section 9.4.1 that a large value of  $\rho$  is required. However this would cause a phaseshift between the local oscillator reflected directly off the cavity and the squeezed field coming out from the IOPO, meaning that only a mixture of the noise in the squeezed and the antisqueezed quadratures would be observed.

It should be pointed out that all our results rely on perfect spatial modematching of the fundamental pump into the IOPO cavity. In case of nonperfect modematching the threshold will be raised by the amount  $\mu^{-1}$  where  $\mu$  is the degree of modematching. However the quantum noise reduction observed in the cavity reflection will suffer by the additional  $1 - \mu$  units of vacuum noise which would be mixed into the local oscillator mode together with the squeezed vacuum. Hence the smallest achievable quantum noise would be  $1 - \mu$  in the case of perfect correlations of the IOPO output.

## 9.5 Summary

In this chapter we have treated the internally pumped OPO (IOPO) in which the fundamental and the subharmonic fields are perfectly resonant and the second harmonic is either nonresonant or resonant with an arbitrary detuning. A threshold pump power marking the onset of parametric oscillations was found in the plane wave approximation and this was seen to depend critically on the cavity response to the second harmonic field. Below the threshold we derived the steady state intracavity fields, and they turned out to be governed by the function  $\Gamma(\sigma, \rho)$  (9.20). With zero second harmonic detuning, the intracavity second harmonic field, required to drive the OPO above threshold, was seen to be a factor of 2 larger than in the externally pumped OPO described in section 2.2. This is a result of the cascaded process taking place in the IOPO where the second harmonic is generated inside the same medium in which the parametric downconversion takes place. All of our results are valid within the plane wave approximation where focusing and phasematching of the interacting modes are not taken into account. Furthermore the cavity finesse for the second harmonic has been assumed to be a lot smaller than the finesse for the low frequency modes since the former is adiabatically eliminated in our treatment.

In practice when constructing the IOPO one has to decide whether it is worth resonating the second harmonic in the cavity and thereby reducing the threshold, but paying the price of having to stabilize the cavity to yet another field. Alternatively the second harmonic could just be allowed to escape to IOPO in which case the threshold could go as high as several hundreds of milliWatts or even Watts, depending on the cavity configuration. If only squeezing around the FSR is desired, the high sensitivity of the noise reduction to the second harmonic detuning probably makes it disadvantageous to resonate the second harmonic, since very good servo control of the cavity length is needed in this case. However if good squeezing in the fundamental is desired, we have seen that a large value of the parameter  $\rho$  is required. This can only be obtained if the second harmonic is built up in the cavity.

The strong squeezing found in the IOPO reflection around the FSR frequency makes this device an attractive source of high frequency squeezed light which may find its application in certain areas of optical communication. Furthermore the relative simple optical setup needed, as long as the second harmonic is nonresonant, makes it possible to construct the IOPO as a very compact squeezed light source.

# Chapter 10

## Epilogue

The work presented in this thesis has covered a large area of optical and atomic physics. For this reason the thesis will now be concluded with a brief summary of the most important results obtained during this work together with an outlook on possible future experiments.

### 10.1 Conclusions

#### 10.1.1 Frequency tunable squeezed light generation

One of the cornerstones of this thesis has been the generation and detection of frequency tunable squeezed light. In this context we have seen how the squeezed states of light can be generated in an optical parametric oscillator operating below the threshold. In chapter 2 we addressed the quantum properties of the OPO and found that perfect squeezing in the output is obtained around DC when it is operating exactly on threshold. However the loss of squeezing at smaller pump powers was found to be bearable so that 97% quantum noise reduction can be achieved in an ideal OPO when pumping it at only 50% of the threshold power. By an ideal OPO we mean an OPO with no intracavity losses except the output coupler transmission. Since the squeezed vacuum generated in a subthreshold OPO is made up by quantum correlated photon pairs, it is very important that only one port is open to the external reservoir of electromagnetic field modes, namely the output coupler. Any additional loss mechanisms will provide other ports through which one or both photons of a pair can escape and consequently evade detection. A photon inside the OPO cavity has a probability of escaping through the output coupler given by the OPO escape efficiency  $\eta = \mathcal{T}/\mathcal{T} + \mathcal{L}$ , where  $\mathcal{T}$  is the output coupler transmission and  $\mathcal{T} + \mathcal{L}$  are the total OPO losses. Experience from previously performed squeezing experiments has shown that the degree of squeezing typically is limited by the escape efficiency.

High nonlinearity and low passive losses in the near infrared region makes Potassium Niobate an attractive medium for various nonlinear  $\chi^{(2)}$  and  $\chi^{(3)}$  mixing processes and hence we have used this material as the nonlinear medium in our frequency doublers and OPO's throughout this thesis work. A serious drawback of this material is however the nonlinear losses associated with the Blue Light Induced InfraRed Absorption or BLIIRA in short. In chapter 3 this effect was investigated and it was shown that the OPO escape efficiency can be improved by increasing the output coupler transmission and pumping the OPO with more light provided that the BLIIRA does not grow faster than the square root of the pump power. Experimentally it was found that the growth of BLIIRA was very close to this rate and hence no significant improvement in the escape efficiency was observed at pump powers higher than a few hundred mW. This necessitated the search for ways to inhibit the BLIIRA and a shift to longer wavelengths and consequently higher phasematching temperatures turned out to be fruitful. The BLIIRA turned out to decrease with increasing temperature of the  $\text{KNbO}_3$  crystals and this effect was particularly strong in Magnesium doped samples where a drop of an order of magnitude was observed. However in

the latter the BLIIRA was much higher at small temperatures than in undoped samples and hence the drop in BLIIRA from the best samples at low temperatures to the best samples at high temperatures was about a factor of 2-3. In order to explain the behavior of the Magnesium doped crystals we put forward an alternative to the two center charge transport model usually employed when light induced absorption processes are modelled. Our model was based upon a cascaded excitation of electrons from the valence band to the conduction band via impurity levels located not far below the conduction band.

In chapter 4 we used our observations of the temperature dependence of BLIIRA to construct a frequency tunable squeezed light source around 917 nm. This wavelength was desirable because it corresponds to the  $6P_{3/2} \rightarrow 6D_{5/2}$  transition in atomic Caesium which we wanted to address in a later experiment described in chapter 5. Furthermore it was attractive to operate around this wavelength because the phasematching temperature in a cut  $\text{KNbO}_3$  is around  $130^\circ\text{C}$  at 917 nm and hence we could expect BLIIRA to be reduced significantly.

Our squeezed light source was made up of a frequency doubler providing the pump at 458 nm for the subthreshold OPO. From our frequency doubler we had 200-250 mW for pumping our OPO and the conversion efficiency from 917 nm to 458 nm was in the vicinity of 80% with 300 mW infrared pump, all depending on the day to day performance. Injecting the frequency doubled light into our OPO, we observed the phase sensitive gain of a seeding beam to be as high as 17. From the gain measurements we could infer the OPO pump parameter  $\sigma = \sqrt{P/P_{th}}$  and hence the threshold power and crystal nonlinearity. Because of the pump power dependent losses from BLIIRA, the OPO threshold was found to depend on the pumping power as well. In fact it was found to increase from 300 mW with small pump powers to around 350 mW with 200 mW pump. By using simultaneous measurements of the BLIIRA we could infer the crystal nonlinearity to be around 0.5 %/W. This, for  $\text{KNbO}_3$  rather small, nonlinearity was attributed to astigmatism in the OPO resonator. By blocking the seeding beam to the OPO and doing balanced homodyne detection of the squeezed vacuum as the relative phase between the local oscillator (LO) and the squeezed vacuum was scanned, we were able to see the phase sensitive vacuum fluctuations emerging from the OPO. At some relative phase the noise level of these fluctuations was 11.5 dB above the free vacuum level corresponding to a gain of 14. But when the relative phase was shifted  $\pi/2$  the fluctuations of the squeezed vacuum dropped -5 dB below the free vacuum level corresponding to residual vacuum fluctuations of 31% of the original level. The BLIIRA was found to be reduced with about a factor of 2 in our experiment relative to previously performed squeezing experiments around 852 nm, but we still found that our quantum noise reduction was limited by the OPO escape efficiency and hence the BLIIRA. However as compared to a similar experiment performed at room temperature, we found our escape efficiency to be increased from around 80% to 88% at  $130^\circ\text{C}$  crystal temperature. Hence for a realistic crystal nonlinearity of 1.5-2 % $\text{W}^{-1}$ , a significantly higher degree of squeezing could be anticipated at the elevated temperature due to the smaller amount of pump power required and the resulting reduction in BLIIRA.

### 10.1.2 MOT spectroscopy and spin noise

With our frequency tunable squeezed light at hand, we wanted to use this for spectroscopy on atomic Caesium. For this purpose a magneto optical trap (MOT) was built in which about  $10^6$  Cs atoms were confined at a density around  $10^8 \text{ cm}^{-3}$ . The atoms were trapped on the  $6S_{1/2}(F=4) \rightarrow 6P_{3/2}(F=5)$  transition using five intense beams from a diode laser. As a result of the strong trapping beams almost 50% of the atoms were in the excited state where they could be probe by our squeezed light on the  $6P_{3/2}(F=5) \rightarrow 6D_{5/2}(F=4,5,6)$  transitions. For this purpose a polarization interferometer (PI) was built around the MOT, with which the change of the polarization angle of a linearly polarized probe could be measured. We found in chapter 5 that the PI was sensitive to the circular birefringence and the linear dichroism of the atomic medium. The first effect is dispersive and hence it is expected to dominate off resonance whereas the latter is dissipative and dominates close to resonance. To achieve sensitivity beyond the standard quantum limit we mixed a coherent state with the squeezed vacuum from our OPO on a polarizing beamsplitter. By adjusting the relative phase between the two fields we saw that it

is possible to squeeze either the Stokes parameter  $s_1$  or  $s_2$ . The first of these describes the difference between the linearly polarized components along axes directed  $\pm 45$  degrees relative to the  $x$  axis and the latter describes the ellipticity of the probe polarization. In the PI the first quantity is measured and hence we squeezed  $s_1$  in our experiment. In this experiment we were able to achieve -3 dB quantum noise reduction in the PI with the relative phase between squeezed vacuum and the coherent state locked.

In order to derive an atomic signal a single trapping beam was intensity modulated at a 3 MHz rate, and the transfer of this modulation to the probe via the atomic  $\chi^{(3)}$  nonlinearity was measured. Using the polarization squeezed probe in the PI we demonstrated an improvement in the signal to noise ratio of a factor of 2 relative to a probe in the coherent state. It was also found that the circular birefringence dominated the atomic signal due to the geometry used in this particular experiment.

To give the atomic signals the attention they deserved, we conducted in chapter 6 a series of experiments in which a purely classical probe was used in the PI. Now the trapping beams were all frequency modulated at a 3 MHz rate and consequently the induced atomic dipole moments were modulated as well. The setup associated with the PI allowed us to measure the modulated polarization rotation as well as the modulated absorption of the probe. Due to the detuned, strongly saturating trapping beams the PI atomic signal displayed Autler Townes splitting and by varying the detuning we could infer the Rabi frequency from the modulated absorption to be 7.5 MHz. The lineshapes of the modulated absorption and polarization rotation were found to be in reasonable qualitative agreement with the results of a three level ladder model. However this model assumed the atoms to follow the modulation adiabatically which was a somewhat crude approximation since the modulation frequency was comparable to the atomic decay rate of 5.3 MHz. As a result we found the theoretical linewidth to be 2-3 times smaller than the experimental, and by comparing to a more elaborate nonadiabatic model we could account for a linebroadening of 1.8 times the natural linewidth. The residual broadening, which is commonly encountered in MOT spectroscopy, is attributed to the quadrupole magnetic field around the MOT together with the linewidth of the trapping laser. From the modulated absorption signals we found that we were sensitive to about  $10^4$  trapped atoms. The modulated polarization rotation signals were at least an order of magnitude smaller than the modulated absorption signals, and their size and shape was found to be very sensitive to the trap alignment and the relative intensity in the trapping beams. Hence polarization spectroscopy may turn out to be useful in future studies of trap dynamics. This series of measurements was concluded by the observation of modulated polarization rotation signals using nothing but the intrinsic phase noise of the semiconductor trapping laser. These lasers are providing light with a stable amplitude but extremely noisy phase and we demonstrated that it is possible to use the latter to provide the FM for spectroscopy. This series of experiments all gave probe shot noise limited signals and they showed the value of modulating the MOT itself rather than the probe in order to derive spectroscopic signals. By applying FM to the probe it is easy to encounter problems of parasitic AM due to imperfect modulation and conversion of FM into AM as a result of dispersion in optical elements as well as in the atoms. Such AM would limit the sensitivity of the measurement and also make it impossible to reach the shot noise limit.

The MOT experiments were concluded with the observation of the quantum noise of the atomic spin in chapter 7. In this experiment the probe laser was locked to the atomic resonance and hence the circular birefringence was not expected to give significant contributions. In order to describe the linear dichroism we defined a pseudospin,  $\vec{J}$ , with  $x$  and  $y$  components proportional to the alignment of the collective atomic magnetic moment along the corresponding axes. The  $z$  component describe the projection of the collective atomic spin on the  $z$  axis set by the propagation of the probe. The mean value of this spin was shown to be controlled in the transverse  $(x, y)$  direction by the relative phase of the  $\sigma^+$  and  $\sigma^-$  pumping fields driving the two transitions. Hence we see that the transverse alignment is parallel to the linear polarization of a pump field. The longitudinal component has a mean value determined by the difference between the intensities of the two pump fields. The quantum noise of the pseudospin was shown to be a result of the spontaneous atomic decay and hence it can be considered a quantum noise in the sense that it is a result of coupling of the atomic dipole moment to the quantum fluctuations of the electromagnetic field. A series of dependencies of the atomic spin noise on various parameters was put forward and the

most important of these was the dependence of the noise power on the number of probed atoms,  $N$ . For technical noise the noise power was found to grow as  $N^2$  whereas the stochastic quantum noise grows like  $N$ . Crude estimates showed that the ratio of quantum spin noise to probe shot noise only was a few percent and hence a setup, in which the latter could be detected for optical powers as small as a few hundred nW, was constructed. The spin noise is maximum for an optical depth of 1/2 and consequently we had to improve our MOT by building a Ti:Sapphire trapping laser to provide the trapping beams. The gain from this was twofold: First we had more power in the trapping beams and hence we could make the trap larger. An optical depth of 1.8 was observed on the probe transition and the total number of trapped atoms was around  $10^8$ . Second the Ti:Sapphire provided light which contained much less technical noise than the diode laser at the detection frequency so that the induced technical spin noise was kept small. We found the detected atomic spin noise to grow linear in  $N$  within 7% and hence we observed the quantum noise of the collective spin of a large number of atoms for the first time. By applying FM to the trapping laser we demonstrated the transition from quantum to technical spin noise manifested in a change of the dependence on the number of trapped atoms from linear to quadratic. Finally we demonstrated a simple experimental situation where the quantum spin noise of the trapped atoms limited the signal to noise in modulation spectroscopy.

### 10.1.3 Quantum teleportation

In chapter 8 the results of the authors visit at the Quantum Optics Group of California Institute of Technology were presented. Here attempts were made to teleport a quantum state defined in a Hilbert space of infinite dimensions. Up to this date only the teleportation of discrete quantum variables over macroscopic distances had been demonstrated.

By utilizing two (almost) independent squeezed fields we were able to create two entangled fields with correlated amplitudes and anticorrelated phases similar to the output of a nondegenerate OPO. The correlations were found to reduce the noise in the difference between the amplitudes of the two fields by -1 dB below the standard quantum limit corresponding to a remaining noise of 79%. One of these entangled fields was used to read out the quantum state to be teleported by means of two homodyne detectors aligned to measure orthogonal quadratures. By performing a continuum of phase space displacements on the other beam depending on the outcome of the homodyne measurements, the input quantum state could be reconstructed at another point in space arbitrarily far away from the detectors. The necessity of broadcasting the results of the measurements classically ensures that no information transfer takes place faster than the speed of light. In the experiment only a RF sideband of the input state was teleported and hence the phase space displacements could be made by means of applying AM or FM to a coherent state being overlapped with the second entangled beam. To verify the teleportation a third homodyne detector was measuring the quadratures of the teleported state. A fidelity of entanglement,  $\mathcal{F}$ , between the input state and the teleported state was proposed as a measure of the quality of the teleportation protocol. A fidelity of 1 corresponds to perfect quantum teleportation.

The best classical performance of such a teleportation setup would return the input quantum state with two additional units of vacuum noise. One of these come from the simultaneous detection of two noncommuting observables at the homodyne detectors and the other comes from the phase space displacements. This quantum tariff has been called the quantum duty or quduty in short. The quduty was seen to limit the fidelity of any scheme, utilizing only classical fields, to be less than 0.5. In the experiment a coherent state was teleported and the quduty was observed in the teleported state in the absence of nonclassical correlations. In the experiment we teleported a coherent state, and by employing the nonclassical light, the noise level of the teleported state was found to drop  $1.2 \pm 0.2$  dB below the classical noise level. Hence the information stored in the input state was transferred with an efficiency better than classical obtainable. The noise level from the two homodyne detections of the input state was found to increase by  $0.55 \pm 0.7$  dB since less information had to be obtained here in order not to violate the no cloning theorem. These issues indicated that quantum teleportation of continuous quantum variables was demonstrated for the first time. Further evidence was provided by a series of

measurements of the noise of the teleported state as the strength of the phase space displacements was varied. From these we inferred a maximum fidelity of  $\mathcal{F} = 0.58 \pm 0.03$  clearly higher than the best classical value of 0.5. This high fidelity could not have been achieved without the use of a nonlocal state and hence we concluded that we performed quantum teleportation of the continuous quadrature phases of the electromagnetic field. A series of measurements without the use of nonclassical light gave a highest fidelity of  $\mathcal{F} = 0.48 \pm 0.03$ , close to 0.5. This shows that our teleportation setup was nearly optimized to perform ideal classical teleportation.

Our teleportation scheme held the advantage over previous schemes, intended for teleportation of discrete variables, that the input state was teleported with an efficiency better than 90%. In contrast to this the efficiencies of the discrete teleportation schemes are on the order of  $10^{-8}$ . Furthermore our scheme teleported in real time without the necessity of any detection protocol, in which the specific events of interest could be selected. In the previous schemes the detection played an essential role for the teleportation process. As a result the teleported state was always absorbed on the detectors and could not be used in other contexts.

### 10.1.4 Internally pumped OPO

In chapter 9 this thesis was concluded with the result of a theoretical project that the author has been working with in parallel to the experimental work. Here the Internally pumped OPO (IOPO) was treated semiclassically. This device is simply a frequency doubler in which the second harmonic drives a nondegenerate OPO. The treatment included the possibility of having the second harmonic resonant in the cavity with an arbitrary detuning or having the second harmonic escaping the cavity. The threshold for parametric oscillations in the IOPO was derived and this was found to depend critically on whether the second harmonic was resonant or nonresonant and on the detuning of this field. For the resonant second harmonic and no detuning the threshold was found to become very small as a result of the large build up, and with large detuning the threshold grows very high as a result of the destructive interference of the second harmonic. The quantum noise of the fundamental and the downconverted fields was calculated below the IOPO threshold using a linearization procedure. In the former field a quantum noise reduction of  $1/3$  was found with no detuning of the second harmonic. Allowing for a finite detuning the noise reduction in the fundamental can be improved to  $2/3$  as a result of the negative feedback of the second harmonic field driving the degenerate parametric downconversion into this mode.

The squeezing in subharmonic fields was found to resemble the output of the conventional externally pumped OPO. The major differences are that the threshold of the IOPO was described in terms of the fundamental pump, whereas the externally pumped OPO is driven by the second harmonic. Furthermore in the externally pumped OPO the noise reduction is found in the quadratures describing the difference between the amplitudes and the sum of the phases. Due to the cascaded interaction with the nonlinear medium in the IOPO an additional  $\pi/2$  phaseshift occurs and hence squeezing is found in the orthogonal quadratures describing the sum of the amplitudes and the difference of the phases of the subharmonic fields. This turned out to be important for the noise properties of the field reflected off the IOPO cavity around the fundamental frequency. If we consider the pump field reflected directly off the cavity to act as a local oscillator for a heterodyne measurement, the additional phaseshift in the IOPO results in strong squeezing at frequencies being an integer times the cavity free spectrum range since longitudinal cavity modes placed symmetrically around the fundamental are strongly correlated due to the nondegenerate downconversion. Around zero frequency the interaction with the second harmonic field reduce this squeezing to  $1/4$  close to threshold. A finite second harmonic detuning would cause a mixing of the squeezed and antisqueezed quadratures and hence noise spikes show up in the spectrum of amplitude noise.

The simplicity of the IOPO setup makes it attractive for purposes where squeezing at high frequencies are desired. In fact monolithic versions of this device has already been operated above threshold and they have proven to be stable sources of widely tunable light. However the quantum noise of the reflection of the IOPO is still left to be investigated experimentally.

## 10.2 Outlook

The experimental and theoretical work described in this thesis holds the potential to be extended in new directions. This section, concluding the thesis, will provide an outlook on the potential paths which can be followed.

### 10.2.1 Spin squeezing and entangled atomic ensembles

A natural continuation of the atomic spin noise experiment will be to seek to reduce this noise by creating a Squeezed Spin State. These states have been proposed created by absorbing squeezed vacuum in the atomic medium and thereby transferring the correlations from the light to the atoms. As we saw in chapter 7, a problem with this approach is the spontaneous decay of the collective atomic spin, which couples the spin to the fluctuations of the free vacuum in addition to the squeezed vacuum. However it has been shown that in a steady state situation where a perfectly squeezed field is absorbed completely in the atomic medium, a 50% reduction of the spin fluctuations is achievable[100]. By mixing squeezed vacuum with a coherent state on a polarizing beamsplitter as described in chapter 5 and sending the combined field through a quarter wave retarder, a  $\sigma^+$  polarized squeezed field and a  $\sigma^-$  polarized coherent field can be created. These can now interact with  $\Delta m = +1$  and  $\Delta m = -1$  transitions in an ensemble of cold, trapped atoms. As a result one of the transverse components of the pseudospin defined in chapter 7 can be squeezed. The direction along which the spin is squeezed is set by the relative phase between the coherent state and the squeezed vacuum[10]. Due to the coherent  $\sigma^-$  polarized field, the mean spin will point in the negative  $z$  direction. The direction of this spin vector will be defined within an ellipse in the  $(x, y)$  plane with major and minor axes set by the noise in the two quadratures of the squeezed vacuum and the orientation is set by the relative phase between squeezed vacuum and the coherent field.

It may prove possible to evade the problem of losing the spin squeezing due to atomic decay. By employing two Raman transitions using a strong coherent field and one part of a set of entangled fields in each transition, it may be possible to reach another hyperfine level of the ground state or a metastable excited state. As a result entangled pairs of atoms in different spin states can be created resulting in a squeezed collective spin. Because the final states of the Raman transitions can have a long lifetime, the correlations may survive for several milliseconds or even seconds depending on the collision rate in the atomic medium. The entangled fields used here could for instance be the output of a nondegenerate OPO or the probe used in the polarization interferometer in chapter 5 which can be shown to consist of quantum correlated  $\sigma^+$  and  $\sigma^-$  polarized photons.

The last idea may be extended one step further by considering two distinguishable atomic ensembles such as a double MOT or two magnetic substates trapped in a magnetic trap. By exciting one atomic ensemble with one entangled field and the other ensemble with the second field, the two macroscopic atomic ensembles can be made entangled in the EPR sense. Such entangled ensembles may prove useful for quantum computation and key distribution in quantum cryptography.

The present work in the Aarhus Quantum Optics Lab is devoted to realizing the above outlined ideas experimentally, however the obstacles to cross before reaching these goals are still considerable.

### 10.2.2 Quantum communication for teleportation and cryptography

Teleportation of a quantum state over macroscopic distances requires transfer of the quantum information stored in the state. Hence the teleportation setup described in chapter 8 could relatively easily be modified to test other aspects of the theory of Quantum Communication. One of these is the quantum cryptography where information can be stored in a quantum state which is broadcast from Alice to Bob. According to the Heisenberg uncertainty principle this quantum state and hence the information cannot be detected by an eavesdropper without altering the state, in which case the eavesdropping can be revealed. In our teleportation experiment the classical photocurrent sent from the homodyne detectors at Alice to the actuator at Bob was very noisy as a result of the increased noise in a single of the entangled

beams. A weak signal could easily be encoded in the quantum state to be teleported, and due to the noisy photocurrent it would be impossible to extract the signal without the second entangled beam to cancel the noise. In this way the second beam could be made the key with which the information encrypted by Alice can be decrypted, and the photocurrent could act as a public communication channel. Provided the ideas outlined in section 10.2.1 works, it may even turn out to be possible to store the quantum information of the second beam in a long lived atomic system, which then can be transported by courier from Alice to Bob where the stored information can be extracted and the transmitted signal decrypted. It should be stressed here that these ideas rely only on handwaving arguments so far, and that the security of this kind of quantum cryptography may turn out to be very difficult to prove as a result of the infinite number of dimensions in the Hilbert space used.

Another field of Quantum Information, into which the quantum teleportation experiment could be extended, is the dense coding of information. In analogy to the dense coding of digital information demonstrated using entangled two state particles[112], the entangled fields, driving the quantum teleportation in chapter 8, could be used for superdense coding of analogue signals. Clearly this could be of great interest in optical communication, where increasingly higher bandwidths are needed in order to deal with the massive amounts of information broadcast in our modern society.

### 10.2.3 The IOPO as a compact squeezer

Finally the quantum noise reduction in the reflection of the internally pumped OPO around the free spectrum range of the IOPO cavity deserves to be investigated experimentally. Two major problems arise in this context: First the free spectrum range of an optical resonator is typically several hundreds of MHz to a few GHz and hence fast photodiodes with high quantum efficiency are needed in order to observe the squeezing. Second the optical power reflected off the IOPO is considerable unless the threshold can be made very low. This could cause problems with saturation of the detector. The first problem can be solved by constructing an IOPO cavity several meters long. For a 3 m long resonator for instance, the free spectrum range is 100 MHz which is within the bandwidth of standard high frequency detectors. A solution to the second problem could be to resonate the second harmonic, for instance in a separate resonator with a high finesse in which case the threshold in principle could be made arbitrarily low. However this adds the additional complication of another servoloop keeping the second harmonic resonator on resonance, and as we saw in chapter 9 any detuning of the second harmonic should be avoided in order to keep the subharmonic quadratures aligned to the pump.

Currently attempts are being made in the Aarhus Quantum Optics Lab to construct an IOPO and observe the squeezing in the reflection of this.

# Appendix A

## Classical OPO theory

In this appendix the OPO will be treated classically taking into account the focused Gaussian beams entering the nonlinear interaction. The goal of this calculation is to identify the focusing which will minimize the OPO threshold and consequently maximize the parametric gain.

The starting point of our classical calculations is the wave equation with sources derived from the Maxwell equations

$$\left(\nabla^2 - \frac{n^2}{c^2} \frac{\partial}{\partial t^2}\right) \vec{E}(\vec{r}, t) = \mu_0 \frac{\partial^2 \vec{P}}{\partial t^2} \quad (\text{A.1})$$

Here  $\vec{E}$  is the electric field and  $\vec{P}$  is the macroscopic polarization of the nonlinear medium.  $c$  is the speed of light,  $n$  is the index of refraction and  $\mu_0$  is the vacuum permeability. Making now the following ansatz for our signal and idler electric fields  $\vec{E}_\pm$ , and the second harmonic pump field  $\vec{E}_2$

$$\vec{E}_j(\vec{r}, t) = \hat{\epsilon}_j \mathcal{E}_j(\vec{r}) e^{i(k_j z - \omega_j t)}, \quad j = \{+, -, 2\} \quad (\text{A.2})$$

where  $\hat{\epsilon}$  is the polarization unit vector, and employing the slowly varying envelope approximation

$$\left| \frac{\partial^2 \mathcal{E}_\pm}{\partial z^2} \right| \ll k_\pm \left| \frac{\partial \mathcal{E}_\pm}{\partial z} \right|, \quad \left| \frac{\partial \mathcal{E}_\pm}{\partial z} \right| \ll k_\pm |\mathcal{E}_\pm|, \quad \left| \frac{\partial \mathcal{E}_\pm}{\partial t} \right| \ll \omega_\pm |\mathcal{E}_\pm| \quad (\text{A.3})$$

we end up with the paraxial wave equation with sources

$$e^{i(k_\pm z - \omega_\pm t)} \left( \nabla_T^2 + 2ik_\pm \frac{\partial}{\partial z} \right) \mathcal{E}_\pm(\vec{r}) = \mu_0 \hat{\epsilon}_\pm \cdot \frac{\partial^2 \vec{P}}{\partial t^2} \quad (\text{A.4})$$

The wavenumbers have been defined as  $k_\pm = n_\pm \omega_\pm / c$ , and the transverse Laplacian is given by  $\nabla_T^2 = \partial^2 / \partial x^2 + \partial^2 / \partial y^2$ . So far the approach has been quite general and can be applied to any linear or nonlinear process. Turning now towards the process of parametric downconversion we consider the source term of the form

$$\mu_0 \hat{\epsilon}_\pm \cdot \frac{\partial^2 \vec{P}}{\partial t^2} = \sum_{i,j,k} (\epsilon_\pm)_i \chi_{ijk} [E_2(\vec{r}, t)]_j [E_\mp^*(\vec{r}, t)]_k, \quad \{i, j, k\} = \{x, y, z\} \quad (\text{A.5})$$

where  $E_2$  is the pump field and  $\chi_{ijk}$  is the second order nonlinear tensor. We now define an effective nonlinear interaction strength  $\chi$  such that

$$\mu_0 \hat{\epsilon}_\pm \cdot \frac{\partial^2 \vec{P}}{\partial t^2} = \chi \left[ \hat{\epsilon}_2^* \cdot \vec{E}_2(\vec{r}, t) \right] \left[ \hat{\epsilon}_\mp \cdot \vec{E}_\mp^*(\vec{r}, t) \right] \quad (\text{A.6})$$

Obviously  $\chi$  is depending on the geometry of the problem.

Given that our OPO cavity is bounded by spherical mirrors, the intracavity field mode is known to be Gaussian. The Gaussian field is characterized by four parameters: The waist position ( $z = 0$ ), the Rayleigh length  $z_0$  and two indices specifying the angular field distribution. The latter will be omitted in the following for simplicity. The explicit form of the Gaussian TEM<sub>00</sub> mode is

$$\mathcal{E}_j(\vec{r}) = \frac{A_j(u)}{1+iu} \exp\left(-\frac{\rho^2}{1+iu}\right), \quad u = \frac{z}{z_0}, \quad \rho^2(\lambda) = \frac{\pi(x^2 + y^2)}{\lambda z_0}, \quad j = \{+, -, 2\} \quad (\text{A.7})$$

Here  $\lambda$  is the wavelength in vacuum and  $A$  is the field amplitude. We note that the Rayleigh length  $z_0$  is independent on the wavelength, whereas the radial coordinate  $\rho$  does depend on  $\lambda$ . The total power in a Gaussian beam is found to be

$$P(u) = \frac{1}{4} c \varepsilon_0 \lambda z_0 |A(u)|^2 \quad (\text{A.8})$$

where  $\varepsilon_0$  is the vacuum permittivity.

Inserting (A.7) in (A.4), we find the equations of motion for the Gaussian amplitudes

$$\frac{1}{A_{\pm}} \frac{dA_{\pm}}{du} \mathcal{E}_{\pm} = -i \frac{\xi}{4} \frac{A_2 A_{\mp}^*}{1+u^2} e^{-i\kappa u} e^{-\frac{2\rho^2}{1+iu}} e^{-\frac{\rho^2}{1-iu}} \quad (\text{A.9})$$

where the dimensionless nonlinear coupling constant  $\xi$  has been defined as  $\xi = \lambda z_0 \chi / \pi$  and the dimensionless phasemismatch is given by  $\kappa = z_0(k_+ + k_- - k_2)$ . Deriving (A.9) a small splitting between signal and idler frequencies has been assumed, such that  $\lambda_- - \lambda_+ \ll (\lambda_+ + \lambda_-)/2$ . Finally the  $\rho$  used in (A.9) is defined according to (A.7) for the wavelength  $\lambda = 2\pi c/\omega$ , where  $\omega$  is half the pump frequency.

From (A.9) it is clear that the spatial mode of downconverted fields in the OPO is not a pure TEM<sub>00</sub>, even though the pump mode is. If however the OPO cavity is stabilized to be resonant for the TEM<sub>00</sub> modes of the frequencies  $\omega_{\pm}$ , the expansion of the downconverted field modes on the cavity TEM modes will only have an appreciable amplitude on the TEM<sub>00</sub>. Consequently all higher order modes will be ignored when the right and left hand sides of (A.9) are expanded on TEM modes of  $E_{\pm}$ , and as a result we find

$$\frac{1}{A_{\pm}} \frac{dA_{\pm}}{du} \int_S |\mathcal{E}_{\pm}|^2 dS = -i \frac{\xi}{4} \frac{A_2 A_{\mp}^* A_{\pm}^*}{1-iu} e^{-i\kappa u} \int_S \frac{e^{-\frac{4\rho^2}{1+u^2}}}{1+u^2} dS \quad (\text{A.10})$$

Performing now the integration over the transverse coordinates,  $S$ , we find the longitudinal equation of motion of the OPO

$$\frac{dA_{\pm}}{du} = -i \frac{\xi}{8} A_2 A_{\mp}^* \frac{e^{-i\kappa u}}{1-iu} - \Gamma_{\pm} A_{\pm} \quad (\text{A.11})$$

In the equation above we have added the intracavity losses for the signal and idler modes  $\Gamma_{\pm}$  by hand in the attempt to take into account the role of the cavity around our  $\chi^{(2)}$  medium. We note that in the limit of small intracavity losses  $\Gamma_{\pm} \ell / z_0 \simeq (\mathcal{T}_{\pm} + \mathcal{L}_{\pm})/2$ , where  $\ell$  is the cavity optical length and  $\mathcal{T}_{\pm}$  and  $\mathcal{L}_{\pm}$  are the cavity coupler transmission and remaining losses to the signal and idler modes respectively. The distinction between the two sources of loss is convenient when one is looking at the quantum nature of the OPO. The combined system of nonlinear medium and cavity is illustrated in figure A.1(a).

Finally we demand that the signal and idler fields are resonant in the OPO resonator, meaning that when we integrate (A.11) over one cavity roundtrip we must get zero. This is easily seen from the left hand side:  $\int (\partial A_{\pm} / \partial u) du = A_{\pm}(\ell) - A_{\pm}(0) = 0$  for a resonant field. Doing the integration we end up with the following set of coupled homogenous equations

$$\begin{pmatrix} c_+ & c_I & 0 & 0 \\ c_I^* & c_- & 0 & 0 \\ 0 & 0 & c_- & c_I \\ 0 & 0 & c_I^* & c_+ \end{pmatrix} \begin{pmatrix} A_+ \\ A_-^* \\ A_- \\ A_+^* \end{pmatrix} = \mathbf{C} \vec{A} = \vec{0} \quad (\text{A.12})$$

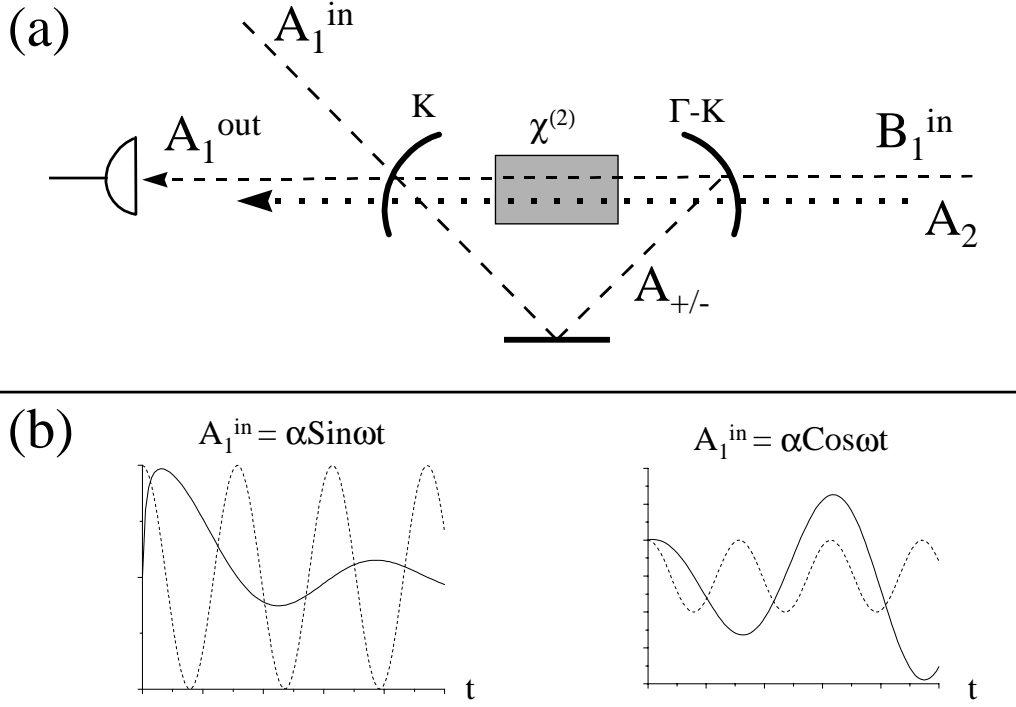


Figure A.1: (a) The Optical Parametric Oscillator, made up by a  $\chi^{(2)}$  crystal embedded in an optical cavity. (b) The phase sensitive gain. The dotted line is the pump field at a frequency  $2\omega$ . Depending on the phase of the fundamental field it is either amplified or deamplified.

The elements of  $\mathbb{C}$  are defined as

$$c_{\pm} = -\Gamma_{\pm}\Lambda_{cav}, \quad c_I = -i\frac{\xi}{8}A_2I \quad (\text{A.13})$$

where  $\Lambda_{cav} = \ell/z_0$ . The integral  $I$  contains the dependence of the nonlinear coupling on the phase mismatch and focusing of the pump, and is defined as

$$I = \int_{-\Lambda_{cr}/2}^{\Lambda_{cr}/2} \frac{e^{-iku}}{1-iu} du \quad (\text{A.14})$$

It has been used that the nonlinear interaction term in (A.11) only picks up a contribution in the  $\chi^{(2)}$  crystal, which is placed symmetrically around the waist, and consequently the limits of the integration are set by  $\Lambda_{cr}/2 = \ell_{cr}/2z_0$ , where  $\ell_{cr}$  is the length of the nonlinear medium. Our calculation assumes undepleted pump, meaning that  $A_2$  is constant over the integration.

In order to obtain nontrivial solutions for the downconverted fields we must demand that

$$|c_I|^2 = c_+c_- \quad (\text{A.15})$$

which defines the pump field amplitude  $A_2^{th}$  required to take the OPO above threshold

$$|A_2^{th}|^2 = 64 \frac{\Gamma_+\Gamma_-\Lambda_{cav}^2}{\xi^2 |I|^2} \quad (\text{A.16})$$

To elaborate a bit more on this threshold, we identify the single pass nonlinearity for second harmonic generation by using the longitudinal equation for this process. This can be derived following the same procedure as above to be

$$\frac{dA_2}{du} = -\frac{i}{4}\xi \frac{e^{i\kappa u}}{1+iu} A_1^2 \quad (\text{A.17})$$

Now integrating over the crystal and using (A.8), we find the single pass second harmonic power  $P_2$  in terms of the fundamental power  $P_1$  and consequently the single pass nonlinearity  $E_{NL}$  defined as

$$E_{NL} = P_2/P_1^2 = \frac{\xi^2 I^2}{16c\varepsilon_0\lambda z_0} \quad (\text{A.18})$$

where we have used that the real part of the integrand of  $I$  is even and the imaginary part is odd in  $u$ . Since we integrate symmetrically around  $u = 0$ ,  $I$  turns out to be real.

If we now apply (A.8) to (A.16) and use the above expression for the single pass nonlinearity we find the threshold pump power for the OPO to be

$$P_2^{th} = \frac{\Gamma_+\Gamma_-\Lambda_{cav}^2}{E_{NL}} \simeq \frac{(\mathcal{T}_+ + \mathcal{L}_+)(\mathcal{T}_- + \mathcal{L}_-)}{4E_{NL}} \quad (\text{A.19})$$

Once the pump power has reached this value inside the crystal, it will remain at this level even if the external power is increased. The physical reason for this is that any additional pump power will be downconverted into the signal and idler fields which are nonzero above threshold. This is nothing but a nonlinear analogue of what is known as gain clamping in (linear) laser systems[142].

To minimize the threshold, we obviously want to minimize the intracavity losses and maximize the nonlinearity of our  $\chi^{(2)}$  crystal. The latter is seen from (A.18) to depend on the focusing and phase mismatch through  $I$  and the  $z_0$  contained in  $\xi$ . Consequently we want to maximize the quantity

$$E_{NL}/\beta = \frac{1}{\Lambda_{cr}} \left( \int_{-\Lambda_{cr}/2}^{\Lambda_{cr}/2} \frac{\cos \kappa u + u \sin \kappa u}{1+u^2} du \right)^2 \quad (\text{A.20})$$

where  $\beta = \lambda \ell_{cr} \chi^2 / 8\pi^2 c \varepsilon_0$  is a constant independent on the focusing. The maximum value of  $E_{NL}/\beta$  is 2.135 corresponding to  $\Lambda_{cr} = 5.675$  and  $\kappa = \kappa_{opt} = 0.574$ , in agreement with previously achieved results calculated by using diffraction theory[143]. From figure A.2 it is seen that the maximum of the nonlinearity is rather broad and consequently a change in  $\Lambda_{cr}$  of 25% only reduces the nonlinearity with about 10%. It is also noted that the optimum conversion occurs for nonzero phase mismatch. This is a direct consequence of the divergence of a Gaussian beam. The divergence results in a beam which is composed of wavevectors that are not parallel to the axis of propagation except very close to the center of the beam. This is in contrast to a plane wave, where the wavevectors everywhere in the beam are parallel to the axis of propagation. As a result we need the phase mismatch to be nonzero for the Gaussian beam in order to get an appreciable contribution to the nonlinear conversion from the outer parts of the beam. From figure A.2 we find that zero phase mismatch  $\kappa = 0$  will reduce the nonlinearity with almost 50%, indicating that the beam divergence is indeed an important issue when the nonlinear conversion has to be optimized.

The above treatment can be applied to the degenerate OPO as well. All we need to do is to set  $\Gamma_+ = \Gamma_- = \Gamma$ . With this in mind we are now turning towards the phase sensitive degenerate Optical Parametric Amplifier, with the goal of calculating the phase sensitive gain of this device.

The equation of motion for the degenerate OPO is obtained from (A.11) by putting  $A_+ = A_- = A_1$ . We imagine that the gain is measured by seeding the OPO with a weak coherent beam, and measuring the transmission of this beam through the output coupler. In this case we find the equation of motion

$$\frac{dA_1}{du} = -i\frac{\xi}{8} A_2 A_1^* \frac{e^{-i\kappa u}}{1-iu} - \Gamma A_1 + \sqrt{\frac{\ell}{c}} \left[ \sqrt{2K} A_1^{in} + \sqrt{2(\Gamma-K)} B_1^{in} \right] \quad (\text{A.21})$$

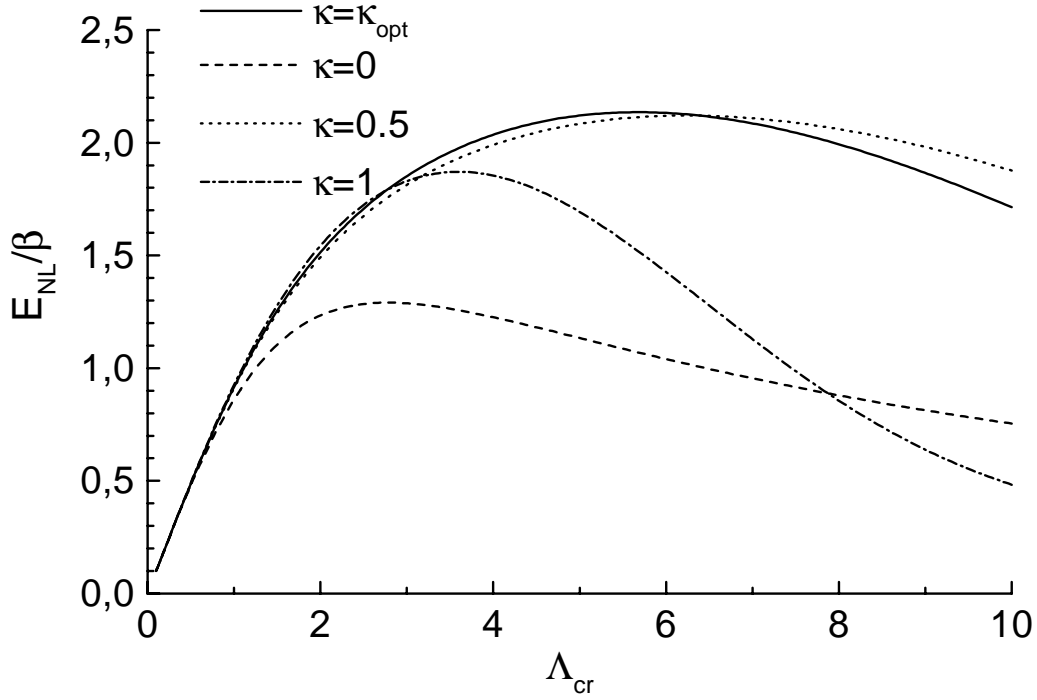


Figure A.2: Single pass nonlinearity vs.  $\Lambda_{cr} = \ell_{cr}/z_0$  for different values of the phase mismatch  $\kappa = (k_+ + k_- - k_2)z_0$ .

where  $K$  is the dimensionless decay rate through the output coupler, and  $A_1^{in}$  and  $B_1^{in}$  are the input fields through the output coupler and another mirror respectively. This is shown in figure A.1. If we again demand that  $A_1$  is resonant in the OPO cavity, and defining the phase  $\theta$  of  $A_1$  we obtain

$$A_1 = \sqrt{\frac{\ell}{c}} \frac{\sqrt{2K} A_1^{in} + \sqrt{2(\Gamma - K)} B_1^{in}}{(1 + ie^{-2i\theta}\sigma)\Gamma} \quad (\text{A.22})$$

where we have defined the OPO pump parameter  $\sigma = A_2/A_2^{th} = \sqrt{P_2/P_2^{th}}$ , and found the threshold to be  $A_2^{th} = 8\Gamma\Lambda_{cav}/\xi I$ . The phase of the pump has been chosen to be zero, meaning that  $A_2$  is real. By applying the boundary condition on the output coupler in the limit of high mirror reflectivity

$$A_1^{out} = \sqrt{\frac{c}{\ell}} \sqrt{2K} A_1 - A_1^{in} \quad (\text{A.23})$$

we find the OPO output field to be

$$A_1^{out} = \frac{2\eta A_1^{in} + 2\sqrt{\eta(1-\eta)} B_1^{in}}{1 + ie^{-2i\theta}\sigma} - A_1^{in} \quad (\text{A.24})$$

where we have defined  $\eta = K/\Gamma$ . It should be noted that here we have chosen the input fields to have zero phase, and the phase relative to the pump expressed through  $\theta$  can now be adjusted by varying the pump phase.

The power transmitted through the OPO normalized to the input power  $\tau$  can now be written up directly as

$$\begin{aligned}\tau &= \left| \frac{1-ie^{-2i\theta}\sigma}{1+ie^{-2i\theta}\sigma} \right|^2, B_1^{in} = 0, \eta \simeq 1 \\ \tau &= \frac{4\eta(1-\eta)}{|1+ie^{-2i\theta}\sigma|^2}, A_1^{in} = 0\end{aligned}\tag{A.25}$$

Here we are not interested in the case where both input fields are nonzero. The phase sensitive gain  $G(\theta, \sigma)$  defined as  $\tau(\sigma)/\tau(\sigma = 0)$  can now be found to be

$$\begin{aligned}G_A &= \left| \frac{1-ie^{-2i\theta}\sigma}{1+ie^{-2i\theta}\sigma} \right|^2, B_1^{in} = 0, \eta \simeq 1 \\ G_B &= \left| \frac{1}{1+ie^{-2i\theta}\sigma} \right|^2, A_1^{in} = 0\end{aligned}\tag{A.26}$$

Obviously it makes a difference whether the gain is measured by seeding the OPO through the output coupler ( $B_1^{in} = 0$ ) or through a high reflector ( $A_1^{in} = 0$ ). In both cases the gain is maximum for  $\theta = -\pi/4$ , in which case we find  $G_A = (1+\sigma)^2/(1-\sigma)^2$  and  $G_B = (1-\sigma)^{-2}$ . For an OPO on threshold ( $\sigma = 1$ ) the phase sensitive gain is seen to diverge. This indicates that our theory is not valid around this point, since infinite gain requires infinite energy pumped into the system. Clearly this energy is not available from the pump. Close to threshold the pump depletion becomes important due to the large energy transfer from the pump field to the subharmonics. This effect was neglected in our treatment, hence we get the absurd result of infinite gain. Minimum gain is found for  $\theta = \pi/4$ , where  $G_A = (1-\sigma)^2/(1+\sigma)^2$  and  $G_B = (1+\sigma)^{-2}$ . Here the difference between the two methods of seeding strikes us, since on threshold  $G_A = 0$  whereas  $G_B = 1/4$ . The same mechanisms responsible for the phase sensitive gain of the degenerate OPO, are responsible for the squeezed output.

## Appendix B

# Teleportation of discrete Quantum Variables

With the goal of visualizing the basic physical ingredients needed in quantum teleportation, we present here the original proposal of Bennett *et. al.*[113], in which the quantum state of a spin 1/2 particle is teleported. The work horse in this scheme is a so called EPR singlet, in which two particles, labeled '2' and '3', are entangled in the state  $|\Psi^{(-)}\rangle_{23} = 2^{-1/2} (|\uparrow\rangle_2 |\downarrow\rangle_3 - |\downarrow\rangle_2 |\uparrow\rangle_3)$ , where  $|\uparrow\rangle$  describes one particle with spin up and  $|\downarrow\rangle$  describes a particle with spin down. Clearly this is a highly correlated state, entangling the physical observables (the spin projection in this case) of the two particles being arbitrarily far away from each other. The quantum state to be teleported is the spin state  $|\phi\rangle_1 = \alpha |\uparrow\rangle_1 + \beta |\downarrow\rangle_1$  of a particle labeled '1'.

Since no information about the state  $|\phi\rangle_1$  must be obtained in the detection, the joint system of particles '1' and '2' is projected on the orthonormal basis of eigenstates for the Bell operator[144]. For a two particle system this is given by the following four states

$$|\Psi^{(\pm)}\rangle_{12} = 2^{-1/2} (|\uparrow\rangle_1 |\downarrow\rangle_2 \pm |\downarrow\rangle_1 |\uparrow\rangle_2) \quad |\Phi^{(\pm)}\rangle_{12} = 2^{-1/2} (|\uparrow\rangle_1 |\uparrow\rangle_2 \pm |\downarrow\rangle_1 |\downarrow\rangle_2) \quad (\text{B.1})$$

Clearly a projection onto any of these four states reveals nothing about the initial spin state of particle '1'. Furthermore measuring any one of the Bell states is equally likely regardless of the unknown quantum state  $|\phi\rangle_1$ .

The total quantum state of the combined three particle system is given by

$$|\Psi\rangle_{123} = |\phi\rangle_1 |\Psi^{(-)}\rangle_{23} \quad (\text{B.2})$$

This can be expanded in the Bell basis as

$$|\Psi\rangle_{123} = \frac{1}{2} [|\Psi^{(-)}\rangle_{12} (-\alpha |\uparrow\rangle_3 - \beta |\downarrow\rangle_3) + |\Psi^{(+)}\rangle_{12} (-\alpha |\uparrow\rangle_3 + \beta |\downarrow\rangle_3) + |\Phi^{(-)}\rangle_{12} (\beta |\uparrow\rangle_3 + \alpha |\downarrow\rangle_3) + |\Phi^{(+)}\rangle_{12} (-\beta |\uparrow\rangle_3 + \alpha |\downarrow\rangle_3)] \quad (\text{B.3})$$

From (B.3) it is clear that depending on the outcome of the Bell measurement a simple unitary transformation on the final quantum state of particle '3' is required in order to regain the original quantum state,  $|\phi\rangle$ . The correspondence between the measurements and the transformations is as follows

$$\begin{aligned} |\Psi^{(+)}\rangle_{12} &\rightarrow \begin{pmatrix} -1 & 0 \\ 0 & 1 \end{pmatrix}, & |\Psi^{(-)}\rangle_{12} &\rightarrow \begin{pmatrix} -1 & 0 \\ 0 & -1 \end{pmatrix} \\ |\Phi^{(+)}\rangle_{12} &\rightarrow \begin{pmatrix} 0 & 1 \\ -1 & 0 \end{pmatrix}, & |\Phi^{(-)}\rangle_{12} &\rightarrow \begin{pmatrix} 0 & 1 \\ 1 & 0 \end{pmatrix} \end{aligned} \quad (\text{B.4})$$

The quantum teleportation scheme has been illustrated in figure B.1.

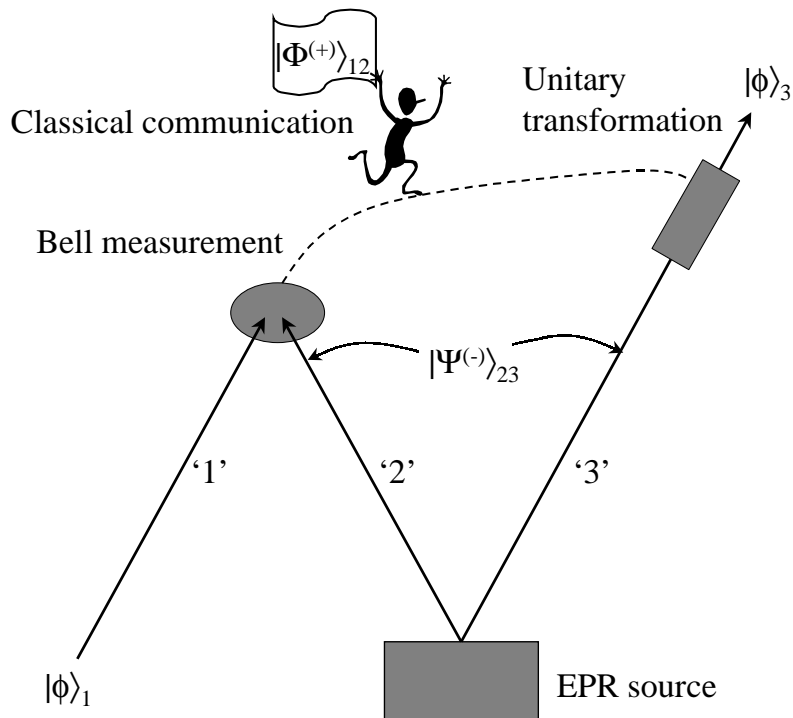


Figure B.1: The quantum teleportation scheme as it is proposed by Bennett *et. al.* for spin 1/2 particles. A joint Bell measurement on the input quantum state and one particle of an EPR pair results in the collapse of the wavefunction of the other particle in the EPR pair onto a coherent superposition of spin states. This is related to the input state by a simple unitary transformation.

It should be noted that without the information about, which unitary transformation to perform, the particle '3' will be in a random mixture of the four possible states in (B.3), and hence no information about the input quantum state  $|\phi\rangle_1$  can be extracted by performing a measurement on the particle. In order to complete the teleportation the information obtained in the Bell measurement must be transferred classically from the site of the measurement to the site of the transformation in order to perform the right operation on '3'. Whereas the quantum information stored in the nonlocal wavefunction  $|\Psi^{(-)}\rangle_{23}$  is transferred instantaneous, the classical information obtained in the measurement must obey the theory of relativity. Since both pieces of information are needed in order to project the original quantum state onto '3', causality is preserved in the teleportation process. This distinction between quantum and classical information should be understood in the following way. The Bell measurement leaves particle '3' in a coherent superposition of the two possible spin states. Although it is not possible to learn about the original quantum state from this, it is still closely related to the input state via the unitary transformations. This is a result of the quantum information that has been transferred. The classical part of the information is the outcome of the Bell measurement. This could for instance be an electrical current, which can be copied and broadcast without violating any rules of quantum mechanics.

The argumentation above has used only on linear transformations of the states, and hence it is straight forward to generalize the formalism to teleportation of mixed states as well as pure states.

Quantum teleportation of discrete quantum variables has been realized experimentally in the Quantum Optics groups in Innsbruck[115] and Rome[116]. In both experiments the polarization state of a

single photon was teleported, but whereas the first group used a polarization entangled EPR pair, the second group used EPR entangled optical paths.

## Appendix C

# Equations of motion for the IOPO quadrature phases

By combining the equations of motion for the IOPO (9.6) with the definitions for the quadrature phase operators (9.10) and (9.11), we obtain the equations of motion for the quadrature phases. For the fundamental field these are given by

$$\begin{aligned}
\frac{d}{dt} \begin{pmatrix} X_1 \\ Y_1 \end{pmatrix} &= \sqrt{8\kappa\mathcal{E}} \begin{pmatrix} \cos\theta_1 \\ \sin\theta_1 \end{pmatrix} - (\kappa + \gamma) \begin{pmatrix} X_1 \\ Y_1 \end{pmatrix} - A \left[ (X_1^2 + Y_1^2) \begin{pmatrix} 1 & -\rho \\ \rho & 1 \end{pmatrix} + \right. \\
&+ (X_+^2 - Y_+^2 - X_-^2 + Y_-^2) \begin{pmatrix} [C_1 + \rho S_1] & [\rho C_1 - S_1] \\ [\rho C_1 - S_1] & -[C_1 + \rho S_1] \end{pmatrix} \left. + \right. \\
&+ 2(X_+ Y_+ - X_- Y_-) \begin{pmatrix} -[\rho C_1 - S_1] & [C_1 + \rho S_1] \\ [C_1 + \rho S_1] & [\rho C_1 - S_1] \end{pmatrix} \left. \right] \begin{pmatrix} X_1 \\ Y_1 \end{pmatrix} + \sqrt{2\kappa} \begin{pmatrix} q_1^{in} \\ p_1^{in} \end{pmatrix} + \sqrt{2\gamma} \begin{pmatrix} Q_1^{in} \\ P_1^{in} \end{pmatrix} + \\
&+ \frac{\xi j_R}{\sqrt{\tau}} \begin{pmatrix} [X_1(C_2 - \Sigma S_2) + Y_1(\Sigma C_2 + S_2)] & -[X_1(\Sigma C_2 + S_2) - Y_1(C_2 - \Sigma S_2)] \\ [X_1(\Sigma C_2 + S_2) - Y_1(C_2 - \Sigma S_2)] & [X_1(C_2 - \Sigma S_2) + Y_1(\Sigma C_2 + S_2)] \end{pmatrix} \begin{pmatrix} q_2^{in} \\ p_2^{in} \end{pmatrix}
\end{aligned} \tag{C.1}$$

where we have defined  $A = \xi^2 g_R / 4\tau$  and the  $C$ 's and  $S$ 's are the abbreviations

$$\begin{aligned}
C_1 &= \cos(2\phi - 2\theta_1), & C_2 &= \cos(2\theta_1 - \theta_2) \\
S_1 &= \sin(2\phi - 2\theta_1), & S_2 &= \sin(2\theta_1 - \theta_2)
\end{aligned} \tag{C.2}$$

The 'in' quadratures describing the vacuum fields are defined in analogy with (9.10) as

$$\begin{aligned}
q_1^{in} &= a_1^{in} e^{i\theta_1} + (a_1^{in})^\dagger e^{-i\theta_1}, & Q_1^{in} &= \alpha_1^{in} e^{i\theta_1} + (\alpha_1^{in})^\dagger e^{-i\theta_1}, & q_2^{in} &= b^{in} e^{i\theta_2} + (b^{in})^\dagger e^{-i\theta_2} \\
p_1^{in} &= a_1^{in} e^{i\theta_1} - (a_1^{in})^\dagger e^{-i\theta_1}, & P_1^{in} &= \alpha_1^{in} e^{i\theta_1} - (\alpha_1^{in})^\dagger e^{-i\theta_1}, & p_2^{in} &= b^{in} e^{i\theta_2} - (b^{in})^\dagger e^{-i\theta_2}
\end{aligned} \tag{C.3}$$

Similarly we find the equations of motion for the subharmonics to be

$$\begin{aligned}
\frac{d}{dt} \begin{pmatrix} X_\pm \\ Y_\pm \end{pmatrix} &= -(\kappa + \gamma) \begin{pmatrix} X_\pm \\ Y_\pm \end{pmatrix} - A \left[ (X_\pm^2 + Y_\pm^2) \begin{pmatrix} 1 & -\rho \\ \rho & 1 \end{pmatrix} - (X_\mp^2 - Y_\mp^2) \begin{pmatrix} 1 & \rho \\ \rho & -1 \end{pmatrix} - \right. \\
&- 2X_\mp Y_\mp \begin{pmatrix} -\rho & 1 \\ 1 & \rho \end{pmatrix} + (X_+^2 - Y_+^2) \begin{pmatrix} [C_1 - \rho S_1] & [\rho C_1 + S_1] \\ [\rho C_1 + S_1] & -[C_1 - \rho S_1] \end{pmatrix} \left. + \right. \\
&+ 2X_+ Y_+ \begin{pmatrix} -[C_1 + \rho S_1] & [\rho C_1 - S_1] \\ [\rho C_1 - S_1] & [C_1 + \rho S_1] \end{pmatrix} \left. \right] \begin{pmatrix} X_\pm \\ Y_\pm \end{pmatrix} + \sqrt{2\kappa} \begin{pmatrix} q_\pm^{in} \\ p_\pm^{in} \end{pmatrix} + \sqrt{2\gamma} \begin{pmatrix} Q_\pm^{in} \\ P_\pm^{in} \end{pmatrix} + \\
&+ \frac{\xi j_R}{\sqrt{2\tau}} \begin{pmatrix} [(X_\pm - Y_\pm)(C_3 - \Sigma S_3) + (X_\mp - Y_\mp)(\Sigma C_3 + S_3)] \\ [(X_\pm - Y_\pm)(\Sigma C_3 + S_3) - (X_\mp - Y_\mp)(C_3 - \Sigma S_3)] \\ -[(X_\pm - Y_\pm)(\Sigma C_3 + S_3) - (X_\mp - Y_\mp)(C_3 - \Sigma S_3)] \\ [(X_\pm - Y_\pm)(C_3 - \Sigma S_3) + (X_\mp - Y_\mp)(\Sigma C_3 + S_3)] \end{pmatrix} \begin{pmatrix} q_2^{in} \\ p_2^{in} \end{pmatrix}
\end{aligned} \tag{C.4}$$

where we have used the abbreviations

$$C_3 = \cos(2\phi - \theta_2), \quad S_3 = \sin(2\phi - \theta_2) \quad (\text{C.5})$$

and the 'in' quadratures again are defined as

$$\begin{aligned} q_{\pm}^{in} &= \frac{1}{\sqrt{2}} [(a_+^{in} \pm a_-^{in}) e^{i\phi} + ((a_+^{in})^\dagger \pm (a_-^{in})^\dagger) e^{-i\phi}] \\ p_{\pm}^{in} &= \frac{-i}{\sqrt{2}} [(a_+^{in} \pm a_-^{in}) e^{i\phi} - ((a_+^{in})^\dagger \pm (a_-^{in})^\dagger) e^{-i\phi}] \\ Q_{\pm}^{in} &= \frac{1}{\sqrt{2}} [(\alpha_+^{in} \pm \alpha_-^{in}) e^{i\phi} + ((\alpha_+^{in})^\dagger \pm (\alpha_-^{in})^\dagger) e^{-i\phi}] \\ P_{\pm}^{in} &= \frac{-i}{\sqrt{2}} [(\alpha_+^{in} \pm \alpha_-^{in}) e^{i\phi} - ((\alpha_+^{in})^\dagger \pm (\alpha_-^{in})^\dagger) e^{-i\phi}] \end{aligned} \quad (\text{C.6})$$

Finally we find the second harmonic quadratures after the nonlinear medium to be

$$\begin{aligned} X_2(\ell) &= B [(X_1^2 - Y_1^2) (C_2 + RS_2) - 2X_1Y_1 (RC_2 - S_2) + (X_+^2 - Y_+^2 - X_-^2 + Y_-^2) (C_3 + RS_3) - \\ &\quad - 2(X_+Y_+ - X_-Y_-) (RC_3 - S_3)] \\ Y_2(\ell) &= B [(X_1^2 - Y_1^2) (RC_2 - S_2) - 2X_1Y_1 (C_2 + RS_2) + (X_+^2 - Y_+^2 - X_-^2 + Y_-^2) (RC_3 - S_3) + \\ &\quad + 2(X_+Y_+ - X_-Y_-) (C_3 + RS_3)] \end{aligned} \quad (\text{C.7})$$

with  $B$  defined to be  $B = \xi h_R/2$  and the abbreviations for the cosines and sines defined above. The functions  $\rho$ ,  $\Sigma$  and  $R$  have been defined in (9.7). In the equations (C.7) we have omitted the vacuum input terms since we are only interested in calculating the steady state values of the second harmonic fields.

With the goal of simplifying the complicated structure of (C.1) and (C.4) in order to obtain the steady state fields, we now seek to choose the phases  $\theta_1$  and  $\phi$  in a way such that the steady state quadratures  $\bar{Y}_1 = \bar{X}_- = \bar{Y}_+ = 0$ . Keeping in mind that the expectation values of the 'in' fields are zero, we readily see that we can put  $\bar{Y}_1 = 0$  provided we choose  $\theta_1$  so that

$$\sin \theta_1 = A \bar{X}_1 \frac{\rho \bar{X}_1^2 - (\rho C_1 + S_1) Z^2}{\sqrt{8\kappa\mathcal{E}}} \quad (\text{C.8})$$

where we have defined  $Z^2 = \bar{X}_+^2 + \bar{Y}_-^2$ . With this choice of  $\theta_1$  we find in a similar way that we can choose  $\bar{X}_- = \bar{Y}_+ = 0$  when  $\phi$  is chosen so that the equation

$$\rho Z^2 + \bar{X}_1^2 (\rho C_1 + S_1) = 0 \quad (\text{C.9})$$

is obeyed. It can be checked that it is always possible to choose  $\phi$  so that (C.9) is fulfilled. Below threshold  $Z = 0$  and  $\bar{X}_1 \neq 0$ . As a result we have to demand that  $\rho C_1 + S_1 = 0$  in order to satisfy (C.9). This gives us the natural choice of  $\phi$  which should be used in order to separate the squeezed from the antisqueezed quadratures. Now the steady state solutions for the subharmonics reduce to

$$\begin{aligned} A \bar{X}_+ [\bar{X}_1^2 (C_1 - \rho S_1) + Z^2 + \frac{\kappa + \gamma}{A}] &= 0 \\ A \bar{Y}_- [\bar{X}_1^2 (C_1 - \rho S_1) + Z^2 + \frac{\kappa + \gamma}{A}] &= 0 \end{aligned} \quad (\text{C.10})$$

Clearly these have the solution  $\bar{X}_+ = \bar{Y}_- = 0$  corresponding to IOPO operation below threshold, however above threshold we must demand that the square brackets in (C.10) are zero. Combining this with our choice of  $\phi$  (C.9) in order to eliminate  $C_1$  and  $S_1$ , we arrive at the excitation of the subharmonics above threshold which is given by the solution of

$$\left[ Z^2 + \left( \frac{\kappa + \gamma}{A} \right)^2 \right] + \rho^2 Z^4 = (1 + \rho^2) \bar{X}_1^4 \quad (\text{C.11})$$

Similarly we find the fundamental field from (C.1) to be the solution of

$$\left[ \frac{\sqrt{8\kappa\mathcal{E}} \cos \theta_1}{A \bar{X}_1} - \bar{X}_1^2 - \frac{\kappa + \gamma}{A} \right]^2 - \left( \frac{Z}{\bar{X}_1} \right)^4 = Z^4 (1 + \rho^2) \quad (\text{C.12})$$

and below threshold ( $Z = 0$ ) this reduces to

$$\bar{X}_1 \left( \bar{X}_1^2 + \frac{\kappa + \gamma}{A} \right) = \frac{\sqrt{8\kappa\mathcal{E}}}{A} \cos \theta_1 \quad (\text{C.13})$$

Here  $\theta_1$  can be found from (C.8) which below threshold simplifies to

$$\sin \theta_1 = \frac{\rho A}{\sqrt{8\kappa\mathcal{E}}} \bar{X}_1^3 \quad (\text{C.14})$$

Finally we find from (C.7) that the steady state second harmonic quadrature after the nonlinear medium  $\bar{X}_2(\ell)$  becomes zero below threshold if  $\theta_2$  is chosen in such a way that  $C_2 + RS_2 = 0$ .

# Bibliography

- [1] L. Lugiato. *Europhys. News*, page 130, July / August 1998.
- [2] R. C. Eckardt, C. D. Nabors, W. J. Kozlowsky, and R. L. Byer. *J. Opt. Soc. Am. B*, 8:646, 1991.
- [3] R. Loudon. *The Quantum Theory of Light*. Oxford University Press, New York, second edition, 1983.
- [4] C. M. Caves and B. L. Schumaker. *Phys. Rev. A*, 31:3068, 1985.
- [5] D. F. Walls. *Nature*, 306:141, 1983.
- [6] E. S. Polzik, J. Carri, and H. J. Kimble. *Phys. Rev. Lett.*, 68:3020, 1992.
- [7] E. S. Polzik, J. Carri, and H. J. Kimble. *Appl. Phys. B*, 55:279, 1992.
- [8] N. Ph. Georgiades, E. S. Polzik, K. Edamatsu, H. J. Kimble, and A. S. Parkins. *Phys. Rev. Lett.*, 75:3426, 1995.
- [9] N. Ph. Georgiades, E. S. Polzik, and H. J. Kimble. *Phys. Rev. A, Rapid Comm.*, 55:R1605, 1997.
- [10] E. S. Polzik, J. L. Sørensen, and J. Hald. *Appl. Phys. B*, 66:759, 1998.
- [11] J. L. Sørensen, J. Hald, and E. S. Polzik. *Phys. Rev. Lett.*, 80:3487, 1998.
- [12] P. H. Souto Ribeiro, C. Schwob, A. Maitre, and C. Fabre. *Opt. Lett.*, 22:1893, 1997.
- [13] S. Kasapi, S. Lathi, and Y. Yamamoto. 7th rochester conference on coherence and quantum optics, June 1995.
- [14] D. C. Kilper, A. C. Schaefer, J. Erland, and D. G. Steel. *Phys. Rev. A*, 54:R1785, 1996.
- [15] S. Kasapi, S. Lathi, and Y. Yamamoto. *Opt. Lett.*, 22:478, 1997.
- [16] F. Marin, A. Bramati, V. Jost, and E. Giacobino. *Optics Comm.*, 140:146, 1997.
- [17] Y. Li, P. Lynam, M. Xiao, and P. J. Edwards. *Phys. Rev. Lett.*, 78:3105, 1997.
- [18] S. Reynaud and A. Heidmann. *Opt. Comm.*, 71:209, 1989.
- [19] S. Chaturvedi and P. D. Drummond. *Phys. Rev. A*, 55:912, 1997.
- [20] C. J. Mertens, T. A. B. Kennedy, and S. Swain. *Phys. Rev. Lett.*, 71:2014, 1993.
- [21] S. M. Barnett and P. L. Knight. *J. Opt. Soc. Am. B*, 2:467, 1985.
- [22] B. Yurke. *Phys. Rev. A*, 32:300, 1985.
- [23] J. C. Baumert, P. Gunter, and H. Melchior. *Opt. Comm.*, 48:215, 1983.

- [24] H. Mabuchi, E. S. Polzik, and H. J. Kimble. *J. Opt. Soc. Am. B*, 11:2023, 1994.
- [25] A. Motes and J. J. Kim. *J. Opt. Soc. Am. B*, 4:1379, 1987.
- [26] L. Shiv, J. L. Sørensen, E. S. Polzik, and G. Mizell. *Opt. Lett.*, 20:2270, 1995.
- [27] L. Holtmann, M. Unland, E. Kratzig, and G. Godefroy. *Appl. Phys. A*, 51:13, 1990.
- [28] L. Holtmann, K. Buse, A. Groll, H. Hesse, and E. Kratzig. *Appl. Phys. A*, 53:81, 1991.
- [29] R. D. Guenther. *Modern Optics*. John Wiley and Sons, USA, 1990.
- [30] E. S. Polzik and H. J. Kimble. *Opt. Lett.*, 16:1400, 1991.
- [31] G. A. Brost, R. A. Motes, and J. R. Rotge. *J. Opt. Soc. Am. B*, 5:1879, 1988.
- [32] M. Exner. *Computer simulation of extrinsic and intrinsic defects in  $KTaO_3$  and  $KNbO_3$* . PhD thesis, 1994.
- [33] L. E. Busse, L. Goldberg, M. R. Surette, and G. Mizell. *J. Appl. Phys.*, 75:1102, 1993.
- [34] L. Shiv. Blue light induced infrared absorption in  $knbo_3$ . Master's thesis, Institute of Physics and Astronomy, University of Aarhus, Denmark., 1995.
- [35] L. A. Lugiato, G. Strini, and F. De Martini. *Opt. Lett.*, 8:256, 1983.
- [36] G. Milburn and D. F. Walls. *Opt. Comm.*, 39:401, 1981.
- [37] H. P. Yuen and J. H. Shapiro. *Opt. Lett.*, 4:334, 1979.
- [38] K. Schneider, M. Lang, J. Mlynek, and S. Schiller. *Optics Express* (<http://epubs.osa.org/opticsexpress/>), 2:59, 1998.
- [39] K. Schneider, S. Schiller, J. Mlynek, M. Bode, and I. Freitag. *Opt. Lett.*, 21:1999, 1996.
- [40] A. Ashkin, G. D. Boyd, and J. M. Dziedzic. *IEEE J. Quantum Electron.*, QE-2:109, 1966.
- [41] G. C. Bjorklund, M. D. Levenson, W. Lenth, and C. Ortiz. *Appl. Phys. B*, 32:145, 1983.
- [42] L. Mandel. *Phys. Rev. Lett.*, 49:136, 1982.
- [43] K. Schneider, P. Kramper, S. Schiller, and J. Mlynek. *Opt. Phot. News*, 8:51, 1997.
- [44] J. J. Zayhowski. *Opt. Lett.*, 22:169, 1997.
- [45] R. G. Batchko, D. R. Weise, T. Plettner, G. D. Miller, M. M. Fejer, and R. L. Byer. *Opt. Lett.*, 23:168, 1998.
- [46] J. E. M. Goldsmith, E. W. Weber, and T. W. Hansch. *Phys. Rev. Lett.*, 41:1525, 1978.
- [47] D. N. Stacey. *Physica Scripta*, T40:15, 1992.
- [48] T. W. Hänsch and C. Wieman. *Phys. Rev. Lett.*, 36:1170, 1976.
- [49] D. S. Alavi, R. S. Hartman, and D. H. Waldeck. *J. Chem. Phys.*, 92:4055, 1990.
- [50] T. W. Hansch and B. Couillaud. *Opt. Comm.*, 35:441, 1980.
- [51] J. Hald. Quantum noise in cold atomic spin measurements. Part a progress report, Institute of Physics and Astronomy, University of Aarhus, Denmark, 1997.

- [52] E. L. Raab, M. Prentiss, A. Cable, S. Chu, and D. E. Pritchard. *Phys. Rev. Lett.*, 59:2631, 1987.
- [53] C. W. Oates, K. R. Vogel, and J. L. Hall. *Phys. Rev. Lett.*, 76:2866, 1996.
- [54] R. W. Fox, S. L. Gilbert, L. Hollberg, and J. H. Marquardt. *Opt. Lett.*, 18:1456, 1993.
- [55] T. Van der Veldt, J. Roch, P. Grelu, and P. Grangier. *Opt. Comm.*, 137:420, 1997.
- [56] N. Ph. Georgiades, E. S. Polzik, and H. J. Kimble. *Opt. Lett.*, 19:1474, 1994.
- [57] M. Drewsen, Ph. Laurent, A. Nadir, G. Santarelli, A. Clarion, Y. Castin, D. Grison, and C. Salomon. *Appl. Phys. B*, 59:283, 1994.
- [58] K. E. Gibble, S. Kasapi, and S. Chu. *Opt. Lett.*, 17:526, 1992.
- [59] Y. Castin, H. Wallis, and J. Dalibard. *J. Opt. Soc. Am. B*, 6:2046, 1989.
- [60] P. Lett, R. Watts, C. Westbrook, W. D. Phillips, P. Gould, and H. Metcalf. *Phys. Rev. Lett.*, 61:169, 1988.
- [61] Y. Shevy, D. S. Weiss, P. J. Ungar, and S. Chu. *Phys. Rev. Lett.*, 62:1118, 1989.
- [62] J. Dalibard and C. Cohen-Tannoudji. *J. Opt. Soc. Am. B*, 6:2023, 1989.
- [63] S. Stenholm. *Foundations of Laser Spectroscopy*. John Wiley and Sons, USA, 1984.
- [64] A. S. Chirkin, A. A. Orlov, and D. Yu. Paraschuk. *Quantum Electron.*, 23:870, 1993.
- [65] A. P. Alodjants, S. M. Arakelian, and A. S. Chirkin. *JETP*, 81:34, 1995.
- [66] V. N. Beskrovnyi and A. S. Chirkin. *Quantum Electron.*, 26:843, 1996.
- [67] V. N. Beskrovnyi and A. S. Chirkin. *Quantum Semiclass. Opt.*, 10:263, 1998.
- [68] P. Grangier, R. E. Slusher, B. Yurke, and A. LaPorta. *Phys. Rev. Lett.*, 59:2153, 1987.
- [69] J. M. Jauch and F. Rohrlich. *The Theory of Photons and Electrons*. Springer Verlag, USA, second expanded edition, 1980.
- [70] M. Gehrtz, G. C. Bjorklund, and E. A. Whittaker. *J. Opt. Soc. Am. B*, 2:1510, 1985.
- [71] E. A. Whittaker, M. Gehrtz, and G. C. Bjorklund. *J. Opt. Soc. Am. B*, 2:1320, 1985.
- [72] X. Zhu and D. T. Cassidy. *J. Opt. Soc. Am. B*, 14:1945, 1997.
- [73] J. M. Supplee, E. A. Whittaker, and W. Lenth. *Appl. Opt.*, 33:6294, 1994.
- [74] M. Weissbluth. *Atoms and Molecules*. Academic Press, USA, 1978.
- [75] J. L. Sørensen, J. Hald, and E. S. Polzik. *Opt. Lett.*, 23:25, 1998.
- [76] M. Mitsunaga, T. Mukai, K. Watanabe, and T. Mukai. *J. Opt. Soc. Am. B*, 13:2696, 1996.
- [77] W. Gawlik, J. Kowalski, R. Neumann, and F. Trager. *Phys. Lett. A*, 48:283, 1974.
- [78] S. Giraud-Cotton, V. P. Kaftandjian, and L. Klein. *Phys. Lett. A*, 88:453, 1982.
- [79] K. H. Drake, W. Lange, and J. Mlynek. *Opt. Comm.*, 66:315, 1988.
- [80] A. Weis, J. Wurster, and S. I. Kanorsky. *J. Opt. Soc. Am. B*, 10:716, 1993.

- [81] S. Machida, Y. Yamamoto, and Y. Itaya. *Phys. Rev. Lett.*, 58:1000, 1987.
- [82] T.-C. Zhang, J.-Ph. Poizat, P. Grelut, J.-F. Roch, P. Grangier, F. Marin, A. Bramati, V. Jost, M. D. Levenson, and E. Giacobino. *Quantum Semiclass. Opt.*, 7:601, 1995.
- [83] P. Lodahl. Noise of the frequency doubled diode laser. Master's thesis, Institute of Physics and Astronomy, University of Aarhus, 1997.
- [84] Y. Shevy and H. Deng. *Opt. Lett.*, 23:472, 1998.
- [85] T. Yabuzaki, T. Mitsui, and U. Tanaka. *Phys. Rev. Lett.*, 67:2453, 1991.
- [86] D. H. McIntyre, C. E. Fairchild, J. Cooper, and R. Walsler. *Opt. Lett.*, 18:1816, 1993.
- [87] S. Lathi, S. Kasapi, and Y. Yamamoto. *Opt. Lett.*, 21:1600, 1993.
- [88] E. B. Aleksandrov and A. B. Mamyrin. *Sov. Phys. JETP*, 45:247, 1977.
- [89] A. Lambrecht, E. Giacobino, and S. Reynaud. *Quantum Semiclass. Opt.*, 8:457, 1996.
- [90] V. P. Kozlov. *Sov. Phys. JETP*, 45:249, 1997.
- [91] E. B. Aleksandrov and V. S. Zapasski. *Sov. Phys. JETP*, 54:64, 1981.
- [92] H. Ritsch, P. Zoller, and J. Cooper. *Phys. Rev. A*, 41:2653, 1990.
- [93] A. M. Bacon, H. Z. Zhao, L. J. Wang, and J. E. Thomas. *Phys. Rev. Lett.*, 75:1296, 1995.
- [94] H. Z. Zhao, Z. H. Lu, and J. E. Thomas. *Phys. Rev. Lett.*, 79:613, 1997.
- [95] W. M. Itano, J. C. Bergquist, J. J. Bollinger, J. M. Gilligan, D. J. Heinzen, F. L. Moore, M. G. Raizen, and D. J. Wineland. *Phys. Rev. A*, 47:3554, 1993.
- [96] K. Blum. *Density matrix theory and applications*. Plenum Press, USA, 1981.
- [97] F. Laloë, M. Leduc, and P. Minguzzi. *J. Physique*, 30:277, 1969.
- [98] R. J. Thompson, G. Rempe, and H. J. Kimble. *Phys. Rev. Lett.*, 68:1132, 1992.
- [99] C. J. Hood, M. S. Chapman, T. W. Lynn, and H. J. Kimble. *Phys. Rev. Lett.*, 80:4157, 1998.
- [100] A. Kuzmich, K. Mølmer, and E. S. Polzik. *Phys. Rev. Lett.*, 79:4782, 1997.
- [101] M. Kitagawa and M. Ueda. *Phys. Rev. A*, 47:5138, 1993.
- [102] D. J. Wineland, J. J. Bollinger, W. M. Itano, and D. J. Heinzen. *Phys. Rev. A*, 50:67, 1994.
- [103] T. Sleator, E. L. Hahn, C. Hilbert, and J. Clarke. *Phys. Rev. Lett.*, 55:1742, 1985.
- [104] A. M. Bacon, H. Z. Zhao, L. J. Wang, and J. E. Thomas. *Applied Optics*, 34:5326, 1995.
- [105] E. B. Alexandrov and V. A. Bonch-Bruевич. *Optical Engineering*, 31:711, 1992.
- [106] A. Einstein, B. Podolsky, and N. Rosen. *Phys. Rev.*, 47:777, 1935.
- [107] N. Bohr. *Phys. Rev.*, 48:696, 1935.
- [108] D. Bohm and Y. Aharonov. *Phys. Rev.*, 108:1070, 1957.
- [109] J. S. Bell. *Speakable and unspeakable in quantum mechanics*, volume 1. Cambridge University Press, Cambridge UK, 1991.

- [110] A. Aspect, J. Dalibard, and G. Roger. *Phys. Rev. Lett.*, 49:1804, 1982.
- [111] S. L. Braunstein. *Nature*, 394:47, 1998.
- [112] K. Mattle, H. Weinfurter, P. G. Kwiat, and A. Zeilinger. *Phys. Rev. Lett.*, 76:4656, 1996.
- [113] C. H. Bennett, G. Brassard, C. Crepeau, R. Jozsa, A. Peres, and W. K. Wootters. *Phys. Rev. Lett.*, 70:1895, 1993.
- [114] W. K. Wootters and W. H. Zurek. *Nature*, 299:802, 1982.
- [115] D. Bouwmeester, J. Pan, K. Mattle, M. Eibl, H. Weinfurter, and A. Zeilinger. *Nature*, 390:575, 1997.
- [116] D. Boschi, S. Branca, F. De Martini, L. Hardy, and S. Popescu. *Phys. Rev. Lett.*, 80:1121, 1998.
- [117] L. Vaidman. *Phys. Rev. A*, 49:1473, 1994.
- [118] S. L. Braunstein and H. J. Kimble. *Phys. Rev. Lett.*, 80:869, 1998.
- [119] Z. Y. Ou, S. F. Pereira, and H. J. Kimble. *Appl. Phys. B*, 55:265, 1992.
- [120] H. J. Kimble. Quantum fluctuations in quantum optics - squeezing and related phenomena. Lecture notes, Les Houches LIII, 1990.
- [121] J. L. Sørensen, J. Hald, N. Jørgensen, and E. S. Polzik. *Quantum and Semiclass. Opt.*, 9:239, 1997.
- [122] C. W. Gardiner. *Phys. Rev. Lett.*, 56:1917, 1986.
- [123] A. K. Ekert. *Phys. Rev. Lett.*, 67:661, 1991.
- [124] C. H. Bennett, G. Brassard, and N. D. Mermin. *Phys. Rev. Lett.*, 68:557, 1992.
- [125] M. A. M. Marte. *Phys. Rev. A*, 49:R3166, 1994.
- [126] M. A. M. Marte. *Phys. Rev. Lett.*, 74:4815, 1995.
- [127] M. A. M. Marte. *J. Opt. Soc. Am. B*, 12:2296, 1995.
- [128] S. Schiller and R. L. Byer. *J. Opt. Soc. Am. B*, 10:1696, 1993.
- [129] S. Schiller, G. Breitenbach, R. Paschotta, and J. Mlynek. *Appl. Phys. Lett.*, 68:3374, 1996.
- [130] A. G. White, P. K. Lam, M. S. Taubman, M. A. M. Marte, S. Schiller, D. E. McClelland, and H. A. Bachor. *Phys. Rev. A*, 55:4511, 1997.
- [131] A. G. White, J. Mlynek, and S. Schiller. *Europhys. Lett.*, 35:425, 1996.
- [132] A. G. White, M. S. Taubman, T. C. Ralph, P. K. Lam, D. E. McClelland, and H. A. Bachor. *Phys. Rev. A*, 54:3400, 1996.
- [133] S. F. Pereira, M. Xiao, H. J. Kimble, and J. L. Hall. *Phys. Rev. A*, 38:R4931, 1988.
- [134] S. Schiller, R. Bruckmeier, and A. G. White. *Opt. Comm.*, 138:158, 1997.
- [135] J. Maeda and K. Kikuchi. *Opt. Lett.*, 21:821, 1996.
- [136] M. J. Collett and R. B. Levien. *Phys. Rev. A*, 43:5068, 1991.
- [137] S. Reynaud, C. Fabre, and E. Giacobino. *J. Opt. Soc. Am. B*, 4:1520, 1987.

- [138] M. J. Collett and D. F. Walls. *Phys. Rev. A*, 32:2887, 1985.
- [139] R. Paschotta, M. J. Collett, P. Kurz, K. Fiedler, H. A. Bachor, and J. Mlynek. *Phys. Rev. Lett.*, 72:3807, 1994.
- [140] M. D. Reid and P. D. Drummond. *Phys. Rev. A*, 40:4493, 1989.
- [141] P. D. Drummond and M. D. Reid. *Phys. Rev. A*, 41:3930, 1990.
- [142] P. W. Milonni and J. H. Eberly. *Lasers*. Wiley and Sons, USA, 1988.
- [143] G. D. Boyd and D. A. Kleinman. *J. Appl. Phys.*, 39:3597, 1968.
- [144] S. L. Braunstein, A. Mann, and M. Revzen. *Phys. Rev. Lett.*, 68:3259, 1992.